Experimental Investigation of Heat Transfer and Pressure Drop of Pipes with Internal Roughness

by

Abdolreza Raoufi

A thesis submitted in partial fulfillment of the requirements for the degree of

Master of Science

Department of Mechanical Engineering
University of Alberta

ABSTRACT

In many industrial heat exchangers, it is desirable to improve the rate of heat transfer from a pipe wall to the fluid flow. This improvement is commonly made by adding some form of roughness to the pipe surface. However, the added roughness often leads to an increase in the pressure drop of the flow. The objective of this study is to experimentally compare the rate of heat transfer enhancement and friction factor for fully developed turbulent pipe flows with different roughness elements.

The experiments were conducted on a smooth pipe and four pipes with different internal roughness elements manufactured using steel mesh and ball bearings. The nominal diameter of all pipes was two inches. The working fluid was air, and the flow properties were measured at Reynolds numbers of 20,000 to 90,000 in increments of 10,000 under a constant pipe wall temperature of 375°C. The Nusselt number and friction factor of the rough pipes were evaluated, and the results were compared to the smooth pipe. It was found that Nusselt number of the pipes with mesh-type roughness increases by approximately 5%, while the Nusselt number of the pipes with roughness elements made from ball-bearings increased by 23 to 33%. The increase of friction factor was 66% for the pipes covered with mesh and 33 to 43% for pipes with ball bearings. The experimental results indicate that adding ball bearings to the internal surface of the pipe can lead to a significant improvement in the rate of heat-transfer. Adding a mesh-type roughness to the pipes can have marginal improvements in heat transfer and a large increase in frictional losses, and therefore it is not recommended.

ACKNOWLEDGEMENTS

I would like to express my deepest appreciation to my supervisor, Dr. Sina Ghaemi, for his valuable time and extraordinary effort he dedicated to help me during the last two years. You gave me honest feedbacks and kindly encouraged me to continue. Your invaluable ideas, intellectual support, high standards and values, and passionate dedication to research paved my way through the course of my research. I would also like to sincerely thank my supervisory committee, Dr. Morris R. Flynn and Dr. Joshua Brinkerhoff for their guidance, supports, and invaluable comments.

This research was conducted in collaboration with Quantiam Technologies Inc. The financial support of the industrial partners and of the Natural Sciences and Engineering Research Council of Canada is gratefully acknowledged. I would also acknowledge the support provided by industry partner and all personnel who participated in this study. I would like to thank Dr. Paul-Emile Trudeau, Mr. Andrew Williams, and Dr. Craig Metcalfe who diligently helped in the process.

I would like to take this opportunity to thank all individuals, colleagues and friends who assisted me during this research. I particularly recognize Mr. Les Dean, Dr. Prashant Waghmare, Mr. Saqeeb Islam, Mr. Lucas Warwaruk, Mr. Sen Wang, and Mr. Jack Zheng for all their help during my studies.

Finally, I would like to express my deepest gratitude to my beloved family. My special thanks go to my mother, Mitra Abdollahian, and my father, Abdolraouf Raoufi, for their never-ending love and supports. Your love, supports, and encouragements are my reliable resources in the journey of

life. I also express my appreciation to my siblings, Ghazaleh, Nassim, and Mohammad, for their love and encouragement.

TABLE OF CONTENTS

NOMENCLATURE AND ACRONYMS

Symbols	Definition
$\dot{m}$	Mass flow rate
μ	Dynamic viscosity
μ_f	Average viscosity of the fluid at the test section
A	Pipe cross section area
A_{st}	Heated pipe surface area
B	Intercept constant of the log-law
C_p	Specific heat capacity
D	Internal diameter of the pipe
f	Friction factor
f_f	Friction factor in test section at T_t
k	Thermal conductivity
L	The distance between the test section pressure ports
Nu	Nusselt number
R	Pipe internal radius

r	Radial distance from pipe centerline
Re	Reynolds number of the flow where the Pitot tube is located
Re_t	Average Reynolds number at the test section
$RMSE$	Root mean square error
T	temperature
t	time
T_b	Bulk temperature
$T_{b,d}$	Downstream bulk temperature
$T_{b,u}$	Upstream bulk temperature
T_m	Mean flow temperature
T_r	Room temperature
T_s	Surface temperature
T_t	Flow temperature along test section
U_b	Bulk velocity at Pitot tube
$U_{t,b}$	Bulk velocity along section
U_c	Centerline velocity
u_τ	Friction velocity
ΔP	Pressure drop along the test-section
ΔP_P	Pitot tube differential pressure

ε	Roughness
κ	von Karman constant
v	Kinematic viscosity
ρ	Density of the flow where the Pitot tube is located
ρ_2	Average density of the flow at the test section

Abbreviations

MB37	Pipe with ball bearings with 37 mm spacing
MB50	Pipe with ball bearings with 50 mm spacing
MC1	Pipe covered with mesh and one layer of coating
MC2	Pipe covered with mesh and one layer of coating
PP	Pressure port
R	Rake
RPM	Revolutions per minute
RT	Rake thermocouple
SM	Smooth pipe
TC	Thermocouple
W	Wall
WT	Wall Thermocouple

LIST OF TABLES

LIST OF FIGURES

Chapter 1.

Introduction

The increase in the internal roughness of pipes can increase the skin-friction drag and the rate of heat-transfer from the flow to the surrounding medium. In the design of many mechanical equipment such as heat exchangers, it is desirable to improve the rate of heat transfer. Thus, increasing the internal roughness of pipes seem to be a good practice. However, the greater roughness would also result in a larger skin-friction drag. The objective of this research is to compare pipes with different internal roughness based on their ability to transfer heat while maintaining a small skin-friction drag.

The impact of roughness elements, such as corrugations, dimples, and twisted tape inserts, on pressure drop and heat transfer of pipe flow have been investigated in the past literature, but there are still major gaps that need to be filled. Wang et al. (2017) studied heat transfer in helically corrugated tubes to find the optimum values for height-to-diameter and pitch-to-diameter ratios of the corrugation for maximizing the rate of heat transfer relative to the increase in friction. Bunker et al. (2003) conducted experimental studies on circular pipes with dimples and found a correlation between Nusselt, Prandtl and Reynolds number. Eiamsa-ard et al. (2010) studied the effects of twisted tape parameters, such as twist angle, on the rate of heat transfer. The shortcomings of the previous studies include the limited range of *Re*, the limited pipe surface temperature and the size of the pipe itself. To extend the investigations to other types of internal roughness, and to fill these gaps in past literature, this research will conduct an experimental investigation on pipes with mesh- and bearing-type roughness.

A pipe with an internal diameter of 2 inch, at a wall temperature of 375°C, and a wide range of Reynolds numbers from 20,000 to 90,000 is considered. The relatively higher wall temperature,

larger pipe size and wider range of Reynolds number in this study compared to previous research aims to match the working condition with that of cracking furnaces used for ethylene production.

Chapter two provides a literature review on fluid dynamics and thermal properties of pipe flows as well as studies conducted on pipes with different roughness. Chapter three presents the details of the experimental facility. In Chapter four, the methodology used for evaluating the flow properties from measurements are explained. Chapter five presents the results of experiments on a reference pipe with smooth walls, while Chapter six compares the thermal and hydrodynamics performance of the pipes with internal roughness. This study improves the understanding of heat transfer in pipes which in turn can help conserve energy and can address environmental problems such as those related to carbon emissions in power plant boilers and in furnaces.

Chapter 2.

Literature Review

The use of three-dimensional roughness geometries inside a turbulent pipe flow to enhance heat transfer from the wall to the flow has been extensively studied due to the broad range of its applications. Some of the more commonly used enhancement techniques include swirl generators, dimples or other forms of integral roughness, and inserted devices such as coils and twisted tapes. In this chapter, first the basic science behind the hydrodynamics of laminar and turbulent pipe flow is explored. After that, the fundamentals of convective heat transfer from a pipe at higher surface temperature to the flow is provided. Finally, a review of the more recent literature on different heat transfer techniques is provided.

2.1 Equations of motion for pipe flows

The equations of motion in pipe flows can be derived from applying the conservation laws for mass, and momentum to a control volume. The equations of motion relate the acceleration of a fluid particle to the surface and net body forces. By expressing the viscous stresses that act on a fluid particle as a function of local deformation or strain rate, the Navier-Stokes momentum equations can be obtained for Newtonian fluids.

2.1.1 Navier-Stokes equations for incompressible pipe flow

The continuity and Navier-Stokes momentum equations for Newtonian fluids under the assumptions of incompressible flow and constant viscosity in a cylindrical coordinate system is given in

$$\frac{1}{r}\frac{\partial ru\prime}{\partial r}+\frac{1}{r}\frac{\partial v\prime}{\partial \theta}+\frac{\partial u\prime}{\partial x}=0, \tag{2.1}$$

$$\frac{\partial v\prime}{\partial t}+\frac{1}{r}\frac{\partial rv\prime^2}{\partial r}+\frac{1}{r}\frac{\partial w\prime v\prime}{\partial \theta}+\frac{\partial u\prime v\prime}{\partial x}-\frac{w\prime^2}{r}=-\frac{1}{\rho}\frac{\partial p\prime}{\partial r}+\nu\left(\Delta v'-\frac{v\prime}{r^2}-\frac{2}{r^2}\frac{\partial w\prime}{\partial \theta}\right), \tag{2.2}$$

$$\frac{\partial w\prime}{\partial t}+\frac{1}{r}\frac{\partial rv\prime w\prime}{\partial r}+\frac{1}{r}\frac{\partial w\prime^2}{\partial \theta}+\frac{\partial u\prime w\prime}{\partial x}+\frac{v\prime w\prime}{r}=-\frac{1}{\rho}\frac{\partial p'}{r\partial \theta}+\nu\left(\Delta w'-\frac{w'}{r^2}-\frac{2}{r^2}\frac{\partial v'}{\partial \theta}\right), \text{and} \tag{2.3}$$

$$\frac{\partial u'}{\partial t}+\frac{1}{r}\frac{\partial ru'w'}{\partial r}+\frac{1}{r}\frac{\partial w'u'}{\partial \theta}+\frac{\partial u'^2}{\partial x}=-\frac{1}{\rho}\frac{\partial p'}{\partial x}+\nu\Delta u' \tag{2.4}$$

where Δ is Laplacian operator (also shown by ∇^2) in cylindrical coordinate system, P' is pressure, ρ is density, v is kinematic viscosity, and u', v' and w' are instantaneous components of velocity in the x, r, and θ directions respectively. Here, r represents the radial direction of the pipe, x the axial direction, θ the angular direction. The origin of r in this coordinate system ($r = 0$) is located at the centerline of the pipe. The origin of x is the inlet of the pipe. The above equations are only valid in cases where the fluid viscosity and density are constant. When the working fluid is incompressible, the density of the fluid can be ignored (except when it is multiplied by gravitational acceleration). A dimensionless number called Mach number, defined as the ratio of the flow velocity to the speed of sound, can be used to distinguish between compressible and incompressible gas flows. If the Mach number is less than 0.3, the flow can be assumed to be incompressible. The viscosity of incompressible Newtonian fluids changes with temperature which means that the viscosity of the fluid is not constant when there are temperature variations inside a fluid flow. However, according to Incropera et al. (2007) we can assume that the viscosity is constant when pipe surface temperature is constant. This constant viscosity is evaluated at a temperature equal to the arithmetic mean between the inlet and outlet bulk temperatures of the pipe flow. The evaluation of viscosity will be explained in more detail in chapter four. In many applications, the knowledge of the mean velocity field is enough to give a description of the flow behaviour. To find the mean (time-averaged) velocity field, we first need to decompose turbulent velocity into mean velocity and turbulent fluctuations. This decomposition is shown in

$$u'_i = u_i + \tilde{u}_i. \tag{2.5}$$

where u'_i depicts the ith component of the velocity field, u_i is the ith component of ensemble average of the velocity field, and $\tilde{u}_i$ is the ith component of the fluctuating velocity. The ensemble average of velocity is given in

$$u_i = \frac{1}{N}\sum_{n=1}^{N} u'(x,t:n) \tag{2.6}$$

where $u(x,t:n)$ is the nth independent realization of the velocity field. Similarly, other instantaneous flow properties can be separated into their mean and fluctuating components. The average of fluctuating velocity, $\overline{\tilde{u}_i}$, is zero. By substituting the velocity terms in equations 2.1 to (2.4) with their mean and fluctuating components, we find

$$\frac{1}{r}\frac{\partial rv}{\partial r} + \frac{1}{r}\frac{\partial w}{\partial \theta} + \frac{\partial u}{\partial x} = 0, \tag{2.7}$$

$$\frac{1}{r}\frac{\partial rv^2}{\partial r} + \frac{1}{r}\frac{\partial vw}{\partial \theta} + \frac{\partial vu}{\partial x} - \frac{w^2}{r} = -\frac{1}{\rho}\frac{\partial p}{\partial r} + \vartheta\left(\Delta v - \frac{v}{r^2} - \frac{2}{r^2}\frac{\partial w}{\partial \theta}\right) - \frac{1}{r}\frac{\partial r\overline{\tilde{v}^2}}{\partial r} - \frac{1}{r}\frac{\partial \overline{\tilde{v}\tilde{w}}}{\partial \theta} - \frac{\partial \overline{\tilde{v}\tilde{u}}}{\partial x} + \frac{\overline{\tilde{w}^2}}{r}, \tag{2.8}$$

$$\frac{1}{r}\frac{\partial rvw}{\partial r} + \frac{1}{r}\frac{\partial w^2}{\partial \theta} + \frac{\partial wu}{\partial x} + \frac{wv}{r} = -\frac{1}{\rho}\frac{\partial p}{r\partial \theta} + \vartheta\left(\Delta w - \frac{w}{r^2} - \frac{2}{r^2}\frac{\partial v}{\partial \theta}\right) - \frac{1}{r}\frac{\partial r\overline{\tilde{w}\tilde{v}}}{\partial r} - \frac{1}{r}\frac{\partial \overline{\tilde{w}}^2}{\partial \theta} - \frac{\partial \overline{\tilde{w}\tilde{u}}}{\partial x} - \frac{\overline{\tilde{w}\tilde{v}}}{r}, \text{ and} \tag{2.9}$$

$$\frac{1}{r}\frac{\partial rwu}{\partial r} + \frac{1}{r}\frac{\partial uw}{\partial \theta} + \frac{\partial u^2}{\partial x} = -\frac{1}{\rho}\frac{p}{\partial x} + \vartheta\Delta u - \frac{1}{r}\frac{\partial r\overline{\tilde{v}\tilde{u}}}{\partial r} - \frac{1}{r}\frac{\partial \overline{\tilde{u}\tilde{w}}}{\partial \theta} - \frac{\partial \overline{\tilde{u}}^2}{\partial x}. \tag{2.10}$$

These equations are called Reynolds-Averaged Navier Stokes (RANS) equations. Each term in $\rho\left[-\frac{1}{r}\frac{\partial r\overline{\tilde{v}^2}}{\partial r}-\frac{1}{r}\frac{\partial\overline{\tilde{v}\tilde{w}}}{\partial\theta}-\frac{\partial\overline{\tilde{v}\tilde{u}}}{\partial x}+\frac{\overline{\tilde{w}}^2}{r}\right]$, $\rho\left[-\frac{1}{r}\frac{\partial r\overline{\tilde{w}\tilde{v}}}{\partial r}-\frac{1}{r}\frac{\partial\overline{\tilde{w}}^2}{\partial\theta}-\frac{\partial\overline{\tilde{w}\tilde{u}}}{\partial x}-\frac{\overline{\tilde{w}\tilde{v}}}{r}\right]$ and $\rho\left[-\frac{1}{r}\frac{\partial r\overline{\tilde{w}\tilde{u}}}{\partial r}-\frac{1}{r}\frac{\partial\overline{\tilde{u}\tilde{w}}}{\partial\theta}-\frac{\partial\overline{\tilde{u}}^2}{\partial x}\right]$ is a component of Reynolds stress tensor. As can be seen, in the absence of Reynolds stress terms, Navier- stokes equations and RANS equations appear to be similar, and it is the appearance of Reynolds stress terms that creates a disparity between laminar and turbulent flow. The number of unknowns in the Reynolds equations are more than the number of equations. Therefore, RANS equations cannot be solved without determining Reynolds stress terms (Pope, 2001). Different methods exist that solve this closure problem by modeling Reynolds stresses as a function of the mean flow field like eddy viscosity models. In addition to RANS, large-eddy simulation (LES) solves Navier-Stokes equations by combining modeling and numerically simulating a range of turbulent eddies (Kundu et al., 2012). Navier-Stokes equations can also be solved by Direct numerical simulation (DNS).

2.1.2 Simplification of RANS for fully-developed pipe flow

When the statistics of a pipe flow become independent of the downstream direction, the flow field is considered fully developed. In fully developed pipe flow, flow characteristics are independent of axial coordinate and the flow is axisymmetric. Therefore, the velocity statistics depend only on the radial coordinate *r*. A more simplified RANS equations, given by Merzkirch et al. (2005), are

$$\frac{1}{r}\frac{\partial rv}{\partial r}+\frac{\partial u}{\partial x}=0, \tag{2.11}$$

$$\frac{1}{r}\frac{d(r\tau)}{dr}-\frac{\partial P}{\partial x}=0, \text{ and} \tag{2.12}$$

$$\rho\left[\frac{d\overline{\tilde{v}^2}}{dr}+\frac{\overline{\tilde{v}^2}-\overline{\tilde{w}^2}}{r}\right]+\frac{\partial P}{\partial r}=0 \tag{2.13}$$

where τ is mean shear stress given by

$$\tau=\mu\frac{du}{dr}-\rho\overline{\tilde{u}\tilde{v}} \tag{2.14}$$

where μ is dynamic viscosity. Integrating (2.13) yields

$$P(x,r)=P_w-\rho\overline{\tilde{v}^2}+\rho\int_r^R\frac{\overline{\tilde{v}^2}-\overline{\tilde{w}^2}}{r}\,dr \tag{2.15}$$

where R is the pipe radius and p_w is flow pressure at the wall. This shows that the difference between the local pressure and wall pressure is proportional to turbulent fluctuations, which are typically small. Because both $\overline{\tilde{v}^2}$ and $\overline{\tilde{w}^2}$ are independent of x in fully developed flow, from (2.15) we can find that

$$\frac{\partial P}{\partial x}=\frac{dP_w}{dx}, \tag{2.16}$$

and from (2.12)

$$\frac{1}{r}\frac{d(r\tau)}{dr}-\frac{\partial P_w}{\partial x}=0, \text{ or} \tag{2.17}$$

$$\tau=\frac{r}{2}\frac{dP_w}{dx}+c. \tag{2.18}$$

where c is the constant of the integral. From (2.18) at the pipe wall we have

$$\tau_w = \frac{R}{2}\frac{dP_w}{dx}. \tag{2.19}$$

This correlation between pressure gradient and stress near the wall surface means that the pressure gradient can be used to measure wall shear stress. From equation 2.14 we find that that the total shear stress can be decomposed into a viscous, τ_v, and a turbulent, τ_t, part

$$\tau = \tau_v + \tau_t = \mu\frac{du}{dr} - \rho\overline{\tilde{u}\tilde{v}}. \tag{2.20}$$

2.2 Mean velocity profile

The fully developed turbulent pipe flow has two main regions: the core region, and the region closer to the wall. Flow behaviour is significantly different in these regions. In the core region, turbulent Reynolds stress is much larger than viscous shear stress, effectively making the effects of viscosity negligible. Near the wall, however, viscous stress cannot be neglected. Because the flow behaves differently in different regions of the bounded flow, two different scaling laws exist based on the location of the fluid particles and based on the dominance of viscosity and Reynolds stresses. In the first scaling, the law of the wall is applied to the regions closer to the wall where the viscosity is dominant. The law of the wall states that the profile of near-wall velocity only depends on the near-wall parameters. This region is called the inner region where the largest length scale is the distance from the wall. In the second scaling, velocity defect law is applied to the core region where flow characteristics are independent of viscosity. This region is called the outer region where the largest length scale is the pipe radius, R. The region where the inner and outer regions overlap is called the overlap region.

2.2.1 Law of the wall (inner layer)

For flow near a smooth wall, the wall-layer thickness (also called the viscous length scale), δ_v, and friction velocity, u_T, are defined as

$$\delta_v = \frac{\nu}{u_T}, \text{ and} \tag{2.21}$$

$$u_T = \sqrt{\frac{\tau_w}{\rho}}. \tag{2.22}$$

At the pipe wall, the boundary conditions dictate that both v' and w' be equal to zero. Therefore, in equation 2.20, the Reynolds stress term is zero at the wall, and the wall shear stress (τ_w) can be obtained by

$$\tau_w = \rho\nu \frac{du}{dy}. \tag{2.23}$$

The wall distance, y, is defined as the distance of a fluid particle from the pipe surface ($y = R - r$). A dimensionless wall distance, y^+, is also introduced to determine the velocity profile inside the wall layer given by

$$y^+ = \frac{y}{\delta_v}. \tag{2.24}$$

In the wall region, $y^+ < 50$, viscosity directly affects shear stress. The law of the wall which implies that near-wall velocity only depends on near-wall parameters and viscous length scale is given by

$$U^+ \equiv \frac{u}{u_T} = f(y^+) \tag{2.25}$$

where f is an undetermined universal function and U^+ is a dimensionless parameter representing normalized velocity. The region of the flow that is very close to the wall $y^+ < 5$ is called the viscous sublayer. Here, although velocity fluctuations still exist to some extent, the Reynolds stresses are negligible, and only viscous stresses contribute to wall shear stress. At very high Reynolds numbers, the thickness of viscous sublayer is very small. This means that the stress is uniform and equal to wall shear stress. The mean velocity profile in the viscous sublayer has a linear distribution, and it is given by

$$U^+ = y^+. \tag{2.26}$$

2.2.2 Velocity defect law (outer layer)

In the outer region $y^+ > 50$, the effects of viscosity are negligible. Here, the characteristics of turbulent flow resemble that of inviscid flow, and the drag on the flow created by Reynolds stresses generate a velocity defect. This defect is the difference between the mean velocity and the centerline velocity. The velocity defect law is given by

$$\frac{u_\infty - u}{u_T} = F\left(\frac{y}{R}\right) \tag{2.27}$$

where u_∞ is centerline velocity and u is the mean velocity in the x direction at a distance y from the pipe wall. It is important to note that the velocity defect law function F is not a universal function, and it is different for different flows.

2.2.3 Logarithmic law (overlap layer)

The velocity profile in the overlap region (also called the logarithmic region) can be given by

$$U^+ = f(y^+) = \frac{1}{\kappa}\ln(y^+) + B, \text{and} \tag{2.28}$$

$$F(\xi) = -\frac{1}{\kappa}\ln(\xi) + A \tag{2.29}$$

where $\xi = \frac{y}{R}$, κ is the von Karman constant, and A and B are constants with values of around 4 or 5. The von Karman constant depends on the flow and pressure gradient but overall, it is around 0.41 with a variation of 5%. These equations are only valid for large y^+ and small $\frac{y}{R}$. Figure 2.1, originally developed by Oweis et al., (2010) and adopted by Kundu et al. (2012), shows the log-linear plot of velocity profile versus the dimensionless wall distance. The vertical dashed lines indicate the extent of different layers of a wall-bounded turbulent flow. For $y^+ < 5$, the velocity distribution of the viscous sublayer appears as a curve. The logarithmic velocity profile is shown to have a linear behaviour for $10^2 < y^+ < 10^4$. The buffer layer range is $5 < y^+ < 30$ where the distribution is neither logarithmic nor nonlinear. A summary of the height of each region of bounded turbulent flow is given in Table 2.1.

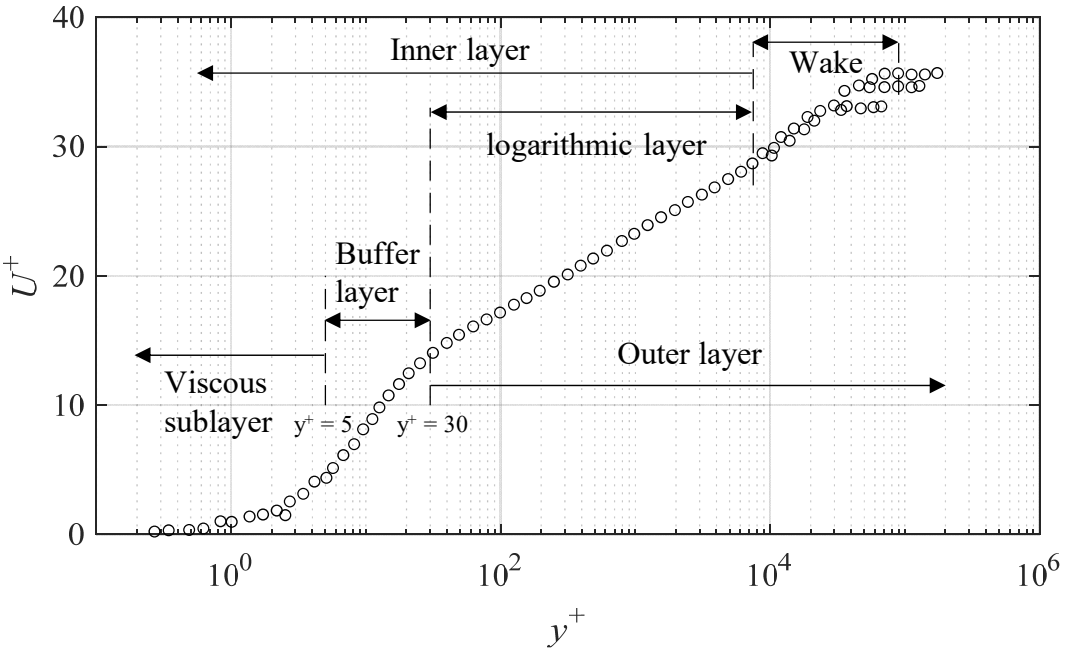

Figure 2.1. Log-linear plot of mean velocity profile for a smooth-flat-plate turbulent boundary layer adopted from Kundu et al., (2012).

Table 2.1. Wall regions (adopted from Pope, 2001).

Region	location
Inner layer	$y/R < 0.1$
Viscous wall region	$y^+<50$
Viscous sub layer	$y^+<5$
Outer layer	$y^+>50$
Overlap region	$y^+ > 50$, $y/R < 0.1$
Log-law region	$y^+ > 30$, $y/R < 0.3$
Buffer layer	$5 < y^+ < 30$

2.3 Flow in smooth pipes

The Reynolds number for pipe flow is given by

$$Re = \frac{2RU_b}{\nu} \tag{2.30}$$

where U_b is the bulk velocity and R is the radius of the pipe. Bulk velocity for a pipe flow is found using

$$U_b = \frac{1}{\pi R^2} \int_0^R u \, 2\pi r dr, \tag{2.31}$$

and the mass flow rate, $\dot{m}$, is given in

$$\dot{m} = \rho U_b (\pi R^2), \tag{2.32}$$

For Re < 1350, the flow is laminar, and for Re > 1800 it is fully turbulent. Transitional effects can be observed up to Re = 3000. The hydrodynamic entry length, $l_{e,h}$, of a pipe flow is the distance from the inlet of the pipe until the flow becomes fully developed, and for a turbulent flow it given by Munson et. al (2013) as

$$\frac{l_{e,h}}{D} = 4.4 \, Re^{1/6} \tag{2.33}$$

Where D is the pipe inner diameter. According to Pope (2000), the relationship between the bulk velocity, U_b, centerline velocity, U_c, and friction velocity is u_τ using the logarithmic defect law for the pipe flow given in

$$\frac{U_c - U_b}{u_\tau} = \frac{3}{2\kappa} + B_1 \tag{2.34}$$

where u_τ is the friction velocity and the constants κ and B_1 are 0.4 and zero, respectively. The relationship between the friction factor, f, and friction velocity is given in

$$\frac{u_\tau}{U_b} = \sqrt{\frac{f}{8}}. \tag{2.35}$$

Friction factor is defined in the next section (section 2.3.1).

2.3.1 Friction factor

For incompressible, steady, turbulent flow in a smooth pipe with diameter D and length L, the pressure drop is a function of bulk velocity U_b, μ, and ρ. The total pressure loss ΔP for horizontal pipes is given in

$$\Delta P = f \frac{l}{D} \frac{\rho U_b^2}{2} \tag{2.36}$$

where f is friction factor. A correlation between f and Re, commonly used for smooth pipes, is the Prandtl friction law given in

$$\frac{1}{\sqrt{f}} = 2.0 \log\left(\sqrt{f}\, Re\right) - 0.8. \tag{2.37}$$

2.3.2 Heat transfer

When there is a difference between the temperature of the pipe and the working fluid, convective heat transfer occurs and a thermal boundary layer develops. If the pipe surface temperature or the heat flux is constant over the length of the pipe, the flow will eventually reach a thermally fully developed condition. The thermal entry length, $l_{e,t}$, of a pipe flow is the distance from the inlet of the pipe until the flow becomes thermally fully developed, and for a turbulent flow it given by Incropera et al. (2007) as

$$\frac{l_{e,t}}{D} = 10 \tag{2.38}$$

To calculate the heat transfer from the pipe to the flow it is important to define the mean fluid temperature, T_m, that is given by

$$T_m = \frac{2}{U_b R^2} \int_0^R uT(r) r dr \tag{2.39}$$

where $T(r)$ is the time averaged local temperature of a fluid particle at distance r from the centreline of the pipe. For a heated pipe, the convective heat flux (flow of heat energy per unit area), q'', from the pipe surface to the flow, can be expressed as

$$q" = h_{local}(T_s - T_m) \tag{2.40}$$

where h_{local} is the coefficient of local convection heat transfer, and T_s is the temperature of the pipe surface. From Fourier's law at $r = R$, we have

$$q" = -k \frac{\partial T}{\partial r}. \tag{2.41}$$

By applying the energy balance to pipe flow of finite length, L, shown in Figure 2.2, the amount of convective heat transfer from the pipe wall to the fluid is given by

$$q = \dot{m} C_P \left(T_{m,o} - T_{m,i}\right) \tag{2.42}$$

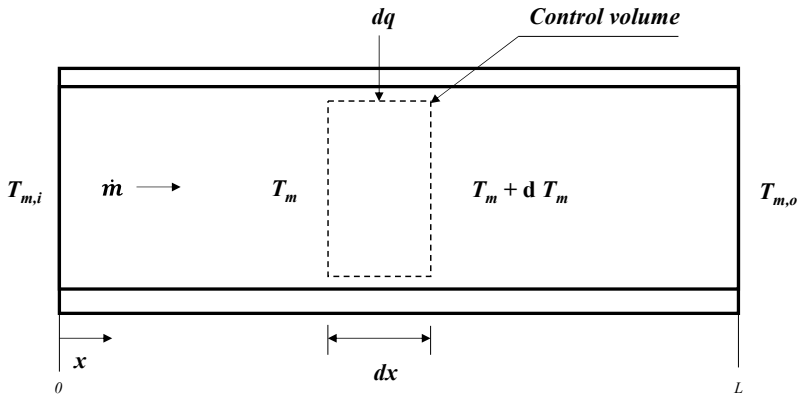

Figure 2.2. Control volume in a heated pipe flow adopted from Incropera et al. (2007).

where q is the rate of convective heat transfer from the pipe surface to the flow, and C_P is specific heat capacity. For the control volume of shown in Figure 2.2 applying the energy balance gives the differential convective heat transfer in the form

$$dq = \dot{m}C_P dT_m = q"(\pi DL)dx. \tag{2.43}$$

Substituting q'' from equation 2.40 gives an expression for the rate of changes of mean temperature with x, distance from the inlet of the pipe, given in

$$\frac{dT_m}{dx} = \frac{q"\pi D}{\dot{m}C_P}, and \tag{2.44}$$

$$\frac{dT_m}{dx} = \frac{\pi D}{\dot{m}C_P} h_{local}(T_s - T_m). \tag{2.45}$$

The above equations hold true for all forms of heat transfer from the pipe wall to the fluid. However, a more detailed analysis of heat transfer in a pipe can be given in special cases where the surface temperature is constant over the length of the pipe. In this case, ΔT is defined as $T_s - T_m$. Equation 2.45 is rewritten in terms of ΔT in the from of

$$\frac{d\Delta T}{dx} = \frac{\pi D}{\dot{m}C_P} h_{local}(\Delta T). \tag{2.46}$$

Integrating equation 2.46 from the inlet of the pipe at $x = 0$ to the outlet at $x = L$ gives

$$ln\frac{\Delta T_o}{\Delta T_i} = \frac{T_S - T_{m,o}}{T_S - T_{m,i}} = \frac{\pi DL}{\dot{m}C_P} h, \text{ or} \tag{2.47}$$

$$\frac{\Delta T_o}{\Delta T_i} = \frac{T_s - T_{m,o}}{T_s - T_{m,i}} = exp\left(-\frac{\pi DL}{\dot{m}C_P} h\right) \tag{2.48}$$

where h is the average heat transfer coefficient over the length of the pipe. Integrating equation 2.46 from zero to an axial position of x gives

$$\frac{T_s - T_m(x)}{T_s - T_{m,i}} = exp\left(-\frac{\pi Dx}{\dot{m}C_P} h\right) \tag{2.49}$$

where h is now the average heat transfer coefficient of the flow form inlet to x. Expressing equation 2.42 in the form of

$$q = \dot{m}C_P(\Delta T_o - \Delta T_i), \tag{2.50}$$

and substituting $\dot{m}C_P$ from equation 2.47 gives an equation for convective heat transfer rate in the form of

$$q = h(\pi DL)\Delta T_{lm} \tag{2.51}$$

where ΔT_{lm} is the log mean temperature difference given in

$$\Delta T_{lm} = \frac{\Delta T_o - \Delta T_i}{ln(\Delta T_o / \Delta T_i)}. \quad (2.52)$$

The average Nusselt number, *Nu* is defined as

$$Nu = \frac{hL}{k} \quad (2.53)$$

where *k* is thermal conductivity. *Nu* is a dimensionless number that gives a measure of the ratio between convective to conductive heat transfer. Different correlations exist in the literature for the evaluation of *Nu*. For fully developed turbulent flow in smooth pipe, Dittus-Boetler and Blasius correlations can be used given in

$$Nu = 0.23Re^{0.8}Pr^{n} \text{ and} \quad (2.54)$$

$$f = 0.79Re^{-1/4} \quad (2.55)$$

Where *n* is 0.3 for cooling and 0.4 for heating of the fluid. equations 2.54 and 2.55 have been proven to be within 20% range of accuracy for most experimental studies (Ji et al. 2017). For a fully developed turbulent pipe flow with constant surface temperature a correlation provided by Gnielinski (1976) can also be used to find the *Nu* as a function of friction factor, Reynolds number and Prandtl number given in

$$Nu = \frac{(f/8)(Re - 1000)Pr}{1 + 12.7(f/8)^{\frac{1}{2}}(Pr^{\frac{2}{3}} - 1)} \quad (2.56)$$

where *Pr* is the Prandtl number, defined as the molecular diffusivity of momentum divided by molecular diffusivity of heat, is given in

$$Pr = \frac{c_p \mu}{k}. \tag{2.57}$$

2.4 Pipes with internal roughness

The wall surface is considered rough when the average height of the roughness elements protrudes out of the viscous sublayer. In this case, the flow parameters in the inner layer are not affected by viscosity, but instead they are affected by the wake region developed behind the roughness element. Figure 2.3 shows the distribution of logarithmic velocity for smooth and rough surfaces. The viscous sublayer is diminished for flow near rough surfaces, thus the entire axial velocity profile is governed by the logarithmic law. The entire velocity profile in this case is given in

$$U^+ = \frac{1}{\kappa} \ln\left(\frac{y}{y_0}\right) \tag{2.58}$$

where y_0 is defined as the wall distance at which $u = 0$.

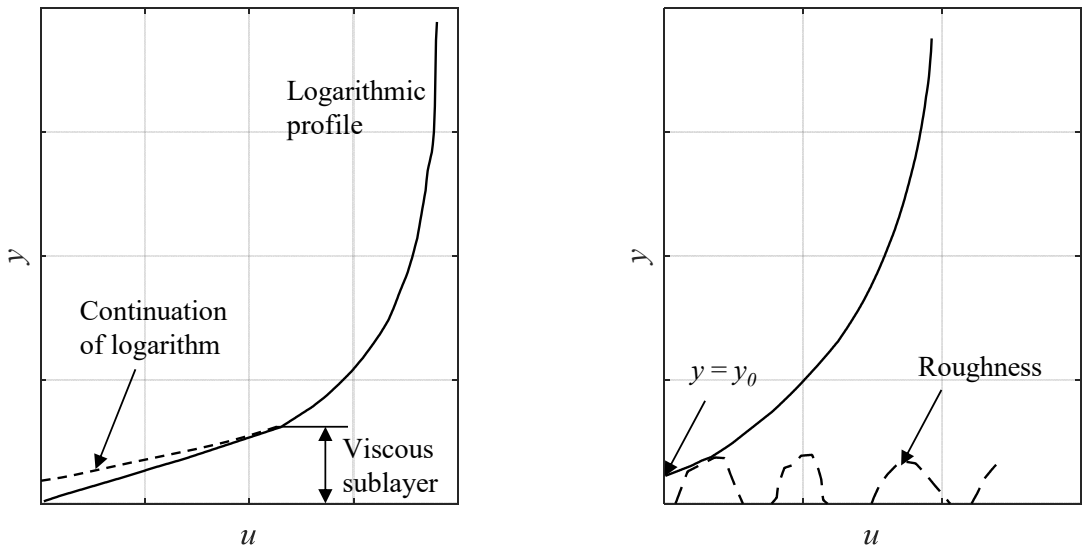

Figure 2.3. Logarithmic velocity distribution for (a) smooth surfaces, and (b) rough surfaces adopted from Kundu et al. (2012).

2.5 Friction factor

To account for the effect of roughness on the velocity profile and pressure drop in turbulent pipe flows, a variable ε, which is a measure of the height of the roughness element, is introduced. For rough pipes friction factor is both a function of Re and ε or

$$f = F\left(Re, \frac{\varepsilon}{D}\right). \tag{2.59}$$

The theoretical formula for function F is unknown, but it can be estimated from experimental studies. These studies usually present the value of friction factor in a graphical form or in terms of a curve fitting formula. The relationship of friction factor with Reynolds number and relative roughness is mostly based on the pioneering work of Nikuradse (1950). In Nikuradse's work, the pipes were artificially roughened by gluing sand grains of different sizes to the pipe walls. Then the pressure drop and flow rate were measured for a wide range of Reynolds number and roughness elements. The data from these tests were used to determine the dependence of friction factor with Reynolds number and roughness. Although the internal roughness of commercial pipes used for enhancing heat-transfer is not as uniform as the artificially roughened pipes, similar experiments have been conducted to find a measure of the effective roughness and the friction factor for commercial applications. Based on the work of Moody (1944) and Colebrook (1939), the dependence of friction factor to Reynolds number and roughness is typically depicted in the form of a diagram called the Moody chart(Munson et. al 2013). As can be seen for flows with very large Reynolds numbers, known as completely turbulent flows, the friction factor is independent of the Reynolds number. This is because for such flows, the pressure drop is a result of turbulent shear stress rather than viscous stress (Gerhart et al., 2009).

While a theoretical formula is not yet available for all ranges of flow characteristics, semiempirical expressions have been given in the literature for pipe flows that are confined to a small region of the Moody chart. An empirical fit of the Moody chart is given in the form of an implicit equation known as the Colebrook formula which is

$$\frac{1}{\sqrt{f}} = -2.0 \log\left(\frac{\varepsilon/D}{3.7} + \frac{2.51}{Re\sqrt{f}}\right). \tag{2.60}$$

Simple explicit formula for turbulent pipe flow is given in

$$\frac{1}{\sqrt{f}} = -1.8 \log\left(\frac{\varepsilon/D^{1.11}}{3.7} + \frac{6.9}{Re}\right) \tag{2.61}$$

based on the work of Haaland et al (1983).

2.6 Heat transfer augmentation

While in many engineering applications high roughness in pipes is undesirable, there are instances where roughness is artificially added to the pipe flow to improve mixing and thermal performance. The improvement to the thermal performance, also called heat transfer augmentation, can be achieved using active and passive methods. In active methods, some form of external activator or power input is used to enhance heat transfer. Some examples of active method include fluid vibration, surface vibration and electrostatic fields (Elshafei et al., 2008). In passive methods, artificial roughness elements are added to the flow by either modifying the geometry of the pipe walls or by inserting extra components inside the pipe. Some examples of this method include swirl flow devices, rough surfaces, treated surfaces and coiled tubes. A combination of different methods can also be implemented. An example of these compound methods is heat transfer enhancement using internal rough and pipe vibration (Alamgholilou et al. 2012). Heat transfer

augmentation methods that add roughness elements increase the friction factor of the flow. This is synonymous to higher pumping costs. Therefore, augmentation devices and methods need to be optimized to maximize heat transfer while minimizing frictional losses.

2.6.1 Thermohydraulic performance

Thermohydraulic performance refers to the study of hydraulic and thermal performance of heated flow. A passive method with a high thermohydraulic performance can increase heat transfer coefficient with minimal increase in friction factor. Different thermohydraulic performance parameters have been proposed in the literature to compare different augmentation methods. A performance parameter, η, based on equal pumping power was first defined by Webb et al. (1972) given in

$$\eta = \frac{Nu/Nu_0}{(f/f_0)^{1/3}} \tag{2.62}$$

where *Nu* and *f* are Nusselt number and friction factor for a pipe with augmentations, and Nu_0 and f_0 are the same parameters for a smooth pipe with identical inside diameter.

Fan et al. (2009), proposed a logarithmic scale for evaluating the thermohydraulic performance, which is known as the "evaluation plot". In the evaluation plot, the smooth pipe is used as a reference pipe meaning that *Nu* and *f* of the augmented pipes are normalized by Nu_0 and f_0, respectively. Assuming correlations for f_0 and Nu_0 can be expressed in the form of

$$f_0(Re) = c_1 Re^{m_1}, \text{ and} \tag{2.63}$$

$$Nu_0(Re) = c_2 Re^{m_2} \tag{2.64}$$

where c_1, c_2, m_1, and m_2 are constants.

When both the smooth pipe and augmented pipes are at the same *Re*, the ratios of *f* over f_0, as well as *Nu* over Nu_0 are shown in Equations

$$\left(\frac{f}{f_0}\right)_{Re} = \frac{f(Re)}{f_0(Re)}, \text{ and} \tag{2.65}$$

$$\left(\frac{Nu}{Nu_0}\right)_{Re} = \frac{Nu(Re)}{Nu_0(Re)}. \tag{2.66}$$

When the smooth pipe and augmented pipes are at different *Re* the same ratios are shown as

$$\frac{f}{f_0} = \frac{f(Re)}{f_0(Re_0)}, \text{ and} \tag{2.67}$$

$$\frac{Nu}{Nu_0} = \frac{Nu(Re)}{Nu_0(Re_0)}. \tag{2.68}$$

Substituting equations 2.63 and 2.64 into 2.65 and 2.66 respectively gives

$$\frac{f}{f_0} = \left(\frac{f}{f_0}\right)_{Re} \left(\frac{Re}{Re_0}\right)^{m_1}, \text{ and} \tag{2.69}$$

$$\frac{Nu}{Nu_0} = \left(\frac{Nu}{Nu_0}\right)_{Re} \left(\frac{Re}{Re_0}\right)^{m_2}. \tag{2.70}$$

Equations 2.69 and 2.70 can be used to determine the ratios of *f* over f_0, as well as *Nu* over Nu_0 at different *Re* based on the same ratios at the same *Re*.

The ratio of power consumption, *PC*, of the enhanced pipe over the reference pipe is presented as

$$\frac{PC}{PC_0} = \frac{(AU_b f L \rho {U_b}^2/D)}{(AU_b f L \rho {U_b}^2/D)_0} \tag{2.71}$$

where A is the cross-sectional area of the pipes. To simplify the equations, it is assumed that the thermophysical properties of flow are constant. It can also be assumed that the smooth pipe and enhanced pipe have the same heat transfer area, A_L, and the same cross-sectional area, A. Under these assumptions, equation 2.71 is simplified to

$$\frac{PC}{PC_0} = \frac{f(Re)}{f_0(Re_0)}\left(\frac{Re}{Re_0}\right)^3. \tag{2.72}$$

The ratio of heat transfer rates can be presented as

$$\frac{q}{q_0} = \frac{(hA_L\Delta T)}{(hA_L\Delta T)_0} = \frac{(NukA_L\Delta T/D)}{(NukA_L\Delta T/D)_0} \tag{2.73}$$

where ΔT is wall to fluid temperature or $T_s - T_m$. Assuming that ΔT and k are also the same between the augmented and smooth pipe flow, equation 2.73 simplifies to

$$\frac{q}{q_0} = \frac{Nu}{Nu_0} \tag{2.74}$$

If the smooth pipe and augmented pipes consume the same amount of pumping power, similar pumping power constraint, equation 2.72 becomes

$$\frac{f}{f_0} = \left(\frac{Re}{Re_0}\right)^{-3}. \tag{2.75}$$

Substituting equation 2.75 into 2.69 gives

$$\frac{Re}{Re_0} = \left(\frac{f}{f_0}\right)_{Re}^{\frac{-1}{3+m_1}}, \text{ and} \tag{2.76}$$

From equations 2.70, 2.74 and 2.76 we have

$$\frac{q}{q_0} = \frac{Nu}{Nu_0} = \left(\frac{Nu}{Nu_0}\right)_{Re} \left(\frac{f}{f_0}\right)_{Re}^{\frac{-m_2}{3+m_1}}, \tag{2.77}$$

which gives the ratio of heat transfer under identical pumping power constraint. Similar equations can be derived for heat transfer ratio under identical pressure drop constraint. The ratio of pressure drop of enhanced pipe over smooth pipe is given in

$$\frac{\Delta P}{\Delta P_0} = \frac{(fL\rho {U_b}^2/D)}{(fL\rho {U_b}^2/D)_0}, \text{ and} \tag{2.78}$$

based on the assumptions mentioned above equation 2.78 can be simplified to

$$\frac{\Delta P}{\Delta P_0} = \frac{f(Re)}{f_0(Re_0)} \left(\frac{Re}{Re_0}\right)^2. \tag{2.79}$$

Therefore, heat transfer ratio under identical pressure drop constraint becomes

$$\frac{q}{q_0} = \frac{Nu}{Nu_0} = \left(\frac{Nu}{Nu_0}\right)_{Re} \left(\frac{f}{f_0}\right)_{Re}^{\frac{-m_2}{2+m_1}}. \tag{2.80}$$

Finally, heat transfer rate ratio under identical flow rate is simply

$$\frac{q}{q_0} = \left(\frac{Nu}{Nu_0}\right)_{Re}. \tag{2.81}$$

Equations 2.77, 2.80 and 2.81 can be unified in

$$C_{q,i} = \left(\frac{Nu}{Nu_0}\right)_{Re} \Big/ \left(\frac{f}{f_0}\right)_{Re}^{a_i} \tag{2.82}$$

where $C_{q,i}$ is the ratio of heat transfer rate under the constraints of identical pumping power ($i = PC$), identical pressure drop ($i = \Delta P$) and identical flow rate ($i = Re$). The power a_i takes the value

of $m_2/(3+m_1)$, $m_2/(2+m_1)$ and 1 under the identical pumping power, identical pressure-drop, and identical flow rate constraints respectively.

Taking the logarithm of equation 2.82 gives

$$\ln\left(\frac{Nu}{Nu_0}\right)_{Re} = b_i + a_i \ln\left(\frac{f}{f_0}\right)_{Re} \tag{2.83}$$

where b_i is equal to $\ln(C_{q,i})$. Equation 2.83 is the basis of the performance evaluation plot shown in Figure 2.4. If $\ln(Nu/Nu_0)_{Re}$ is taken as the ordinate and $\ln(f/f_0)_{Re}$ as the abscissa, then equation (2.83) presents lines with the slopes of a_i and intercepts of b_i. These lines are called the performance lines and are shown in Figure 2.4 as dashed lines. The dashed lines represent the identical pumping power, identical pressure drop, and identical flow rate constraints. According to Fan et al. (2009), the value of m_1 is -0.25 and m_2 is 0.8. Using these values, a_i in equation 2.83 takes the value of a_{PC} = 16/55, $a_{\Delta P}$ = 16/35 and a_{Re} = 1. Thus, the dashed lines in Figure 2.4 that represent the identical pumping power, identical pressure drop, and identical flow rate constraints have slopes of 16/55, 16/35 and 1 respectively.

If the intercept, b_i, is zero, all three lines pass through the point with coordinates (1,1) in the evaluation plot. The performance lines divide the evaluation plot into four regions indicated by boldface numbers. In region one, the pumping power consumption increase due to the enhancement is larger than the increase in heat transfer rate. In region two, the enhanced pipe transfers more heat under identical power consumption constraint. In region three, the augmented pipe has a higher heat transfer compared to the reference pipe under identical pressure drop constraint. Finally, in region four, increase in heat transfer is larger than increase in friction under identical flow rate constraint. In terms of performance and energy consumption, pipes that can

operate in regions three and four are the most favourable ones while those that operate in region one consume more power than they increase heat transfer.

To plot the experimental data in the evaluation plot, the *Nu* and *f* need to be normalized by Nu_0, and f_0 at the same thermal and hydraulic conditions. This means that the *Re* of the smooth pipe and augmented pipes need to be the same, and the constant wall temperature of the smooth and augmented pipe also need to be the same during the experiments.

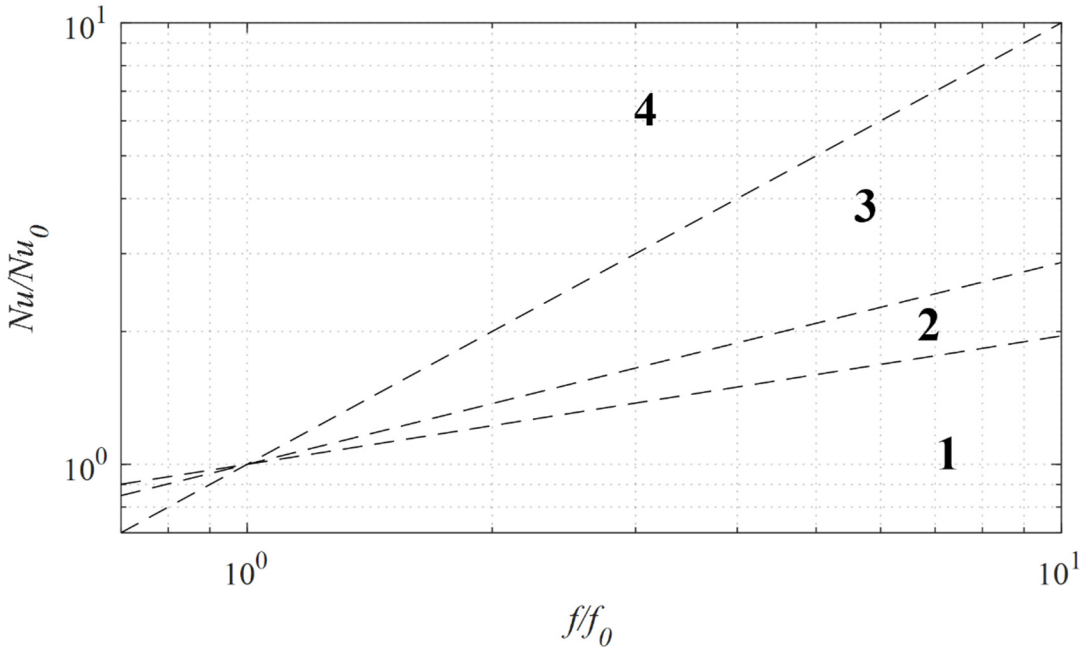

Figure 2.4. Performance evaluation plot used for comparing different enhancement techniques adopted from Fan et al. (2009).

The aim of many studies in recent years have been to find a correlation between the Nusselt number, Prandtl number and friction factor. This correlation can then be used to optimize passive augmentation methods. Reviews on the more recent studies on different passive augmentations

methods are given by Ji et al. (2017) and Kumar et al. (2017). A few passive techniques are discussed below.

2.6.2 Internally finned tubes

Internally finned tubes are produced by adding protruding fins inside the inner pipe which increases the surface area of the inner pipe and improves heat transfer. For fins with narrow spacing, the pressure drop can be very high. The geometric characteristics of the finned pipes include inner fin height (e), pipe diameter (D), helix angle (α), Number of starts (N_s), fin pitch (p), and fin base thickness (t_b). Correlations for heat transfer rate with respect to flow and geometric parameters have been reported by various studies including Kim and Webb (1993) and Kader and Yaglom (1977) given in

$$Nu = \frac{1.42(f/2)^{0.5} Re\ Pr}{5e^{0.25} + 3\ln\left(\frac{e}{d}\right) + 5.6 - \frac{4.5}{\left(1-\frac{e}{d}\right)^2} + 9.5(f/2)^{0.5}} \tag{2.84}$$

However, it should be noted that the modeling of heat transfer and fluid flow of internally finned tubes is complex, and it need to be experimentally validated. Many of the models that are reported are only verified for a small range of experimental parameters and may not produce accurate predictions of thermal and mechanical behaviour of the flow. Main geometrical parameters that affect the thermal performance of finned tubes include rib height, fin number per cycle, and helix angle. The increase in the height of the fins lead to an increase in both heat transfer and pressure drop until a critical height is reached. Above this height, very minor heat transfer enhancement can be achieved.

The performance of fined tubes has been experimentally and numerically studied in the past. Carnavos (1979) determined the thermal performance of 21 tubes with spiral and longitudinal fins experimentally. It was found that finned tubes performed better than the smooth pipe by factors of 1.2 to 2.0 under constant pumping power. Gee and Webb (1980) studied the effect of three different helix angles of 30,49 and 70º with a pitch ratio of 15 on heat transfer rate and found that the preferred angle was approximately 45 º. Han (1984) performed experimental studies on turbulent channel flows in the *Re* range of 7,000 to 90,000 to determine the effect rib height and rib pitch has on heat transfer coefficient and friction factor. The Stanton number, the ratio of heat transfer coefficient to heat capacity, of the ribbed channel was found to be 1.5 to 2.5 times, and the friction factor was 2.1 to 6.0 times that of the smooth channel. Islam and Mozumder (2009) studied turbulent flows inside finned pipes at *Re* of 20,000 to 50,000 under constant pipe heat flux condition and found that the friction factor and heat transfer coefficient were five and two times higher than the smooth pipe respectively. Yu et al. (1999) experimented on tubes with longitudinal fins and compared the two cases in which inner tube was blocked in one case, and inner tube was unblocked in the other case. They found that the blocked case had a superior heat transfer increase. Saad et al. (2012) compared longitudinal fins that were continuous and interrupted in the steam wise direction in a staggered and in-line manner. They found that the heat transfer coefficient for *Re* between 20,000 to 50,000 was the highest for the staggered interrupted fins, followed by the staggered inline fins and the continuous fins respectively. Peng et al. (2016) conducted numerical simulation on finned tubes with different geometrical properties. They found that increasing the width and height of fins, as well as, decreasing the spacing between fins can both lead to an increase in *Nu* and *f*. The helix angle was also found to have a significant effect on thermal

performance of the tubes. They observed that tubes with smaller angles had higher *Nu* and lower pressure drop.

2.6.3 Swirl generators (twisted tape and wire coil inserts)

Swirl generators induce a spiral motion into the flow by creating a swirl velocity component, which is also called tangential or azimuthal velocity component. The swirling pipe flow is generally classified into two types: continuous swirl flow and decaying swirl flow. In contrast to the decaying swirl, the continuous swirl flow maintains its characteristics over the pipe length. Some of the swirl generators that are commonly used in the industry include coil inserts and twisted tape inserts. As noted by Liu and Saker (2013), twisted tapes are strips of metal that are mechanically twisted and inserted inside the pipe. Twisted tapes are widely used in heat exchanger, and they can promote high heat transfer rates with small friction factor penalties. To enhance heat transfer, these tapes introduce swirling motion into the flow and disrupt the boundary layer at the surface of the pipe. In other words, they induce turbulence and decrease boundary layer thickness which leads to higher heat transfer coefficient and Nusselt number. However, the insertion of twisted tapes increases the pressure drop of the flow, and the challenge in designing twisted tapes is to limit the pressure drop while increasing heat transfer. Two of the main geometrical characteristics that are considered in designing twisted tape inserts are the pitch and the twist ratio. Twist ratio is defined as the ratio of pitch to the diameter of the pipe. Different types of twisted tapes are classified into different categories which include: typical twisted tapes that have a length equal to the length of the exchanger tube; Tubes with varying geometries that do not have a length equal to the length of the tube and can have shorter length with different pitches; Multiple twisted tapes that are devices with more than one twisted tape used in the heat exchanger; twisted tape with attached baffles and

fins; Twisted tapes with cuts, slots and holes. Liu et al. (2013) provided a review of the impacts of different types of twisted tapes on the enhancement efficiency.

Eiamsa et al. (2012) performed experimental investigations on turbulent flows in heated tubes with twisted tape inserts with twist rations of 2, 2.5 and 3, and pitch ratios of 1, 1.5 and 2 for *Re* between 6000 to 20,000. They found that the enhancement of heat transfer rate and friction factor increases with an increase in twist ratio and decrease in pitch ratio. The largest thermal performance, calculated by h/h_0 where h is augmented pipe heat transfer coefficient and h_0 is smooth tube heat transfer coefficient under identical pumping power consumption, of 1.29 was found by using a tape with twist ratio of three and pitch ratio of two at Re of 6000. Bhuiya et al. (2012) investigated turbulent flow inside a heated tube with perforated twisted tape inserts in a *Re* range 15,000 to 47,000 and found that the thermal performance of different perforated twisted tapes in heated tubes turbulent flow and found that friction factor and heat transfer coefficient were 1.8 and 2.8 times higher than a smooth tube. The heat transfer performance that was also found in this study by evaluating Nu/Nu_0 under identical pumping power consumption, and it was reported to be 2.3 times that of the smooth tube. Eiamsa and Promvonge (2005) compared the thermal performance of three twisted tape configurations: full-length twisted tape without a central rod, full-length twisted tape without a central rod, and regularly spaced twisted tape without a central rod. They found that full-length twisted tape with central rod had the highest *Nu* increase of 160% compared to a smooth tube, followed by full-length twisted tape without central rod with an increase of 150%, and regularly spaced twisted tapes with an increase of 145%. Chang et al. (2007) performed experimental studies to compare broken twisted tape inserts (twisted tapes formed by twisting a serrated metal strip) with smooth twisted tape inserts. They observed that broken twisted tapes

enhanced the *Nu*, *f* and thermal performance under identical pumping power consumption, based on equation 2.50, by 1.28 to 2.4, 2 to 4.7 and 0.99 to 1.8 times that of smooth twisted tape inserts. Wire coil inserts are helical coiled wire springs that are inserted inside a tube to enhance thermal performance. According to Dewan et al. (2004) wire coil inserts have higher thermohydraulic performance compared to twisted tape inserts because coil inserts can create more turbulent mixing in the viscous sublayer, and generate lower pressure drops. The reverse is true for laminar flow where the twisted tapes have better thermohydraulic performance because they induce more mixing in the bulk flow. The thermohydraulic performance of coil inserts are reported in different studies in the past. Yakut and Sahin (2004) conducted experimental studies on coil inserts with pitch ratios o 0.2, 0.4 and 0.6 inside a heated tube at *Re* of 6000 to 38,000, and reported *Nu* increases of 1.9 to 3.5 times and *f* increase of 18.8 to 22.3 times that of the reference smooth pipe. The highest *Nu* and *f* increase was associated with the coil insert with pitch ratio of 0.6 and the lowest was associated with pitch ratio of 0.2. Promvonge (2008) conducted experimental studies on coil inserts with square and circular wires with pitch ratios of 0.3 and 0.4 in the *Re* range of 5000 to 25,000. The coil inserts with square wires showed and overall larger *Nu* and *f* compared to coil inserts with wires at all *Re*. An overall heat transfer augmentation, Nu/Nu_0, of 1.8 to 2.6 and friction factor increase, f/f_0, of 5.8 to 8.5 was observed. A performance, h/h_0 under identical pumping power consumption, improvement of 1.2 to 1.3 at *Re* of 5000 and 1.1 to 1.15 at *Re* of 25,000 was also reported. Gunes et al. (2010) conducted an experimental investigation into the thermohydraulic performance of coil insert wires with a triangular cross section over a *Re* range of 3500 to 27,000 under uniform heat flux condition. Two different wires were used in the coils with wire triangle length to tube diameter ratios of 0.0714 and 0.0892 and three different coil pitch ratios of 1, 2 and 3 were experimented on. A heat transfer enhancement, Nu/Nu_0, of 1.27 to 2.5

was observed as well as a friction factor increase, f/f_0, of 6 to 6.5. The highest overall thermohydraulic performance, h/h_0 under identical pumping power consumption, of 36.5% was reported for the wire triangle length to tube diameter ratios of 0.0892 and coil pitch ratios of one at *Re* of 3858. The twisted tapes and coil inserts were combined and used at the same time inside a heat exchanger tube in a study conducted by Eiamsa-Ard et al. (2010). The combination of these two enhancement devices led to a $Nu\backslash Nu_0$ of 2.6 to 3.1 but this came at the cost of a large f/f_0 of 32.6 to 33.

2.6.4 Corrugated tubes

Corrugated tubes are produced by creating deformations on the tube wall. These deformations take various shapes including twists, spirals, waves and indentations. Corrugations can have a single start or multiple starts. Corrugated tubes enhance the convective heat transfer by increasing the heat transfer area and promoting mixing. The spiral indentations disturb the flow in the core region of the pipe and also reduce the viscous sublayer thickness.

According to a survey conducted by Ji et al. (2017), corrugated tubes are mainly used to enhance the heat transfer of liquids, and only a relatively small number of studies have focused on gas flows. Different heat transfer coefficient and friction factor ratios has been reported in the past literature. Li et al. (2011), investigated the relation of heat transfer and flow friction in corrugated tubes, with an internal diameter of 17mm, and found that increase in Reynolds number does not always lead to an increase in Nusselt number for a fixed roughness height. Harleß et al. (2016) conducted experiments on 18 helically corrugated tubes with varying geometrical parameters (pitch ratios of 0.27 to 1.5, corrugation heights ratios of 0.02 to 0.056, and corrugation angles of 9.2 to 36.9º). Overall, a heat transfer augmentation, Nu/Nu_0, of 1.2 to 2.1, and friction factor increase, f/f_0, of to 1.2 to 3.2 was reported for *Re* between 5000 to 23,000. It was also observed

that a tube with pitch ratio of 0.517, corrugation height ratio of 0.040 and corrugation angle of 9.3 had the highest thermal performance. In another study, the same authors, Harleß et al. (2017), conducted experiments on cross-corrugated tubes with pitch ratios of 0.283 to 1.117, corrugation height ratios of 0.024 to 0.087, and corrugation angles of 14.7 to 48.8º. Overall, a Nu/Nu_0 range of 1.3 to 2.3 and f/f_0 range of 1.5 to 6 was reported, and a tube with pitch ratios of 0.769, corrugation height ratio of 0.081 and corrugation angle of 38.4 º was reported to have the highest thermal performance. Nelly et al. (2015) compared the thermal performance of single structured and cross structured corrugated tubes. They reported a Nu and f increase of up to 185% and 580% across both single structured and cross structured tubes. The overall performance, η, of cross structured corrugated tubes were lower than single structured corrugated tubes with similar surface parameters. In addition, the performance of single structured corrugated tubes showed a strong dependence on Re while the performance of cross structured corrugated tubes remained stable with changes of Re.

2.6.5 Dimpled roughened tubes

The roughness of a pipe can be increased by applying three-dimensional roughened elements in the form of protrusions, dimples and wall perturbances. These protrusions can create strong instabilities and fluctuations in the flow resulting in an increase in flow turbulence and mixing. This method is one of the oldest techniques for heat transfer augmentations that can be achieved using relatively simple mechanical procedures such as casting, forming, blasting, machining or welding. The pressure drop and heat transfer for these tubes are mostly affected by protrusion ratio (the ratio of protrusion height to the pipe diameter) and the axial and transverse pitch of protrusions.

Wang et al. (2010) conducted experiments on tubes with outward facing staggered and aligned in the *Re* range of 16,000 to 54,000. A heat transfer enhancement, Nu/Nu_0, of 18.6 to 22.7% was reported for both staggered and aligned arrangements. Friction factor increase, f/f_0, of 18.6 to 25.9% and 14.3 to 29.8% was also reported for staggered and aligned dimples, respectively. The thermohydraulic performance of staggered and aligned dimples was found to be almost identical. Wang et al. (2009) performed experimental studies on inward facing ellipsoidal and spherical dimpled tubes. They reported a Nu/Nu_0 of 38.6 to 175.1% and 34.1 to 158% for ellipsoidal and spherical dimpled tubes, respectively. A friction factor increase, f/f_0, of 26.9 to 75% and 32.96 to 92% was also reported for ellipsoidal and spherical dimpled tubes respectively.

In summary, there exists several gaps in the previous studies including the limited range of *Re*, the limited pipe surface temperature and the size of the pipe itself. To fill these gaps, this research will conduct an experimental investigation on pipes with mesh- and bearing-type roughness.

Chapter 3.

Experimental Setup

The experimental setup consisted of a pipe flow facility designed to generate a fully developed turbulent flow with maximum pipe-wall temperature of 375℃. To measure the properties of the flow, thermocouples and pressure transducer were mounted on the loop. In this chapter, the main components of the flow loop, and the function and installation of the measurement instruments are described.

3.1 Flow loop components

The components of the setup are shown in Figure 3.1, and they are labeled as A through H. The details of each component are presented below, and the technical drawings can be found in **Appendix A**. The cylindrical coordinate system (r, θ, x) is also shown in the figure, and origin of this system, as can be seen, is located at the inlet of section E (the test section). In this coordinate system, wall-normal distance is defined as $Y = R - r$. Figure 3.2 shows a photo of the setup as installed in the laboratory.

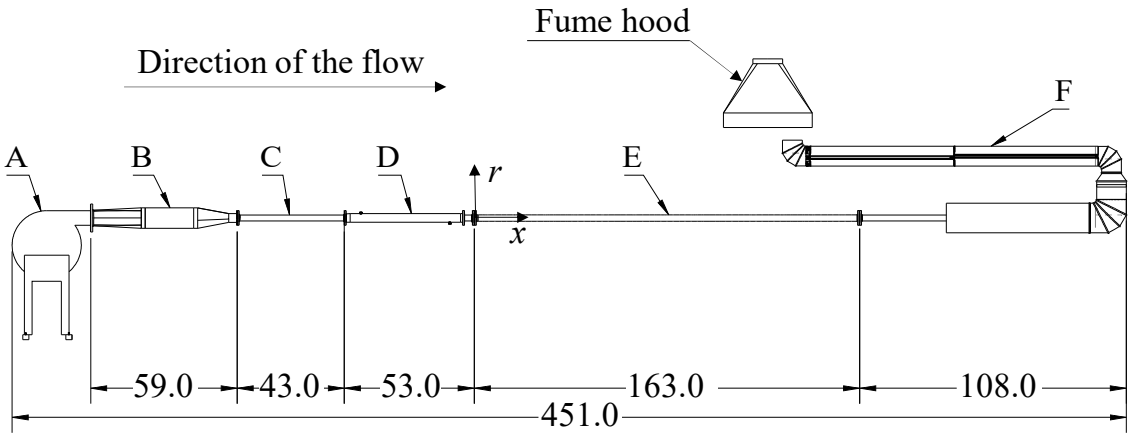

Figure 3.1 A schematic of the experimental setup. The labels A toF indicate different components of the flow loop. Dimensions are in inches.

Figure 3.2 A photo of the pipe flow setup covered with insulation and a protective shield.

3.1.1 Air blower (A)

The airflow was generated by a centrifugal blower (Chicago Blower – Design 53) powered by a 10 hp, 3 phase motor. The flow rate of the blower was controlled by a variable frequency drive (VFD) (VS1GV210-1B Baldor AC drive). The blower exit was rectangular with dimensions of 144 mm × 64 mm. The maximum speed of this blower was 3600 revolutions per minute (RPM) at which point it could potentially generate a mass flow rate of 0.21 kg/s if there is no resistance.

3.1.2 Flow straightener (B)

Figure 3.3 shows a schematic of the flow straightener. As can be seen, the flow straightener consisted of a diverging duct, settling chamber and a reducer. The diverging duct connected the settling chamber to the blower, and it was designed to transport the flow smoothly from the rectangular cross section of the blower exit to the circular cross section of the settling chamber. The settling chamber was approximately 23-inch-long and had an internal diameter of 8 inches. It was fitted with honeycomb mesh and screens to breakdown any large scale vortical structures. Mehta et al. (1979) and Cattafesta et al. (2010) recommended the cell length (CL) to cell diameter (CM) ratio of honeycomb mesh to be between 7 and 10. To conform to this recommendation, the honeycomb mesh in the settling chamber had an effective cell diameter of 0.25 inch and a length of 2.25 inch. The mesh size (the number of openings in one square inch) of the screens was around 600, the wire diameter of the mesh was 0.0075 inch, and the open area was 65%. The settling chamber was connected to the rest of the setup by a reducer.

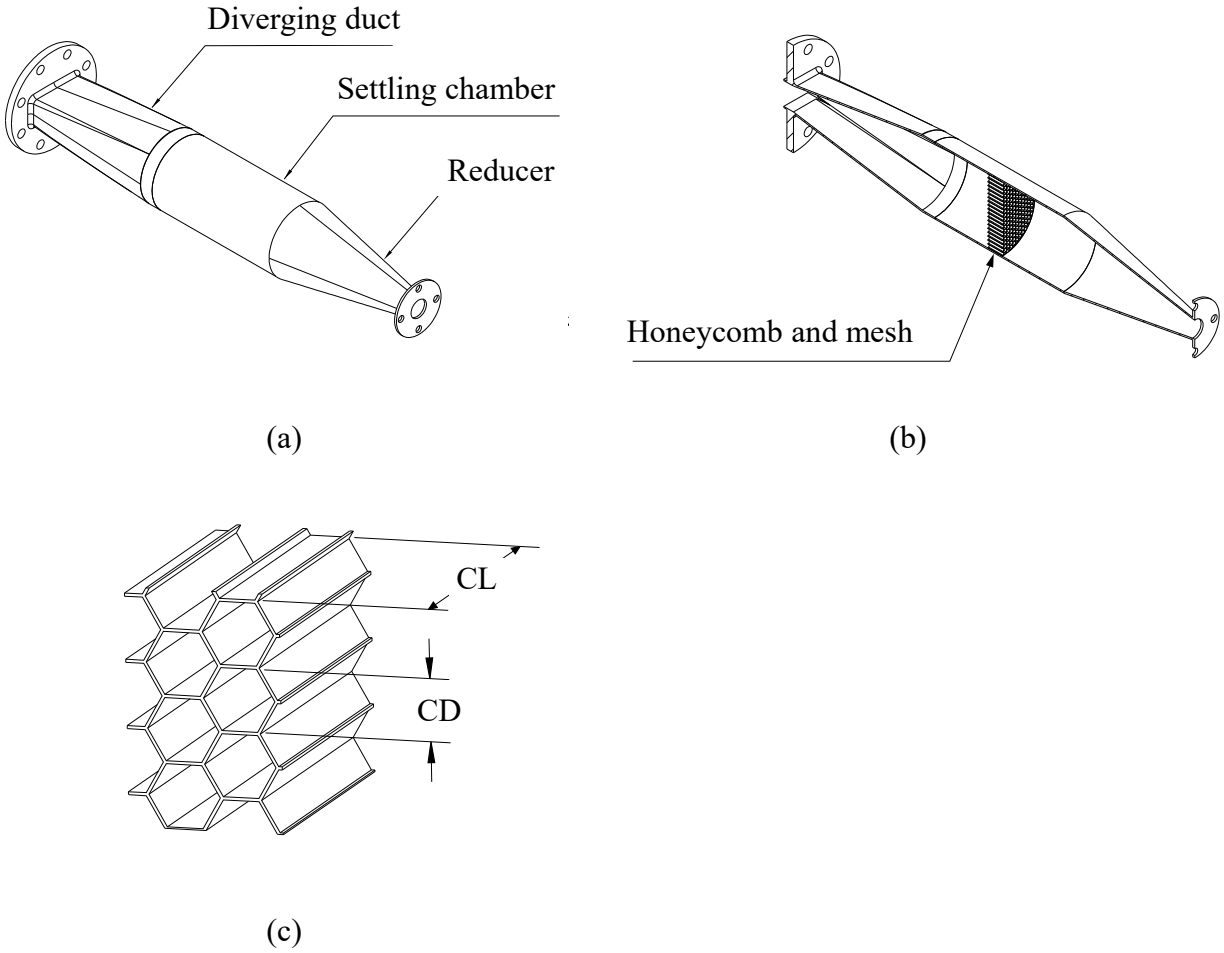

Figure 3.3 A schematic of (a) the isometric view of the flow straightener, (b) the section view of the flow straightener and (c) a detailed view of the honeycomb.

3.1.3 Entrance section (C)

This section was a 45-inch-long stainless-steel schedule 40 steel pipe (2.067 inch inner diameter and 2.375 inch outer diameter).

3.1.4 Cooling section (D)

The cooling section was a 2-inch schedule 40 pipe enclosed by a cooling jacket. The cooling jacket was made of a 3-inch galvanized steel pipe with an inlet and an outlet to circulate tap water. The function of the cooling jacket was to control the temperature of the pipe wall upstream of the heated test section (E) so that the temperature of sections B, C and D would remain close to the

ambient air temperature. The total length of both C and D section corresponded to approximately 43.5*D* where *D* is the inner diameter of a standard 2-inch Schedule 40 pipe, which is 2.067 inches.

3.1.5 Test section (E)

The test section was 163 inches long. The nominal diameter of this section was approximately 2 inches, but the exact inner diameter of the pipes varied slightly for different experiments. In addition to the smooth pipe, four pipes with different internal surface roughness were tested. More information on the pipes can be found in the following sections. For experiments with heated pipes, the pipe wall was heated to a constant surface temperature of 375°C using mica band heaters. A total of 13 mica band heaters (Marathon, 2085 Watts each) were clamped on the pipe. Each band heater was 12 inches long and had an inner diameter of 2.375 inches. A picture of a 12-inch band heater and a schematic of a shorter heater are shown in Figure 3.4 (a) and (b), respectively. Figure 3.4 (c) shows how the heaters were installed on the pipe. To cover the exposed power terminals of the heaters, ceramic caps and skirts were added as shown in Figure 3.4 (d).

(a)

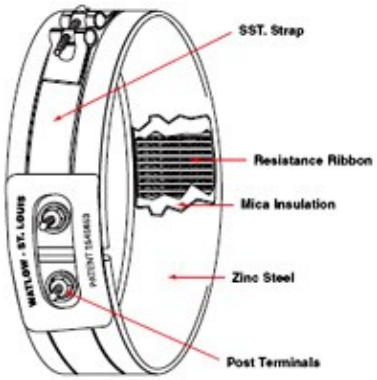

(b)

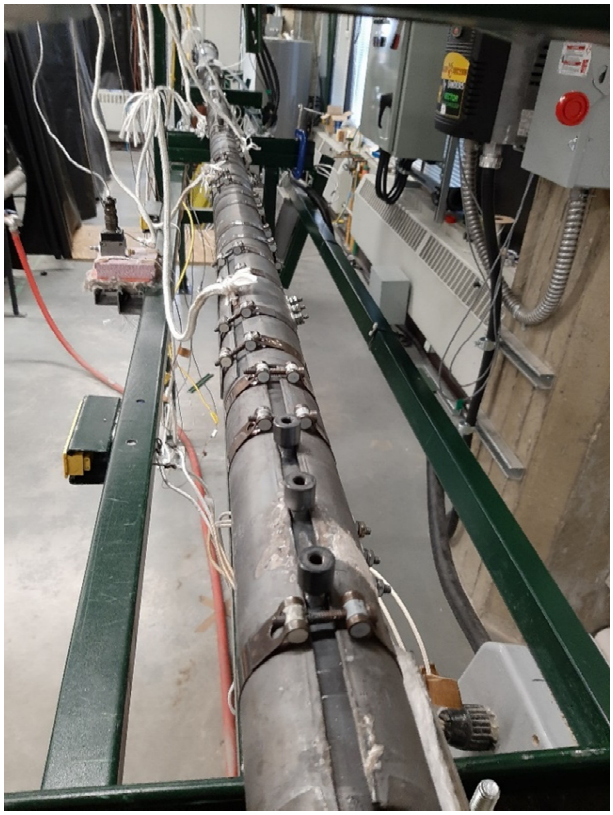

(c)

(d)

Figure 3.4 (a) A photo of a 12-inch Mica band heater, (b) the schematic of a smaller band heater of the same model, (c) a photo of the heaters installed on the pipe and (d) ceramic caps and skirts.

The band heaters were covered with two layers of insulation. The inner layer was made of ceramic fiber insulation sheets (McMaster-Carr No 93315K54) with a density of 144 kg/m^3 and thickness of 25 mm that also acted as an electrical insulation. The outer layer was made of cylindrical

fiberglass insulation with a density of 72 kg/m^3, inner diameter of 114 mm, and thickness of 76 mm (McMaster-Carr No 5556K422). Figures 3.5 (a) and (b) show how the insulations were installed on the test section pipe. The heaters were connected to the power in a parallel. The wiring diagram of the heaters can be found in **Appendix A**.

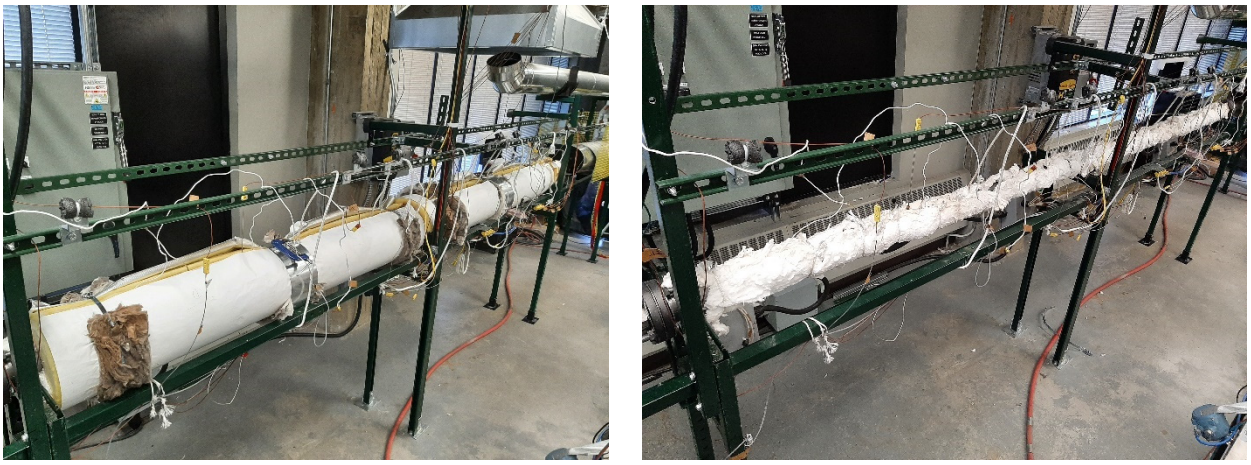

(a) (b)

Figure 3.5 Picture of (a) a fully insulated test section and (b) a test section with only electrical insulation covering it.

The thirteen heaters were connected to three temperature controllers, and each the controllers comprised of a PID based controller (Watlow PM6). The test section was divided into three zones, and the heaters in each zone were controlled by a separate controller. The zone locations and dimensions can be seen in Figure 3.6, and the details of each zone are provided in Table 3.1. The control panel was connected to a 3 phase, 208 Volts, 75 Amp power supply. The temperature feedback to the controller for each of the three zones was provided by a K-type thermocouple installed on the outer surface of the pipe in the midpoint of the zone.

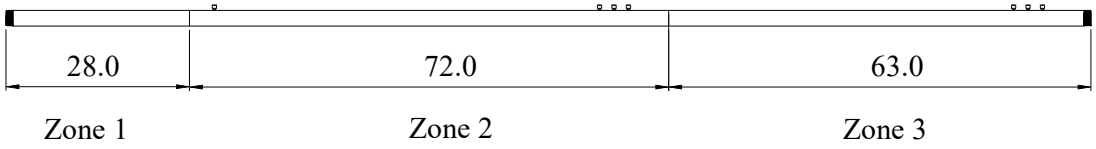

Figure 3.6 A schematic of the locations and dimensions (in inches) of the three heating zones of the test section (section E).

Table 3.1 Zone division of the heated pipe.

	Zone 1	Zone 2	Zone 3
Number of heaters	2	6	5
Total maximum heater power (Watts)	4,170	12,510	10,425

All thirteen Mica band heaters were tested by measuring resistances between the power inlet terminals. There were three power inlet terminals on each heater. These inlets were connected to a multimeter two at a time, and the resistance between them was measured and recorded. The measured resistances can be found in Table B.1 in **Appendix B**. In this table, the ports that were connected to the multimeter are shown by the "O" symbol and the one that was not connected is shown by the "X" symbol. The measurements were very close, varied between 42.5 to 43.5 **Ω**, which shows that that all the heaters were working properly.

3.1.6 Exit section (F)

The exit section consisted of a 45-inch-long galvanized steel pipe. This pipe was connected to a conical diffuser which expanded the internal diameter from 2 to 8 inches. The diffuser was then connected to an 8-inch duct via elbow joints, and the airflow in the duct was directed to a fume hood for exhausting the hot air.

3.2 Instrumentation

Four main flow properties were measured: (a) bulk flow velocity was measured using a Pitot tube, (b) friction factor of the flow along the test section was measured using a differential pressure transducer, (c) pipe-wall temperature was measured using several thermocouples, and (d) air temperature inside the pipe was measured using two temperature rakes.

3.2.1 Measurement of bulk flow velocity

The bulk velocity of air flow was obtained by measuring its static and total pressure at the centerline of the pipe using a Pitot-static tube. The Pitot tube was inserted into the pipe upstream of the test section, approximately 74*D* downstream of the blower where the flow is expected to be fully developed (Figure 3.7). The static and total pressure ports of the pitot tube were connected by soft plastic tubes to a DP15 Validyne differential pressure transducer. This transducer housed replaceable diaphragms, each suitable for a particular pressure range. A dash number 20 diaphragm with full-scale pressure (FSP) of 860 Pa was used. The accuracy of the diaphragms was 0.5% of FSP or ±4.3 Pa. The transducer was connected to a Validyne CD15 carrier demodulator that amplified the transducer signal and provided a DC output signal for the data acquisition unit.

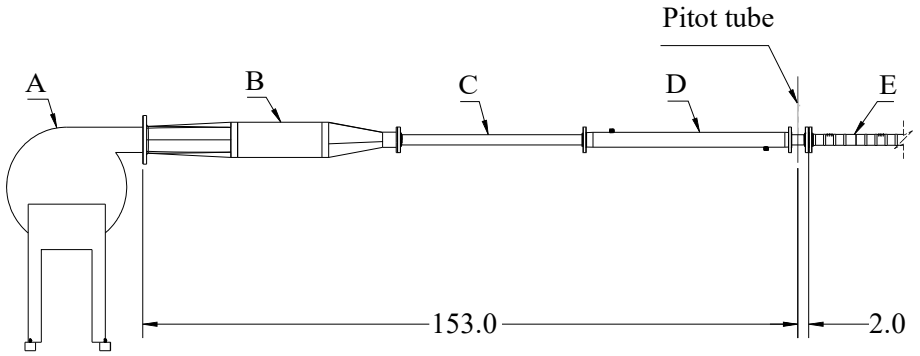

Figure 3.7 The location of the Pitot tube in the setup. Dimensions are in inches.

To accurately convert the voltage of the demodulator into pressure, there needs to be a known relationship between the pressure that the transducer senses and the voltage that the demodulator produces. To find this relationship, the pressure transducers and demodulators need to be

calibrated. The calibration process was carried out in two-steps. In the first step, the demodulator's gain is adjusted. This entails applying room pressure to the transducer and adjusting the demodulator's zero dial until the demodulator's output voltage is zero. After that, full-scale pressure (FSP) is applied to the transducer and span dial is adjusted until the demodulator's output voltage reaches 10 Volts, which was the recommended voltage in the user manual of CD15 and the maximum voltage range of the input module (NI 9201). In the second step, the linearity of the relationship between the applied pressure and measured pressure is investigated. For this reason, at least ten equidistant pressure points between zero and FSP are applied to the transducer, and the demodulator voltage is measured. The relationship between the applied pressure and demodulator voltage output can then be found by interpolating the applied pressure and measured voltages data.

The calibration setup can be seen in Figure 3.8. Pressure was applied by Omega DPI 610 calibrator that has a maximum applicable pressure of 30 Psi (207 kPa). The calibrator displayed the amount of applied pressure with an accuracy of 0.05% of the applied pressure. Because this accuracy was too large for calibrations at the lower end of the measurements range, a Dwyer micro-manometer with an accuracy of 0.07 Pa (0.00001 Psi) was used in conjunction with the calibrator. The calibration plot of the transducers for different experiments ae shown in **Appendix C**.

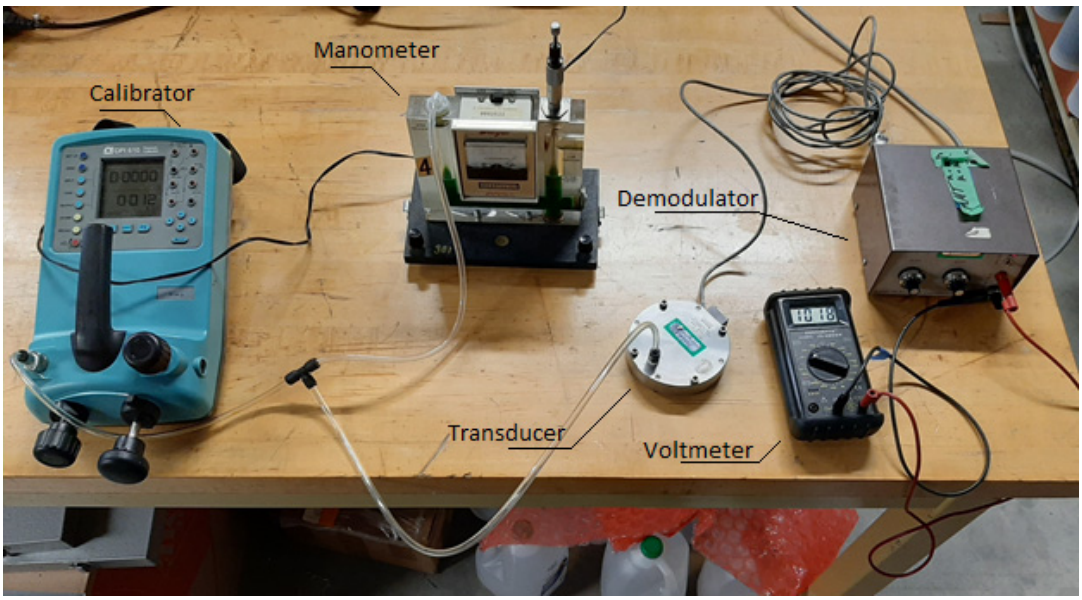

Figure 3.8 The setup used for calibrating the Validyne pressure transducers.

3.2.2 Measurement of friction factor

Friction factor was evaluated by measuring the pressure drop between two pressure ports along the test section. The two ports were connected to a Validyne differential pressure transducer by 1/8-inch stainless steel tubes. The length of these tubes was 5 ft, which ensured that the transducer was thermally isolated and therefore not affected by the heated pipes. The tubes were connected to the test section via threadolet, and straight male threaded stainless steel fittings (McMaster-Carr No 5182K411). The location of ports can be seen in Figure 3.9. A picture of the threadolets can be seen in Figure 3.10, and the dimensions can be found in **Appendix A**. The transducers used for pressure drop measurements were calibrated using the same method described in the above section.

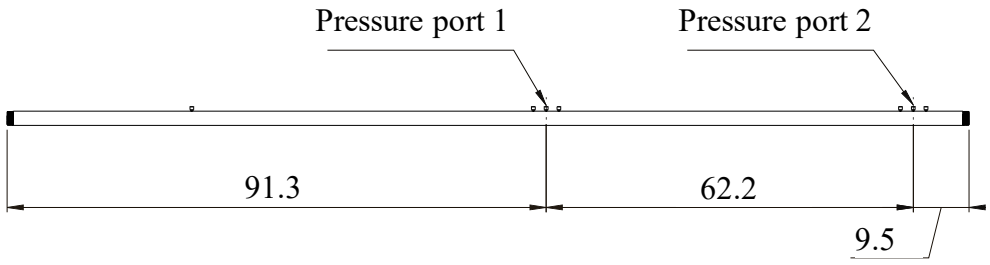

Figure 3.9 A schematic that shows the location (in inches) of pressure ports in the test section (section E).

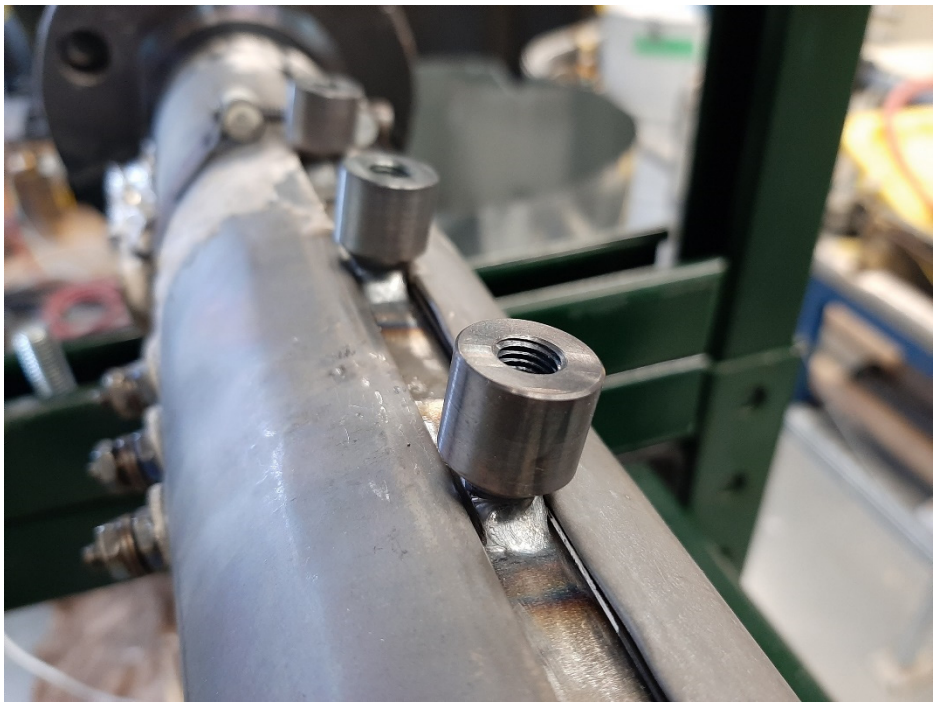

Figure 3.10 A photo of the threadolets welded on a pipe in the test section for connecting the pressure transducer ports to the pipe via straight male fittings.

3.2.3 Measurement of wall temperature

The wall temperature of the test section was measured using various K-type thermocouples (TCs) that were mounted on the outer surface of the pipe. The TC included probe-type, plate-type and spot-welded thermocouples shown in Figure 3.11. Figure 3.12 (a) shows the location of the thermocouples that measured the inlet air temperature. To measure the inlet air temperature at the channel centerline, an ungrounded K-type thermocouple (TC1, Omega Engineering, part number TJC36-CASS-010U-12) with a sheath diameter of 0.01 inch and a probe length of 12 inch was placed approximately one inch prior to the cooling jacket. TC1 was inserted inside the pipe and measured the air temperature at the centerline of section C. In addition to TC1, a thermocouple probe was installed on the pipe wall at the inlet of the test section (TC2). This probe-type thermocouple was an ungrounded K-type thermocouple (Omega Engineering, part number KMQSS-125U-12) with a sheath diameter of 0.125 inch and a probe length of 12 inches. Figure 3.12 (b) shows the location of thermocouples in each zone. The distance of each thermocouple can be found in Table 3.2.

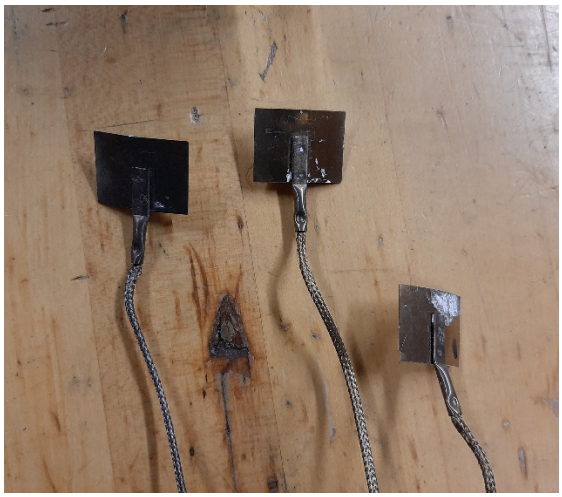

(a)

(b)

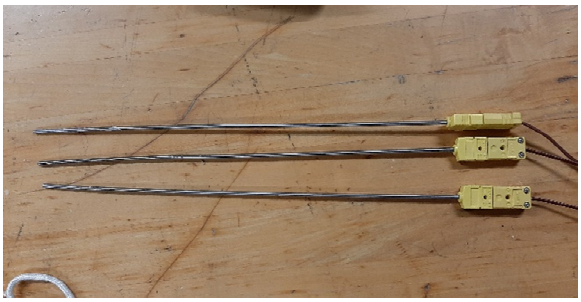

(c)

Figure 3.11 Photos of (a) plate-type thermocouple, (b) spot-welded thermocouples, (c) and probe-type.

Among the thermocouples inside of the test section, three were connected to the controllers. These thermocouples, also called control thermocouples, provided temperature feedback to the controllers. This meant that the controllers regulated the power input of the heaters to keep the temperature of these three thermocouples at a constant set temperature (375°C in experiments conducted at high temperatures) while the experiments were running. In zone two, the thermocouple connected to the controller changed depending on the type of the experiments. TC4, TC8 and TC15 were connected to the controllers of zones one, two and three, respectively.

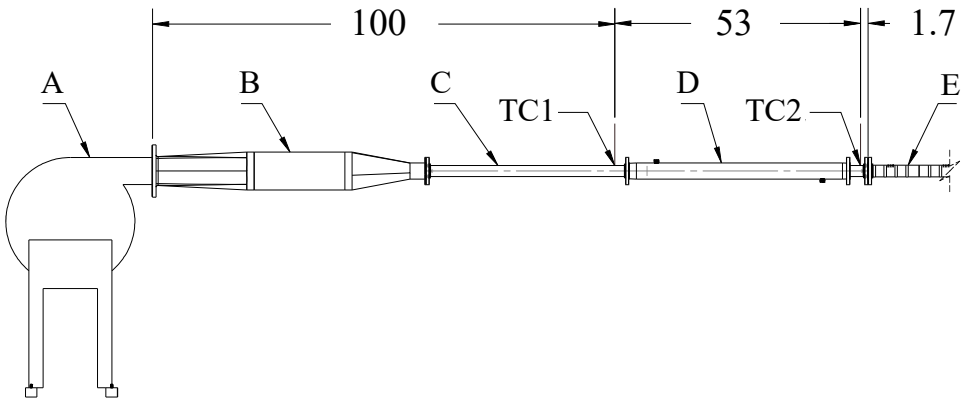

(a)

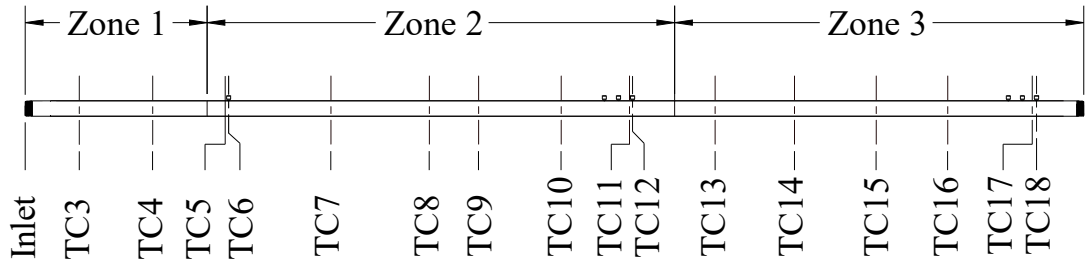

(b)

Figure 3.12 The location of the thermocouples on the pipe wall (dimensions are in inches) (a) outside of the test section (section E) and (b) in the test section.

Table 3.2 Thermocouple types and their location from the inlet along the test section (section E).

TC #	Type of TC	Distance (in)	TC #	Type of TC	Distance (in)
1	Probe	N/A	10	Plate	82.5
2	Probe	N/A	11	Spot welded	93.0
3	Spot welded	8.3	12	Probe	93.5
4	Spot welded	19.6	13	Plate	106.2
5	Spot welded	30.8	14	Plate	118.4
6	Probe	31.3	15	Spot welded	131.0
7	Plate	47.0	16	Plate	142.0
8	Spot welded	62.2	17	Spot welded	155.0
9	Plate	66.0	18	Probe	155.7

The thermocouples were all newly purchased, and they did not require calibration. To make sure that thermocouples were not defected, they were immersed in ice and boiling water (i.e., a medium with known temperature) and the temperature was measured over a period of time, *t*. The results of these tests can be seen in Figure 3.13. This figure shows that the maximum variations in temperature for all thermocouple types in the boiling water were less than 0.2 ℃. In the ice water test the variations were less than 0.1 ℃. Therefore, the measurements in ice water is more accurate than measurement in boiling water.

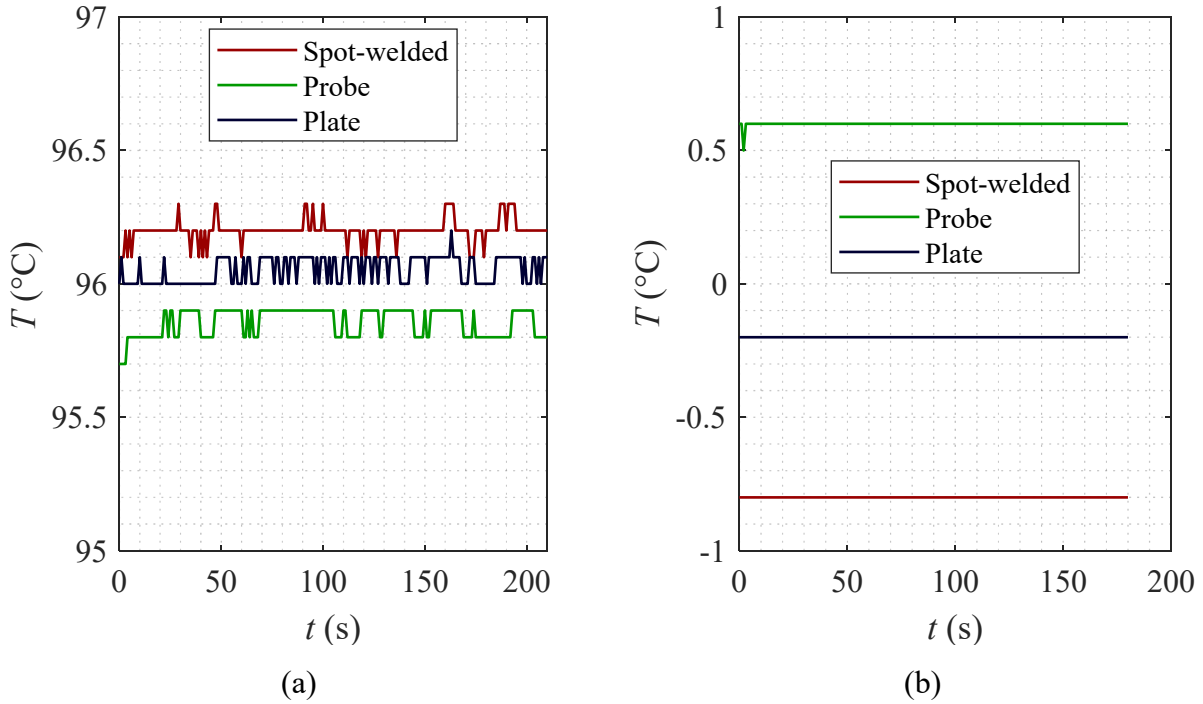

Figure 3.13 Measurement of temperature in (a) boiling water and (b) ice water using different thermocouple types.

3.2.4 Measurement of air temperature

For air temperature measurements, two rakes were inserted into the pipe in the test section at the locations shown in Figure 3.14. The first rake was located approximately 45*D* downstream of the inlet of the test section, where the thermal state is expected to be fully developed (Incropera et al. 2007), and the second rake was placed approximately at 73*D* downstream of the inlet.

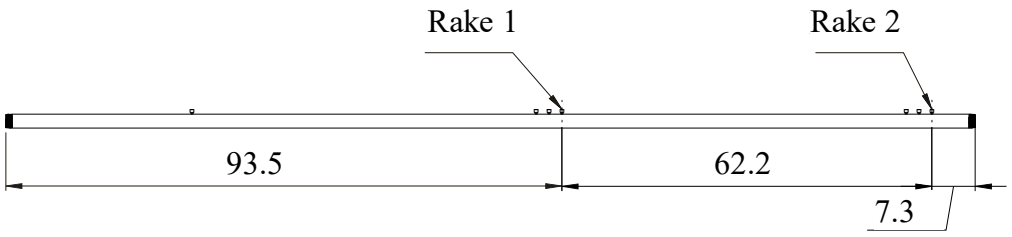

Figure 3.14 The location of the rakes in the test section (section E). Dimensions are in inches.

Each rake consisted of a stainless-steel tube, five thermocouples, and a thermocouple holder. Thermocouple holders were two-piece 3D printed plastic parts that secured the thermocouple wires

in place during the installation of the rake. Detailed drawing of the rake tubes and thermocouple holders can be found in **Appendix A**. The rake tube was made of a hollow standard 1/8-inch tube that housed the thermocouple inside of it. A picture of the two rakes can be seen in Figure 3.15 (a). Figure 3.15 (b) shows how the rake was installed in the pipe. The fitting in this figure is a bore-through straight male threaded stainless steel fittings (McMaster-Carr No 5182K411). The flow is from left to right meaning that the rakes were facing the flow in all experiments.

One end of the rake tube, as can be seen in Figure 3.15 (c), was cut, and had five holes in its wall. The tips of the thermocouples were inserted into these holes, and at least three millimetres of the thermocouple was sticking out of the tube. The thermocouple that is closest to the rake tip is referred to as RT5, and the thermocouple that is farthest from the rake tip is referred to as RT1 (RT1 is located at the centerline of the pipe). The rest of the rake thermocouples are referred to as RT2, RT3 and RT4. The thermocouples were then glued to the tube by epoxy adhesive (Resbond 940 HE). The tip of the tube was cut in a way that allowed only one contact point with the pipe surface. The other end of the tube, where the thermocouple wires protrude out, was connected to a thermocouple holder. The radial location of rake thermocouples is shown in Figure 3.15 (d).

As rake 1 was located between pressure ports 1 and 2 in the test section, it created a disturbance in the flow that could affected the pressure drop measurements. Thus, rake 1 was removed from the pipe in the experiments in which the pressure drop was measured (see Chapter four section 4.2 for more details).

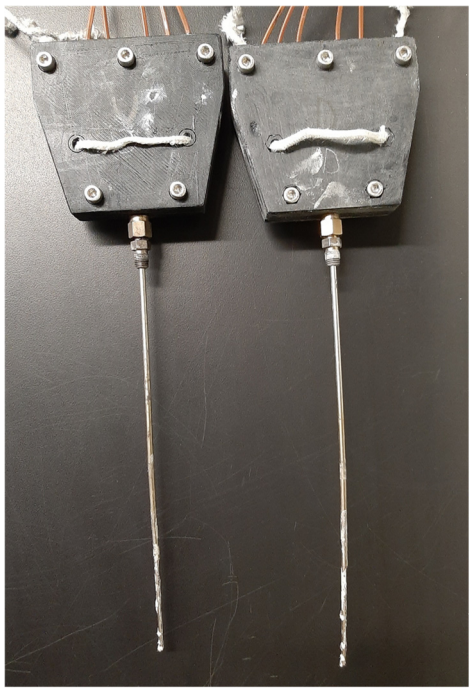

(a)

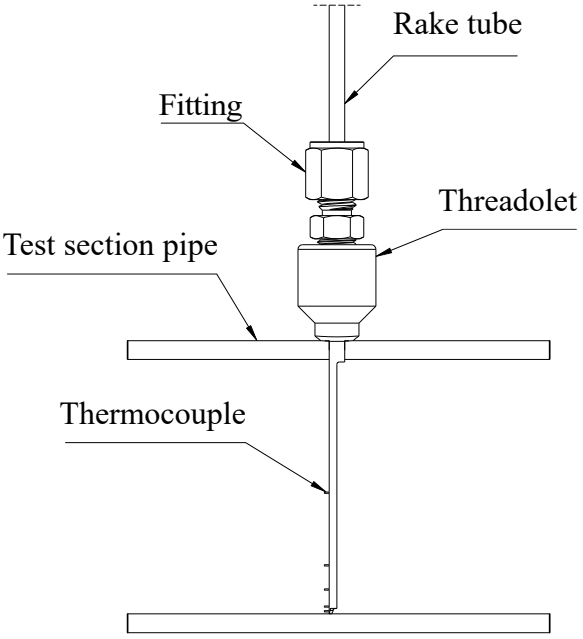

(b)

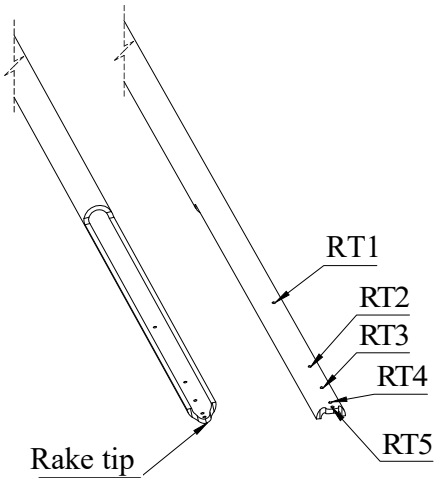

(c)

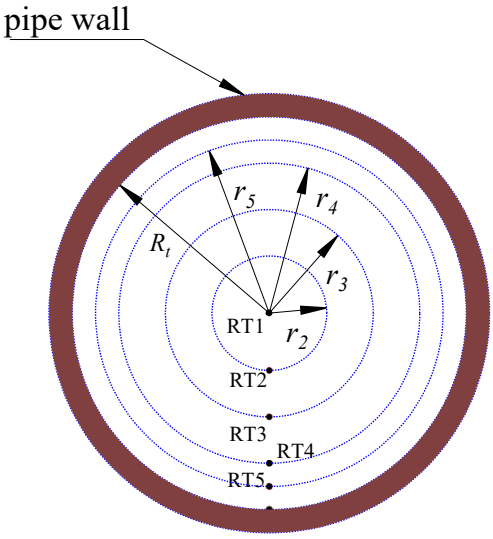

(d)

Figure 3.15 photos and schematics of (a) both rakes, (b) probe of the rakes installed inside the test section, (c) tip of the probe, and (d) the radial distance of RTs from the pipe centerline.

The wall-distances, the distance between the thermocouple and the pipe wall, was found by measuring the distance between each thermocouple and the tip of the rake tube. A sample image of upstream rake thermocouple used in calculating wall distances is shown in Figure 3.16. In this figure, the grid paper is added for visualisation only. The wall distances for this figure are summarised in Table 3.3. Wall distance of each thermocouple is the distance between the thermocouple and the pipe wall. The distance between the thermocouple and the rake tip is measured to determine the wall distance of rake thermocouples. The wall distances of the thermocouples were slightly different in some of the experiments. The details of the wall distance in different experiments are given in **Appendix D**.

Table 3.3 The distance of the rake TCs with respect to rake tip.

location	Thermocouple number	Wall-normal distance (mm)
Rake 1	RT1	25.36
	RT2	9.94
	RT3	4.85
	RT4	1.42
	RT5	0.35
Rake 2	RT1	25.43
	RT2	10.33
	RT3	4.93
	RT4	1.75
	RT5	0.66

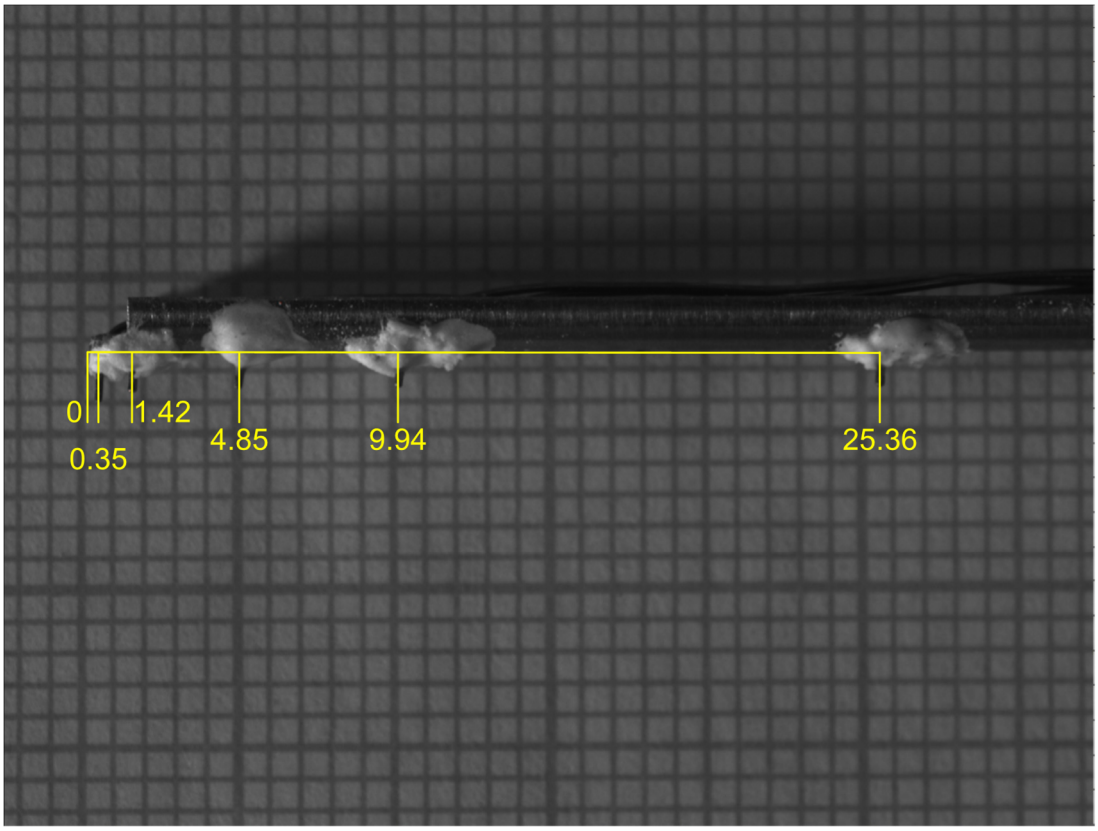

Figure 3.16 The pictures taken from the upstream rake to measure the distance of each thermocouple with respect to the rake tip in millimetre.

The rake thermocouples were newly purchased, and no calibration was required. However, they were immersed in ice and boiling water once before conducting experiments to make sure that non of the thermocouples were defected. The results of these tests can be seen in Figure 3.17.

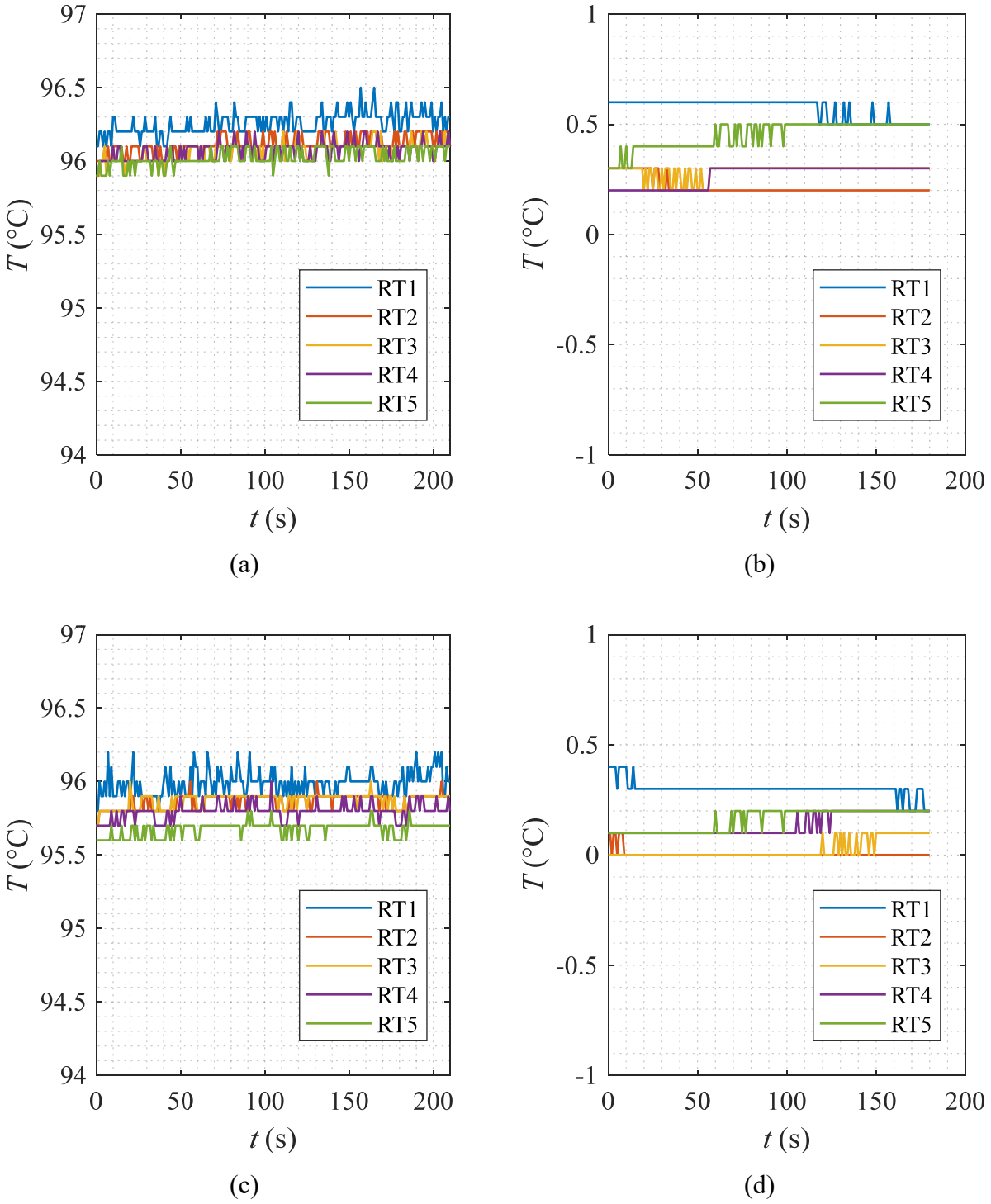

Figure 3.17 Tests conducted on the thermocouples inside rake 1 in (a) boiling and (b) ice water, and inside rakes 2 in (c) boiling and (d) ice water.

3.2.5 Data acquisition

The signals of the thermocouples were acquired by two 16-channel National Instruments (NI) data acquisition cards (NI 9213 module). These modules had a sampling rate of around 100 samples per second. The 100 samples were averaged in LabVIEW and this average was logged every second. The resolution of the analog-to-digital converter was 24 bits. The modules were housed in a NI cDAQ-9174 chassis.

The signal from pressure demodulators were acquired by an 8-channel analog input module (NI 9201). The ADC resolution was 12 bits, maximum sample rate was 5×10^5 samples per second, and the samples were averaged and logged every second. All signals were monitored and recorded using a custom-built LabVIEW (NI) interface. This interface is shown in Figure 3.18. The interface consists of two sections: the panel on the left and the test section schematic on the right of this figure. The panel showed pressure measurements in dials, and measurements of both wall and air temperatures were displayed by two 8×2 tables. These the arrangement of the table cells were similar to the location of the DAQ card thermocouple wire inputs. The zone 1, zone 2 and zone 3 boxes displayed both the set and measured temperatures of heaters and control thermocouples, respectively. The schematic on the right-hand side of the interface showed the same temperature measurements as the panel tables and boxes. However, the schematic had the added benefit of showing the physical location of each measurement on the test section.

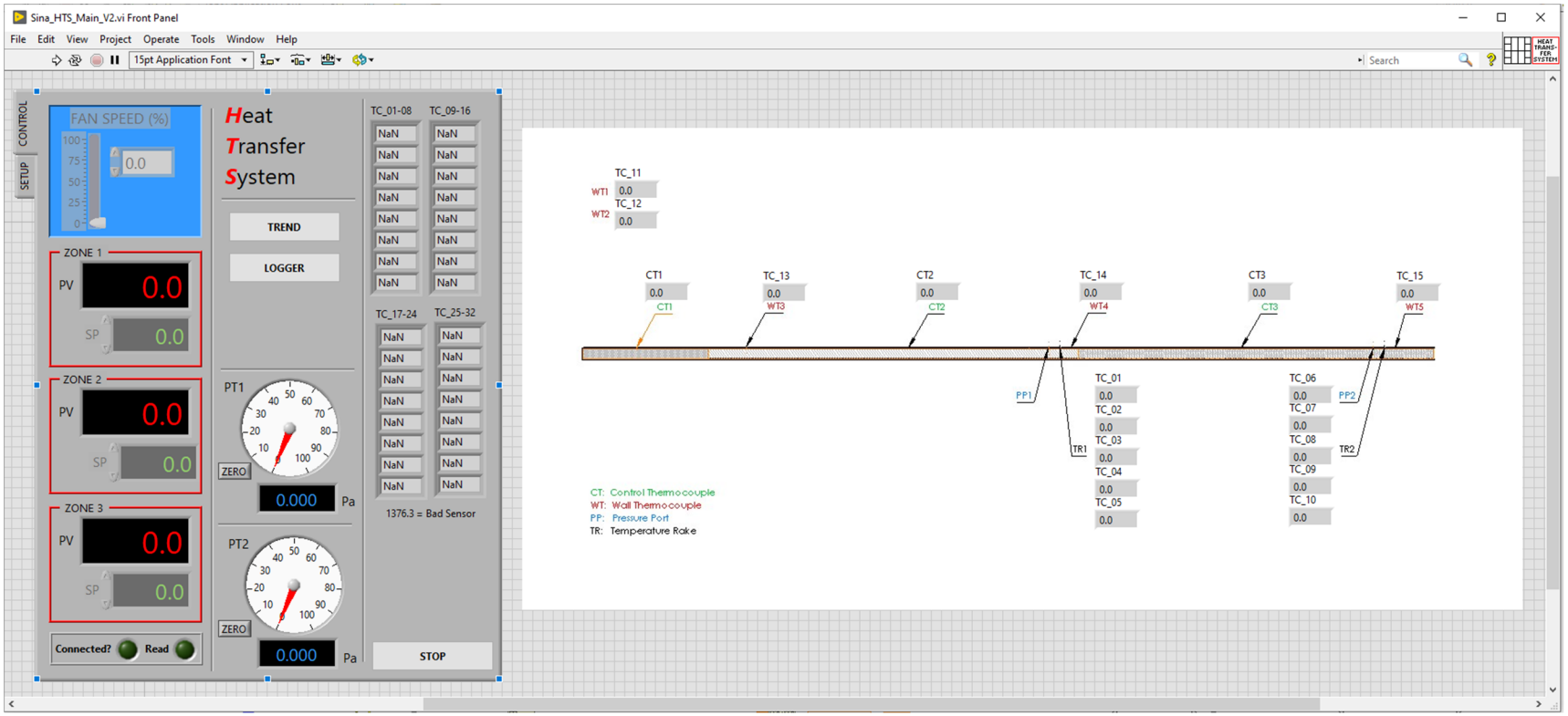

Figure 3.18 The user interface customized for running the experiments in LabVIEW.

Chapter 4.

Methodology

In this chapter, the geometric features of the pipes that were tested, and the experimental methodology are explained. After that, the parameters that were evaluated from the measured variables are explained. Finally, the uncertainty of the measured variables and the propagation of the uncertainty to the evaluated variables is presented.

4.1 The pipe sections

Five two-inch schedule 40 pipes (ASME B36.10) with different internal surfaces were investigated. The pipes were coated on the inside by a proprietary coating of Quantiam Technologies Inc. Figure 4.1 shows the inside of the pipes. The reference pipe had a smooth internal surface, covered with one layer of coating. This pipe is referred to as the “baseline” case, or SM, and it is shown in Figure 4.1 (a).

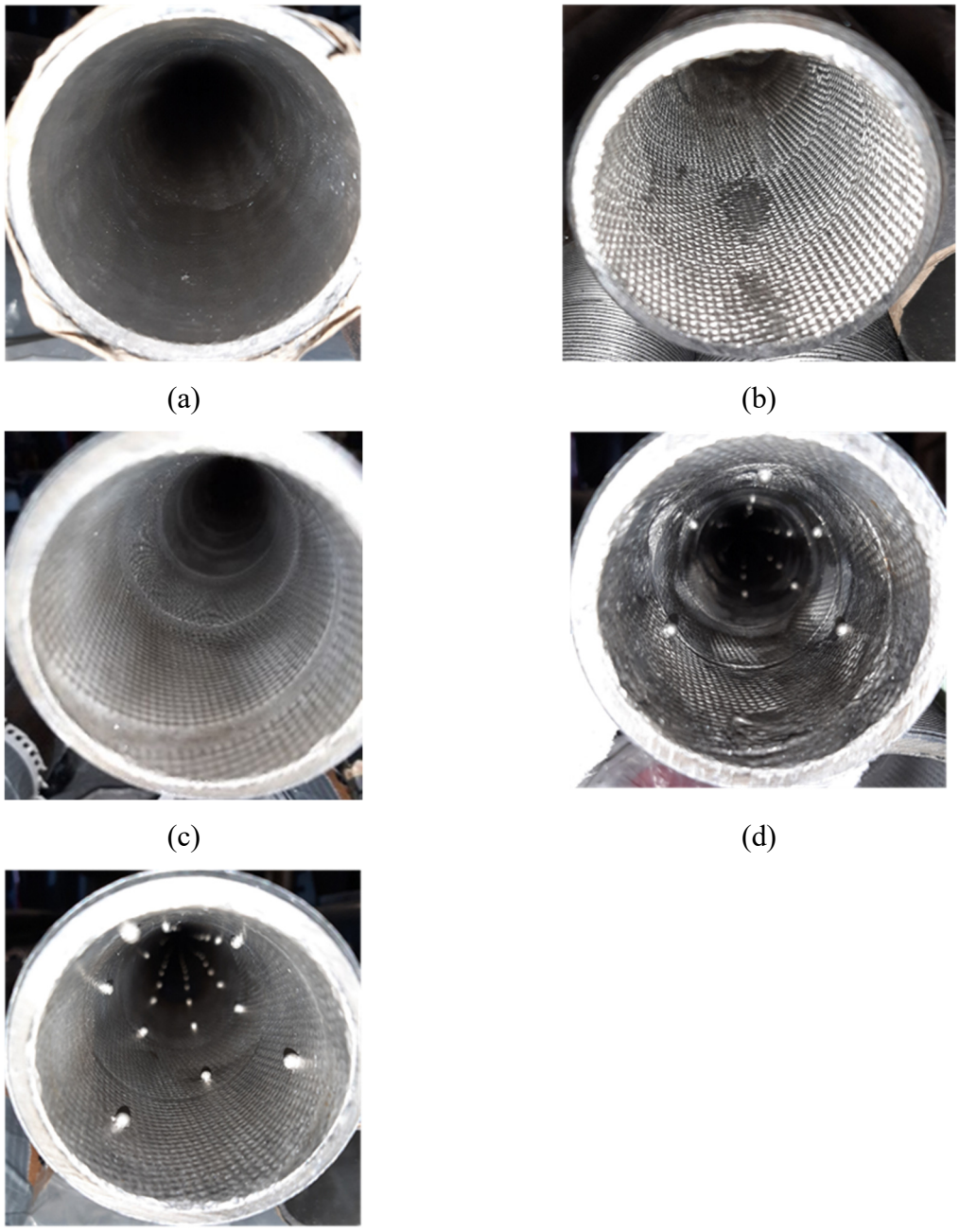

(a) (b)

(c) (d)

(e)

Figure 4.1 Photos of the inside of the (a) SM (b) MC1, (c) MC2, (d) MB50, and (e) MB37.

The internal surface of two of the pipes were covered with mesh screen shown in Figure 4.1 (b) and (c). The difference between the pipes covered with mesh was that one of them had one layer of coating and the other had two layers of coating. The pipe with one layer of coating is referred to as MC1 and it is shown in Figure 4.1 (b). The pipe with two layers of coating is referred to as MC2 and it is shown in Figure 4.1 (c).

Figure 4.1 (d) and (e) shows the pipes with ball bearings. Ball bearings were 3.5 mm in diameter, and they were welded to their inner surface. In additions to the bearings, the internal surface of these pipes was covered with the mesh screen and two layers of coating mentioned above. Figure 4.2 shows schematics of the pipes and the arrangement of the bearings: (a) angular spacing of the bearings, and (b) axial spacing of the bearings.

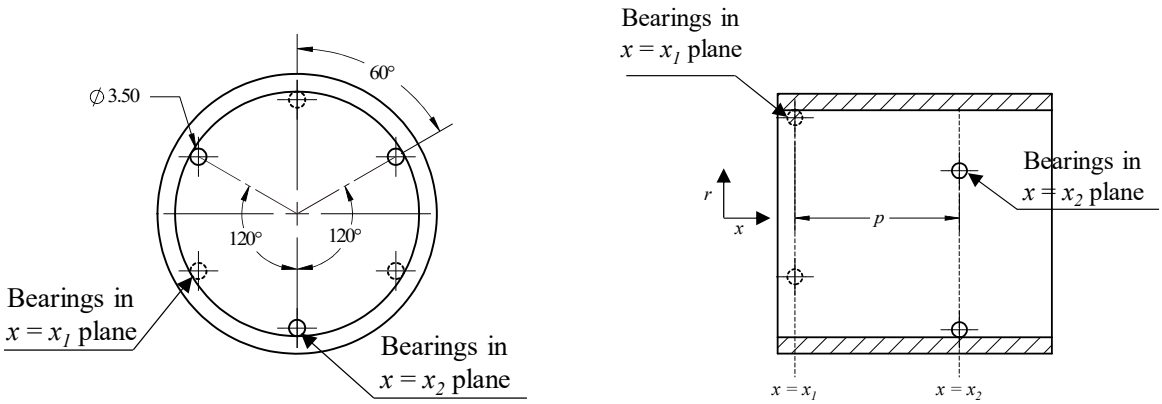

(a) (b)

Figure 4.2. Schematics of the (a) angular and (b) axial spacing of the bearings for MB37 and MB50 pipes (dimensions are in mm).

As can be seen in Figure 4.2 (b), three bearings are present in the x_1 plane. These bearings are shown by dashed circles. In additions, three bearings are present in x_2 plane. These bearings are shown by solid circles. Figure 4.2 (a) shows the angular spacing between the bearings. As can be seen, the bearings in each plane had an angular spacing of 120 degrees. It can also be seen that there was an azimuthal shift of 60º between the bearings in x_1 plane and the bearings in x_2 plane. The distance between the x_1 and x_2 plane, called pitch $p = x_2 - x_1$, was different for the pipes with bearings. The pitch in one of the pipes was 37 mm, hence the pipe is referred to as MB37. The pitch in the other pipe was 50 mm, hence it is referred to as MB50. This arrangement of bearings was repeated over the entire length of both pipes.

The roughness of the internal surface of the pipes was measured using an optical profilometer. Three samples of different sizes were cut from each pipe. Figure 4.3 (a) shows the raw data of roughness heights collected by the profilometer for MC1. The parameter z shows the heights

measured by the profilometer and x and y are the dimensions of the pipe sample. To eliminate the curvature of the pipe on the evaluation of roughness, the data was detrended using a second-degree polynomial. The detrended roughness heights can be seen in Figure 4.3 (b). A black line can be seen in Figure 4.3 (a) and (b). This line is shown in a two-dimensional plot in Figure 4.3 (c).

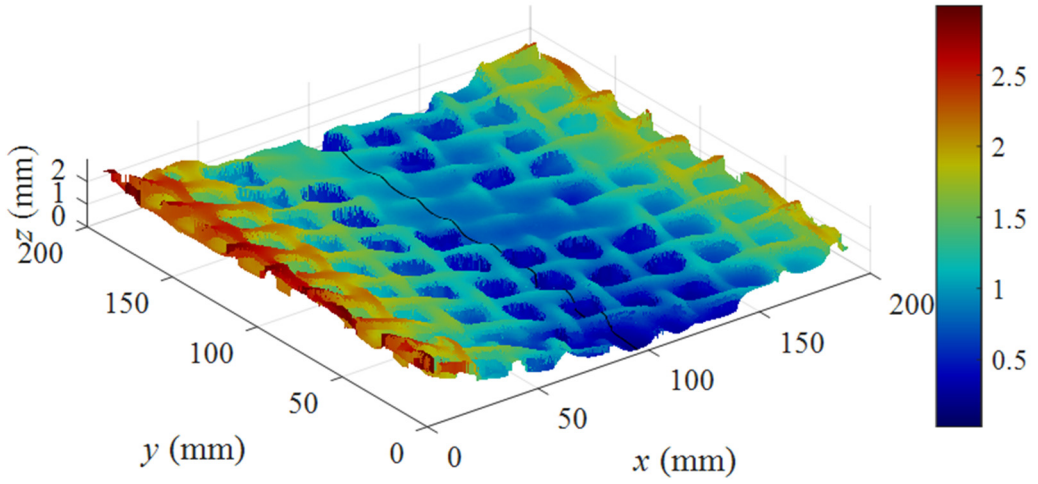

(a)

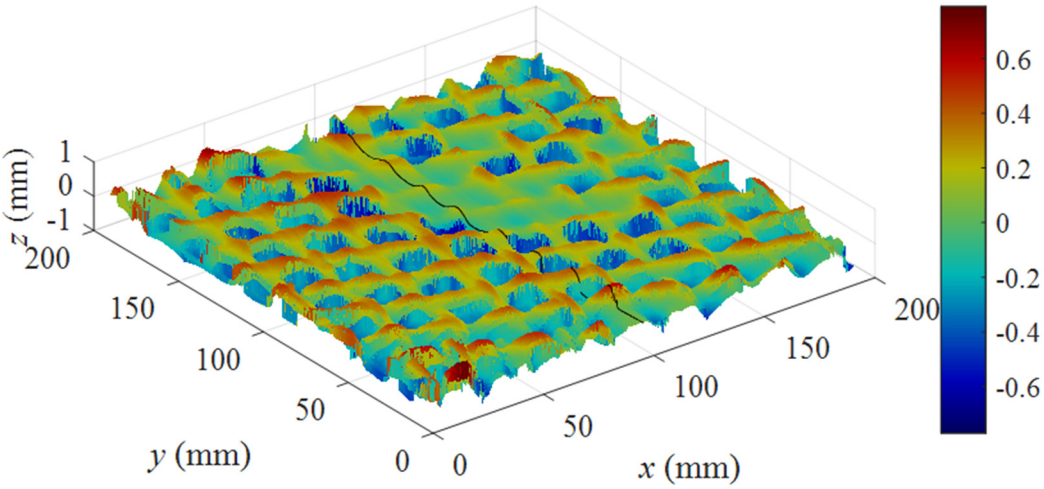

(b)

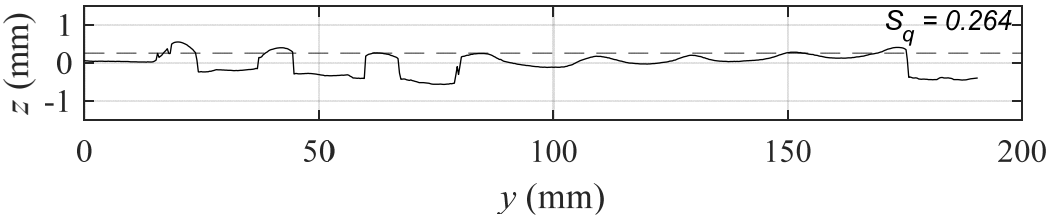

(c)

Figure 4.3 The roughness heights for the raw data (a), detrended data (b), and a line in the *yz* plane at x = 100 mm.

The roughness of a surface was evaluated by two parameters: arithmetic mean height (*Sa*) and root mean square height (*Sq*). *Sa* is the height difference of roughness elements compared to the surface arithmetical mean height, and for a surface with an area *A,* it is given by

$$Sa = \frac{1}{A}\iint_A |z(x,y)|dxdy\,. \tag{4.1}$$

where $z(x,y)$ is the height of the surface elements as a function of x and y. The root mean square height *Sq* for surface with an area *A* is given by

$$Sq = \sqrt{\frac{1}{A}\iint_A z^2(x,y)dxdy}\,. \tag{4.2}$$

The arithmetic mean height (*Sa*) and squared mean height (*Sq*) over the surface of the pipes, evaluated from equations 4.1 and 4.2, were evaluated from the roughness heights of the three samples. Table 4.1 shows the roughness of the pipes used in the experiments.

Table 4.1 The roughness of the pipes that were used in experiments.

Pipe acronym	Internal roughness type	*Sa* (μm)	*Sq* (μm)
SM	Smooth pipe	5	7
MC1	Mesh with one layer of coating	206	264
MC2	Mesh with two layers of coating	18	23
MB50	Mesh with 2-inch spaced bearings	60	89
MB37	Mesh with 1.5-inch spaced bearings	27	31

The roughness of the pipes in Table 4.1 are calculated based on the average of the roughness values of the three samples for each pipe. The roughness values for all pipes, including MB37 and MB50, are evaluated from samples that did not include the ball bearings. The MC1 had the highest surface

roughness followed by MB50, MB37, MC2 and SM, respectively. Although MC1 and MC2 were both covered with mesh, they had different roughness values. This was because MC2 was covered with two layers of coating while MC1 was covered in only one layer of coating. The second layer of coating in MC2 filled some of the valleys between the mesh wires. This made the MC2 much smoother than MC1.

4.2 Experimental methodology

Three different types of experiments were conducted on each pipe, and each experiment was repeated at least three times to see if the results were repeatable. The first set of experiments, referred to as type A, were conducted on each pipe at room temperature to measure the pressure drop at eight *Re* values of 20,000 to 90,000, in intervals of 10,000. In these experiments, the heaters were switched off and the pipe was at room temperature. The blower RPM was adjusted until the desired *Re* was reached, and then no further changes were made to the RPM for three minutes while the data was being logged. After that the blower RPM was varied, measurements were done for three minutes at a different *Re*. This process was continued until the pressure drop data was collected at all eight *Re* cases. During these measurements, the rake one was not installed. Some small variations were observed when the blower RPM was not being changed. These variations in RPM were around one to three percent.

In the second set of experiments, referred to as type B, the temperature of all three controllers was set to 375°C. More information on the distribution of wall temperature is provided in section 3.2.3. The pressure drop of the test section was measured at the same eight *Re* values mentioned above. Because it took around five to eight minutes for the mean pressure measurements to reach a steady state, the data was collected at each *Re* for ten minutes. In these experiments the upstream thermocouple rake was not installed.

In the third experiment, referred to as type C, both thermocouple rakes were installed, and the temperature of all three controllers was set to 375°C. The air temperature was measured using the TC rakes installed at x = 93.5 and 62.2 inches. Because it took around twenty minutes for mean air temperature to reach a steady state, the data was collected at each *Re* for 40 minutes. These experiments were conducted at the same eight *Re* values mentioned above. Table 4.2 shows a list of the experiments that were conducted on different pipes.

Table 4.2 A summary of the experiments conducted on different pipes.

Experiment type	Pipe	Repetitions (*n*)	Duration of data collection (min)	Pipe wall temperature
A	SM	4	3	Room temperature
B	SM	3	10	375℃
C	SM	3	40	375℃
A	MC1	6	3	Room temperature
B	MC1	3	10	375℃
C	MC1	3	40	375℃
A	MC2	3	3	Room temperature
B	MC2	3	10	375℃
C	MC2	3	40	375℃
A	MB50	3	3	Room temperature
B	MB50	3	10	375℃
C	MB50	3	40	375℃
A	MB37	3	3	Room temperature
B	MB37	3	10	375℃
C	MB37	3	40	375℃

4.3 Calculations of flow parameters

The independent variable that was changed by the operator during each repetition was the blower speed. The dependant variables directly measured from the instruments included the differential pressure of the Pitot-static tube, ΔP_P, the static pressure drop between the pressure ports, ΔP, and the air temperature measured by the TC rakes. The velocity of air at the pipe centerline was calculated based on ΔP_P using

$$U_c = \sqrt{\frac{2\Delta P_P}{\rho}}. \tag{4.3}$$

The Prandtl's friction factor, f_P, was used to find the bulk velocity. It was first calculated from the Prandtl's friction law given in

$$\frac{1}{\sqrt{f_p}} = 2\log\left(\frac{D\sqrt{f_p}U_c}{\nu\left(\sqrt{\frac{f_p}{8}}\left(B_1+\frac{3}{2\kappa}\right)+1\right)}\right)-\frac{4}{5} \tag{4.4}$$

where B_1 is zero and κ is 0.4. According to Pope (2000), equation 4.4 is obtained from approximating the mean velocity profile using the logarithmic defect law. After f_p was calculated, U_b and Re was found using

$$U_b = \frac{U_c}{\sqrt{\frac{f_p}{8}}\left(B_1+\frac{3}{2\kappa}\right)+1}, \text{ and} \tag{4.5}$$

$$Re = \frac{U_b D}{\nu}, \tag{4.6}$$

respectively. The physical properties of air was found according to Yaws (2008). The kinematic viscosity, ν, was calculated from

$$\nu = (6.28\times10^{-5}(T_r+273.15)^2+6.26\times10^{-2}(T_r+273.15)-8.65)\times10^{-6} \tag{4.7}$$

where T_r is the room temperature in Celsius measured at TC1. Mass flow rate, $\dot{m}$, was calculated from

$$\dot{m} = \rho U_b \left(\frac{\pi D^2}{4}\right) \tag{4.8}$$

Where ρ was the fluid density calculated from

$$\rho = -6.90 \times 10^{-9}(T_r + 273.15)^3 + 1.42 \times 10^{-5}(T_r + 273.15)^2 - 1.04 \times 10^{-2}(T_r + 273.15) + 3.22. \tag{4.9}$$

The bulk temperature of the flow, T_b, was calculated from the rake measurements. The bulk temperature of rake one is indicated by T_{b1} and the bulk temperature of rake two is indicated by T_{b2}. The bulk temperature T_b for either rake was found using

$$T_b = \sum_{i=1}^{5} \frac{(T_{RTi} + T_{RTi+1})({r_{i+1}}^2 - {r_i}^2)}{2R^2} \tag{4.12}$$

where T_{RTi} is the temperature measured at the ith thermocouple in the rake, and r_i is the radial distance of this thermocouple from the pipe centerline based on the coordinate system defined in Chapter 3 (See Figure 3.15 (d)). Equation 4.12 was obtained from applying an areal average of air temperature over the cross section of the pipe. Because the air temperature was measured in five discrete locations, trapezoidal integration is used to find the areal average. This radial distance was found from the wall distance of the thermocouple found in Table 3.3 and **Appendix D**. T_{RT6} was the temperature of the surface-mounted thermocouple closest to the location of the rakes, which was TC12 for the rake one and TC18 for rake two. The radial distance of RT6 was equal to pipe diameter i.e., R. The average bulk temperature within the test section, T_t, is obtained by averaging the upstream bulk temperature, T_{b1}, and the downstream bulk temperature, T_{b2} following

$$T_t = \frac{T_{b1} + T_{b2}}{2}. \tag{4.13}$$

In type B and C experiments the air temperature of the test section (section E) is different from the air temperature at the Pitot tube location (Section D). Therefore, the fluid properties in section E are also different from Section D. For example, the Reynolds number evaluated from the Pitot tube

pressure measurements is different from the Reynolds number of the test section (due to the higher air temperature). The fluid properties of the test section are depicted by subscript *t* and are estimated at average bulk temperature, T_t. According to Yaws (2008), specific heat capacity $C_{p,t}$, thermal conductivity, k_t, density ρ_t, and dynamic viscosity, μ_t, of the flow in the test section can be calculated using

$$C_{p,t} = -7.15 \times 10^{-8}(T_t + 273.15)^3 + 1.84 \times 10^{-4}(T_t + 273.15)^2 - 4.68 \times 10^{-2}(T_t + 273.15) + 9.76 \times 10^2, \quad (4.14)$$

$$k_t = -1.22 \times 10^{-8}(T_t + 273.15)^2 + 7.53 \times 10^{-5}(T_t + 273.15) + 5.02 \times 10^{-3}, \quad (4.15)$$

$$\rho_t = -6.90 \times 10^{-9}(T_t + 273.15)^3 + 1.42 \times 10^{-5}(T_t + 273.15)^2 - 1.04 \times 10^{-2}(T_t + 273.15) + 3.22, \quad (4.20)$$

and

$$\mu_t = 1.46 \times 10^{-6}(T_t + 273.15)^{1.5}/(T_t + 273.15 + 110). \quad (4.21)$$

the mass flow rate that was calculated at the Pitot tube location according to equation 4.8 is used for calculating the bulk velocity and Reynolds number of the flow in the test section. The Reynolds number, Re_t, and bulk velocity of the fluid at the test section, $U_{t,b}$, was calculated from

$$Re_t = \frac{4\dot{m}}{\pi D \mu_t} \quad (4.22)$$

and

$$U_{t,b} = \frac{4\dot{m}}{\pi D^2 \rho_t}, \quad (4.23)$$

respectively. The Nusselt number, *Nu*, was calculated from

$$Nu = -\frac{\dot{m}C_p}{\pi Lk}\ln\frac{T_s - T_{b2}}{T_s - T_{b1}} \tag{4.24}$$

where L was distance between the thermocouple rakes. T_s was the average pipe temperature calculated as

$$T_s = \sum_{i=13}^{17}\frac{T_{TCi}}{4} \tag{4.25}$$

where T_{TCi} is the ith thermocouple in the test section (Table 3.3). The friction factor of the test section, f, was calculated from

$$f = 2\frac{\Delta P}{L}\frac{D}{\rho_t U_{t,b}^2} \tag{4.26}$$

In addition to calculating Nu number, for comparing the heat transfer capabilities of the pipes, the increase in bulk temperature from rake one to rake two is also considered. Temperature measurements of rake thermocouples are normalized using

$$T_{n,RTi} = \frac{T_s - T_{RTi}}{T_s - T_b} \tag{4.27}$$

where $T_{n,RTi}$ is the normalized temperature of each rake thermocouple, T_{RTi} is the temperature of the ith thermocouple in the rake. This normalized temperature is used to determine whether the pipe flow is thermally fully developed or not. The heat transfer coefficient, h, was calculated from

$$h = \frac{\dot{m}C_p}{A_L}\left(\frac{T_{b2}-T_{b1}}{T_s-T_t}\right). \tag{4.28}$$

4.4 Uncertainty analysis

The total uncertainty of a variable, x, that was directly measured by either the transducers or thermocouples was evaluated from

$$\delta_x = (B_x^2 + P_x^2)^{1/2} \tag{4.29}$$

where the P_x is the random uncertainty and B_x is the systemic uncertainty of x. Because the systemic uncertainty of measurements was much smaller than the random uncertainty, B_x was ignored for both pressure and temperature measurements. Therefore, the uncertainty of x was estimated using

$$\delta_x = \pm t_s \frac{S_x}{\sqrt{n}} \tag{4.30}$$

where n is the number of repetitions, t_s is the parameter t in the student's t distribution which is a type of probability distribution similar to the normal distribution with an adjusted bell shape to account for the number of data points. t_s values were found according to Wheeler et al. (1996). S_x is the standard deviation of x evaluated from

$$S_x = \sqrt{\sum_{i=1}^{n} \frac{x_i - x}{n-1}} \tag{4.31}$$

Where x_i is the mean of x in each repetition and x is the arithmetic mean of all repetitions. For n equal to three, four and six, the t_s was 4.303, 3.182 and 2.571 respectively. The uncertainty of a variable R, evaluated from N measured variables (R is a function of $x_1, x_2, \ldots, x_N$), was found from

$$\delta_R = \left(\sum_{j=1}^{N} \left[\delta_x \frac{\partial R}{\partial x_j} \right]^2 \right)^{1/2}. \tag{4.32}$$

The δ_R of variables in equations 4.3 to 4.28, can be found in **Appendix E**. δ_R of some of the variable from the type C experiment conducted on the smooth pipe is given in Table 4.3.

Table 4.3 Uncertainty of some of the variables measured at *Re* of 20,000 in a type C experiment.

Variable	First measurement	Second measurement	Third measurement	Mean	Standard deviation	δ_R
T_{TC1}	24.5	24.6	24.9	24.6	0.22	0.54
T_{RT1}	167.7	167.6	167.4	167.6	0.15	0.37
Re	19569	19646	19515	19515	164	368
Nu	37.9	38.9	38.8	38.5	0.54	1.22

When the analytical values of a parameter are known, the error of the experimental results is calculated from

$$RMSE = \sqrt{\frac{\sum_{i=1}^{n}(X_{o,i}-X_{P,i})^2}{n}}. \tag{4.33}$$

where, $X_{o,i}$ is the ith observed data (from experiments) and $X_{P,i}$ is the ith predicted data (from analytical values). The root mean square percentage error given in

$$RMSPE = \sqrt{\frac{\sum_{i=1}^{n}\left(\frac{X_{o,i}-X_{P,i}}{X_{o,i}}\right)^2}{n}}(100). \tag{4.34}$$

is also used to calculate the error of the experimental results compared to the analytical values.

Chapter 5.

Smooth Pipe

The experiments on the smooth pipe were carried out to evaluate the results in comparison to the literature. In addition, the results from the smooth pipe experiments are used as a baseline for comparing pipes with different internal roughness elements in later chapters. This chapter also further explains the experimental procedure and the data analysis.

As it was seen in Table 4.2, three different experiment types were conducted, and each experiment was repeated several times. Type A were experiments for the measurement of friction factor at room temperature. Type B were experiments for the measurement of friction factor with heated pipes. Type C were experiments for measurement of *Nu* number with heated pipes (See Chapter 4 for more details of each type of experiments). Each repetition is referred to as a "run" here.

5.1 Inlet flow condition

The mass flow rate and *Re* at the inlet of the test section were calculated from pressure measurements at the Pitot tube. As was mentioned in Chapter 2, equations 2.7, the fluctuating fluid properties are indicated by a tilde symbol (for example $\tilde{u}$ for the x component of velocity and $\tilde{T}$ for temperature), the average over time properties are indicated by no additional symbol (for example u and T), and the total (instantaneous) properties (instantaneous) properties are indicated by prime symbols (for example u' and T').

Figure 5.1 (a) shows the variations of $\Delta P_P'$ (the pressure measured from the Pitot tube) over time during type A experiment. All four runs (i.e., rep1 to rep 4) of type A experiment are included in this figure. The plot shows that $\Delta P_P'$ incrementally increases over time i.e., $\Delta P_P'$ is constant for a duration (of around three minutes) and then it suddenly jumps to a higher value and then remains

constant again. This pattern repeats eight times. This incremental increase of $\Delta P_P'$ is due to the increase of blower RPM. In all of the experiments, the RPM of the blower were set to values that corresponded to Re of 20,000 to 90,000 in steps of 10,000. Therefore, each increment of constant $\Delta P_P'$ in Figure 5.1 (a) corresponds to one of the eight *Re* values from 20,000 to 90,000. At each *Re*, the temperature and pressure measurements were averaged over the last minute of the constant-RPM period.

Similarly, Figure 5.1 (b) and (c) show variations of $\Delta P_P'$ over time for type B and type C experiments respectively. $\Delta P_P'$ incrementally changes over time as well, and each increment represent a *Re* value in the 20,000 to 90,000 range.

Figure 5.1 (d) shows the variations of $\Delta P_P'$ over time for only one increment of the Type C experiment that corresponds to *Re* of 50,000. This figure is presented here to show how the pressure is averaged over time at each *Re*. For example, the mean Pitot tube pressure (ΔP_P) is calculated from the average of all instantaneous pressure measurements during Δt, where Δt is the averaging window. Δt was the last minutes before the RPM was changed in type A experiments, the last two minutes in type B experiments, and the last ten minutes type C experiments. It can be seen in figures 5.1 (a), (b) and (c) that during Δt the mass flow rate was in a steady state.

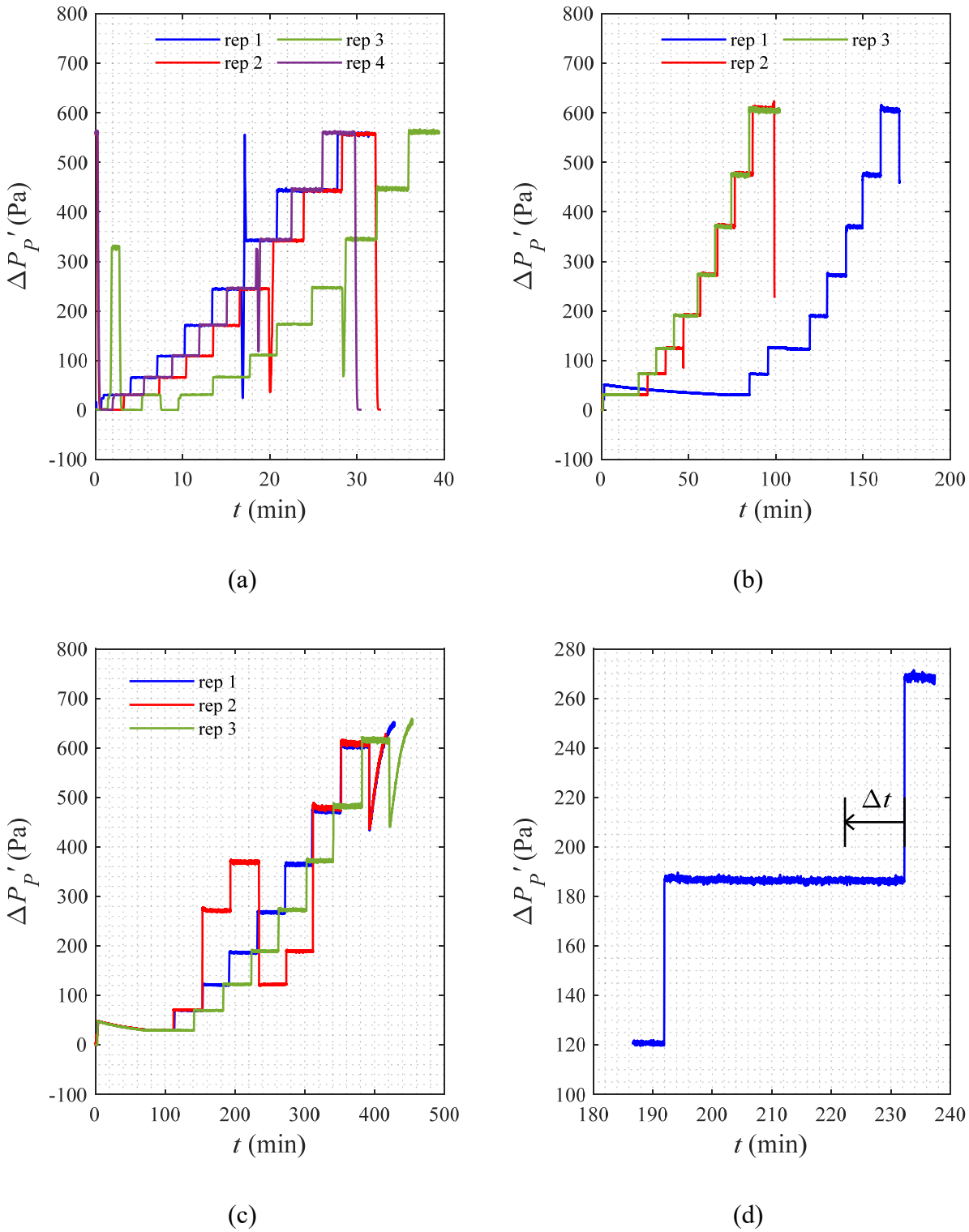

Figure 5.1. Time series of pressure drop measurements for experiments (a) type A, (b) type B and (c) type C, and (d) Δt for the first run of experiment type C at Re = 50,000.

The *Re* and mass flow rate evaluations also depend on the air temperature at the Pitot tube location. This temperature, called the inlet temperature, was measured by TC1, and viscosity and density of air were evaluated at the mean TC1 temperature using equations 4.7 and 4.9 respectively. Figure 5.2 (a), (b) and (c) shows the variations of TC1 temperature over time for type A, type B and type C experiments respectively. Figure 5.2 (a) shows that the changes of inlet air temperature are around one degree Celsius. However, in Figure 5.2 (b) and (c) the variations of inlet temperature were higher. This is because, in the heated pipe experiments, the heaters raised the temperature of the laboratory room by approximately five to six degrees. The increase in the laboratory temperature led to this increased of inlet air temperature. The changes of inlet temperature are taken into account for the calculation of *Re* and mass flow rate.

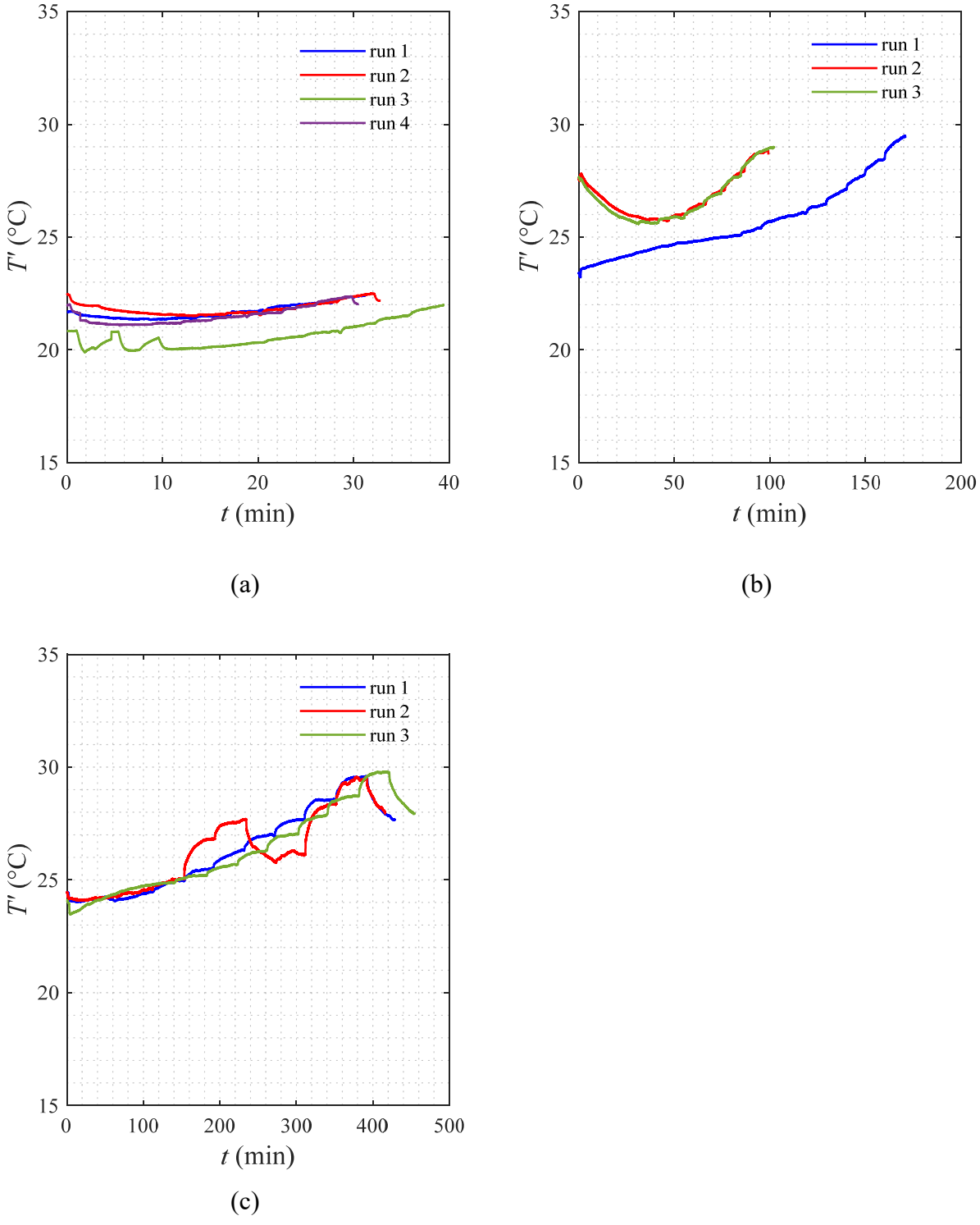

Figure 5.2. Time series of TC1 measurements (a) type A, (b) type B and (c) type C experiments.

5.2 Pipe wall temperature

In the experiments conducted with heated pipes, the incremental changes in *Re* led to a sharp drop or increase of pipe temperature (i.e., transient behaviour). The controllers gradually adjusted the power input of the heaters based on the temperature feedback from the thermocouples to return the pipe temperature back to 375°C. The changes of the temperature of control thermocouples for the first run of the type C experiment is shown in Figure 5.3 (the same plots for run 2 and 3 can be found in **Appendix. B**).

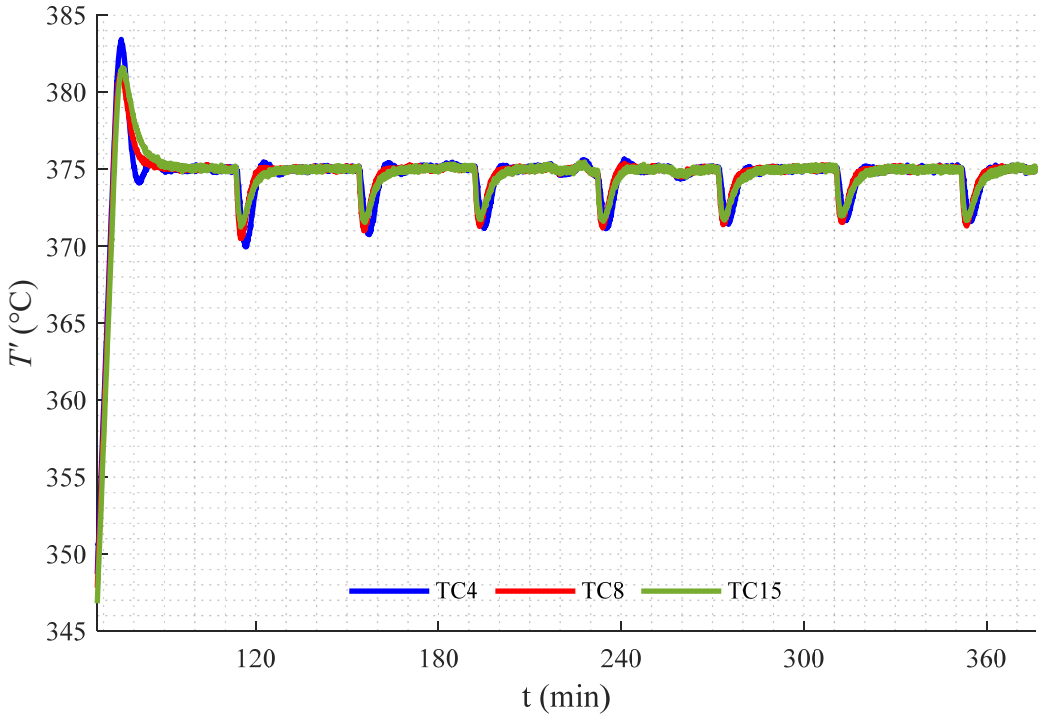

Figure 5.3. The time series of three thermocouples for the first run of type C experiment. These TCs were connected to the temperature controllers.

In figure 5.3, the temperature of the TCs increase to around 383°C at t = 80 minute and then decrease to 375°C. From t = 80 to t = 120 minute the *Re* is constant at 20,000 and the temperature remains constant at 375°C as well. After that at $t = 120^{th}$ minute, the *Re* was increases to 30,000 and the temperatures decreases. This decrease in temperature lasts only for around 5 minutes after which the controllers bring back the pipe temperature to 375°C. The same trend is seen for every increase of *Re* from 20,000 up to 90,000 (seven increments).

The changes in the temperature of the thermocouples mounted on the pipe wall over time for the first run of type C experiment can be seen in Figure 5.4. In this experiment, *Re* was increased over time. As can be seen, the temperature at different locations of the pipe wall followed a trend similar to thermocouples that were connected to the controllers; a small momentary drop in temperature followed by a small increase when the blower speed varied.

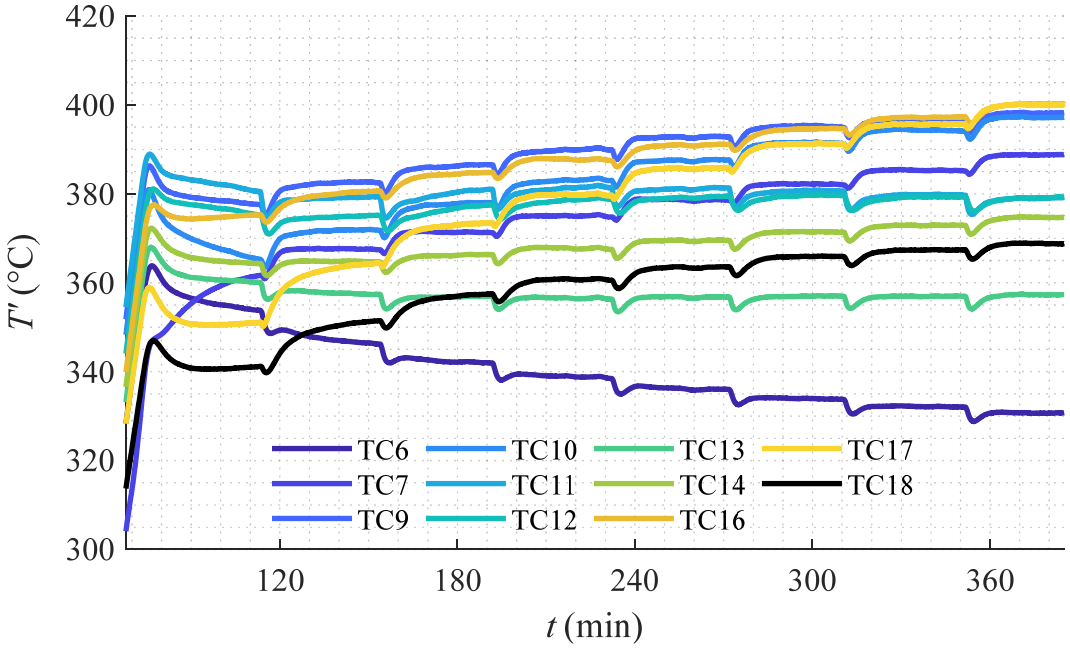

Figure 5.4. Time series of wall-mounted thermocouples for experiment 1 run 1.

To find an averaging window in which the variables are statistically converged, and mean flow is at steady state, the effect of using different averaging windows for type A experiment is investigated. Figure 5.5 shows different parameters averaged over time at Re = 40,000 in the first run of type C experiment. The horizontal axis shows the time when Re = 40,000. This Re started at t = 148 min and ended at t = 188 min. The averaging window for this Re is defined as $\Delta t = t_0 - t$, where t_0 = 188 min. In Figure 5.5 (a), the vertical axis (ΔP_P) shows time-averaged Pitot tube pressure with respect to different averaging windows. In this figure, the value of ΔP_P at a Δt is calculated as the average of instantaneous pressure measurements ($\Delta P_P'$) from the time t to the end of the duration at t_0 = 188 min. For example, the value of ΔP_P at Δt = 20 min is equal to the average of all $\Delta P_P'$, from t = 168 min to t = 188 min. As can be seen in Figure 5.5 (a), when the averaging window is very small, for example for Δt = 0 to 3 min, some fluctuations can be seen in ΔP_P,

which shows that turbulent fluctuations are not averaged over and they still affect the mean value of Pitot tube pressure. When the averaging window is very large, for example Δt = 38 to 40 min, large variations in ΔP_P can be seen. These variations are due to the transient effects of the change in the RPM on the pipe temperature that in turn affect ΔP_P. The graph is almost flat between Δt = 4 min and Δt = 30 min, and the variations in ΔP_P are very small. The same trend can be seen in Figures 5.5 (b), (c) and (d). It can be seen in Figure 5.5 that the mean values are almost constant at around Δt = 10 min. Therefore, as mentioned at the start of this chapter, the averaging window of all variables for type C experiments was 10 minutes before the *Re* was changed.

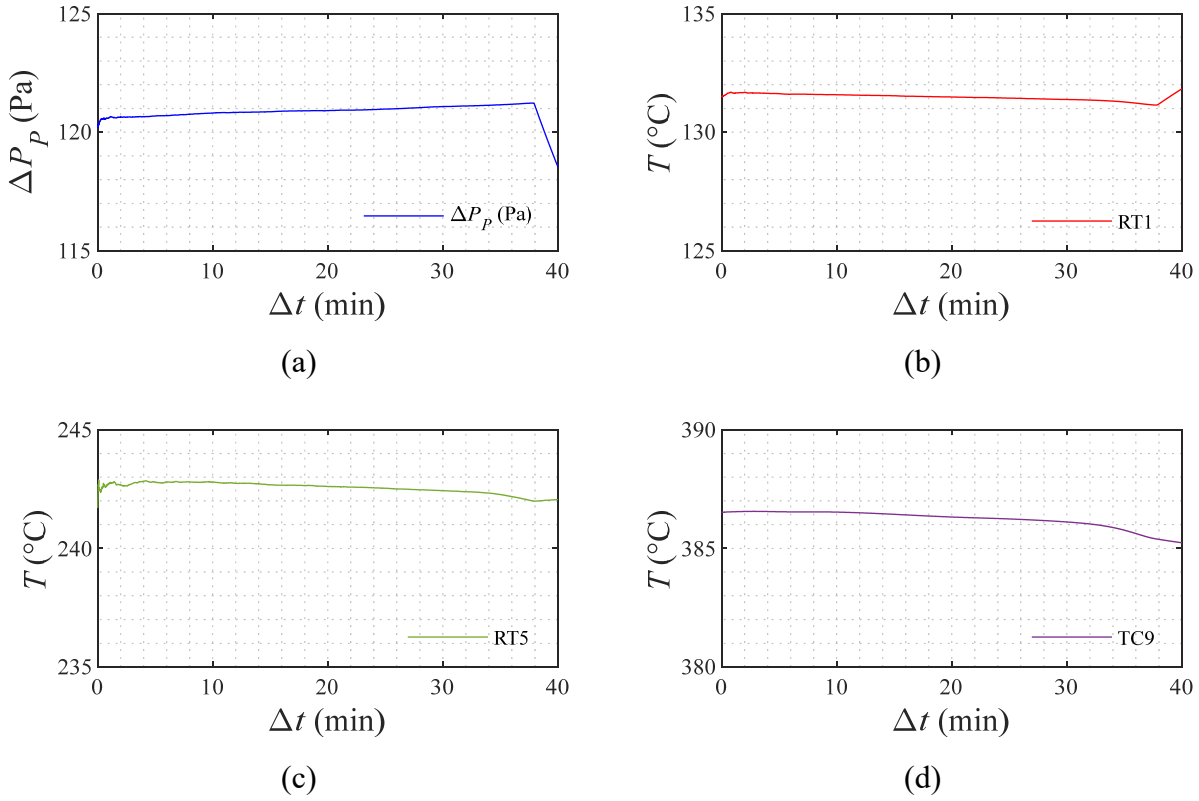

Figure 5.5. The mean of ΔP_P (a), RT1 (b), RT6 (c) and TC9 (d) calculated over different averaging windows.

To evaluate the *Nu* using equation 4.24, the pipe wall temperature should ideally be constant over the length of the pipe. However, it was seen from figure 5.4 that the temperature measured by some of the thermocouples was different from 375°C. To investigate deviations from 375°C, the mean temperature of the thermocouples over the length of the pipe is shown in Figure 5.6.

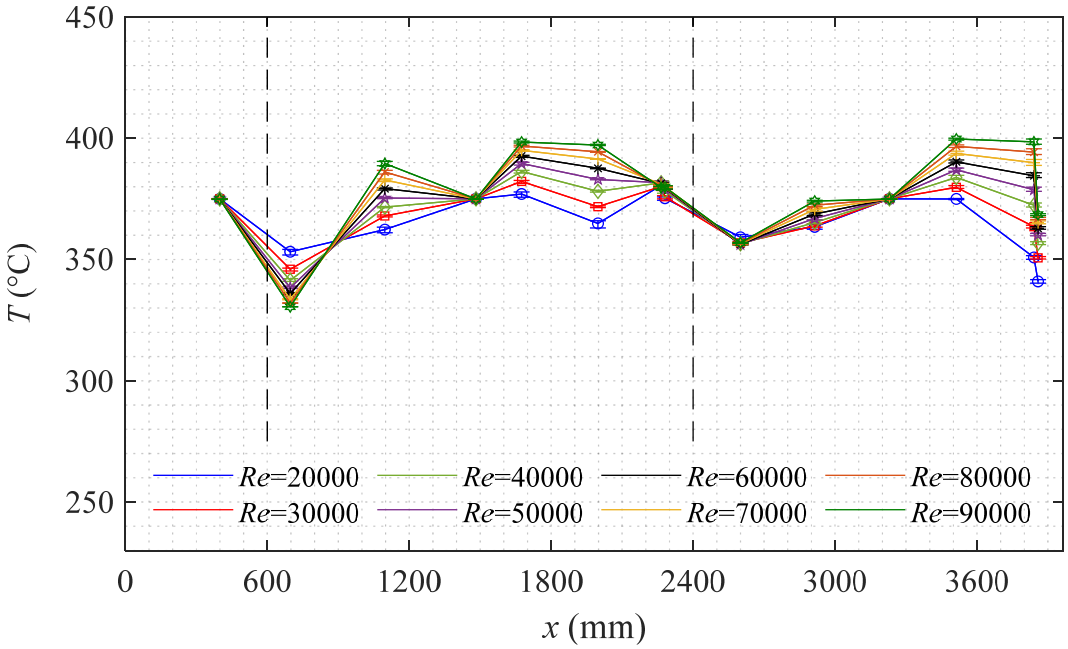

Figure 5.6. Wall temperature distribution over the length of the pipe.

The vertical axis in Figure 5.6 shows the time averaged temperature measurements of wall-mounted thermocouples, and the horizontal axis shows the distance of the thermocouples from the test section inlet (x = 0 is the test section inlet as can be seen in Figure 3.1). Each thermocouple temperature in this figure is evaluated by averaging the data from three repetitions of the experiments. The error bars show the minimum and maximum thermocouple readings of the three repetitions. The vertical dashed line at x = 600 mm shows the location where zone one of the heaters ends and zone two begins. Similarly, the vertical dashed line at x = 2400 mm shows where zone two ends and zone three begins. The results show that the pipe temperature is approximately 366.3 ± 11.4 ℃ for the lowest *Re* of 20,000 over the entire length of the pipe (the ± 11.4 ℃ error is calculated using equation 4.33 in which the perceived data is the average, and the observed data is each data point). The temperature variation along the pipe increases with *Re* and the pipe temperature is 378.4 ±18.2℃ at *Re* = 90,000. The variations were caused due to the limited number of the controllers and the limited number of the zones. The accuracy can be improved by adding more controllers This variation in temperature is believed to have some effect on the estimated *Nu*. Therefore, in Section 5.5 the error percentage in estimating *Nu* is calculated. The overall error of *Nu* is 7.7% across all *Re* which is in a reasonable range considering the variations in pipe

temperature. The average wall temperature and the standard deviation at all *Re* is shown in Table 5.1. The average temperature in this table is the average of measurements from TC04, TC06, TC07, TC08, TC09, TC10, TC11, TC12, TC13, TC14, TC15, TC16, TC17, and TC18.

Table 5.1 The average pipe temperature at different *Re*.

Re	Average temperature (°C)	Standard deviation
20,000	366.3	11.9
30,000	368.8	11.3
40,000	371.2	12.4
50,000	372.9	13.6
60,000	374.6	15.0
70,000	376.1	16.5
80,000	377.2	17.6
90,000	378.4	18.9

5.3 Air temperature

The air temperature within the pipe was measured in type-C experiments using the thermocouples housed in rakes one and two. The time series of the temperature measurements of the rakes are shown in Figure 5.7. This figure shows the results of the first run of the type C experiment. The temperature measurements from the wall-mounted TCs that are close to the rake one and rake two, i.e. TC12 and TC18 respectively, are also included in this figure. The results show an overall decrease of air temperature over time in both rakes. This reduction in air temperature is due to the incremental increase of *Re*. In addition, after each increase in flow rate, a sharp drop in the air temperature is seen. This sharp drop is followed by a slight increase in temperature until a steady-state condition is achieved. This trend is consistent for all *Re*, and therefore the air temperature

measurements were conducted in the steady state for all flow rates. The temperature of TC12 is mostly constant over the course of the experiment with minor drops after each RPM change. The temperature of TC18 increases over time with the increase of *Re*. This is due to the local variations of pipe wall temperature seen in Figure 5.6.

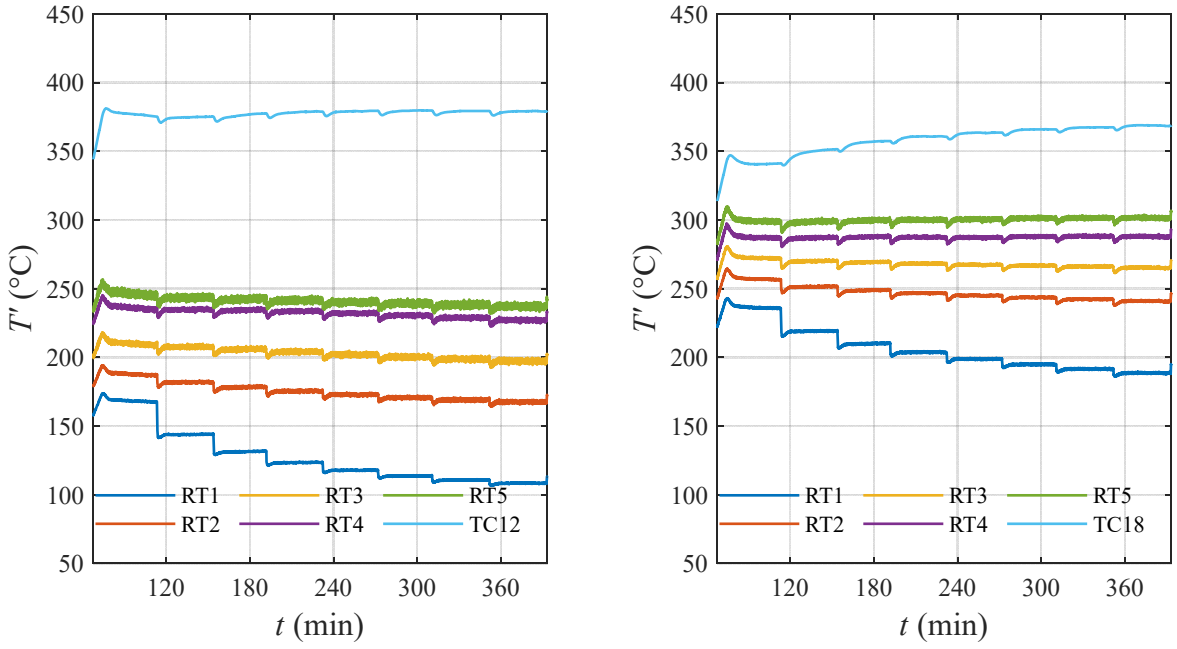

Figure 5.7. Time series of air temperature measurements for rake (a) one and (b) two.

The variations of air temperature for different Reynolds numbers are also studied. Figure 5.8 shows the changes of mean temperatures with Re_t for (a) rake one and (b) rake two. The error bars show the uncertainty of measurements. The results show that the mean rake temperatures decrease with *Re* for almost all RTs. However, this decrease is not equal for different RTs. For example, in Figure 5.8 (a), the mean temperature of RT1 drops from 167.6℃ at Re_t = 13600 to 108.7 ℃ at Re_t = 63800 (i.e., a drop of 58.9℃ for RT1), while the mean temperature of RT5 drops from 243.3℃ at Re_t = 13600 to 236.2 ℃ at Re_t = 63800 (i.e., a drop of 7.1℃ for RT5). This led to an increase in the difference between RT temperatures at higher Re_t. The same trend can also be seen in Figure 5.8 (b) for rake two RTs.

An anomaly can also be seen in Figure 5.8 (b). In this figure, the temperature of RT5 and RT4 slightly increases with Re_t. This anomaly can be explained by the similar behaviour of TC18 with *Re*. It can be seen in figure 5.7 (b) that the temperature of TC18 increases over time. Because RT5 and RT4 are in the close proximity of pipe surface, the increase in the temperature of TC18 affects the temperature of RT5 and RT4. However, Figure 5.8 (b) shows that the increase in TC18 has not changed the trend of RT1, RT2, and RT3. This is because these thermocouples are farther away from the pipe surface and are less affected by local variations of pipe temperature. It should also be noted that equation 4.12 suggests that the effects of RT4 and RT5 on the bulk temperature calculations are much smaller than the effect of RT1, RT2 and RT3.

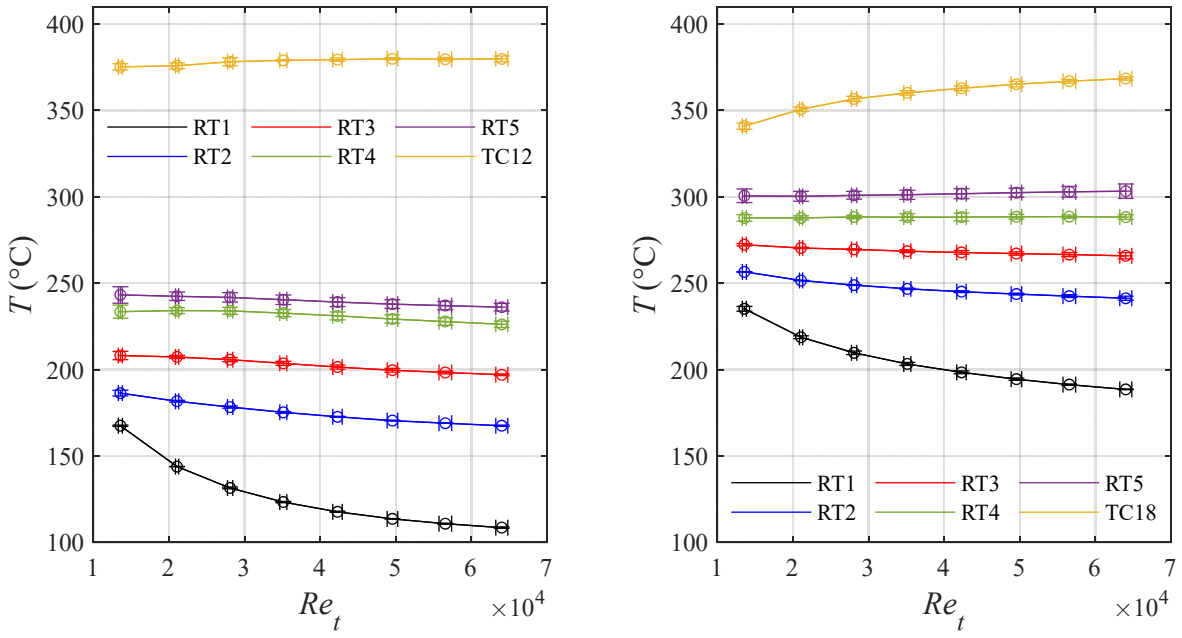

Figure 5.8. The changes of mean temperature with Re_t for (a) rake one and (b) rake two.

Furthermore, the variations of temperature profile at different flow rates are investigated here. The temperature profile of air inside the pipe for the type C experiment at different *Re* can be seen in Figure 5.9. The horizontal axis is the mean temperature, and the vertical axis is the wall distance, *y*, normalized by pipe radius, *R*. The data points are averaged using the repetitions of each experiment and the error bars show the minimum and maximum of the repetitions. Increase in *Re* decreases the air temperature in the core region of the pipe and this drop in temperature is more

significant closer to the pipe centerline. It can also be seen that at a constant *Re*, the temperature gradient is smaller farther away from the pipe wall.

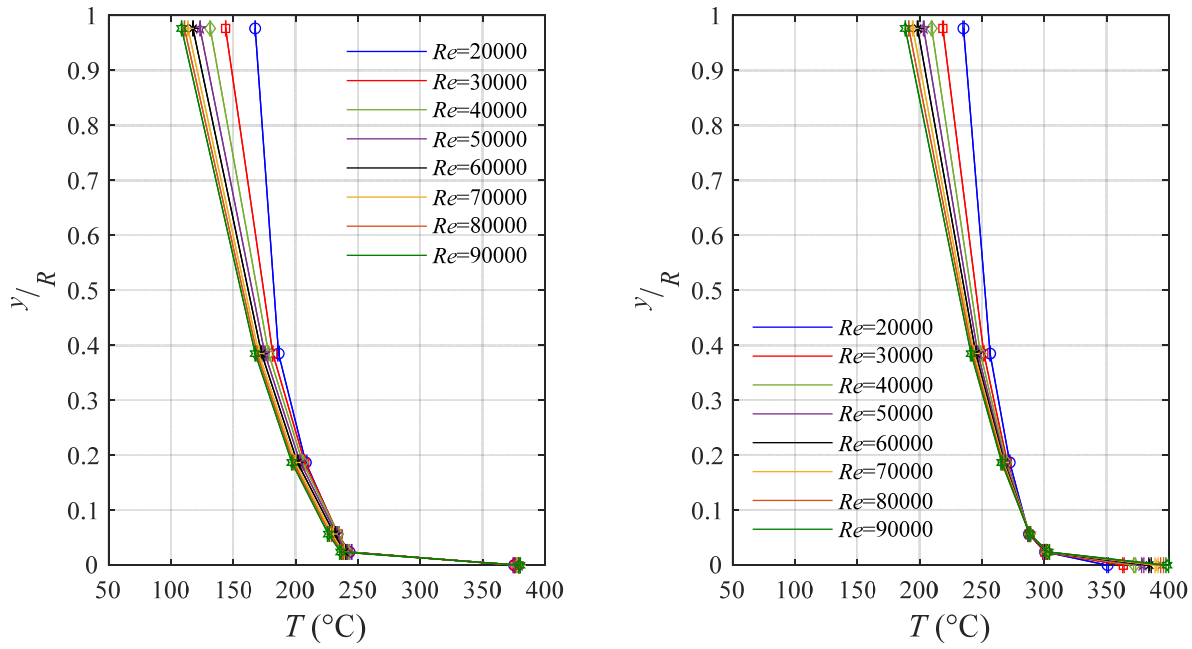

Figure 5.9. The mean temperature of rake thermocouples in Type C experiment for (a) rake one and (b) rake two.

To calculate *Nu* from bulk temperatures, both rakes needed to be in a thermally fully developed region of the pipe (for detailed information see Chapter 2, section 2.3.2). The normalized temperature of rake thermocouples T_n is calculated from equation 4.27. Surface temperature, T_s, is used in this equation, and it is equal to the arithmetic average of the temperature of TC12, TC13, TC14, TC15, TC16, and TC17. Figure 5.10 shows the normalized air temperature measurements for rakes one and two at *Re* of 20,000 to 90,000. In order for the flow to be thermally fully developed the T_n graphs of both rakes should ideally overlap. We can see from Figure 5.10 that closer to the surface (at $y/R = 0$) the T_n of the two rakes is very close. At all *Re* values, rake 1 and rake 2 lines in Figure 5.10 (a-h) overlap at $y/R = 0.4$ which corresponds to the location of RT2 for both rakes. There is larger T_n difference between the two rakes at the pipe centerline (location of RT1 thermocouple). The T_n difference between the two rakes might suggest that the flow was not

thermally fully developed. This might lead to errors in *Nu* evaluation. The error of *Nu* from air temperature measurements is discussed in section 5.4.

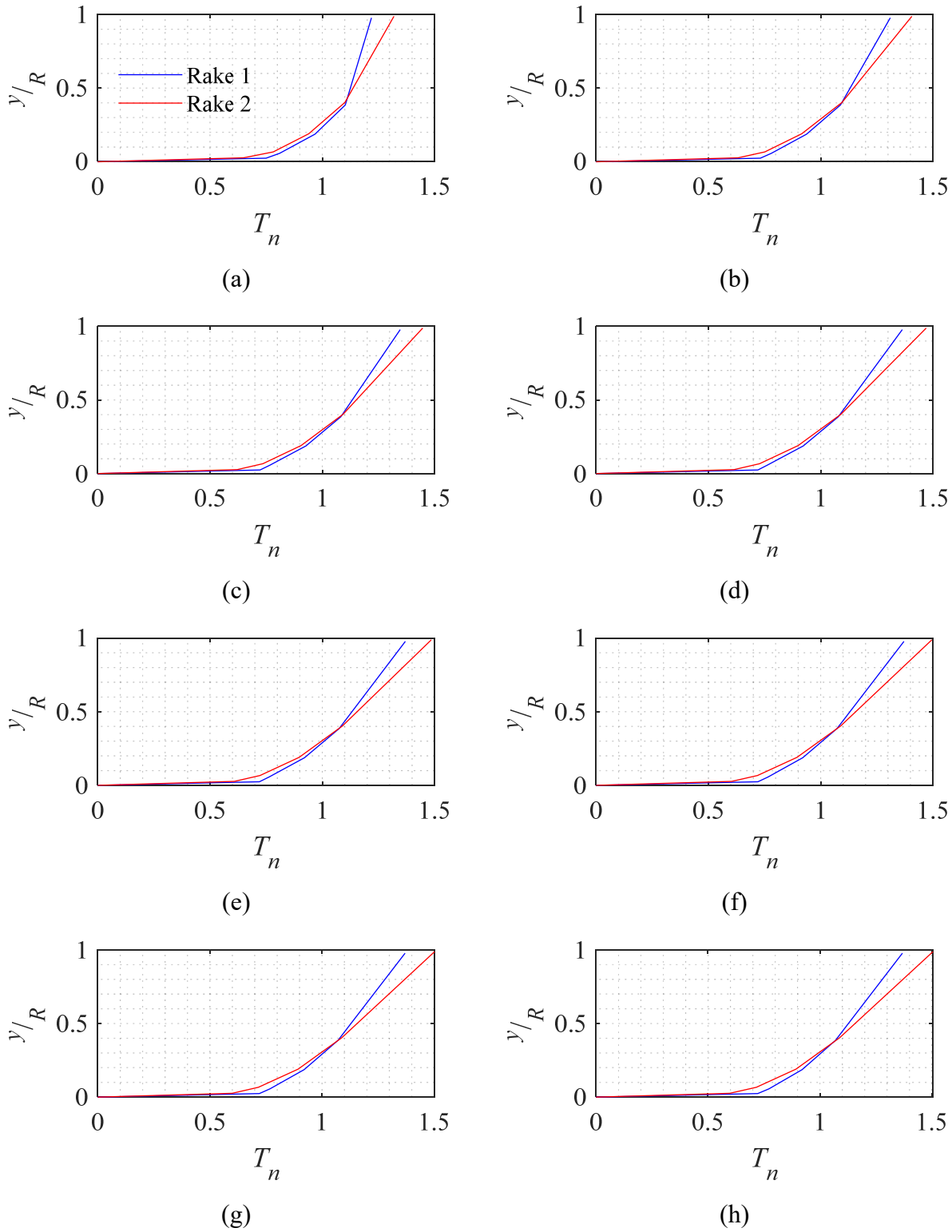

Figure 5.10. Normalized temperature at (a) *Re* = 20,000, (b) *Re* = 30,000, (c) *Re* = 40,000, (d) *Re* = 50,000, (e) *Re* = 60,000, (f) *Re* = 70,000, (g) *Re* = 80,000 and (h) *Re* = 90,000.

5.4 Friction factor and Nusselt number

The friction factor was evaluated from the pressure drop measurements between the pressure ports in the test section pipe (see section 3.2.2) using equation 4.26. f_H corresponds to the friction factor evaluated using properties at the heated T_t temperature in experiment type B. The pressure drop of the smooth pipe was measured both at room temperature and with heated pipes. The changes in ΔP over time for these experiments can be seen in Figure 5.11. The incremental jumps in pressure drop in the pipe are due to the sudden increases in flow rate. The changes of friction factor of the pipe with *Re* in type A and type B experiments are shown in figure 5.12. The fluid properties used in equation 4.26 were evaluated at the mean temperature of TC1 for type A experiment, and at the mean flow temperature in the test section, T_t, for type B experiment. T_t is calculated from equation 4.13. The pipe friction was significantly larger in experiments with heated pipes compared to experiment conducted at room temperature. This was because the increase in pipe wall temperature led to an increase in the viscosity of air which in turn increased the skin friction of the flow. In this figure, the friction from the experiments is compared to analytical model from equation 2.61. The root-mean-square percentage error of the friction factor of type A experiment, evaluated from comparing the measurements to analytical values, was 4.2%. Although the average friction data points in Figure 5.12 were bellow the analytical values, they are still within the range of error seen by the error bars.

The Nusselt number was calculated from the rake measurements of type C experiment using equations 4.24. This Nusselt number was compared to analytical Nusselt values derived from equation 2.56. The friction factor calculated from type B experiment was used in this correlation to derive the analytical *Nu*. Figure 5.13 shows the variations of *Nu* with Re_t for the smooth pipe in type C experiment. The root-mean-square percentage error (equation 2.25) of the Nusselt number for experiment type C was 7.7%. This error is calculated using equation 4.34. Table 5.2 presents different flow parameters evaluated in the Type B and C experiments.

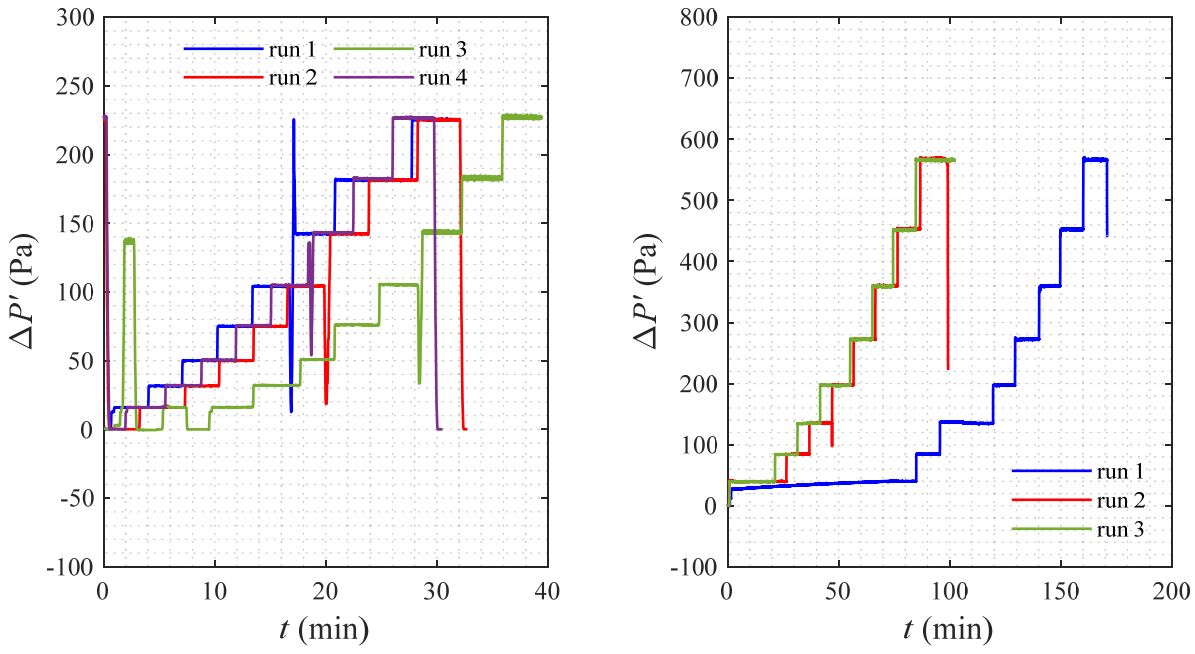

Figure 5.11. Time series of pressure drop measurements for (a) type A experiment and (b) type B experiment.

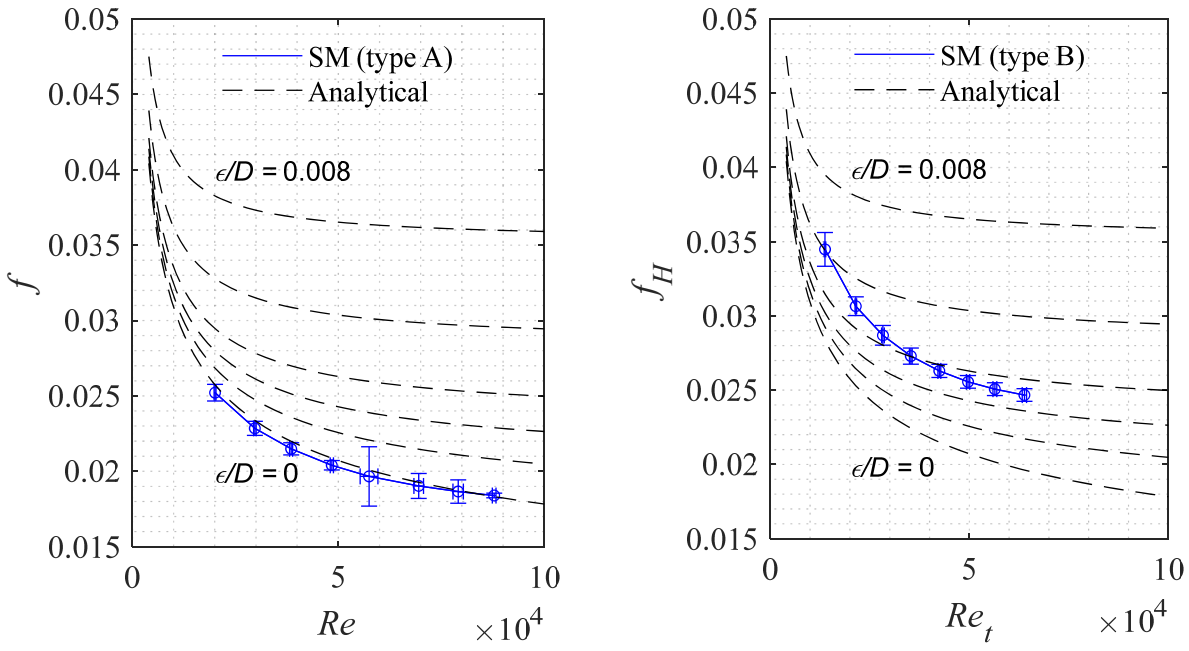

Figure 5.12. Changes of friction factor with Reynolds numbers from (a) type A and (b) type B experiments. The analytical lines are plotted for ε/D of 0, 0.0006, 0.0012, 0.002, 0.004 and 0.008.

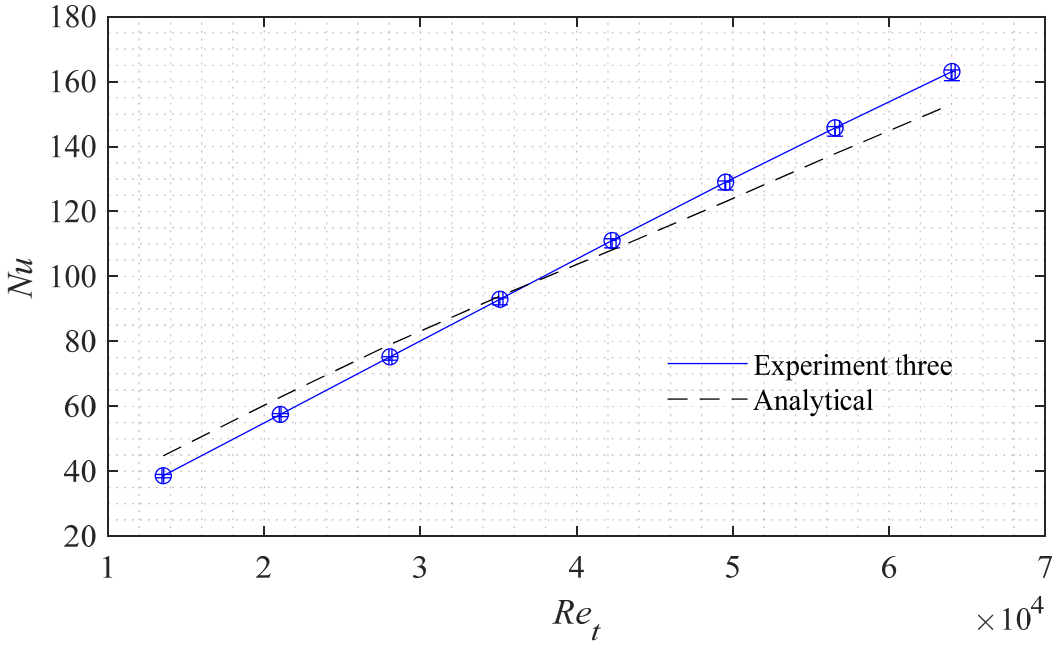

Figure 5.13. Changes of *Nu* with Re_t in type C experiment.

Table 5.2 Flow parameters in the Type B and C experiments.

Re	Nu	$\dot{m}$ [kg/s]	C_P [J/kg.K]	k [W/m.K]	μ_t [N.s/m^2]	f_H	T_{b1} [°C]	T_{b2} [°C]	T_s [°C]
20,000	38.5	0.0148	1037.6	0.0402	2.69E-05	0.0375	202.9	266.4	364.1
30,000	57.3	0.0228	1036.6	0.0398	2.67E-05	0.0342	196.8	261.6	367.0
40,000	75.0	0.0303	1036.1	0.0396	2.66E-05	0.0323	192.9	259.1	369.6
50,000	92.7	0.0377	1035.6	0.0394	2.65E-05	0.0310	189.5	257.1	371.6
60,000	110.7	0.0453	1035.2	0.0393	2.65E-05	0.0300	186.8	255.7	373.6
70,000	128.6	0.0530	1034.9	0.0392	2.64E-05	0.0293	184.5	254.5	375.5
80,000	145.3	0.0604	1034.7	0.0391	2.64E-05	0.0288	182.9	253.4	377.2
90,000	162.5	0.0682	1034.5	0.0390	2.63E-05	0.0285	181.3	252.4	378.8

5.5 Conclusion

In this chapter, the results of the experiments conducted on the smooth pipe was presented. In the experiments, *Re* increased from 20,000 to 90,000 in increments of 10,000. The measured variables were then averaged over a time window, Δt, to evaluate the mean values. It was shown that during Δt the mean values of the variables reached statistical convergence and they were at a steady-state. The variations in the temperature of the pipe over its length was discussed. The temperature of the pipe was 366 ± 11.4 °C at *Re* of 20,000 and 378.4 ± 18.2 °C at *Re* of 90,000. It was also shown that two of the rake thermocouples that were closest to the pipe wall were strongly affected by the local variations of the pipe wall temperature. The rake measurements showed that the temperature gradient of the flow over the radius of the pipe increases with *Re*. Finally, two variables, *Nu* and *f* were compared with their respective analytical values from correlations in the literature to validate the experiments. The friction factor at room temperature was compared to Colebrook correlation at the different *Re*, and it was shown that the root mean square percentage error of the measurements was approximately 4%. The Nusselt number of the smooth pipe was also evaluated at different *Re* and the results were compared to the Gnielinski correlation. The root mean squared percentage error of the *Nu* measurements was 7.7%. The motivation for doing these experiments

was to validate the measurements and use it as a reference to compare profiled pipes in the next chapter.

Chapter 6.

Pipes with Internal Roughness

The results of the experiments using four pipes with internal roughness are presented in this chapter. The thermal performance and pressure drop of these pipes were compared with each other and with the smooth pipe. The chapter first shows the evaluation of the pipe temperature in the axial direction. It then investigates the temperature measurements from the rakes and the change in air temperature between the two rakes. After that, the friction factor and Nusselt number of the pipes are compared. Finally, the friction factor and heat transfer of the pipes are compared using the evaluation plot. For more detailed information regarding the evaluation plot see Chapter 2. To keep this chapter concise, some of the plots presented in the previous chapter, like the time series of the measured variables, are not included, and instead they are presented in **Appendix B**.

For the pipes with internal roughness, the number of experiments, the procedure followed in each experiment, and the number of repetitions of each experiment, were explained in the chapters 4 and 5. As it was seen in Table 4.2, three different experiments were conducted on each pipe, and each experiment was repeated at least three times. One of these three experiments was conducted at room temperature and two were conducted at elevated pipe wall temperatures. For all experiments, during each run, the flow rate was incrementally increased. The RPM remained constant for a duration that was long enough to ensure that the flow reached steady state. It was at least three minutes for type A experiments, ten minutes for type B experiments, and 40 minutes for type C experiments. The incremental increase in *Re* continued until all *Re* from 20,000 to 90,000 were covered. The time series of the Pitot tube pressure and inlet temperature for these experiments can be found in **Appendix B**. Similar to the smooth pipe experiments, the mean values of the measured variables were evaluated by averaging the instantaneous values over Δt which was

one minute for type A experiments, two minutes for type B experiments, and ten minutes for type C experiments.

6.1 Pipe wall temperature

The variations of the temperature of pipes with different internal roughness are investigated in Figure 6.1. The vertical axis shows the mean temperature of the TCs, and the horizontal axis shows the distances of the TCs from the test section inlet (x = 0 is the test section inlet as can be seen in Figure 3.1). Each data point in these figures is evaluated by the averaging the mean temperature of three repetitions of the experiments. The error bars show the minimum and maximum of the repetitions. The vertical dashed line at x = 600 mm shows the location where zone one ends and zone two begins. Similarly, the vertical dashed line at x = 2400 mm shows where zone two ends and zone three begins.

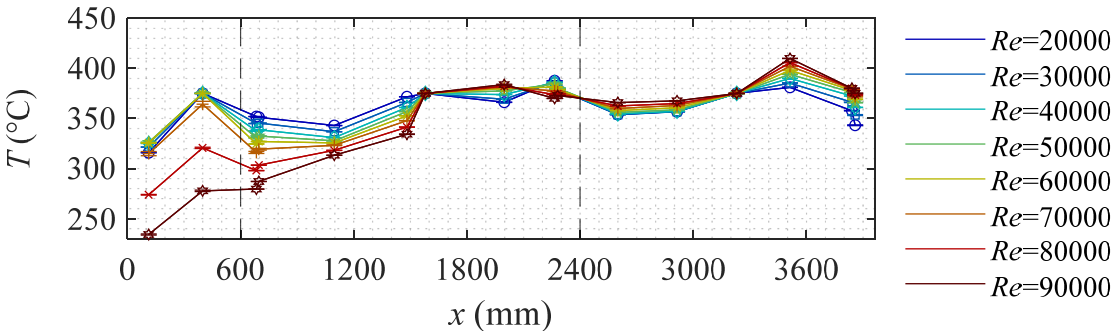
450
400
350
300
250
T (°C)
0
600
1200
1800
2400
3000
3600
x (mm)
Re=20000
Re=30000
Re=40000
Re=50000
Re=60000
Re=70000
Re=80000
Re=90000

(a)

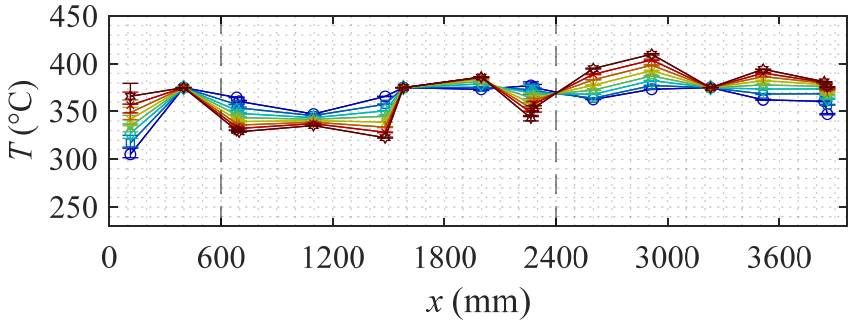
450
400
350
300
250
T (°C)
0
600
1200
1800
2400
3000
3600
x (mm)

(b)

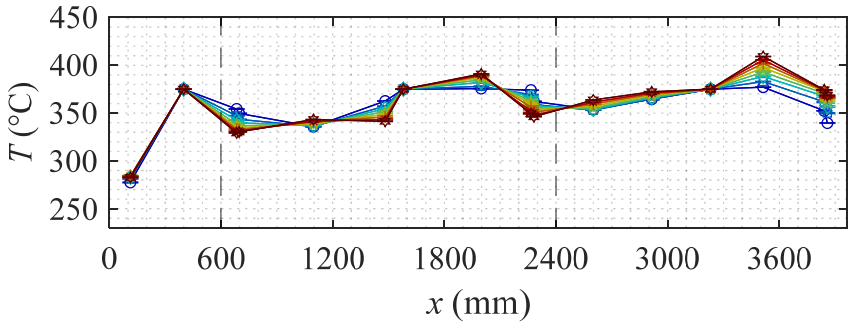
450
400
350
300
250
T (°C)
0
600
1200
1800
2400
3000
3600
x (mm)

(c)

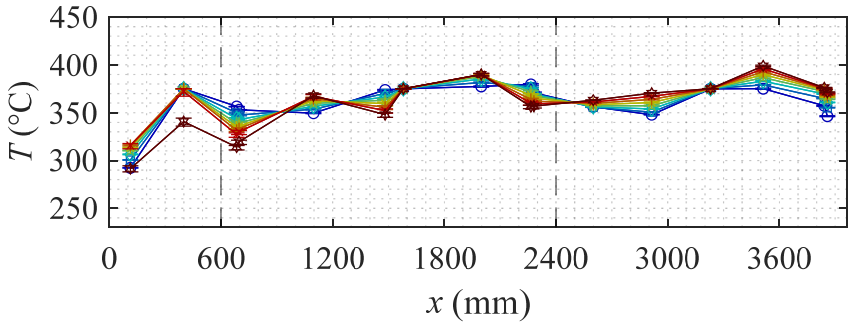
450
400
350
300
250
T (°C)
0
600
1200
1800
2400
3000
3600
x (mm)

(d)

Figure 6.1. The pipe temperature for (a) MC1, (b) MC2, (c) MB50, and (d) MB37.

As can be seen in Figure 6.1 (a) to (d), the mean temperature varies over the length of the pipe. These variations increase with the increase of *Re*. The same trend was also observed for the smooth pipe (see Chapter 5, Figure 5.6). Figure 6.1 (a) shows the results for MC1 pipe, which had the highest wall roughness (*Sq* of 264 μm) compared to the other pipes. For example, the overall temperature of the pipe was 361.7 ± 19.1 ℃ at *Re* of 20,000, and 345.8 ± 45.7℃ at *Re* of 90,000. The temperature of the thermocouple that was connected to the controller in zone one (TC4) reached 375℃ at all *Re* except two highest *Re* (i.e., 80,000 and 90,000). At these *Re* values, zone one heaters were drawing all the available power (the power consumption of zone one reached its limit). This might be due to the higher surface roughness of MC1 compared to the other pipes.

Figure 6.1 (b) shows the changes of mean temperature over the length of MC2 pipe. This pipe had a roughness, *Sq*, of 23 μm. The overall temperature of the pipe was 362.5 ± 17.4 ℃ at *Re* of 20,000, and 365.4 ± 25.9℃ at *Re* of 90,000. The temperature of all zones in MC1 pipe reached 375 ℃ at all *Re*. This suggests that heaters could keep up with the heat transfer from the pipe to the air flow at all *Re*.

Figure 6.1 (c) shows the temperature variations of MB50 pipe with an *Sq* of 89 μm. The pipe temperature was 356.7 ± 24.2 ℃ at *Re* of 20,000 and 358.1 ± 28.7℃ at *Re* of 90,000. The lines for different *Re* are closer together compared to MC1 and MC2 pipes. This indicates that the changes of *Re* had less effects on the temperature variations of MB50 pipe.

Finally, Figure 6.1 (d) shows the temperature variations of MB37 pipe with an *Sq* of 31 μm. The pipe temperature was 360.0 ± 20.9 ℃ at *Re* of 20,000 and 357.2 ± 27.7℃ at *Re* of 90,000. Similar to MB50, there were smaller variations in temperature at different *Re*. This indicates that the increase in turbulence mixing that comes from the ball bearing led to smaller variations in temperature at different *Re*.

Overall, we can see that the pipes with mesh, especially MC1, have higher temperature variations compared to pipes with ball bearing. It will be shown in section 6.3 that the pipes with mesh also have a smaller heat-transfer compared to pipes with ball-bearings. Despite the lower heat-transfer

rate for pipes with mesh, they experience a higher axial wall temperature variation, which is potentially due to smaller turbulent mixing. At the highest *Re*, we can see that MC1 has the highest temperature variation of ± 45.7℃, while MB50 and MB37 had much lower variations of ±28.7℃ and ± 27.7 ℃, respectively.

In addition, we can also observe that the increase in variations of pipe-wall temperature with *Re* is more pronounced in pipes with mesh compared to the pipes with ball bearings. This could potentially be because the pipes with ball bearing have larger wall-normal velocities, and the heat transfer is mostly governed by the large scale eddies. The increase in *Re* does lead to significant changes to in large scales eddites, and therefore the increase in *Re* does not lead to large variations in wall temperature variations in pipes with ball bearings. In contrast, the heat transfer in pipes with mesh is mostly governed by small scale eddies. The increase in *Re* leads to larger changes in the small scales, and as a result, larger variations are seen with increasing *Re* for pipes with mesh.

The overall pipe temperature reported so far are evaluated from the average measurements of all TCs shown in Figure 3.12 (b). The pipe surface temperature, $T_{s,}$ (that is used to evaluate *Nu*) is the average of TC13, TC14, TC15 , TC16 and TC17 as can be seen in equation 4.25. The mean values and standard deviation are calculated from the three repetitions of type C experiment.

Table 6.1 The values of T_s for different pipes at different *Re*

Re	MC1		MC2		MB50		MB37	
	T_s	Sd	T_s	Sd	T_s	Sd	T_s	Sd
20,000	364.5	0.24	366.2	0.10	364.0	0.21	361.8	0.26
30,000	366.7	0.13	369.8	0.18	366.8	0.40	364.3	0.19
40,000	368.9	0.05	373.5	0.15	369.1	0.46	366.6	0.34
50,000	370.8	0.15	376.5	0.23	371.0	0.39	368.5	0.34
60,000	372.6	0.22	379.7	0.20	372.7	0.44	370.1	0.37
70,000	374.3	0.21	382.9	0.31	374.2	0.38	371.6	0.44
80,000	375.8	0.12	385.9	0.32	375.5	0.26	373.2	0.37
90,000	377.7	0.06	389.0	0.31	376.8	0.21	374.7	0.39

6.2 Air temperature

The air temperature of the pipes with internal roughness was measured using the two rakes. The time series of upstream and downstream rake measurements can be found in **Appendix B**. Figure 6.2 shows the variation of mean air temperature with Re_t. Firstly, it can be seen that for all pipes the air temperature measured by rake two shown in Figure 6.2 (b), (d), (f) and (h) was higher than the air temperature measured by rake one shown in Figure 6.2 (a), (c), (e) and (g), respectively. As expected, this indicates that the temperature of the air increased from rake one to rake two. Secondly, in all figures, the air temperature decreased with the increase of Re_t. Finally, the thermocouples closer to the centerline of the pipes are colder than the thermocouples that are farther away from the centerline in all graphs in Figure 6.2. For example, RT1 is colder than RT2, and RT2 is colder than RT3 in all rakes.

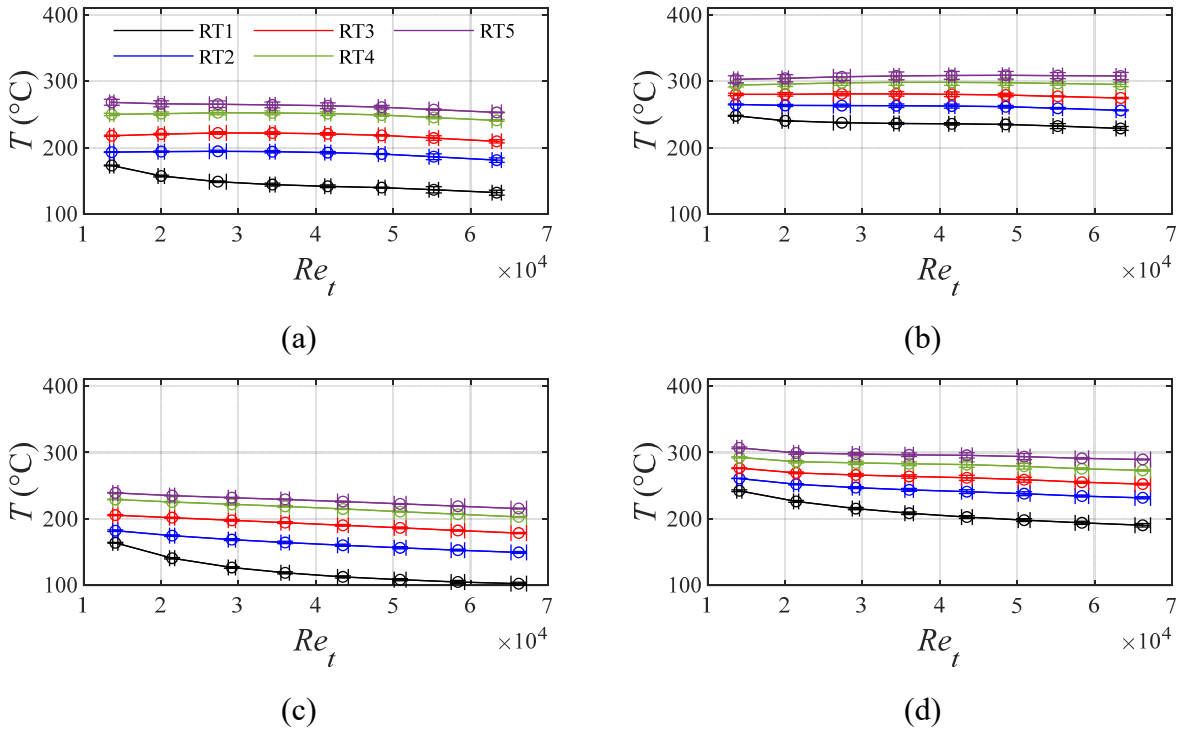

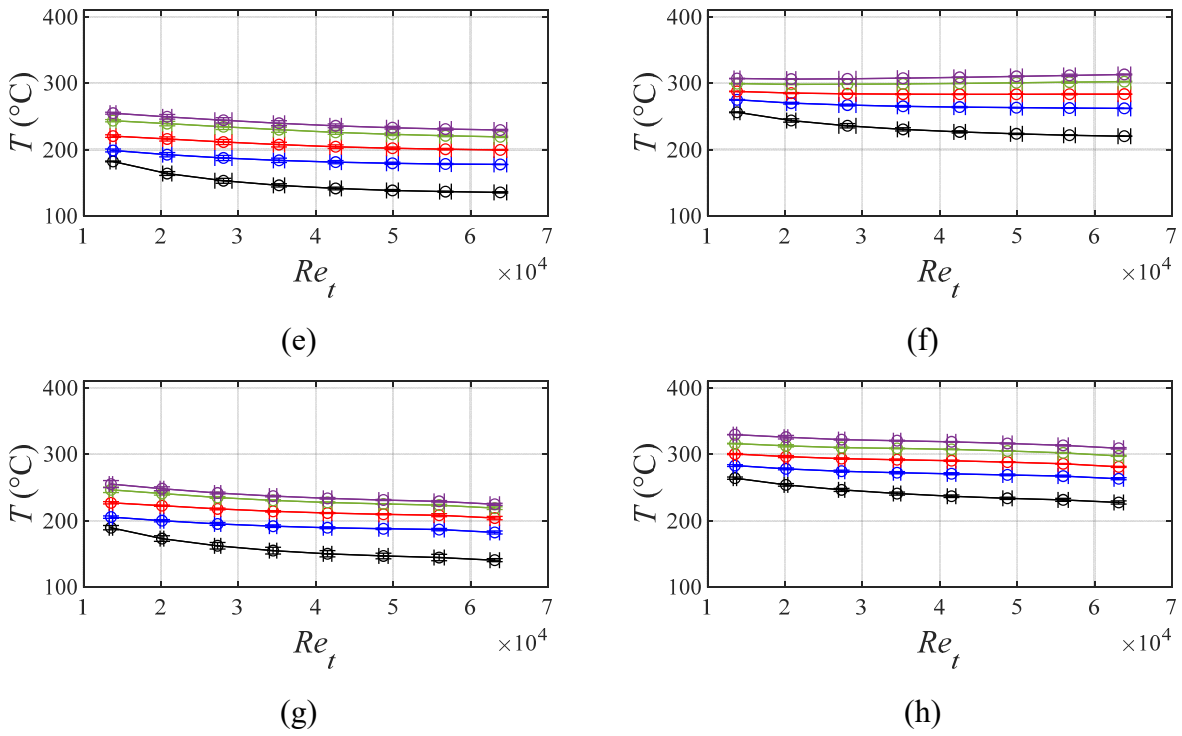

Figure 6.2. The changes of mean temperature with Re_t for (a) rake one of MC1 (b), rake two of MC1, (c) rake one of MC2 (d), rake two of MC2, (e) rake one of MB50 (f), rake two of MB50, (g) rake one of MB37 (h), rake two of MB37.

The bulk temperature of the flow, T_b, is evaluated from the rake measurements using equation 4.12. To compare the heat transfer capabilities of the pipes, the increase in bulk temperature from rake one to rake two are normalized by the difference between the pipe temperature and the average bulk temperature following:

$$T_{inc} = \frac{T_{b2} - T_{b1}}{T_s - T_t} \tag{6.1}$$

The changes of T_{inc}, with Re_t are shown in Figure 6.3 (a). MB37 has the highest T_{inc} followed by MB50, MC1, MC2 and SM, respectively. Figure 6.3 (b) shows the changes of convective heat transfer coefficient, h, defined in equation 4.28, with Re_t. As can be seen, both MB37 and MB50 have significantly higher heat transfer coefficients than both pipes covered with mesh. Between the pipes covered with mesh, MC1 has a significantly higher heat transfer coefficient than MC2, while MC2 has almost the same h as the smooth pipe. The reason why MC2 has a similar heat

transfer to the smooth pipe is because the second layer of coating filled the pores between the mesh wires, and this made the MC2 smoother than MC1. This can be seen by comparing the roughness values presented in Table 4.1 (the *Sq* of SM and MC2 are 7 and 23 μm, respectively). Further evidence of this similarity in heat transfer is shown in the friction factors results provided Figure 6.4. It can also be seen that the heat transfer coefficient increases with Re_t due to the higher turbulence of the flow at higher Re_t. This increase with *Re* is linear for most of the pipes except for MC2 and MB37 pipes at Re_t of 56,000 and 63,000. The nonlinearity of these two pipes could be due to local variations of pipe wall temperature at higher *Re* [see Figure 6.1 (b) and (d)]. Table 6.1 presents the bulk temperatures of rake one and rake two (T_{b1} and T_{b2} respectively) for different pipes in type C experiment.

Table 6.2 The values of T_{b1} and T_{b2} for different pipes at different *Re*.

Re	MC1		MC2		MB50		MB37	
	T_{b1}	T_{b2}	T_{b1}	T_{b2}	T_{b1}	T_{b2}	T_{b1}	T_{b2}
20,000	213.1	275.0	200.0	271.9	215.2	282.5	221.2	294.0
30,000	211.2	273.8	191.4	263.2	207.7	278.2	214.0	289.2
40,000	210.4	274.0	185.1	258.7	201.9	275.9	207.9	285.5
50,000	209.3	274.1	180.7	255.6	197.5	274.4	203.6	283.2
60,000	207.7	273.8	176.3	253.1	194.1	273.6	200.6	281.3
70,000	205.6	273.1	172.5	250.1	191.7	273.2	198.4	279.2
80,000	201.8	271.2	168.8	246.6	190.1	272.9	196.8	276.9
90,000	197.1	268.7	165.3	243.9	189.0	272.8	192.5	272.9

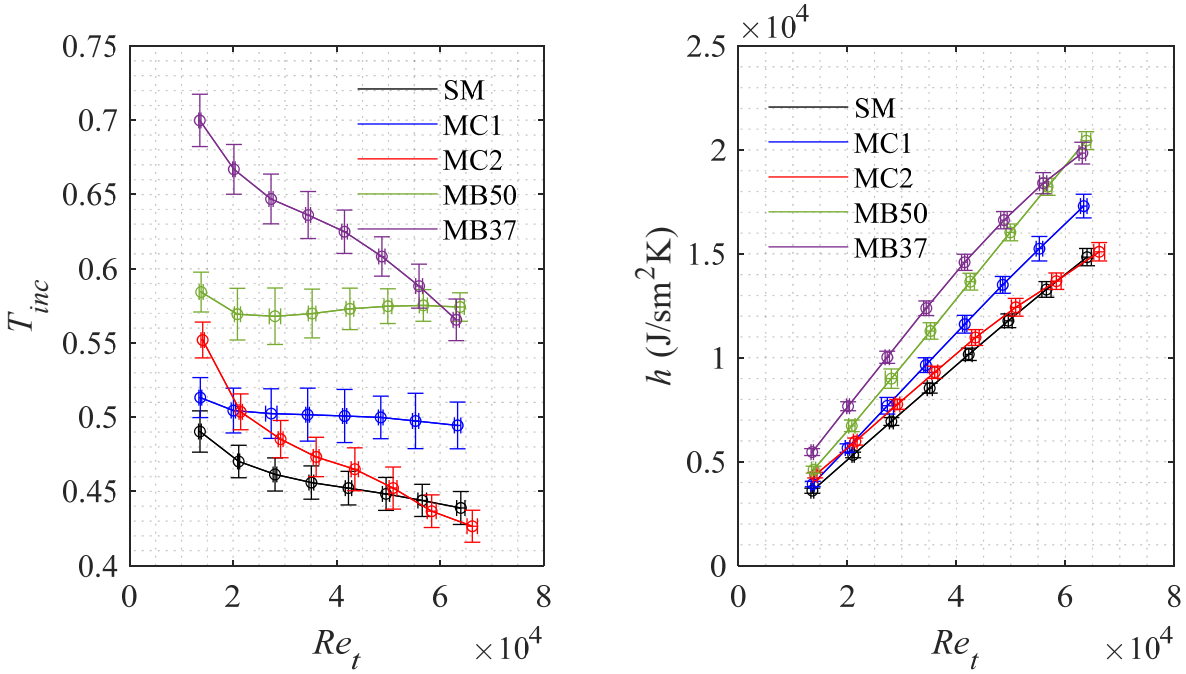

Figure 6.3. The increase in normalized bulk velocity (a) and the heat transfer coefficient (b) for the smooth and the pipes with internal roughness.

6.3 Friction factor and Nusselt number

The friction factor of the pipes with internal roughness is evaluated from the pressure drop measurements between the pressure taps following equation 4.26. The time series of pressure drop measurements for these experiments can be found in **Appendix B**. Figure 6.4 shows the changes of friction factor with Reynolds numbers in (a) type A experiments and (b) type B experiments. The results show that the friction factor of all pipes is significantly larger in experiments conducted at higher fluid temperature compared to experiments conducted at room temperature. This is because temperature increases the viscosity of air. The increase in viscosity leads to an increase in skin friction and consequently an increase in friction factor. The viscosity of gases depends mostly on the exchange of intermolecular momentum, and thus, the viscosity of gases increases with temperature. The rise in temperature leads to an increase in random molecular activity (i.e. , increase in momentum transfer), and as a result, an increase in viscosity. The fluid properties used to calculate the friction factor are evaluated at the mean temperature of TC1 in type A experiments.

The friction factor of the heated pipes is evaluated in Type B experiments using T_t temperature. As can be seen in equation 4.13, T_t is the average of T_{b1} and T_{b2} given in Table 6.2.

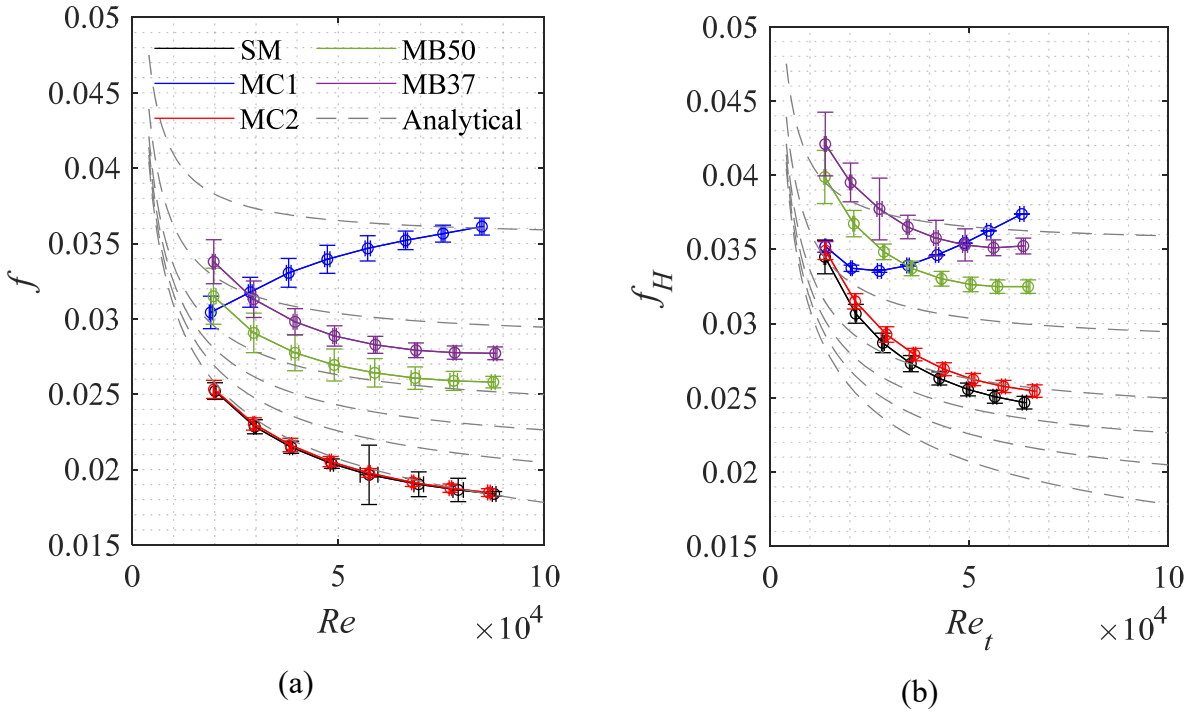

Figure 6.4. The changes of (a) f with Re and (b) f_H with Re_t for smooth and pipes with internal roughness.

The changes of f with Re in experiments conducted at room temperature are shown in Figure 6.4 (a). MC1 has the highest overall friction factor. The friction factor of all pipes decreases with Re except for MC1 pipe. This trend was consistent in all repetitions of the experiments conducted on MC1. The reason of this trend could be the effect of the roughness element itself on the flow structure. The shape of the roughness element itself might also have affected the pressure measurements. The mesh creates hills and valleys on the pipe internal surface. Thus, the location of pressure ports (whether they are located on the hills of in the valleys) might have affected pressure measurements. The friction factor of MC1 is 21% higher than the smooth pipe at Re of 20,000 and 96% at Re of 90,000. On average, the friction factor of MC1 is 66% higher than SM for Re between 20,000 and 90,000. Figure 6.4 (a) shows that the smooth pipe and MC2 had almost the same friction factors at room temperature. This is because the roughness of SM and MC2 is very similar (see Table 4.1). Both MB50 and MB37 have greater f compared to SM. MB50 has a

25% and 40% higher f compared to SM at Re of 20,000 and 90,000, respectively. On average, MB50 has 33% higher friction factor than SM for Re between 20,000 and 90,000. MB37 has a 34% and 51% higher f compared to SM at Re of 20,000 and 90,000, respectively. On average, MB37 has 43% higher friction factor compared to SM for Re between 20,000 and 90,000. Therefore, between the pipes with ball bearings, the friction factor of the pipe with more bearings (i.e., MB37) is larger than the pipe with lower number of bearings (i.e., MB50).

Figure 6.4 (b) shows the variations of f_H with Re_t. Similar to the room temperature experiments, the friction factor of all pipes decreases with Re except for MC1 pipe. The f_H of MC1 is 2% higher than the smooth pipe at Re_t of 13,400 and 52% higher at Re_t of 64,000. Figure 6.4 (a) shows that the smooth pipe and MC2 have almost the same f_H at all Re_H. MB50 has 16% and 32% higher f_H relative to SM at Re_t of 13400 and 64,000, respectively. MB37 has 22% and 43% higher f relative to SM at Re_t of 13,400 and 64,000, respectively. On average, MB37 has the highest f_H increase of 26% followed by MC1 at 23%, MB50 at 20% and MC2 at 4% compared to the smooth pipe.

The Nusselt number of pipes with internal roughness is calculated from the rake measurements in experiment type C using equation 4.24. The variations of Nu with Re_t for all pipes are shown in Figure 6.5. The variations of Nu with Re_t for the pipes with internal roughness show similar trends compared to the variations of h with Re_t shown in Figure 6.3 (b). The Nu of all pipes increases with Re_t. This is because increase in Re_t leads to higher turbulent mixing and enhanced heat transfer in the flow. The increase in Nu with Re_t is approximately linear for all pipes.

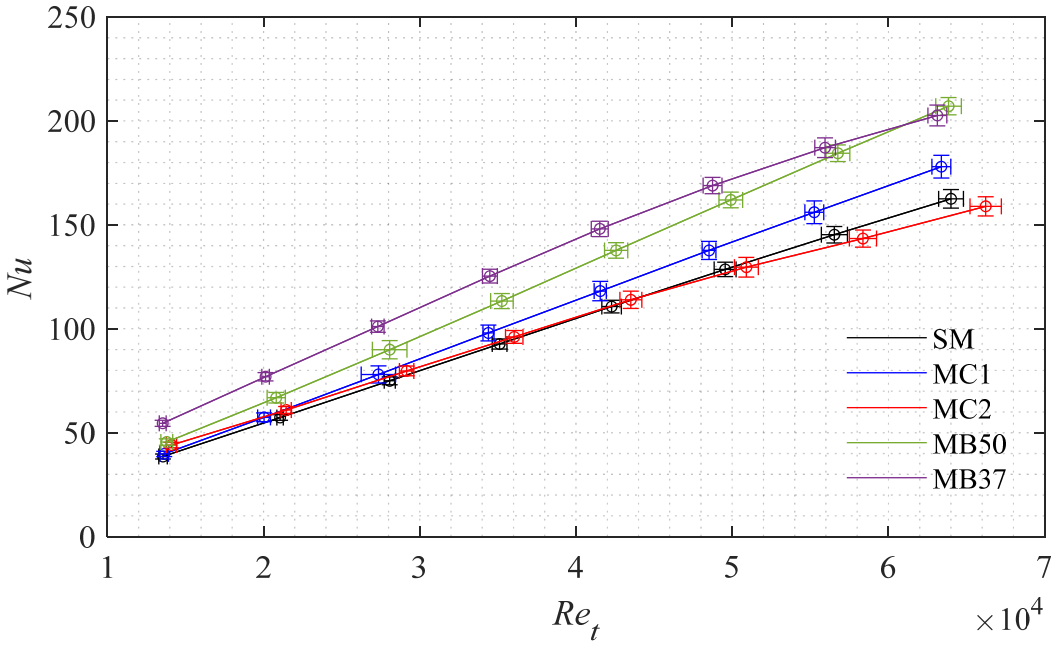

Figure 6.5. The changes of *Nu* with Re_t for the smooth and pipes with internal roughness.

Both MB37 and MB50 have significantly higher *Nu* compared to the MC1 and MC2. The *Nu* of MC1 pipe is 3% higher than the smooth pipe at Re_t of 13400. At Re_t of 64,000, the *Nu* of MC1 is 10% higher than the smooth pipe. MC2 has almost the same *Nu* as the smooth pipe at all Re_t except 57,000 and 64000. MC2 has a similar *Nu* to the smooth pipe because of its smaller roughness as explained in Section 6.2. At *Re* of around 50,000 and above the Nu of MC2 was lower than that of SM. This could be due to the errors caused by the larger variations of pipe wall temperature at higher *Re*. MB50 pipe has 18% and 27% higher *Nu* compared to SM at Re_t of 13,400 and 64,000, respectively. MB37 has 41% and 25% higher *f* compared to SM at Re_t of 13,400 and 64,000, respectively. On average, MB37 has the highest *Nu* increase of 33% followed by MB50 at 23%, and MC1 at 5% compared to the smooth pipe. Considering the two pipes with bearings, the smaller spacing of the ball bearings in MB37 leads to 10% higher *Nu* compared to MB50.

In summary, the addition of mesh to the internal surface of the pipe leads to a significant increase in friction factor but a marginal improvement of Nusselt number. In comparison, the addition of bearings to the internal surface of pipe leads to an increase in both friction factor and Nusselt number. Therefore, the pipes with bearings have a greater overall rate of heat transfer compared

to the pipes covered with only mesh. Tables 6.3 to 6.6 present different flow parameters evaluated from type B and C experiments conducted on the rough pipes.

Table 6.3 Flow parameters in the type B and C experiments conducted on MC1.

Re	*Nu*	$\dot{m}$ [kg/s]	C_P [J/kg.K]	μ[N.s/m^2]	k [W/m.K]	f_H	f
20,000	39.8	0.0147	1039.3	2.73E-05	0.0407	0.0390	0.0304
30,000	57.4	0.0216	1039.0	2.72E-05	0.0406	0.0378	0.0318
40,000	78.0	0.0295	1039.0	2.72E-05	0.0406	0.0377	0.0331
50,000	98.0	0.0371	1038.9	2.72E-05	0.0406	0.0382	0.0340
60,000	118.1	0.0447	1038.7	2.71E-05	0.0405	0.0389	0.0347
70,000	137.7	0.0521	1038.4	2.71E-05	0.0404	0.0398	0.0352
80,000	156.1	0.0592	1037.9	2.70E-05	0.0403	0.0407	0.0357
90,000	178.0	0.0676	1037.3	2.69E-05	0.0400	0.0419	0.0361

Table 6.4 Flow parameters in the type B and C experiments conducted on MC2.

Re	*Nu*	$\dot{m}$ [kg/s]	C_P [J/kg.K]	μ[N.s/m^2]	k [W/m.K]	f_H	f
20,000	44.0	0.0150	1037.8	2.70E-05	0.0402	0.0386	0.0253
30,000	60.9	0.0225	1036.3	2.67E-05	0.0397	0.0354	0.0230
40,000	79.7	0.0304	1035.3	2.65E-05	0.0393	0.0333	0.0216
50,000	96.1	0.0374	1034.7	2.64E-05	0.0391	0.0320	0.0205
60,000	113.9	0.0449	1034.1	2.63E-05	0.0389	0.0311	0.0198
70,000	129.6	0.0523	1033.5	2.61E-05	0.0387	0.0304	0.0192
80,000	143.4	0.0597	1032.8	2.60E-05	0.0384	0.0299	0.0188
90,000	158.9	0.0675	1032.3	2.59E-05	0.0382	0.0297	0.0185

Table 6.5 Flow parameters in the type B and C experiments conducted on MB50.

Re	*Nu*	$\dot{m}$ [kg/s]	C_P [J/kg.K]	μ [N.s/m^2]	k [W/m.K]	f_H	f
20,000	45.5	0.0148	1040.2	2.74E-05	0.0410	0.0428	0.0315
30,000	66.8	0.0222	1039.1	2.72E-05	0.0407	0.0405	0.0291
40,000	89.9	0.0298	1038.4	2.71E-05	0.0404	0.0389	0.0278
50,000	113.4	0.0372	1037.8	2.70E-05	0.0402	0.0378	0.0269
60,000	137.7	0.0448	1037.5	2.69E-05	0.0401	0.0372	0.0264
70,000	162.0	0.0525	1037.2	2.69E-05	0.0400	0.0368	0.0261
80,000	184.4	0.0596	1037.0	2.68E-05	0.0400	0.0366	0.0259
90,000	207.1	0.0670	1036.9	2.68E-05	0.0399	0.0366	0.0258

Table 6.6 Flow parameters in the type B and C experiments conducted on MB37.

Re	*Nu*	$\dot{m}$ [kg/s]	C_P [J/kg.K]	μ [N.s/m^2]	k [W/m.K]	f_H	f
20,000	54.5	0.0148	1041.7	2.77E-05	0.0416	0.0466	0.0338
30,000	76.9	0.0218	1040.6	2.75E-05	0.0412	0.0440	0.0313
40,000	101.1	0.0294	1039.8	2.73E-05	0.0409	0.0422	0.0298
50,000	125.3	0.0370	1039.2	2.72E-05	0.0407	0.0410	0.0289
60,000	148.1	0.0444	1038.7	2.71E-05	0.0405	0.0403	0.0283
70,000	168.9	0.0520	1038.3	2.71E-05	0.0404	0.0399	0.0279
80,000	187.1	0.0595	1038.0	2.70E-05	0.0403	0.0398	0.0278
90,000	202.6	0.0668	1037.3	2.69E-05	0.0400	0.0400	0.0277

6.4 Evaluation of the overall performance

The heat transfer and friction factor of the pipes were studied separately in the previous section. However, in most engineering applications, pipes with higher heat transfer and lower friction factor are desirable, and therefore, both properties need to be studied at the same time. The evaluation plot, proposed by Fen et al. (2009), is used here to compare the performance of the pipes. In the evaluation plot, the smooth pipe is used as a reference pipe. For all pipes with internal roughness, the Nu and f_H are normalized by the Nusselt number and friction factor of the smooth pipe depicted as Nu_0 and f_{H0}, respectively. To be able to normalize Nu and f_H by Nu_0 and f_{H0}, the Reynolds of flow in the rough pipe (Re_t) need to be equal to the Reynolds of the flow in the smooth pipe (Re_{t0}). In the experiments the Re_t was not equal to the Re_{t0}. Therefore, the values of Nu and f_H are evaluated at Re_{t0} through linear interpolation.

Figure 6.6 (a) shows the changes of normalized friction factor with Reynolds number. f_H/f_{H0} increases with Re_{t0} for all pipes except MC2. MC2 has almost the same f_H as the smooth pipe, and therefore the value of f_H/f_{H0} is close to one for all Re_{t0}. MC1 has the highest increase in normalized friction factor with Re_{t0}. The f_H/f_{H0} graph of both MB50 and MB37 have a similar trend, and MB37 has the highest overall normalized friction. Figure 6.6 (b) shows the changes of normalized Nusselt number with Re_{t0}. The Nusselt number of MC1 is almost the same as the smooth pipe, and therefore Nu/Nu_0 of MC2 is close to one for all Re_{t0}. The Nusselt number of MC2 is in general slightly higher by a factor of 1.1 compared to the smooth pipe. The Nusselt number of MB37 is higher than the smooth pipe by a factor of 1.3 to 1.4. This is the highest increase in Nu relative to the smooth pipe. The second highest Nu increase compared to the smooth pipe is achieved by MB50. The Nu of MB50 is 1.2 to 1.3 times that of the smooth pipe.

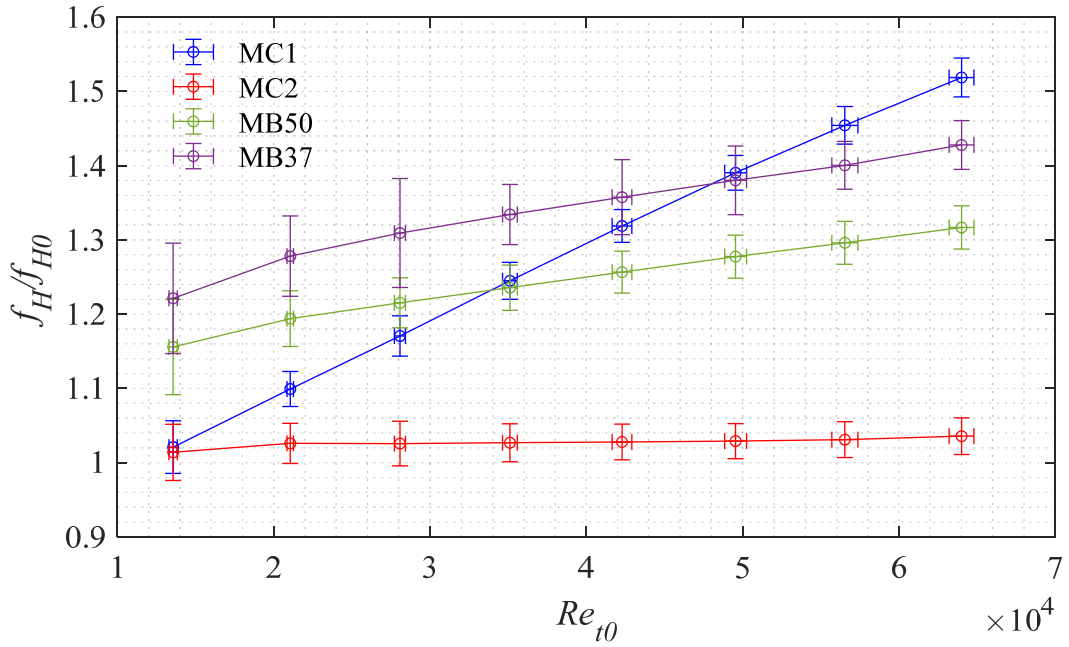

(a)

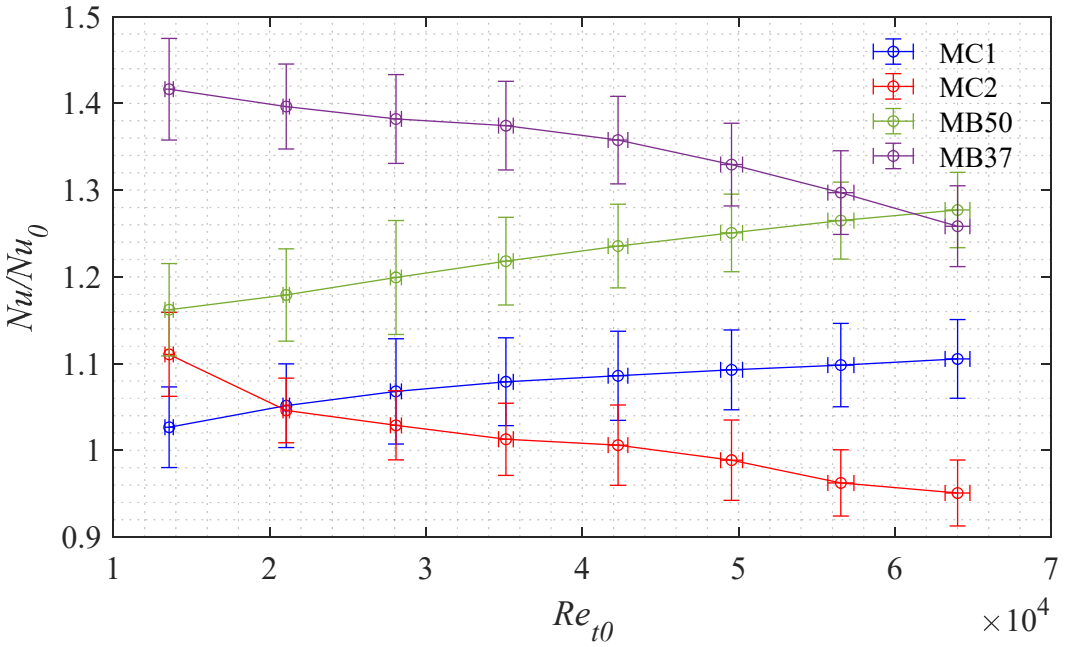

(b)

Figure 6.6 Variations of (a) f_H/f_{H0}, and (b) Nu/Nu_0 with Re_{t0}.

Figure 6.7 (a) shows the plot of normalized Nusselt number versus normalized friction factor for the rough pipes. Pipes with higher Nu/Nu_0 and lower f_H/f_{H0} have an overall higher thermohydraulic performance. As can be seen in Figure 6.7 (a), the pipes with ball bearings, MB50 and MB37, have the highest performance overall. Figure 6.7 (b) shows the evaluation plot suggested by Fen et al. (2009) for comparing pipes based on thermohydraulic performance and energy saving capabilities. The three dashed black lines shown in this figure all cross the (1,1) point and have different slopes of 16/55, 16/35 and 1. These lines divide the plot into four regions indicated by boldface numbers. In terms of performance and energy consumption, pipes that can operate in regions three and four are the most favourable ones while those that operate in region one consumes more power to increase heat transfer. For more detailed information on the evaluation plot see Chapter 2, section 2.6.1.

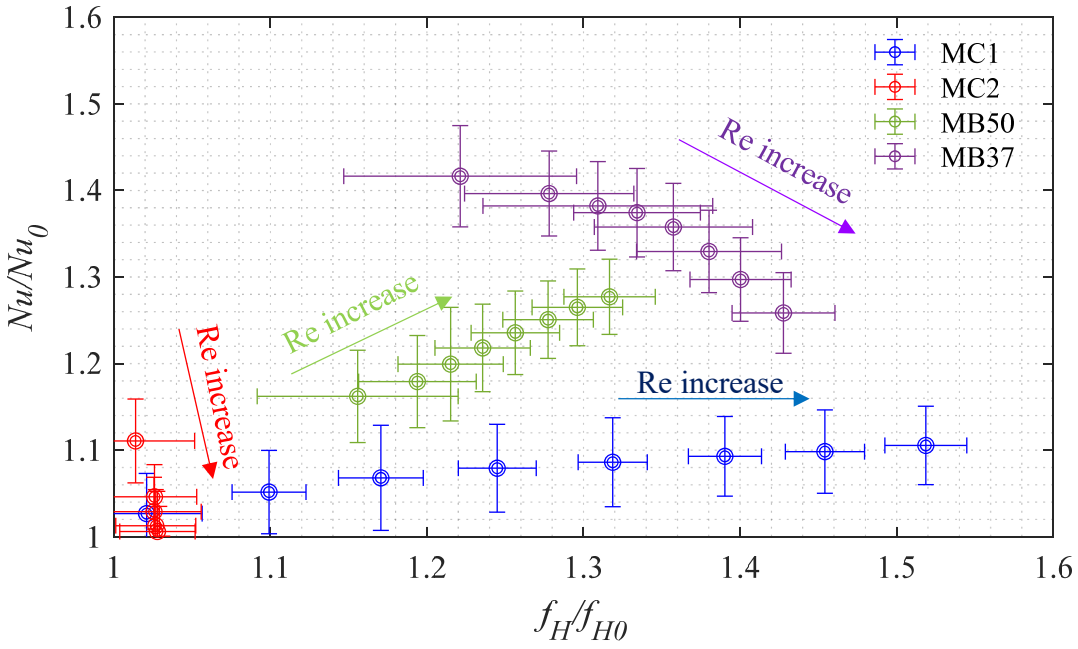

(a)

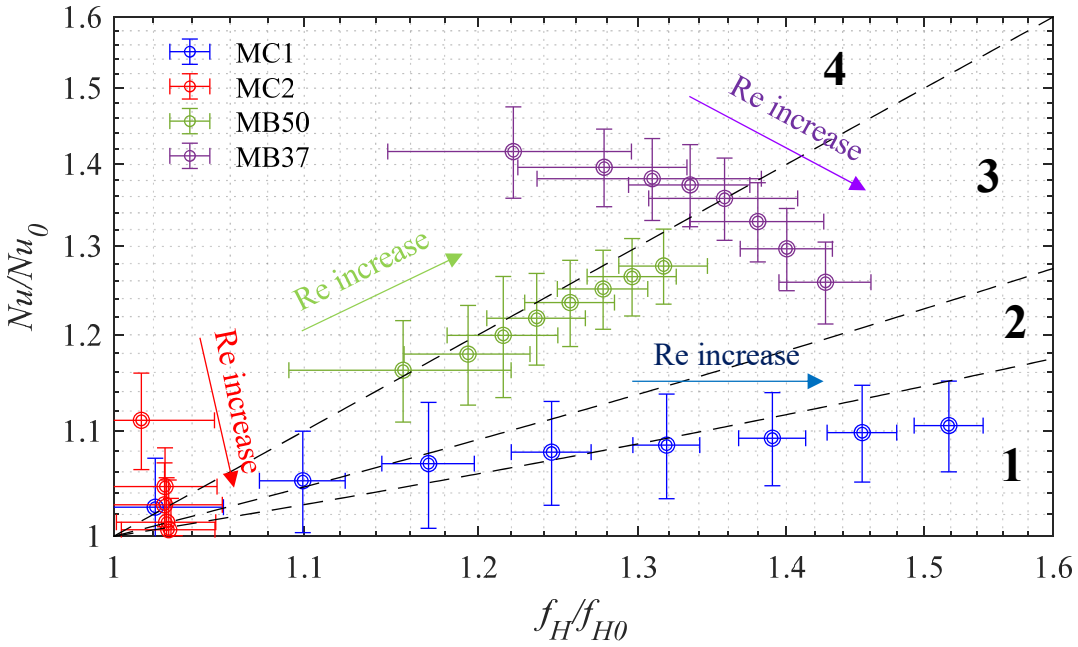

(b)

Figure 6.7. Evaluation of the performace of the pipes with internal roughness.

Figure 6.7 (b) shows that MB37 is in region four for Re_t below 35,000. For Re_t above 35,000, MB37 enters region three, and its performance reduces. MB50 operates in upper section of region three for most Re_t, while MC1 operates mostly in region one. This means that MC1 has the lowest performance of all the pipes. As shown in Figure 6.7 (b), it is difficult to assign a region for MC2 because the data points of MC2 are very close to the smooth pipe. Therefore, Figure 6.7 does not provide information about the performance of MC2 compared to other pipes. However, it has been shown both in the Section 6.3 and Figure 6.7 that MC2 had a similar heat transfer and frictional losses compared to the smooth pipe. Therefore, it is safe to assume that the improvement in heat transfer and the increase in friction factor was marginal for MC2, and that it had a similar performance as the smooth pipe. Overall, adding ball bearings to the pipe can lead to a significant improvement in performance, and increase in the number of the bearings over the length of the pipe can further improve the overall performance. Adding mesh to the pipes can have marginal improvements of heat transfer while it results in a large increase in frictional losses, and therefore it is not recommended. It should be noted that pipes with ball bearings are easy to manufacture. The ball bearing can be added to the internal surface of the pipe by spot-welding. Table 6.7 presents the normalized friction factor and Nusselt number for pipes at different Re_{t0}.

Table 6.7 Normalized friction factor and Nusselt number for pipes at different Re_{t0}.

Re_{t0}	MC1		MC2		MB50		MB37	
	f_H/f_{H0}	Nu/Nu_0	f_H/f_{H0}	Nu/Nu_0	f_H/f_{H0}	Nu/Nu_0	f_H/f_{H0}	Nu/Nu_0
13,600	1.02	1.03	1.01	1.11	1.16	1.16	1.22	1.42
21,100	1.10	1.05	1.03	1.05	1.19	1.18	1.28	1.40
28,100	1.17	1.07	1.03	1.03	1.22	1.20	1.31	1.38
35,100	1.24	1.08	1.03	1.01	1.24	1.22	1.33	1.37
42,300	1.32	1.09	1.03	1.01	1.26	1.24	1.36	1.36
49,500	1.39	1.09	1.03	0.99	1.28	1.25	1.38	1.33
56,500	1.45	1.10	1.03	0.96	1.30	1.26	1.40	1.30
64,000	1.52	1.11	1.04	0.95	1.32	1.28	1.43	1.26

6.5 Conclusion

In this chapter, the result of the experiments conducted on pipes with internal roughness was presented. The changes of convective heat transfer coefficient with *Re* were presented for the pipes with internal roughness and it was found that both MB37 and MB50 had significantly higher heat transfer coefficients than both pipes covered with mesh. Between pipes covered with mesh, MC1 had a higher heat transfer coefficient than MC2 while MC2 had almost the same heat-transfer coefficient as the smooth pipe.

It was observed that the heat transfer coefficient increases with *Re* for all pipes because of higher turbulence mixing. This increase with *Re* was linear for most of the pipes except MC2 and MB37. The changes in the friction factor of the pipes with internal roughness with *Re* was presented and it was shown that compared to the smooth pipe, MB37 had the highest increase in friction factor followed by MC1, MB50 and MC2. The changes of *Nu* with Re_t for the smooth and profiled pipes was compared. It was shown that both MB37 and MB50 had significantly higher *Nu* compared to the pipes covered with mesh and the smooth pipe. Between the pipes with bearings, the higher density of the ball bearings in MB37 led to higher *Nu* increase compared to MB50. Between the two pipes covered with mesh, MC2 had a smaller *Nu* increase than MC1. The evaluation plot was also used to compare the performance of the pipes, and it was again shown that the pipes with ball bearings, MC50 and MC37, had the highest performance while MC1 had the lowest. Although the evaluation plot showed high performance for MC2, it was assumed to have a similar performance to the smooth pipe due to the similar *Nu* and *f* values. Overall, it seems that adding ball bearings to the pipe wall can lead to a significant improvement in hydrodynamic and thermal performance and increase in the density of the bearings over the length of the pipe can also add to this performance. Adding mesh to the pipes can have marginal improvements in heat transfer and a large increase in frictional losses, and therefore it is not recommended.

Chapter 7.

Conclusion

In this study, an experimental investigation was conducted to assess the effect of roughness on both heat transfer and pressure drop in pipes with different internal surface. The study includes the design of an experimental setup and collecting laboratory data on five pipes with various internal roughness to determine their performance in transferring heat from the pipe wall to the air flow. These pipes included a smooth pipe (SM), a pipe covered with mesh and one layer of coating (MC1), a pipe covered with mesh and two layers of coating (MC2), a pipe that was covered with ball bearings at 50 mm spacing (MB50), and a pipe that was covered with ball bearings at 37 mm spacing (MB37). The setup was able to generate fully developed turbulent flows with Reynolds number (*Re*) from 20,000 to 90,000. The setup was also able to raise the temperature of the pipes from room temperature up to around 375°C. The properties of the flow were measured using various thermocouples and pressure transducers that were installed inside and over the pipe. Two main variables, Nusselt number (*Nu*) and friction factor (*f*), were calculated from the experimental data measurements and were used to compare the thermohydraulic performance of the pipes.

The results of the experiments conducted on the smooth pipe (i.e., SM) was presented, and the temperature profile of the air flow was also provided. Both *Nu* and *f* were calculated and compared to their respective analytical values in the literature to find the accuracy of the measurements. The Colebrook correlation was used to find the accuracy of friction measurements at room temperature, and the error of friction factor was around 4%. Gnielinski correlation was used to find the accuracy of Nusselt number measurements, and its error was about 8%.

The results of the experiments conducted on the pipes with internal roughness (i.e., MC1, MC2, MB50, and MB37) were also presented. The variations of friction factor and convective heat

transfer coefficient with *Re* were evaluated for the pipes with internal roughness. The friction factor of MC2 was found to be almost identical to the smooth pipe. This observation was consistent with profilometer measurements that showed MC2 has a negligible roughness. MC1 had the highest friction factor compared to the other pipes at room temperature. MB37 had highest friction factor in heated pipe experiments and the second highest friction factor in experiments that were conducted at room temperature. The friction factor of MB50 was slightly lower than MB37 in experiments conducted with heated pipes and at room temperature. Friction factor of the heated MC1 was lower than the friction factor of heated MB37 and MB50. The heat transfer coefficient and Nusselt number of MC2 were almost identical to the smooth pipe at all *Re*. While MC2 had a higher *Nu* compared to MC2, the highest *Nu* were achieved by MB50 and MB37 in all *Re*. MB37 maintained a higher *Nu* across all *Re* compared to MB50.

The overall performance of the pipes was also compared in terms of pressure drop and heat transfer capabilities. It was shown that MC1 had the lowest performance while MB37 had the highest performance. MB50 had a slightly lower performance compared to MB37. The performance of MC2 was similar to the performance of the smooth pipe. The results show that adding ball bearings to the pipe wall can enhance the thermohydraulic performance of pipes and increasing the number of bearings can lead to further improvements. No benefit with regards to thermohydraulic performance was found by adding mesh to the pipes. Therefore, mesh roughness elements are not recommended to be used.

This study provides a better understanding of the effect of roughness on heat transfer and pressure drop in pipes with various roughness elements. It revealed the importance of adding bearings to the pipe internal surface to enhance its heat transfer capabilities. It also showed that adding mesh to the internal surface of pipes is not an effective method compared to adding bearings due to the high pressure drop in pipes with mesh.

A limitation of this work is that only the bulk properties of the flow was studied, and more detailed investigations of the flow, using particle image velocimetry or simulations, should be conducted in the future to optimize the geometry of roughness elements. Future works that focus on investigating the geometry of roughness elements may provide a better understanding of the behaviour of the flow, especially in case of MC2 and MC1 that had a different *Nu* and *f* patterns

with the changes of *Re* compared to other pipes. The uniformity of pipe temperature can also be improved by using more controllers to keep the temperature near constant along the length of the pipe. Improvements in pipe temperature distribution might lead to lower error ranges in both *Nu* and *f*.

REFERENCES

Bhuiya, M. M. K., Ahamed, J. U., Sarkar, M. A. R., Salam, B., Masjuki, H. H., Kalam, M. A., ... & Sayem, A. S. M. (2012). Heat transfer and pressure drop characteristics in turbulent flow through a tube. *Experimental Heat Transfer*, 25(4), 301-322.

Bunker, R. S., & Donnellan, K. F. (2003, January). Heat transfer and friction factors for flows inside circular tubes with concavity surfaces. In *Turbo Expo: Power for Land*, Sea, and Air (Vol. 36886, pp. 21-29).

Carnavos, T. C. (1979). Cooling air in turbulent flow with internally finned tubes. *Heat Transfer Engineering*, *1*(2), 41-46.

Cattafesta, L., Bahr, C., & Mathew, J. (2010). Fundamentals of wind-tunnel design. *Encyclopedia of Aerospace Engineering*, 1-10.

Chang, S. W., Yang, T. L., & Liou, J. S. (2007). Heat transfer and pressure drop in tube with broken twisted tape insert. *Experimental Thermal and Fluid Science*, 32(2), 489-501.

Chapple, D. D. (1998). *The role of turbulence in pulsation-induced orifice plate flow metering error* [Masters dissertation, University of Alberta].

Córcoles, J. I., Belmonte, J. F., Molina, A. E., & Almendros-Ibáñez, J. A. (2019). Influence of corrugation shape on heat transfer performance in corrugated tubes using numerical simulations. *International Journal of Thermal Sciences*, 137, 262-275.

Córcoles-Tendero, J. I., Belmonte, J. F., Molina, A. E., & Almendros-Ibáñez, J. A. (2018). Numerical simulation of the heat transfer process in a corrugated tube. *International Journal of Thermal Sciences*, 126, 125-136.

Dewan, A., Mahanta, P., Raju, K. S., & Kumar, P. S. (2004). Review of passive heat transfer augmentation techniques. *Proceedings of the Institution of Mechanical Engineers, Part A: Journal of Power and Energy*, 218(7), 509-527.

Eiamsa-ard, S., & Promvonge, P. (2005). Enhancement of heat transfer in a tube with regularly-spaced helical tape swirl generators. *Solar energy*, 78(4), 483-494.

Eiamsa-ard, S., & Promvonge, P. (2010). Thermal characterization of turbulent tube flows over diamond-shaped elements in tandem. *International Journal of Thermal Sciences*, 49(6), 1051-1062.

Eiamsa-Ard, S., Nivesrangsan, P., Chokphoemphun, S., & Promvonge, P. (2010). Influence of combined non-uniform wire coil and twisted tape inserts on thermal performance characteristics. *International Communications in Heat and Mass Transfer*, 37(7), 850-856.

Eiamsa-Ard, S., Yongsiri, K., Nanan, K., & Thianpong, C. (2012). Heat transfer augmentation by helically twisted tapes as swirl and turbulence promoters. *Chemical Engineering and Processing: Process Intensification*, 60, 42-48.

Elshafei, E. A., Mohamed, M. S., Mansour, H., & Sakr, M. (2008). Experimental study of heat transfer in pulsating turbulent flow in a pipe. *International Journal of Heat and Fluid Flow*, 29(4), 1029-1038.

Fan, J. F., Ding, W. K., Zhang, J. F., He, Y. L., & Tao, W. Q. (2009). A performance evaluation plot of enhanced heat transfer techniques oriented for energy-saving. *International Journal of Heat and Mass Transfer*, 52(1-2), 33-44.

Gee, D. L., & Webb, R. L. (1980). Forced convection heat transfer in helically rib-roughened tubes. *International Journal of Heat and Mass Transfer*, 23(8), 1127-1136.

Gunes, S., Ozceyhan, V., & Buyukalaca, O. (2010). Heat transfer enhancement in a tube with equilateral triangle cross sectioned coiled wire inserts. *Experimental Thermal and Fluid Science*, 34(6), 684-691.

Han, J. C. (1984). Heat transfer and friction in channels with two opposite rib-roughened walls, *Journal of Heat Transfer*. 106(4), 774-781.

Harle ß, A., Franz, E., & Breuer, M. (2017). Heat transfer and friction characteristics of fully developed gas flow in cross-corrugated tubes. *International journal of heat and mass transfer*, 107, 1076-1084.

Harleß, A., Franz, E., & Breuer, M. (2016). Experimental investigation of heat transfer and friction characteristic of fully developed gas flow in single-start and three-start corrugated tubes. *International Journal of Heat and Mass Transfer*, 103, 538-547.

Huq, M., Huq, A. A. U., & Rahman, M. M. (1998). Experimental measurements of heat transfer in an internally finned tube. *International Communications in Heat and Mass Transfer*, 25(5), 619-630.

Incropera, F. P., DeWitt, D. P., Bergman, T. L., & Levine, A. S. (2007). *Fundamentals of Heat and Mass Transfer* (6th ed.). John Wiley, NJ: Hoboken.

Islam, A., & Mozumder, A. K. (2009). Forced convection heat transfer performance of an internally finned tube. *Journal of mechanical engineering*, 40(1), 54-62.

Kader, B. A., & Yaglom, A. M. (1977). Turbulent heat and mass transfer from a wall with parallel roughness ridges. *International Journal of Heat and Mass Transfer*, 20(4), 345-357.

Kaood, A., Abou-Deif, T., Eltahan, H., Yehia, M. A., & Khalil, E. E. (2019). Numerical investigation of heat transfer and friction characteristics for turbulent flow in various corrugated tubes. *Proceedings of the Institution of Mechanical Engineers*, Part A: Journal of Power and Energy, 233(4), 457-475.

Kim, N. H., & Webb, R. L. (1993). Analytic prediction of the friction and heat transfer for turbulent flow in axial internal fin tubes, *Journal of Heat Transfer*. 115(3), 553-559.

Kundu, Pijush K., Ira M. Cohen, and David R. Dowling. (2011) *Fluid mechanics*. Academic press, London.

Li, X. W., Meng, J. A., & Li, Z. X. (2011). Roughness enhanced mechanism for turbulent convective heat transfer. *International Journal of Heat and Mass Transfer*, 54(9-10), 1775-1781.

Mehta, R. D., & Bradshaw, P. (1979). Design rules for small low speed wind tunnels. *The Aeronautical Journal*, 83(827), 443-453.

Merzkirch, W., Gersten, K., Hans, V., Lavante, E., Peters, F., & Ram, V. V. (2005). *Fluid mechanics of flow metering* (pp. 95-110). Springer, Berlin.

Munson B. R., Okiishi. T. H., Huebsch W. W., Rothmayer A. P. (2013). *Fundamentals of fluid mechanics*. John Wiley, NJ: Hoboken.

Nelly, S. M., Nieratschker, W., Nadler, M., Raab, D., & Delgado, A. (2015). Experimental and numerical investigation of the pressure drop and heat transfer coefficient in corrugated tubes. *Chemical Engineering & Technology*, 38(12), 2279-2290.

Nikuradse, J. (1950). *Laws of flow in rough pipes*. NASA Center for Aerospace Information (CASI), United States.

Peng, H., Liu, L., Ling, X. and Li, Y., 2016. Thermo-hydraulic performances of internally finned tube with a new type wave fin arrays. *Applied Thermal Engineering*, 98, pp.1174-1188.

Pope, S. B. (2000). *Turbulent flows*, Cambridge university press, NY: New York.

Promthaisong, P., Jedsadaratanachai, W., & Eiamsa-Ard, S. (2018). Effect of geometrical parameters on turbulent flow and heat transfer behaviors in triple-start corrugated tubes. *Journal of Thermal Science and Technology*, 13(1), JTST0008-JTST0008.

Promvonge, P. (2008). Thermal performance in circular tube fitted with coiled square wires. *Energy Conversion and Management*, 49(5), 980-987.

Rainieri, S., Bozzoli, F., & Pagliarini, G. (2012). Experimental investigation on the convective heat transfer in straight and coiled corrugated tubes for highly viscous fluids: Preliminary results. *International journal of heat and mass transfer*, 55(1-3), 498-504.

Saad A, E. S., Sayed A, E. S., & Mohamed M, S. (2012). Experimental study of heat transfer to flowing air inside a circular tube with longitudinal continuous and interrupted fins. *Journal of Electronics Cooling and Thermal Control*, 2012.

Wang, W., Zhang, Y., Li, B., Han, H., & Gao, X. (2017). Influence of geometrical parameters on turbulent flow and heat transfer characteristics in outward helically corrugated tubes. *Energy Conversion and Management*, 136, 294-306.

Wang, Y., He, Y. L., Lei, Y. G., & Zhang, J. (2010). Heat transfer and hydrodynamics analysis of a novel dimpled tube. *Experimental thermal and fluid science*, 34(8), 1273-1281.

Wang, Y., He, Y. L., Li, R., & Lei, Y. G. (2009). Heat transfer and friction characteristics for turbulent flow of dimpled tubes. *Chemical Engineering & Technology: Industrial Chemistry-Plant Equipment-Process Engineering-Biotechnology*, 32(6), 956-963.

Webb, R. L., & Eckert, E. R. G. (1972). Application of rough surfaces to heat exchanger design. *international journal of heat and mass transfer*, 15(9), 1647-1658.

Yakut, K., & Sahin, B. (2004). The effects of vortex characteristics on performance of coiled wire turbulators used for heat transfer augmentation. *Applied Thermal Engineering*, 24(16), 2427-2438.

Yaws, C. L. (2008). Thermophysical properties of chemicals and hydrocarbons. William Andrew, NY: Norwich.

Yu, B. J. J. H., Nie, J. H., Wang, Q. W., & Tao, W. Q. (1999). Experimental study on the pressure drop and heat transfer characteristics of tubes with internal wave-like longitudinal fins. *Heat and Mass Transfer*, 35(1), 65-73.

Appendix A.

CAD drawings and diagrams

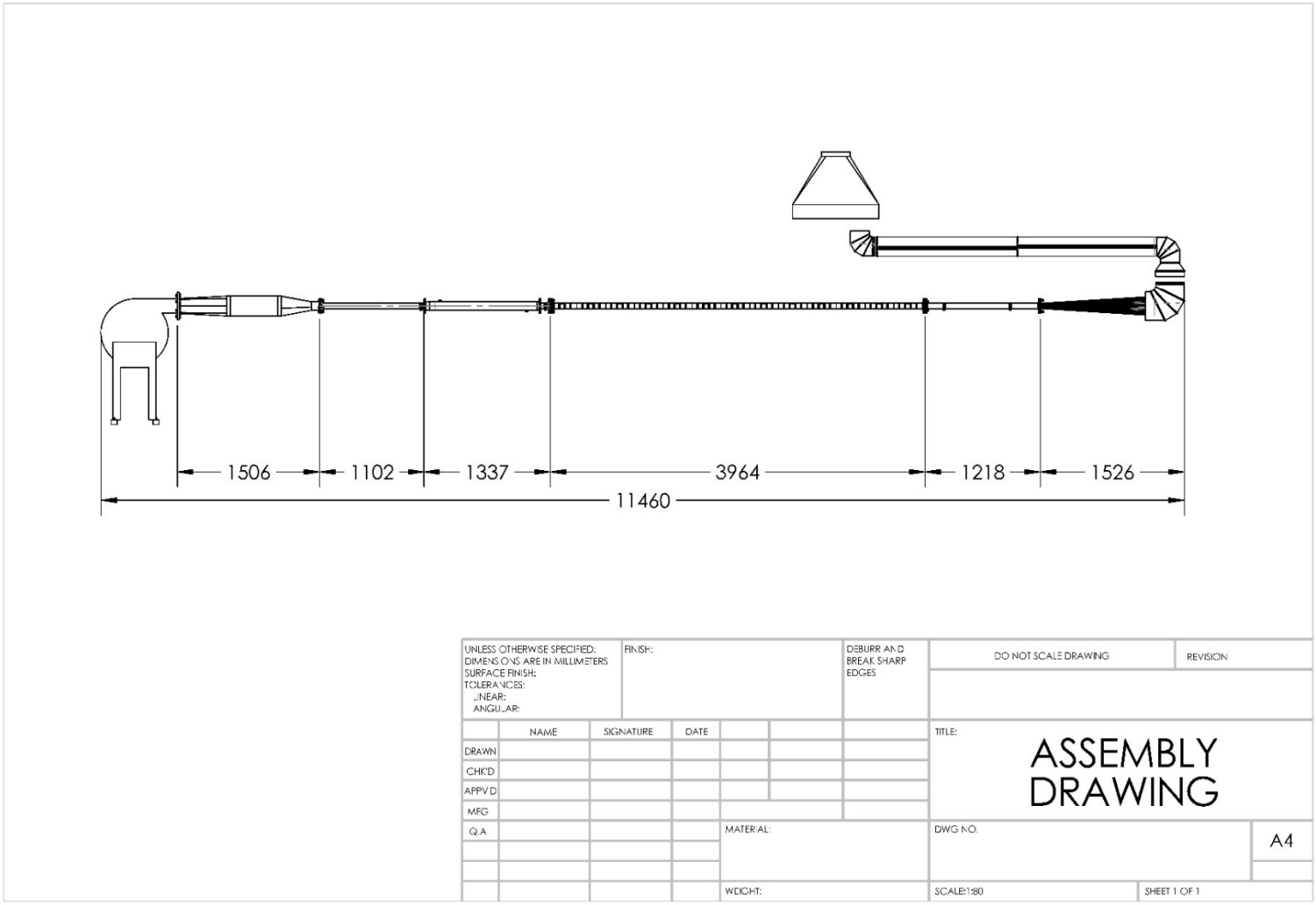

Figure A. 1 The front view drawing of the entire lab setup (dimensions are in mm).

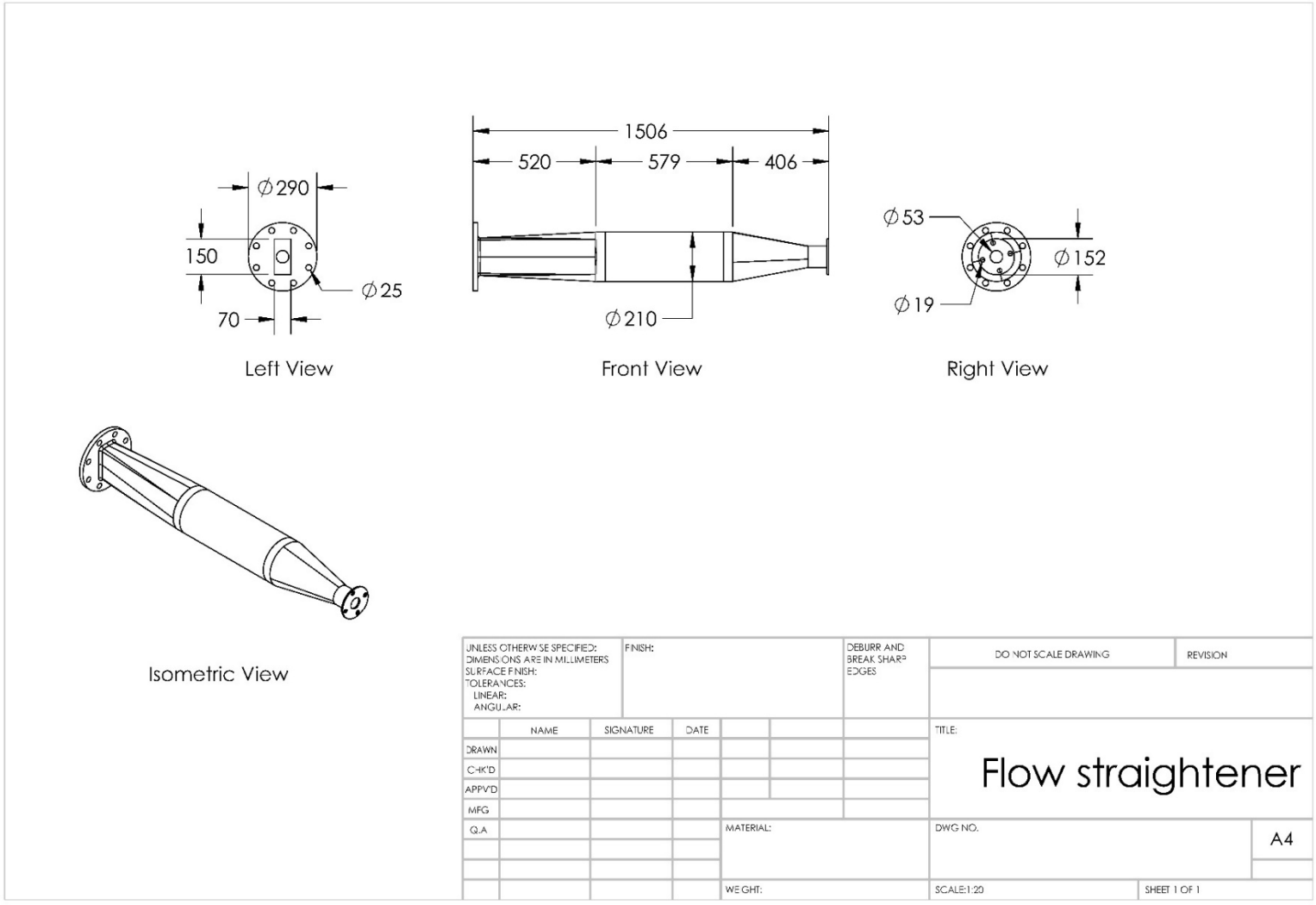

Figure A. 2 The drawing of the settling chamber (dimensions are in mm).

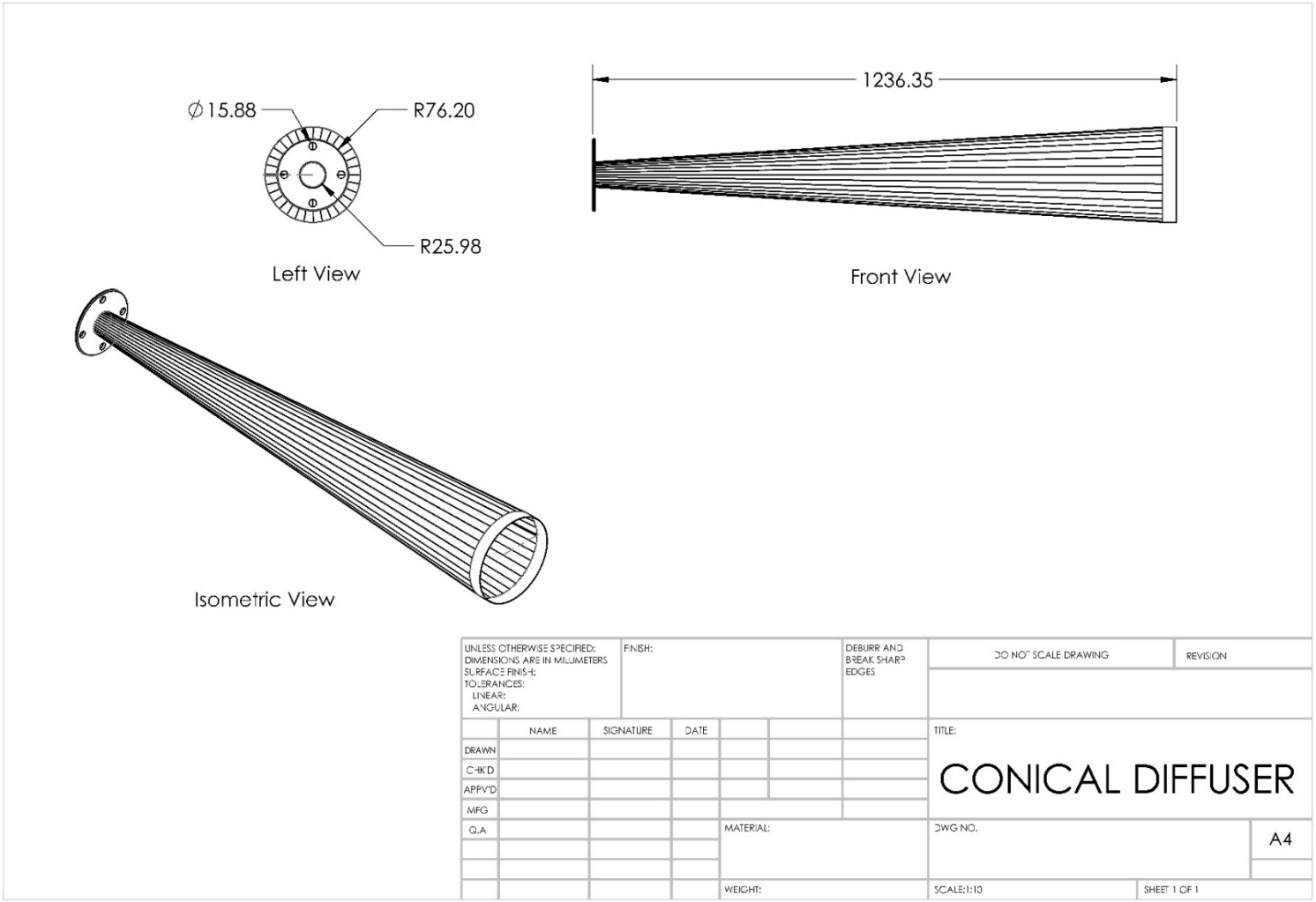

Figure A. 3 The Conical diffuser of the exhaust section of the pipe (dimensions are in mm).

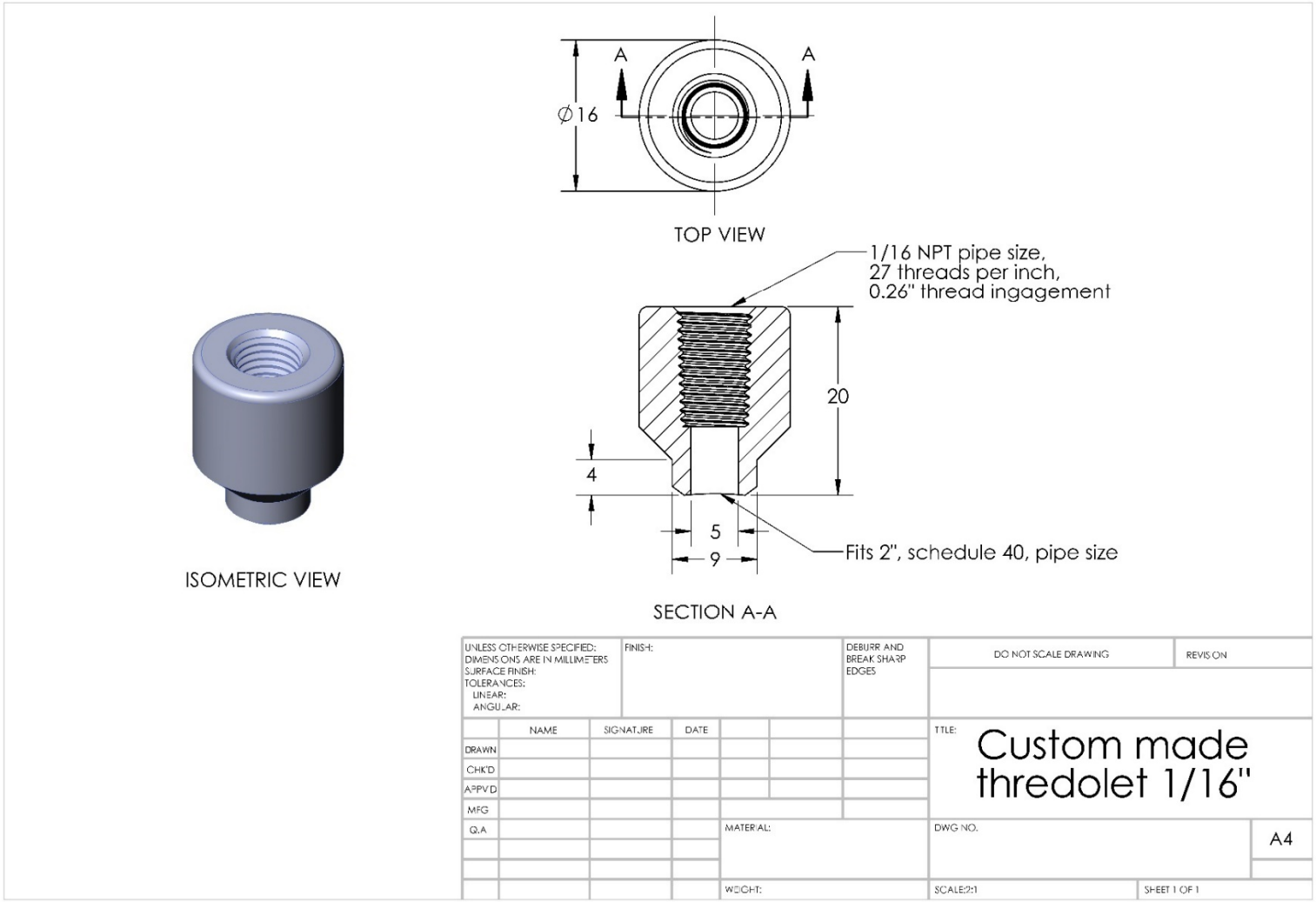

Figure A. 4 The drawing of the threadolets used for connecting the measurement instruments to the test section (dimensions are in mm).

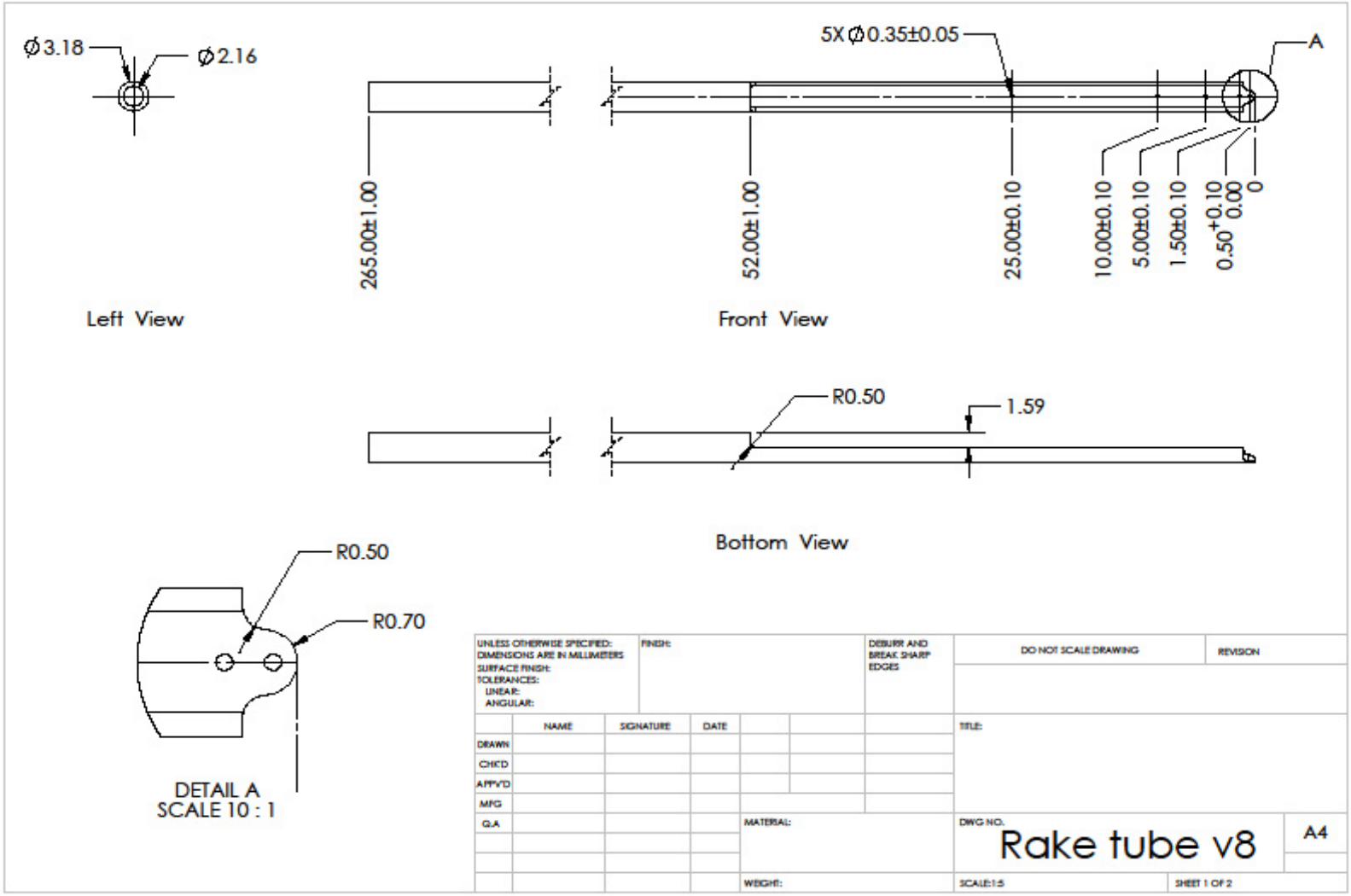

Figure A. 5 Detailed drawing of rake tube (dimensions are in mm).

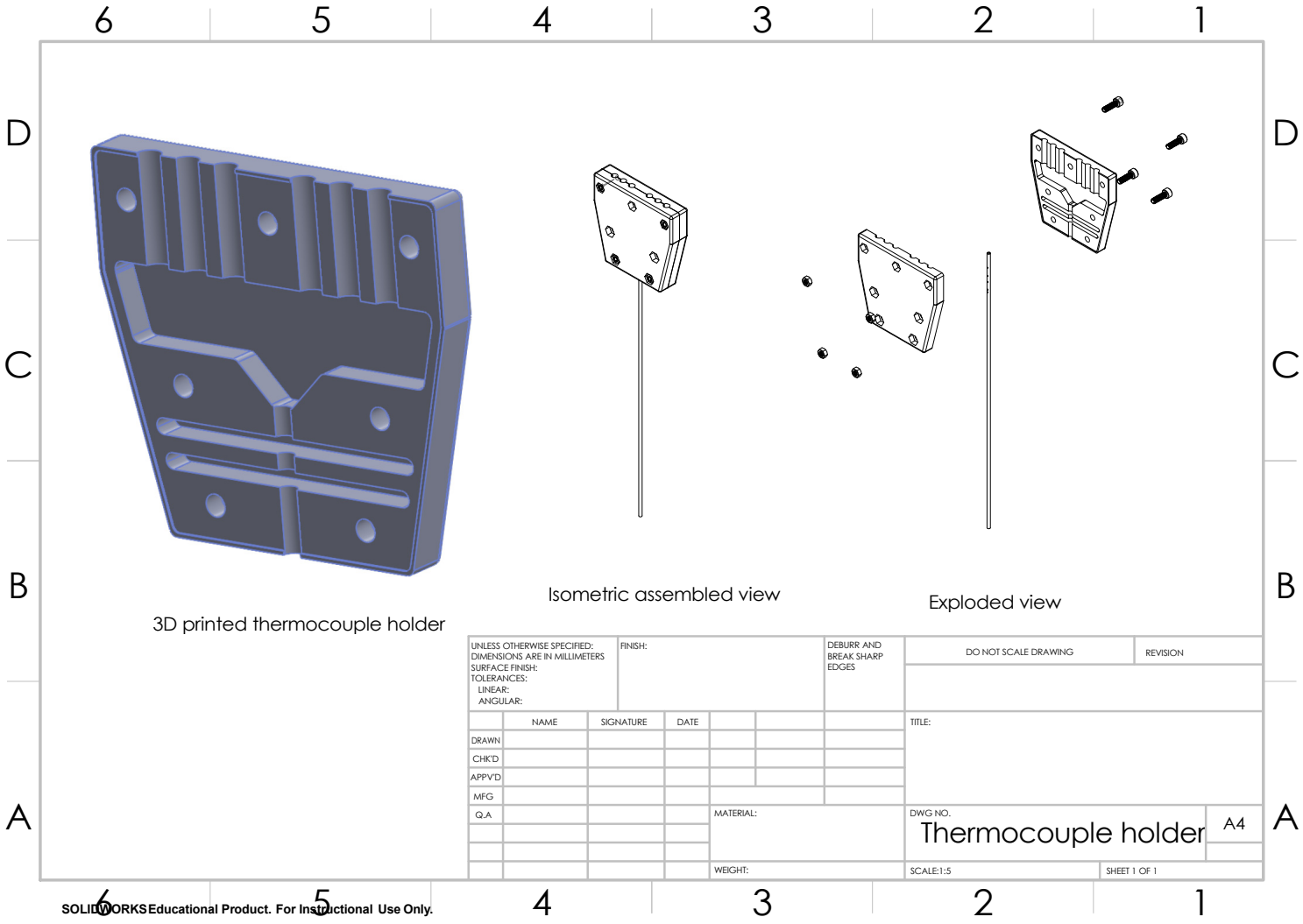

Figure A. 6 drawing of rake holders.

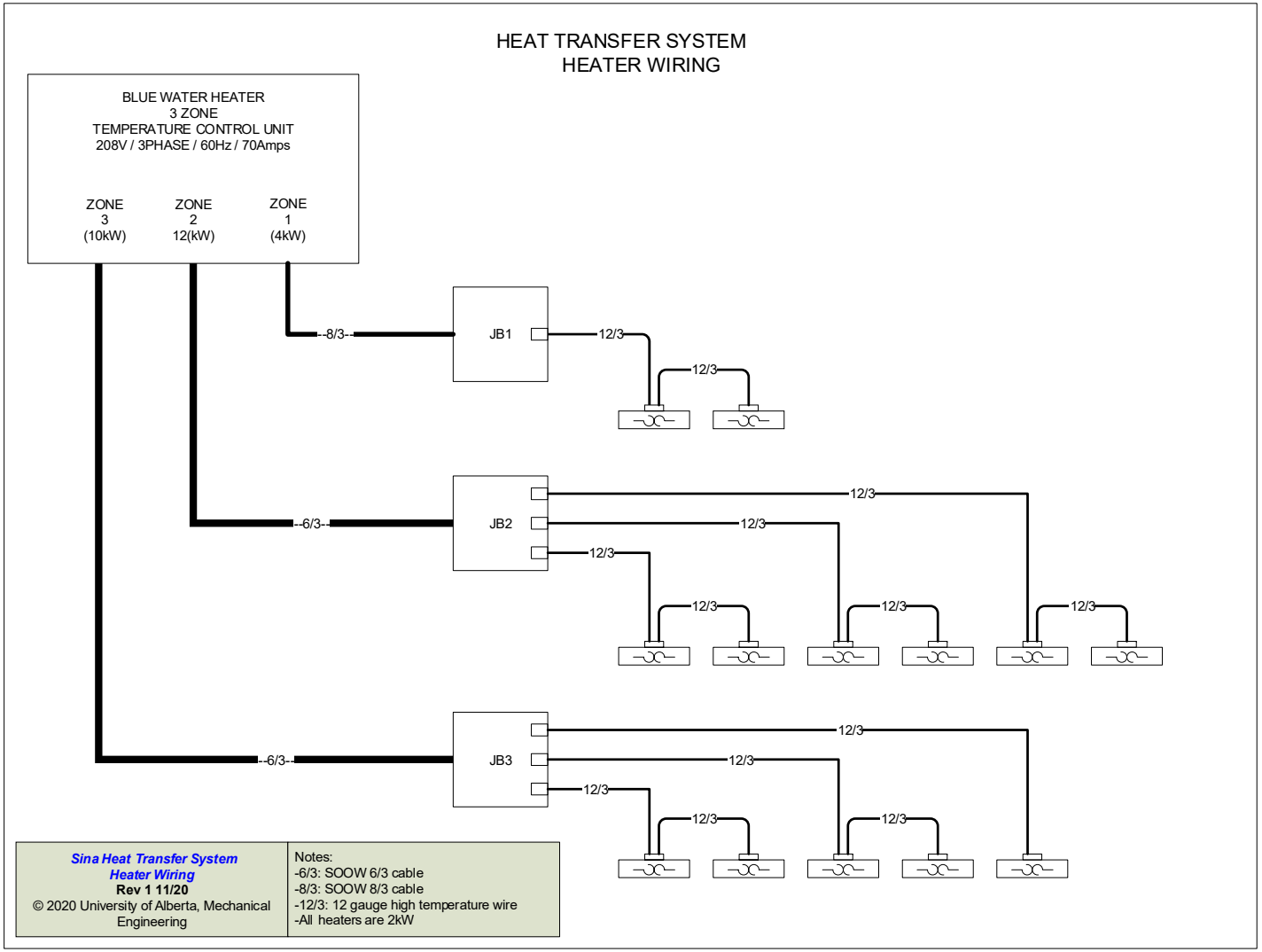

Figure A. 7 Wiring diagram of the heaters in the test section.

Appendix B.

Supplementary plots and tables

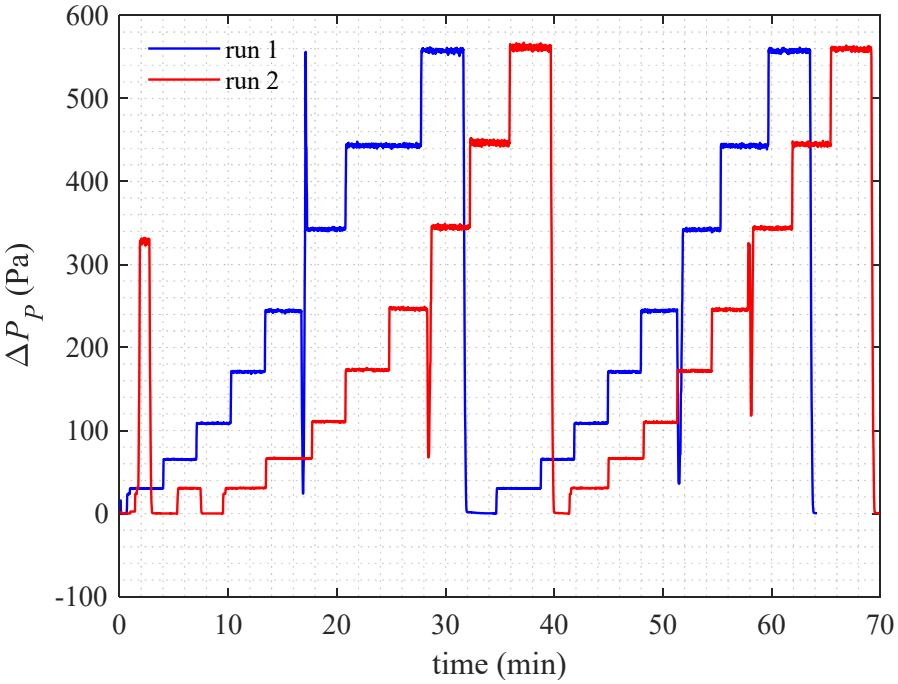

Figure B. 1 Changes of Pitot tube differential pressure over time for type A experiment (SM pipe).

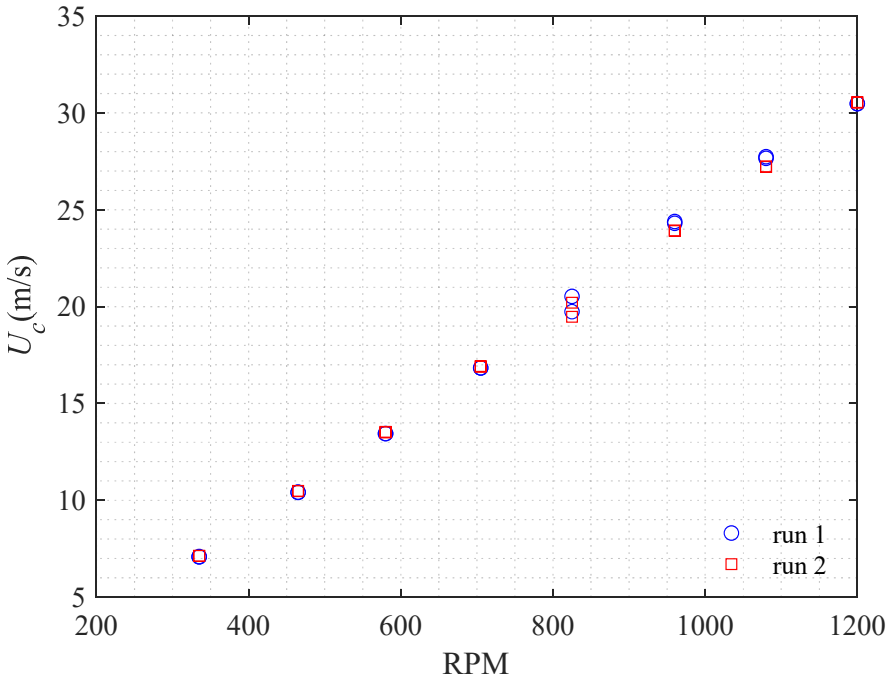

Figure B. 2 Variations of centerline velocity for different RPMs for type A experiment (SM pipe).

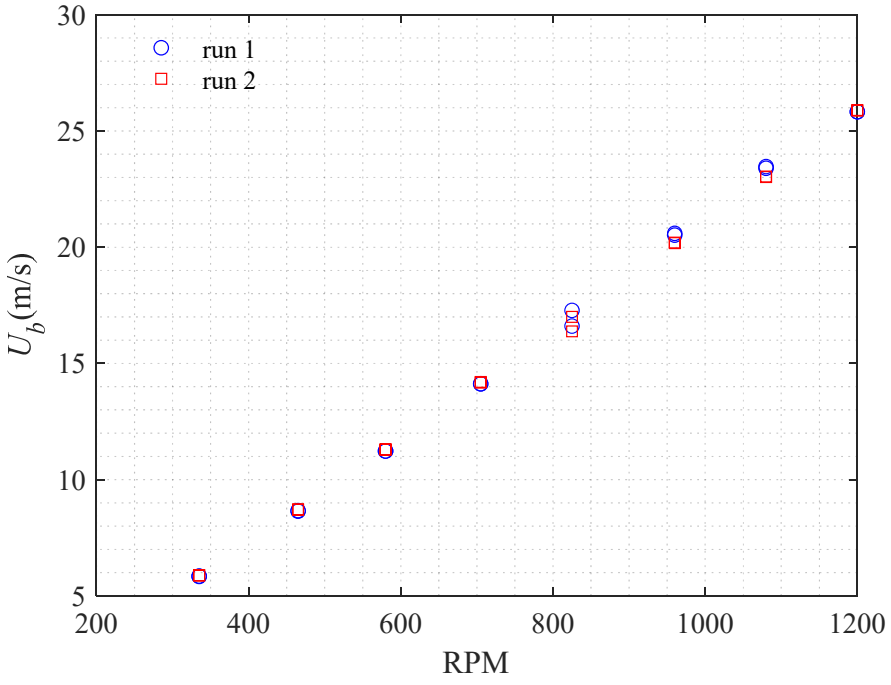

Figure B. 3 Bulk velocity changes with RPM for type A experiment (SM pipe).

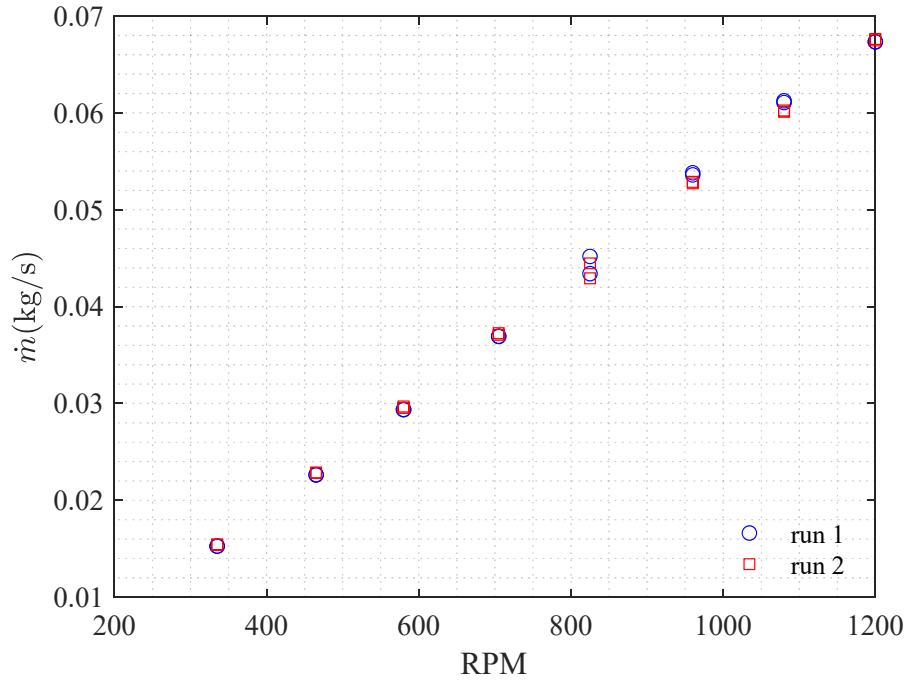

Figure B. 4 Changes of mass flow rate with RPM for type A experiment (SM pipe).

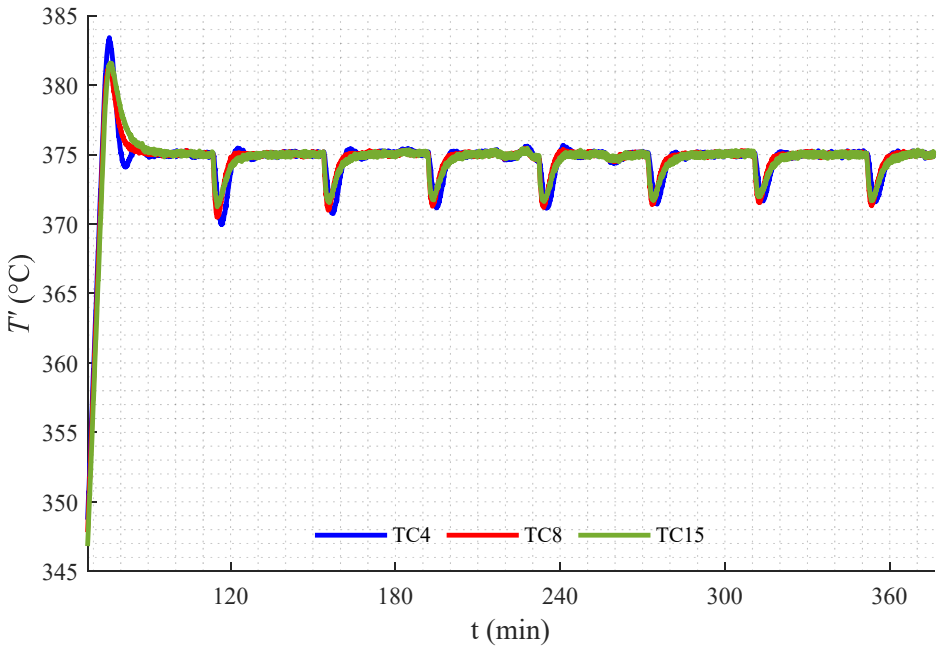

(a)

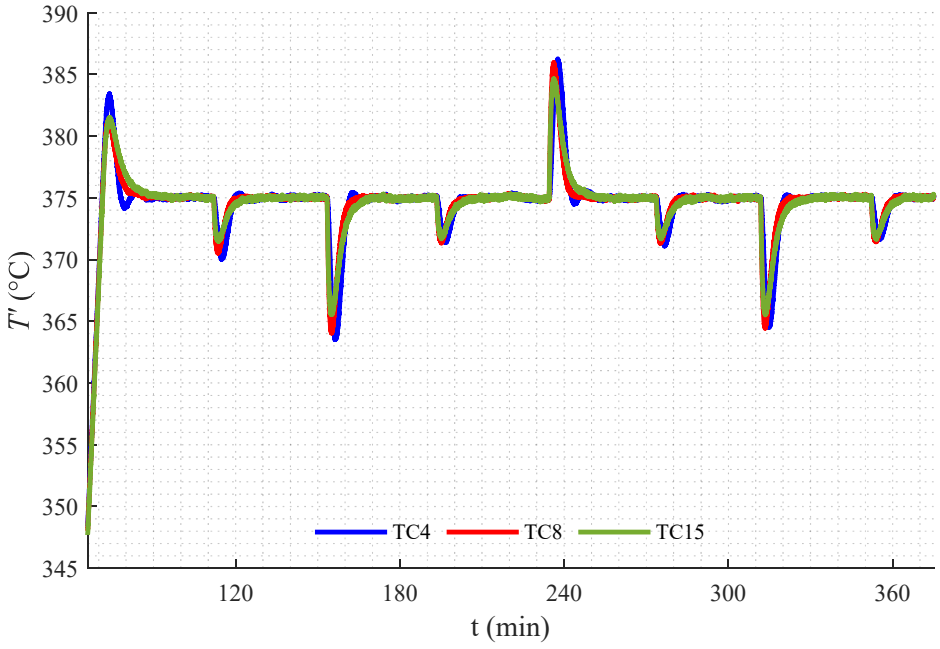

(b)

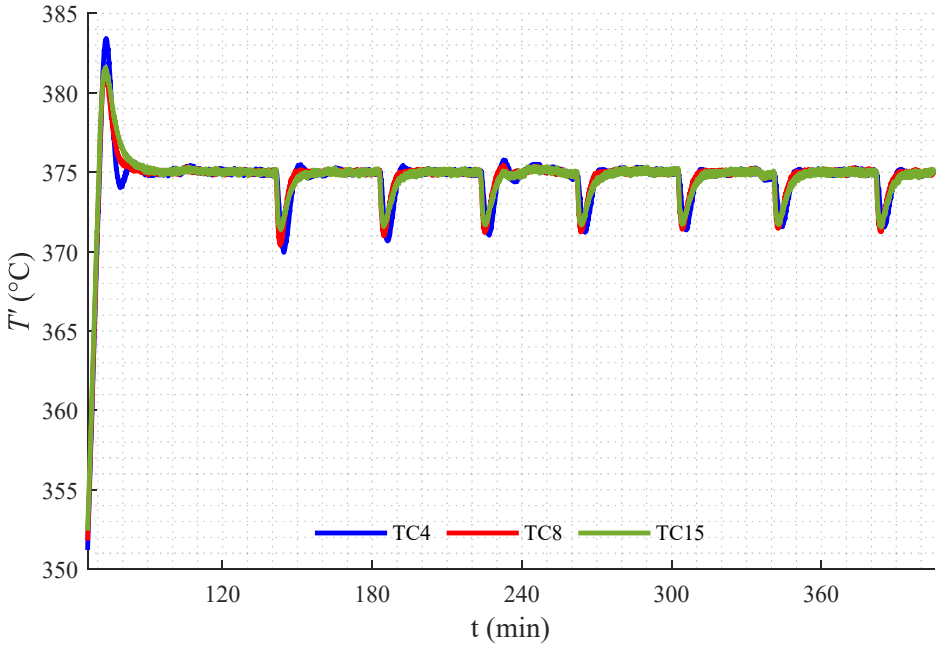

(c)

Figure B. 5 Time series of control thermocouple measurements for (a) run 1, (b) run 2 and (c) run 3 of type C experiment (SM pipe).

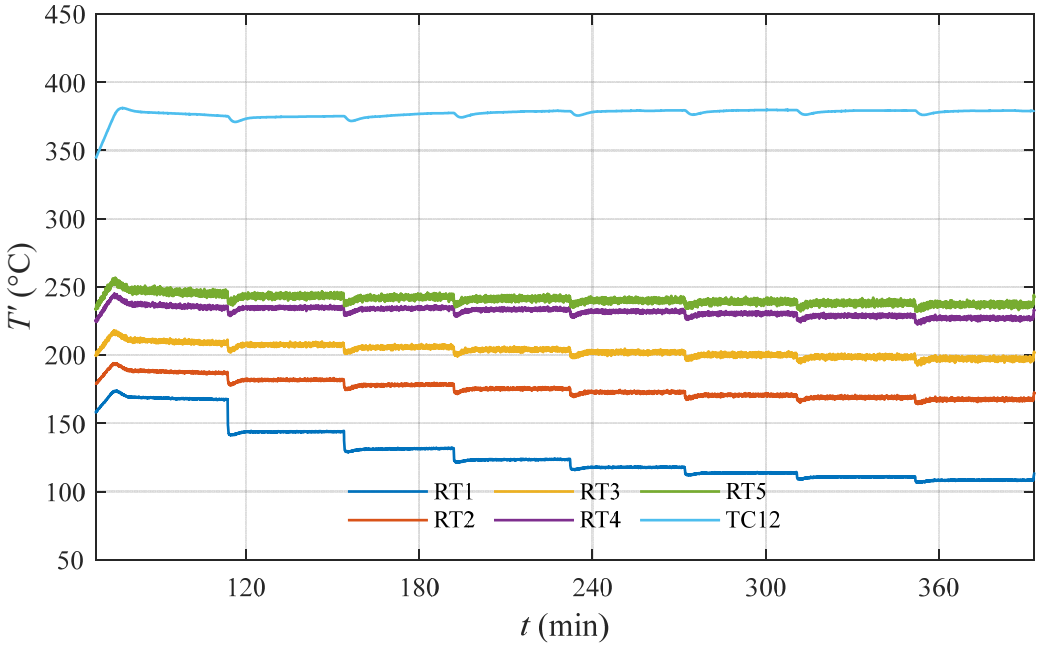
450
400
350
300
250
200
150
100
50
T′ (°C)
120
180
240
300
360
t (min)
RT1
RT3
RT5
RT2
RT4
TC12

(a)

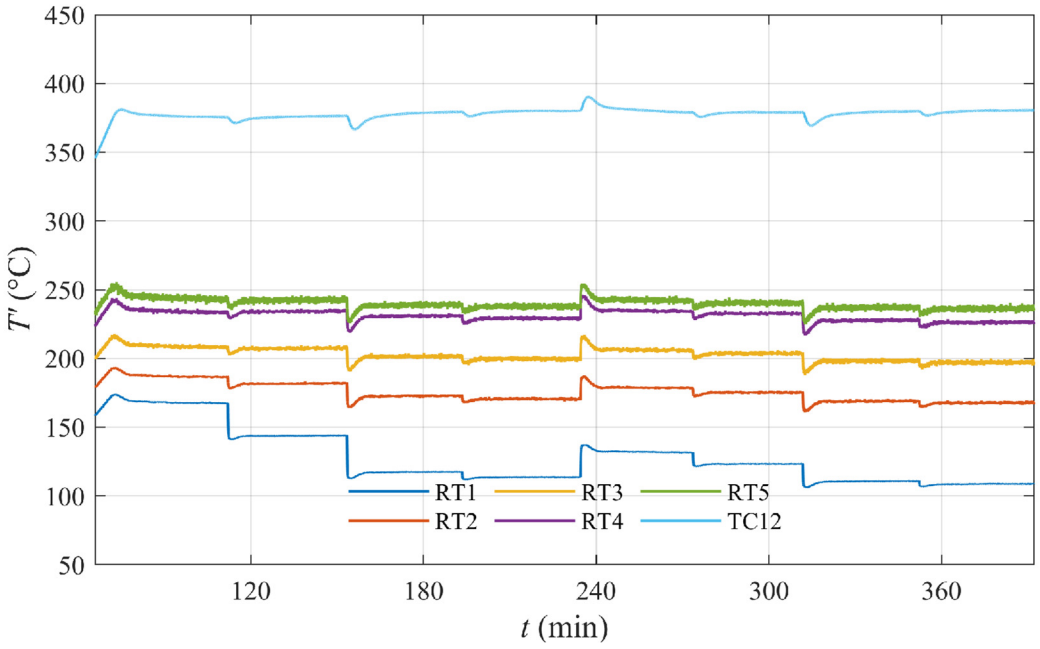
450
400
350
300
250
200
150
100
50
T′ (°C)
120
180
240
300
360
t (min)
RT1
RT3
RT5
RT2
RT4
TC12

(b)

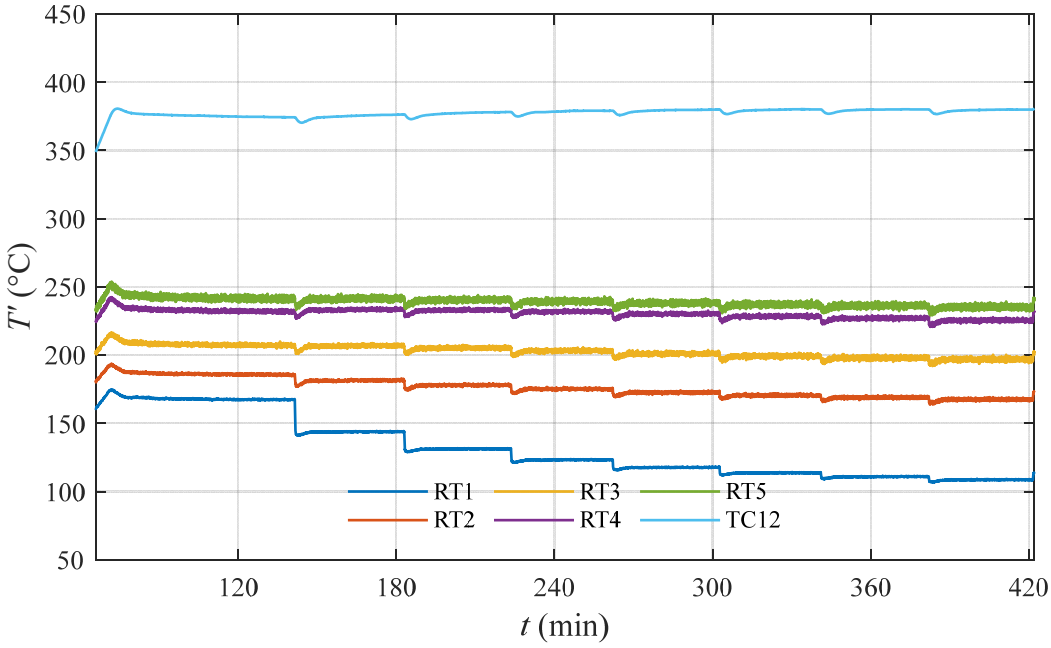

(c)

Figure B. 6 Time series of rake one measurements for (a) run 1, (b) run 2 and (c) run 3 of type C experiment (SM pipe).

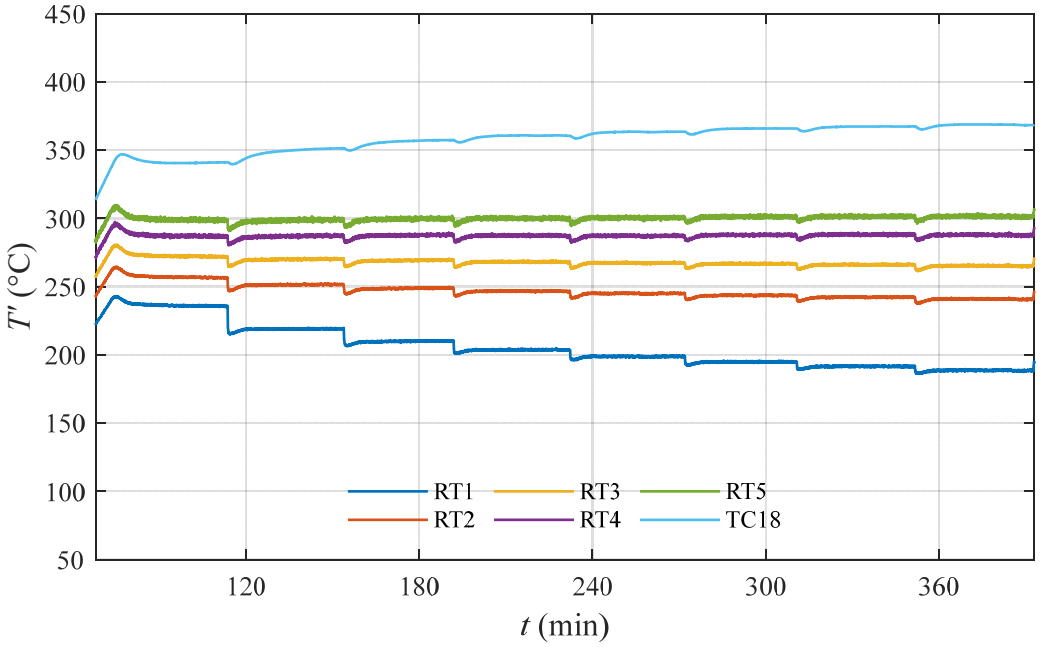

(a)

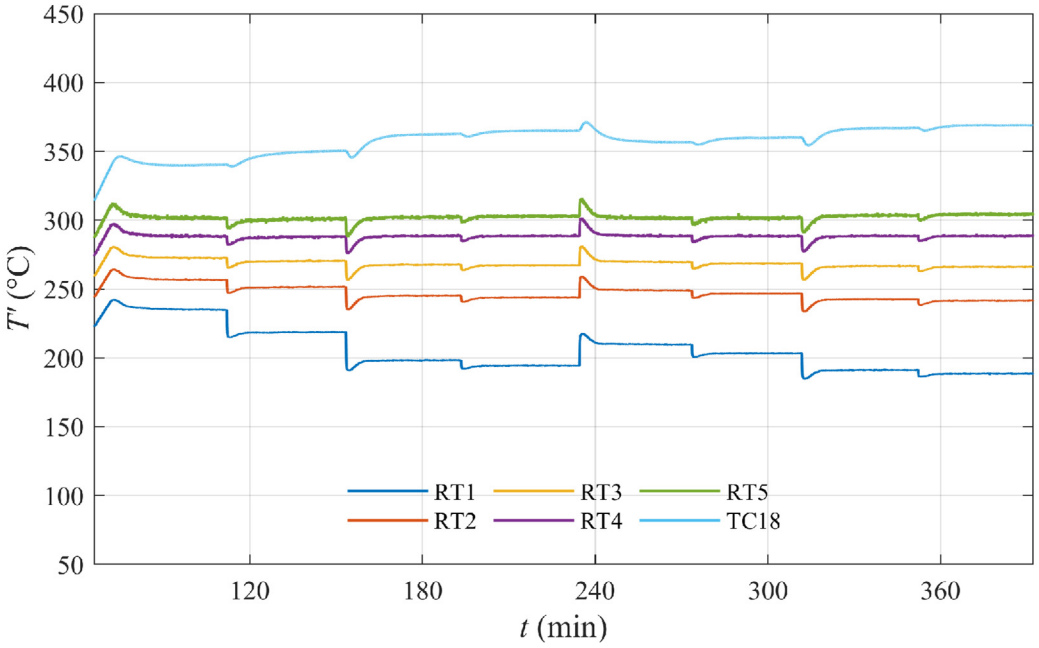

(b)

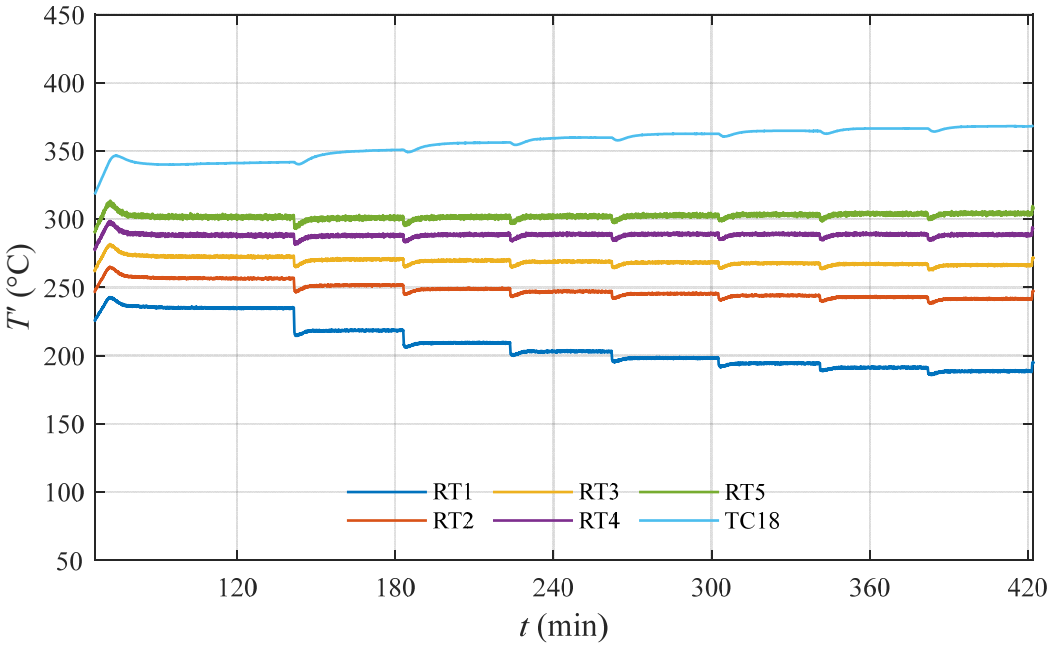

(c)

Figure B. 7 Time series of rake two measurements for (a) run 1, (b) run 2 and (c) run 3 of type C experiment (SM pipe).

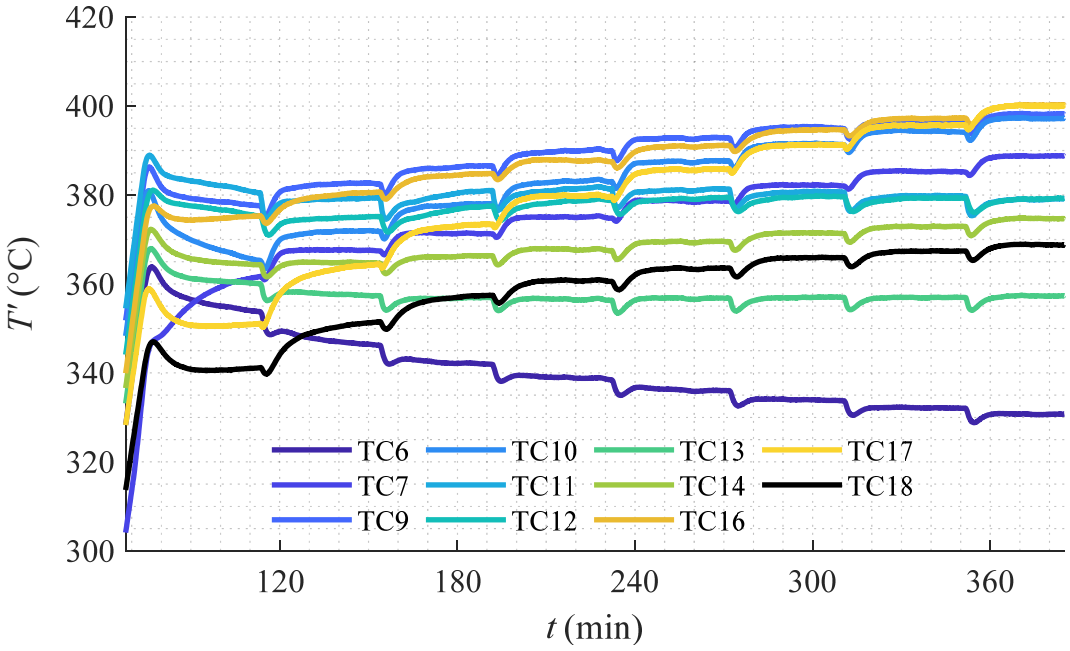
420
400
380
360
340
320
300
T′ (°C)
120
180
240
300
360
t (min)
TC6
TC7
TC9
TC10
TC11
TC12
TC13
TC14
TC16
TC17
TC18

(a)

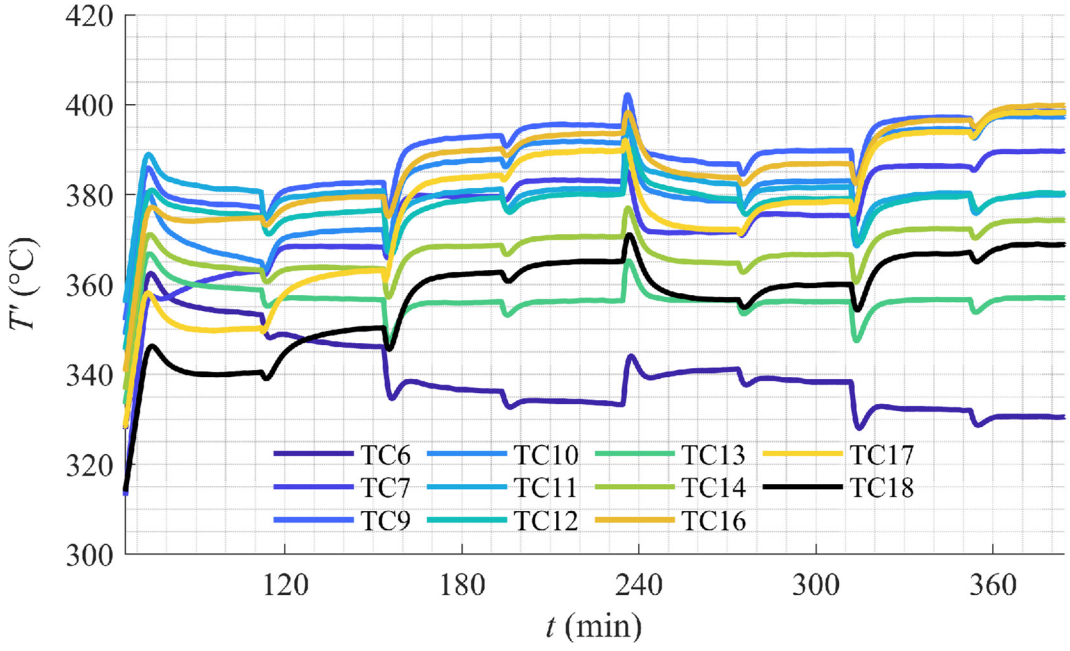
420
400
380
360
340
320
300
T′ (°C)
120
180
240
300
360
t (min)
TC6
TC7
TC9
TC10
TC11
TC12
TC13
TC14
TC16
TC17
TC18

(b)

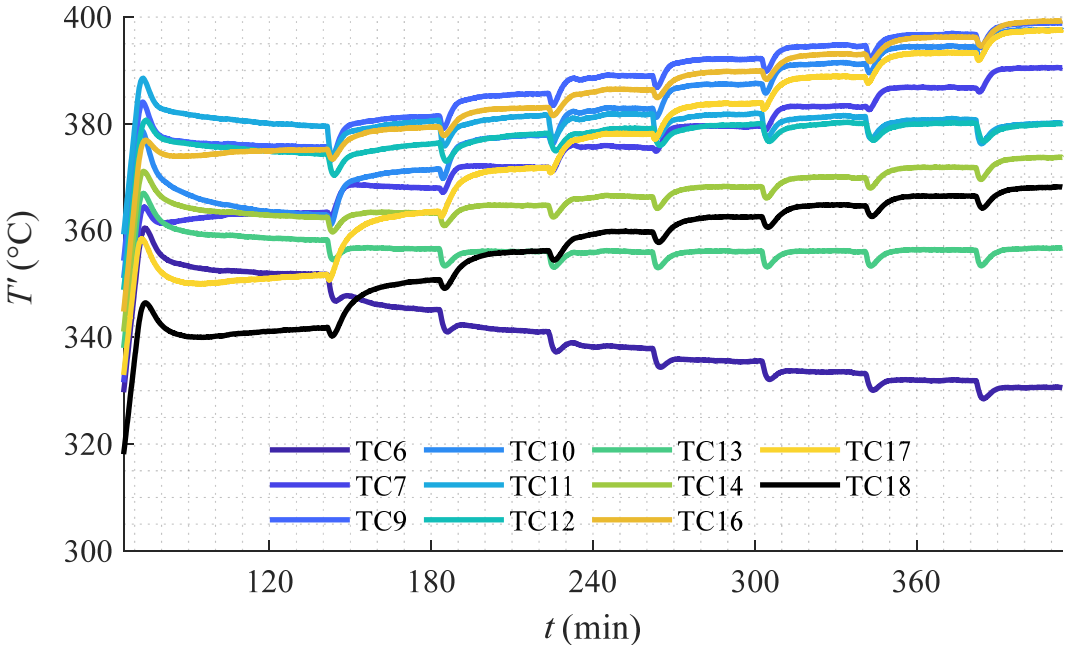

(c)

Figure B. 8 Time series of surface TC measurements for (a) run 1, (b) run 2 and (c) run 3 of type C experiment (SM pipe).

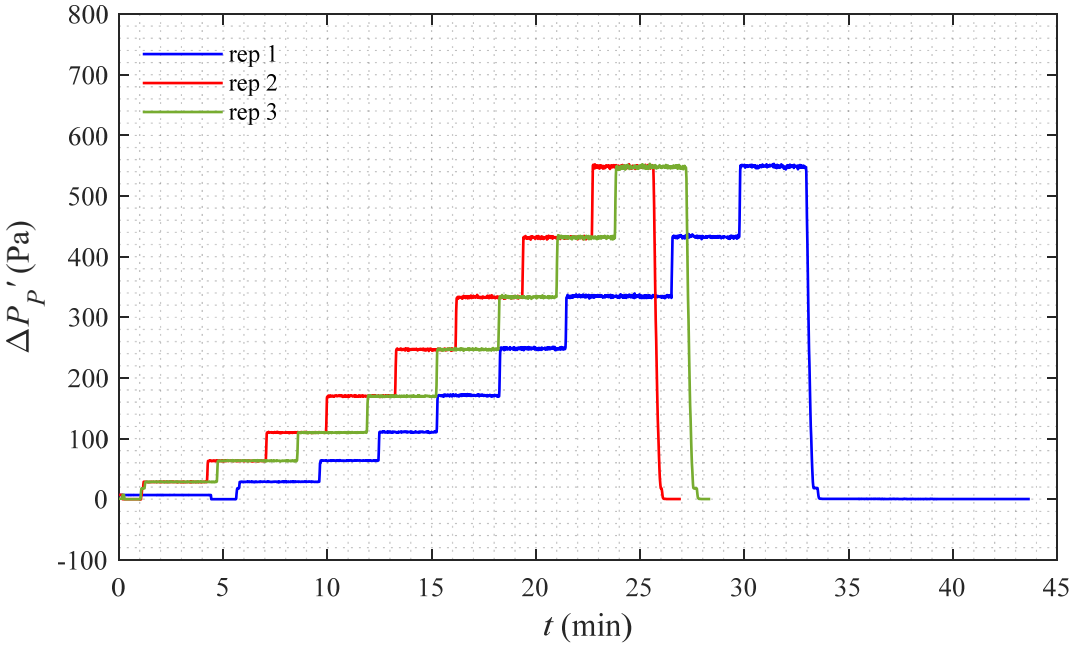

Figure B. 9 Changes of Pitot tube differential pressure over time for type A experiment (MC1 pipe).

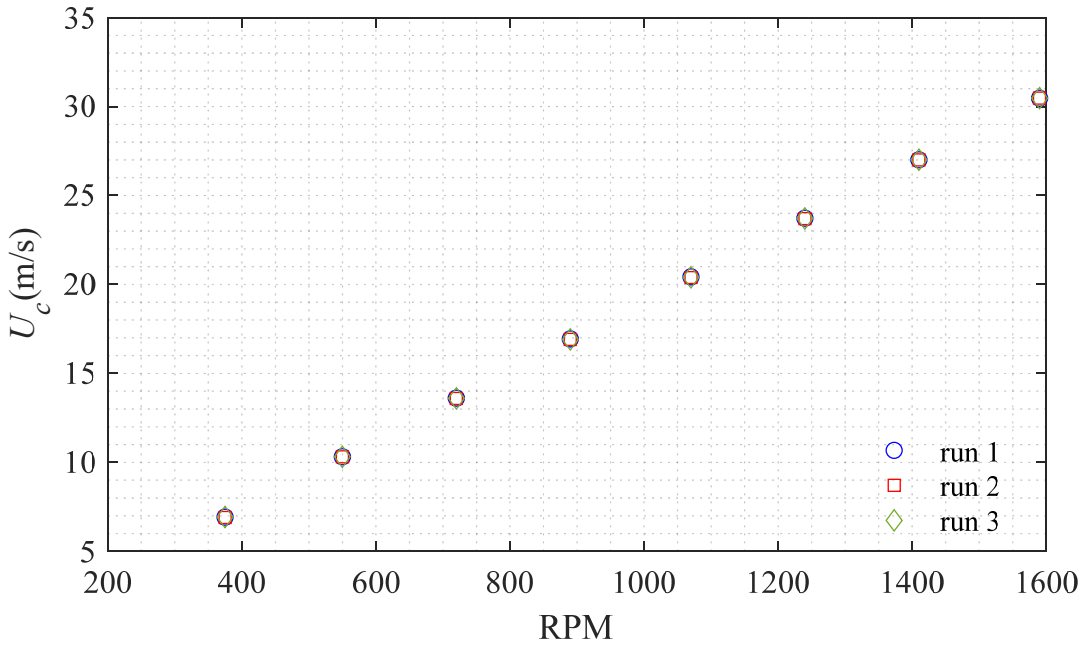

Figure B. 10 Variations of centerline velocity for different RPMs for type A experiment (MC1 pipe).

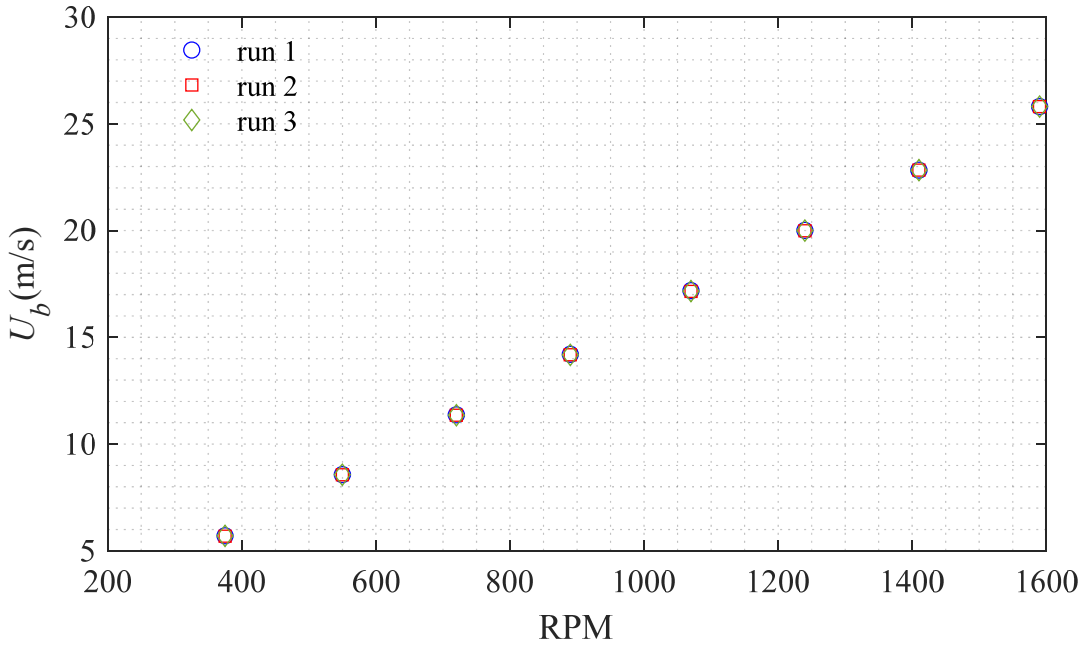

Figure B. 11 Bulk velocity changes with RPM for type A experiment (MC1 pipe).

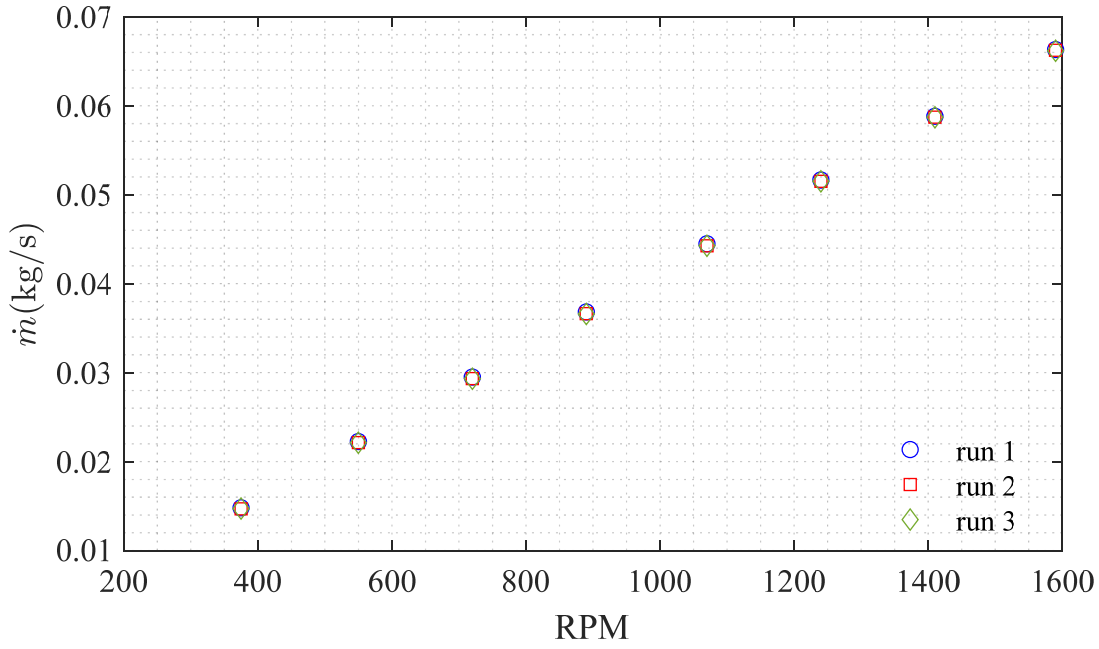

Figure B. 12 Changes of mass flow rate with RPM for type A experiment (MC1 pipe).

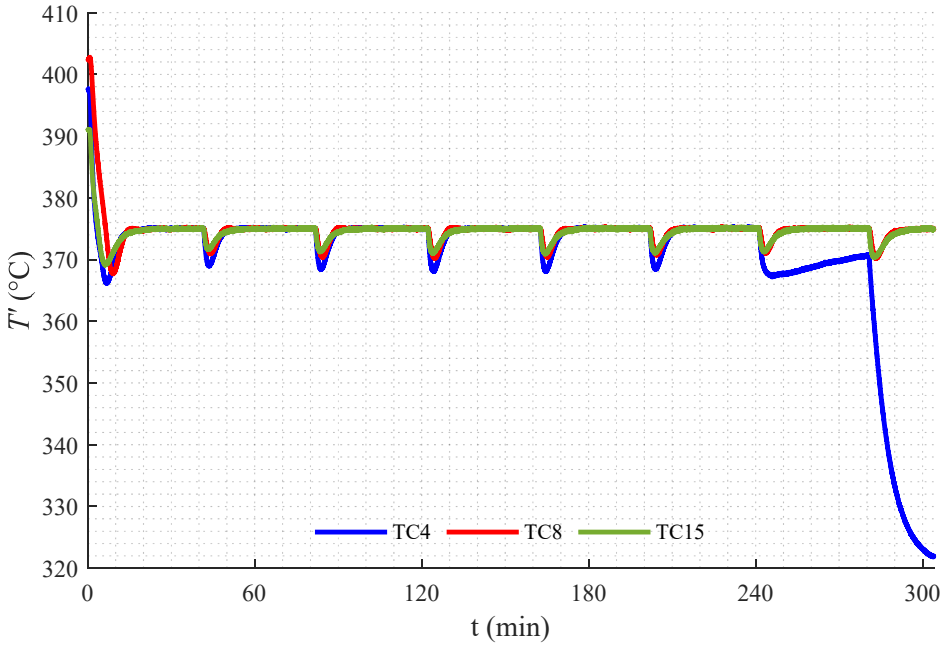
410
400
390
380
370
360
350
340
330
320
T′ (°C)
0
60
120
180
240
300
t (min)
TC4
TC8
TC15

(a)

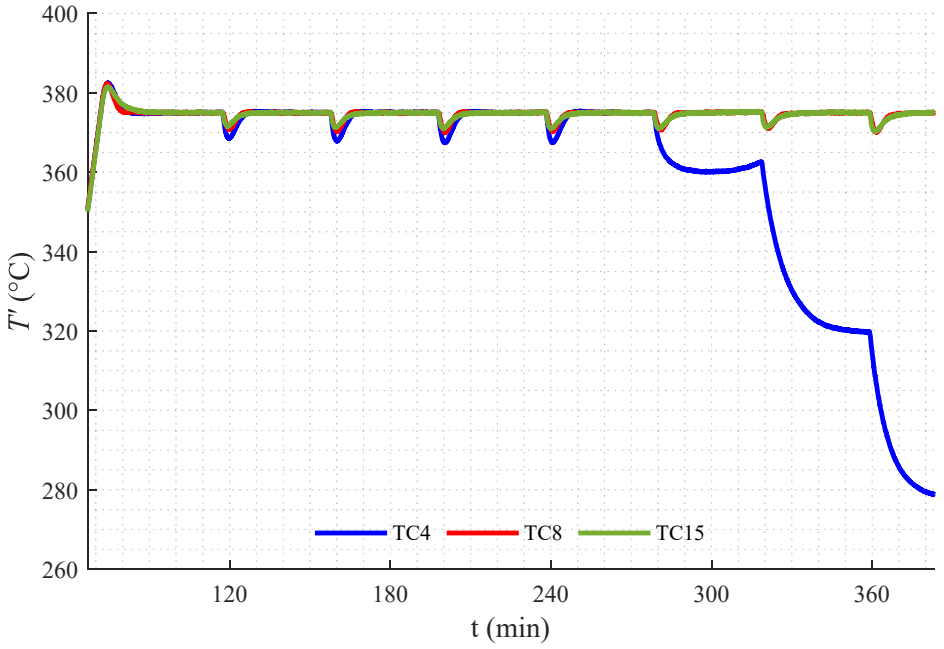
400
380
360
340
320
300
280
260
T′ (°C)
120
180
240
300
360
t (min)
TC4
TC8
TC15

(b)

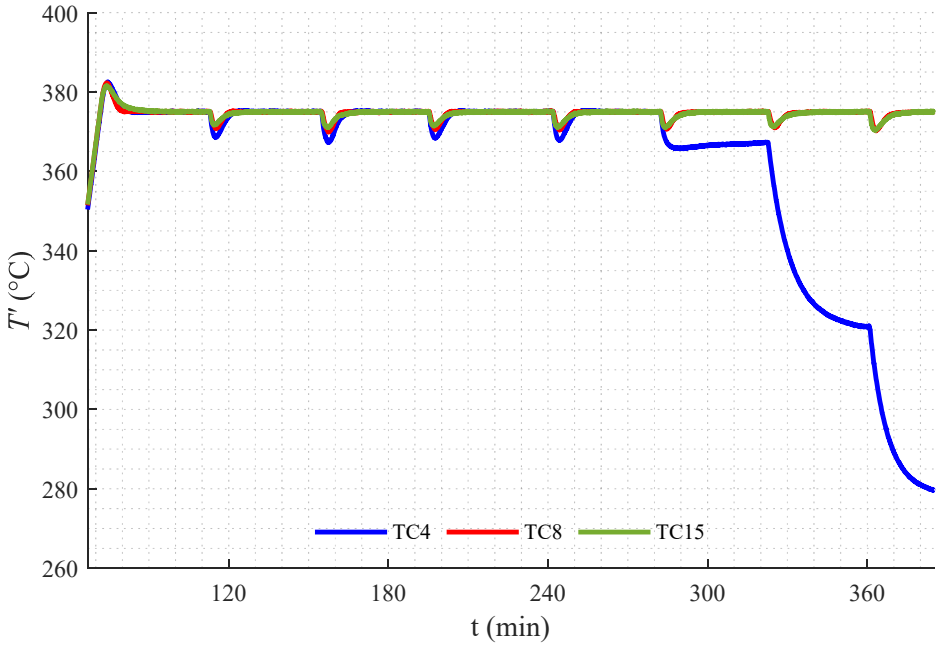

(c)

Figure B. 13 Time series of control thermocouple measurements for (a) run 1, (b) run 2 and (c) run 3 of type C experiment (MC1 pipe).

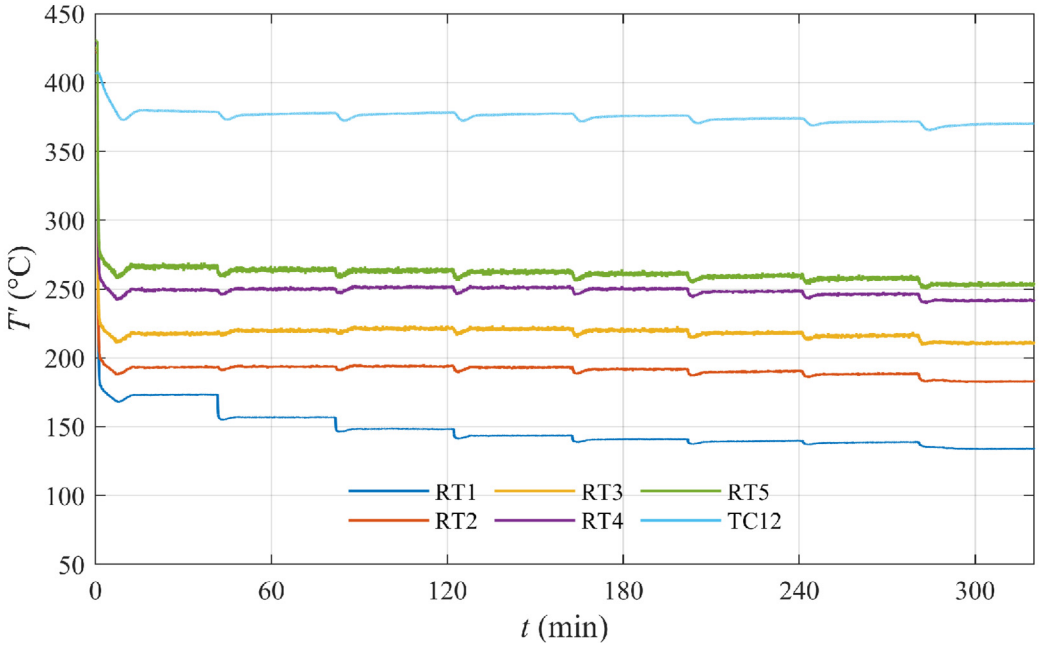
450
400
350
300
250
200
150
100
50
T′ (°C)
0
60
120
180
240
300
t (min)
RT1
RT2
RT3
RT4
RT5
TC12

(a)

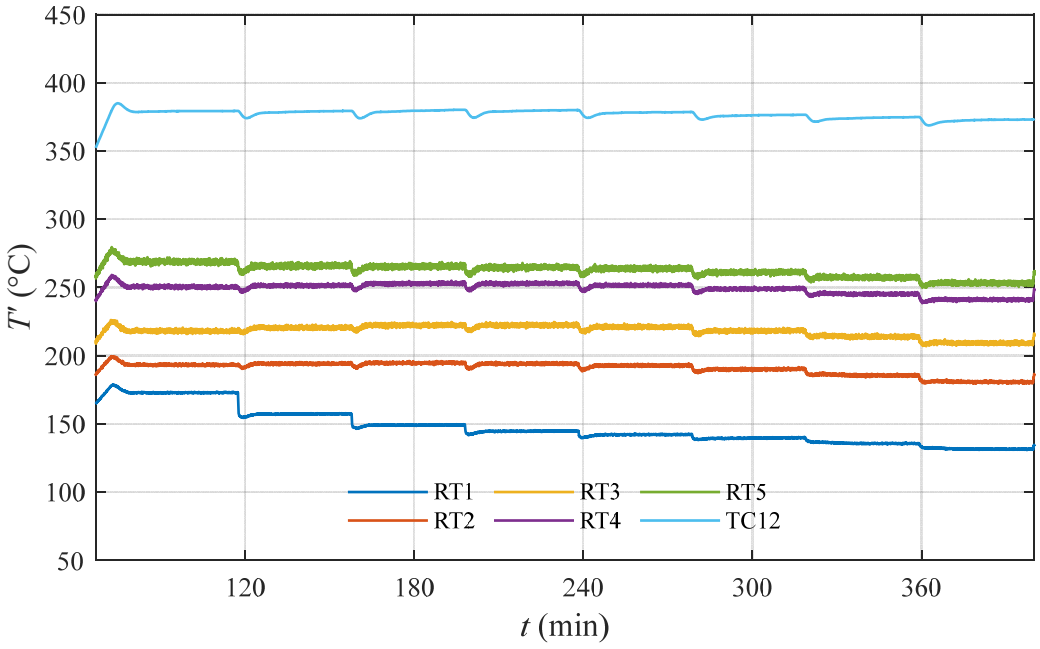
450
400
350
300
250
200
150
100
50
T′ (°C)
120
180
240
300
360
t (min)
RT1
RT2
RT3
RT4
RT5
TC12

(b)

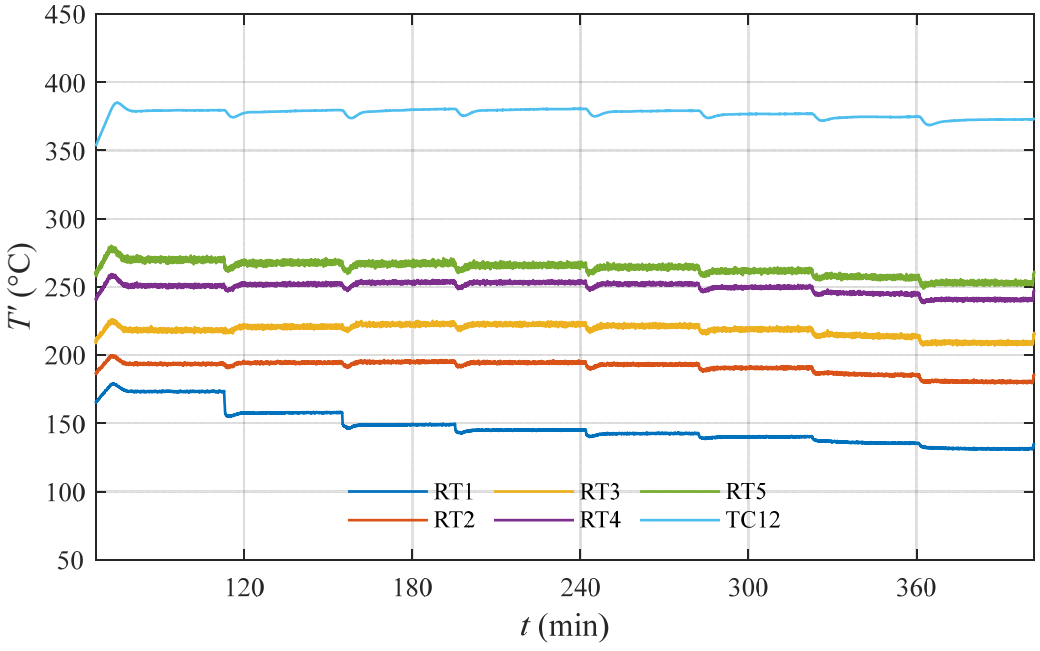

(c)

Figure B. 14 Time series of rake one measurements for (a) run 1, (b) run 2 and (c) run 3 of type C experiment (MC1 pipe).

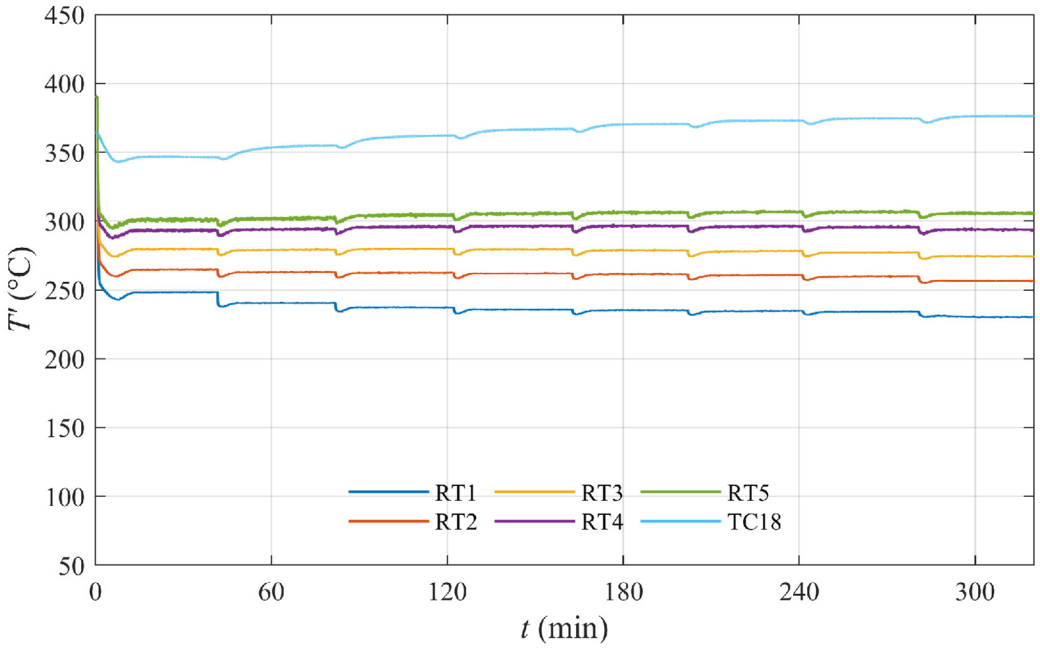

(a)

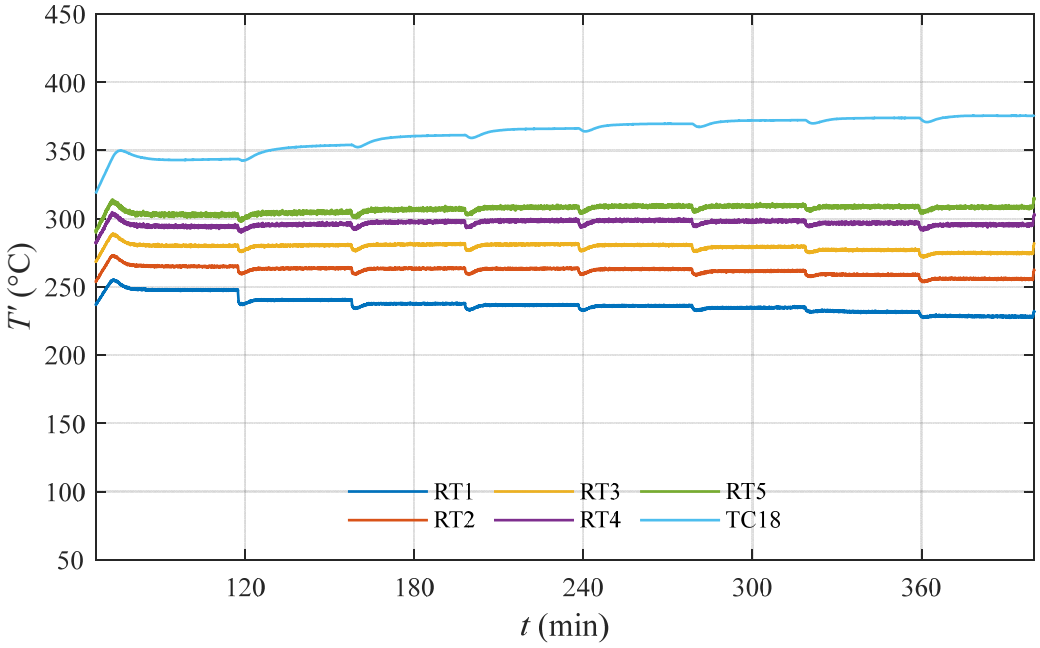

(b)

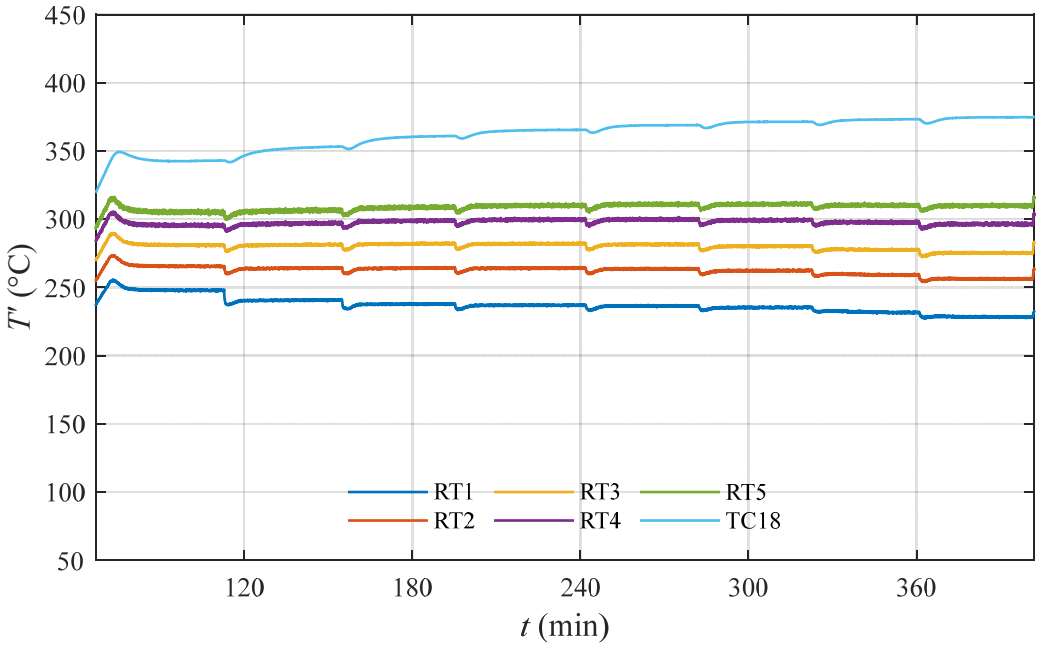

(c)

Figure B. 15 Time series of rake two measurements for (a) run 1, (b) run 2 and (c) run 3 of type C experiment (MC1 pipe).

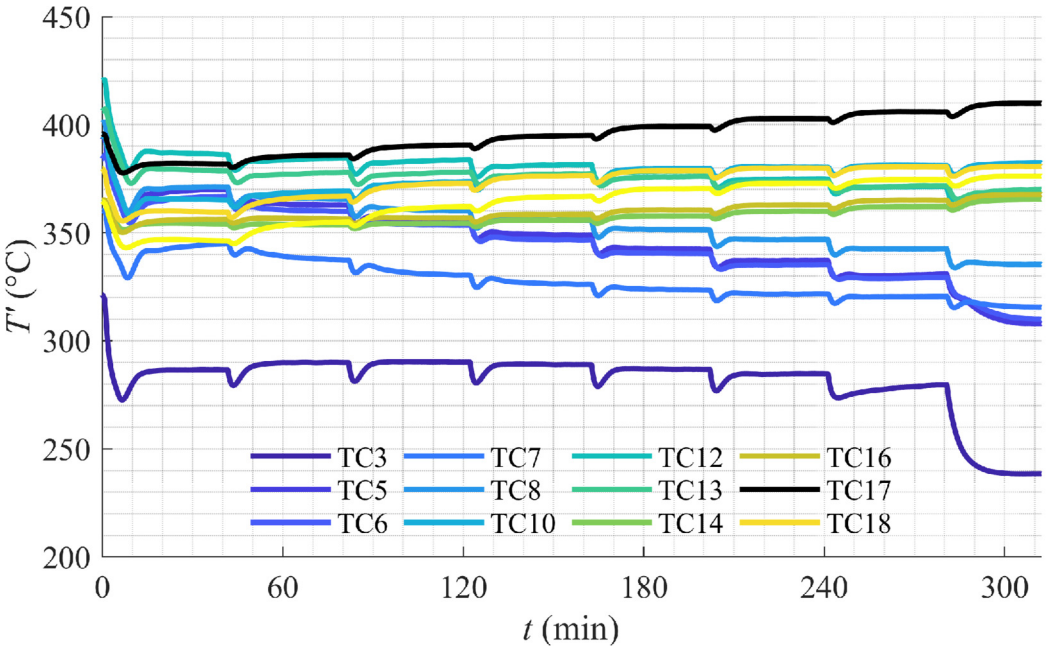
450
400
350
300
250
200
T′ (°C)
0
60
120
180
240
300
t (min)
TC3
TC5
TC6
TC7
TC8
TC10
TC12
TC13
TC14
TC16
TC17
TC18

(a)

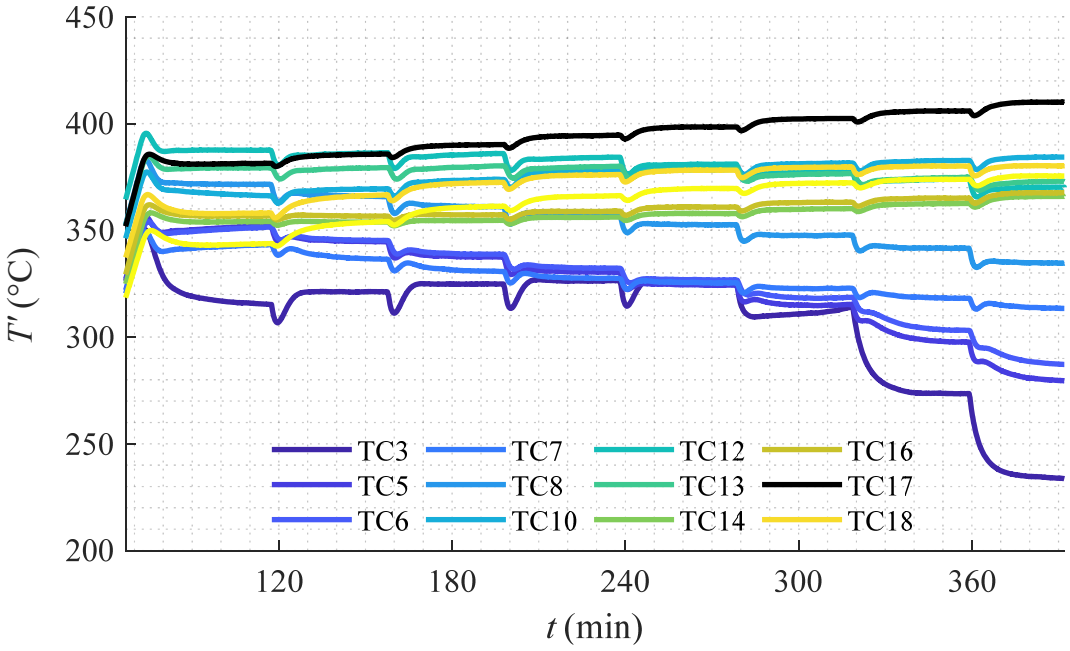
450
400
350
300
250
200
T′ (°C)
120
180
240
300
360
t (min)
TC3
TC5
TC6
TC7
TC8
TC10
TC12
TC13
TC14
TC16
TC17
TC18

(b)

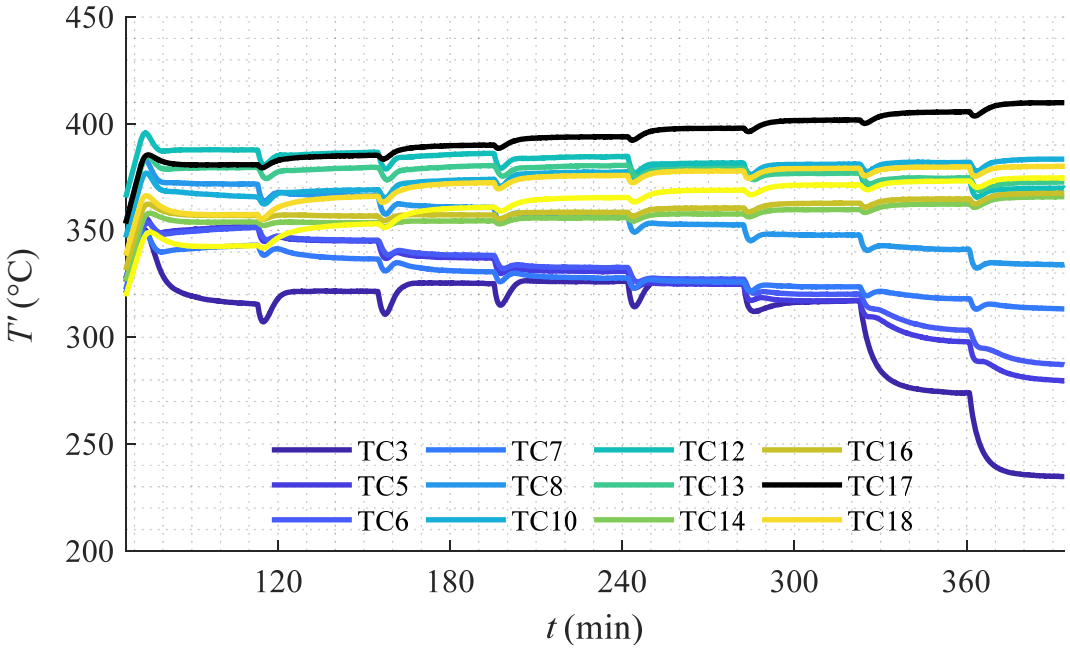

(c)

Figure B. 16 Time series of surface TC measurements for (a) run 1, (b) run 2 and (c) run 3 of type C experiment (MC1 pipe).

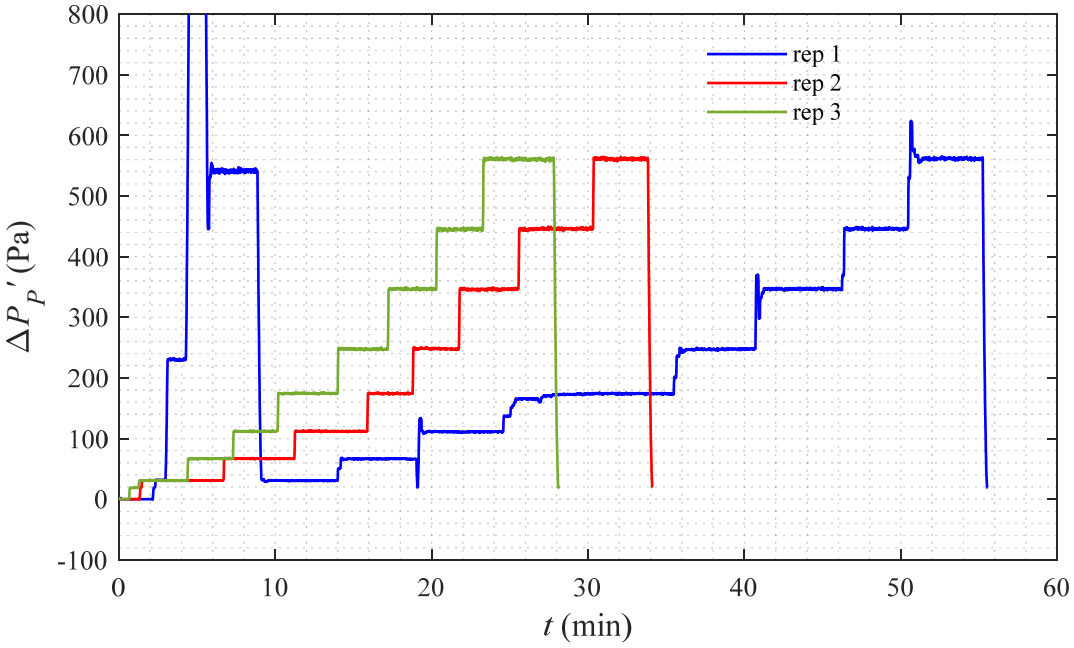

Figure B. 17 Changes of Pitot tube differential pressure over time for type A experiment (MC2 pipe).

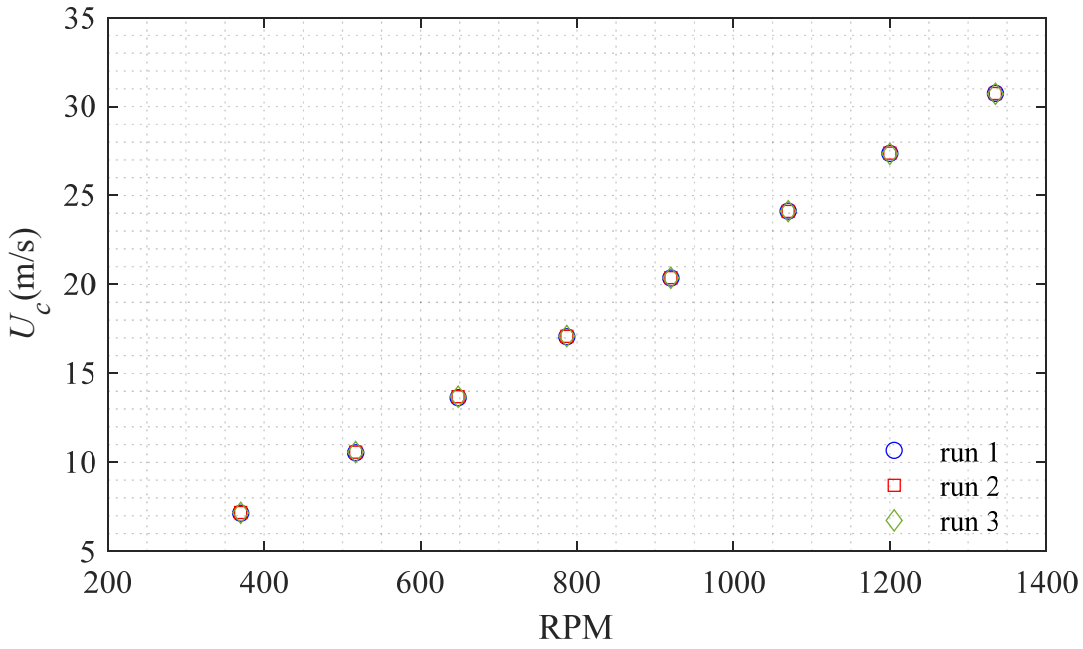

Figure B. 18 Variations of centerline velocity for different RPMs for type A experiment (MC2 pipe).

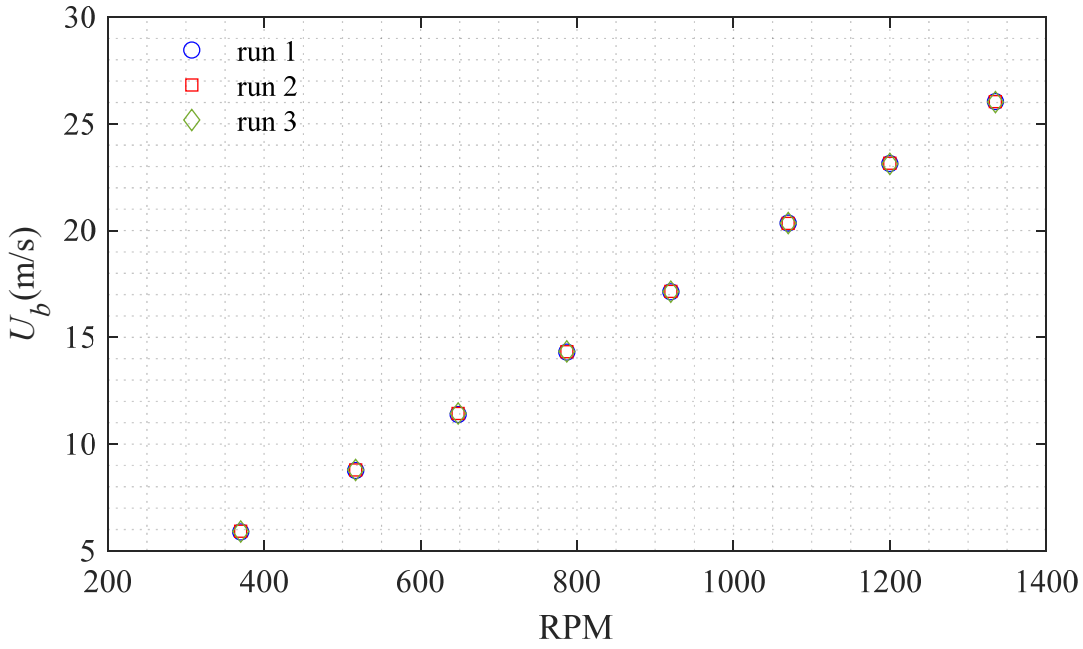

Figure B. 19 Bulk velocity changes with RPM for type A experiment (MC2 pipe).

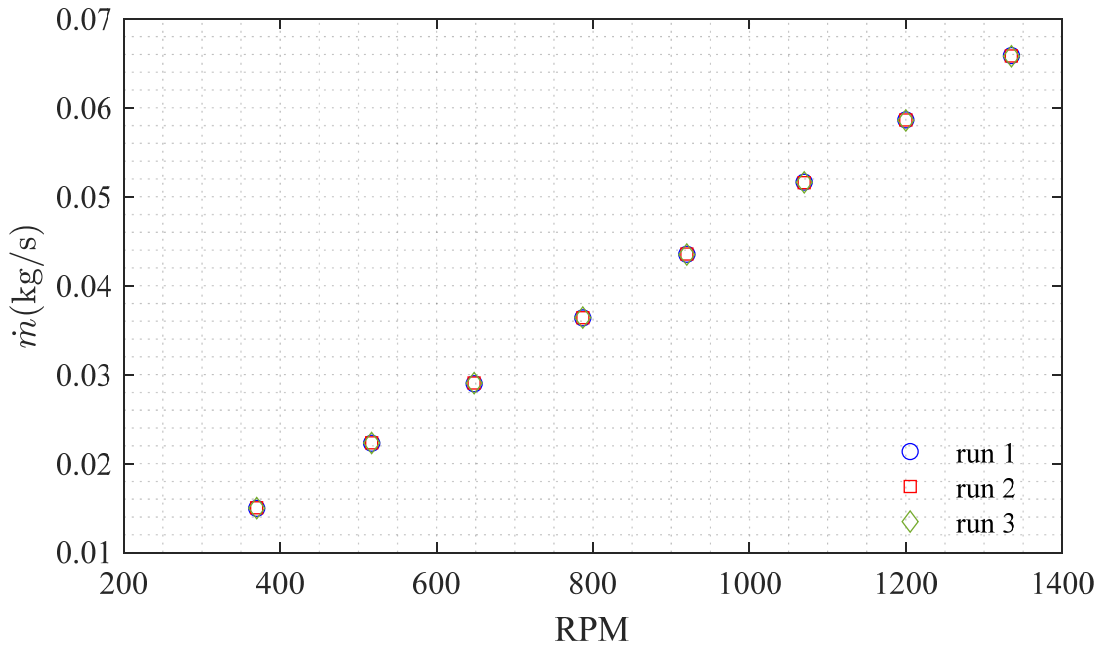

Figure B. 20 Changes of mass flow rate with RPM for type A experiment (MC2 pipe).

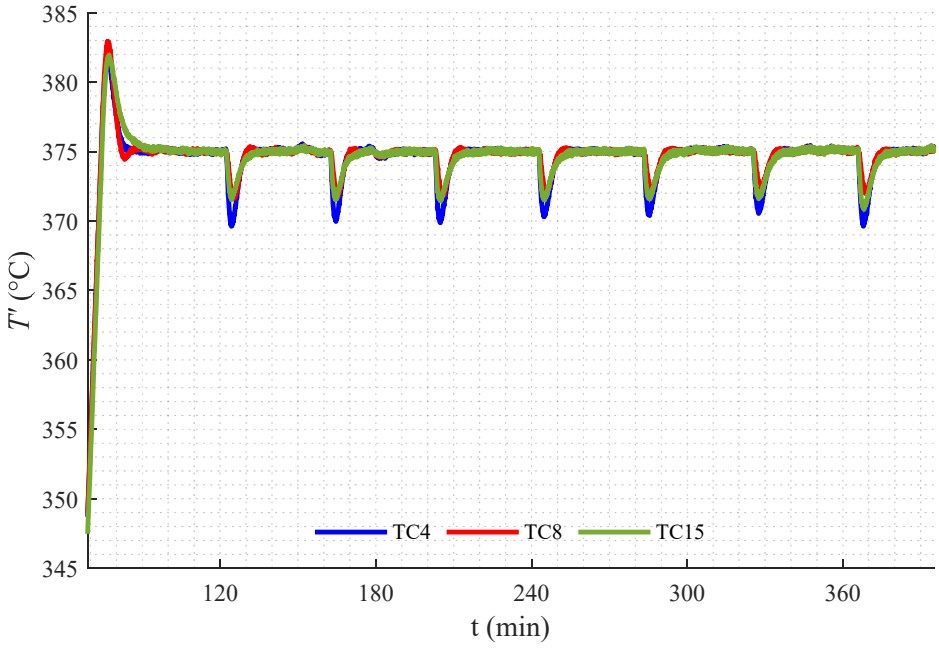
385
380
375
370
365
360
355
350
345
T′ (°C)
120
180
240
300
360
t (min)
TC4
TC8
TC15

(a)

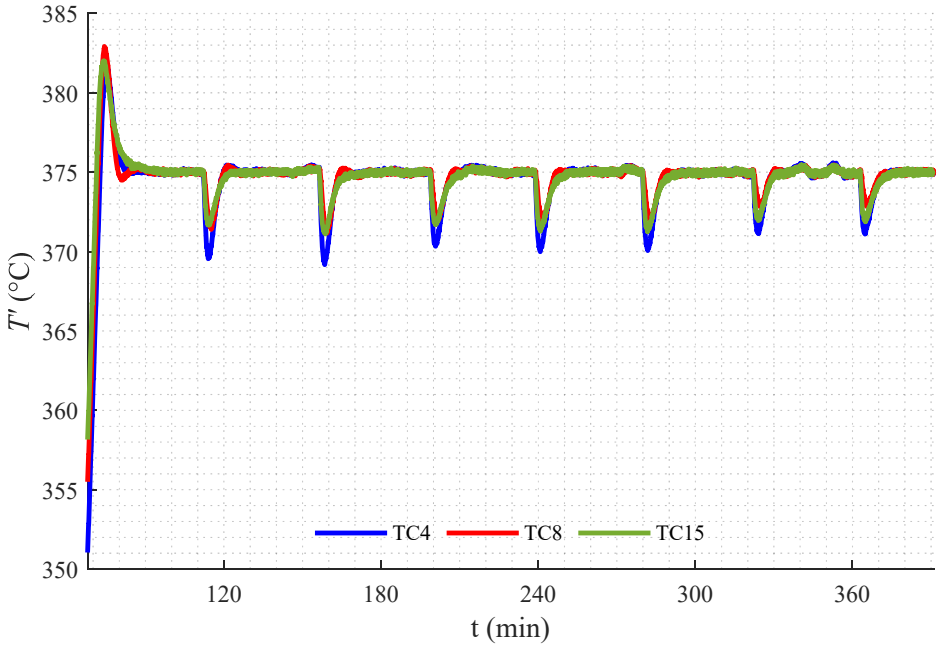
385
380
375
370
365
360
355
350
T′ (°C)
120
180
240
300
360
t (min)
TC4
TC8
TC15

(b)

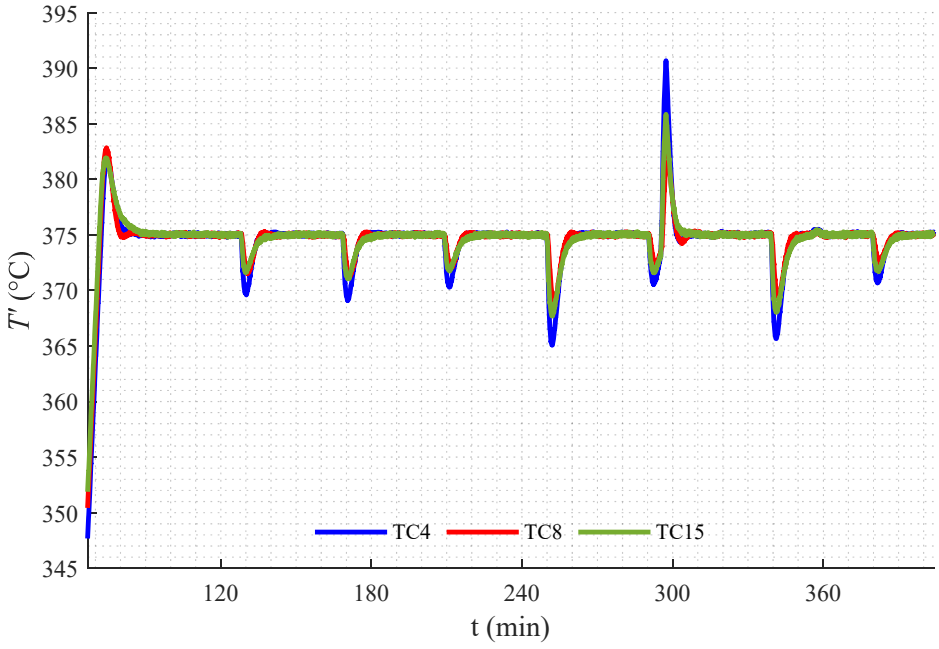

(c)

Figure B. 21 Time series of control thermocouple measurements for (a) run 1, (b) run 2 and (c) run 3 of type C experiment (MC2 pipe).

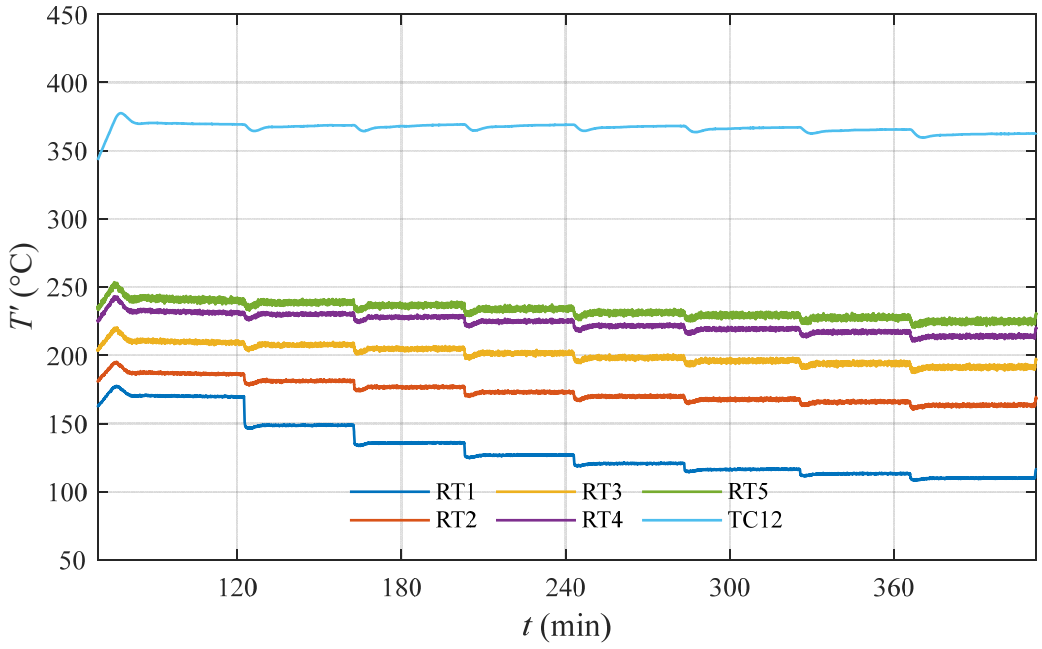

(a)

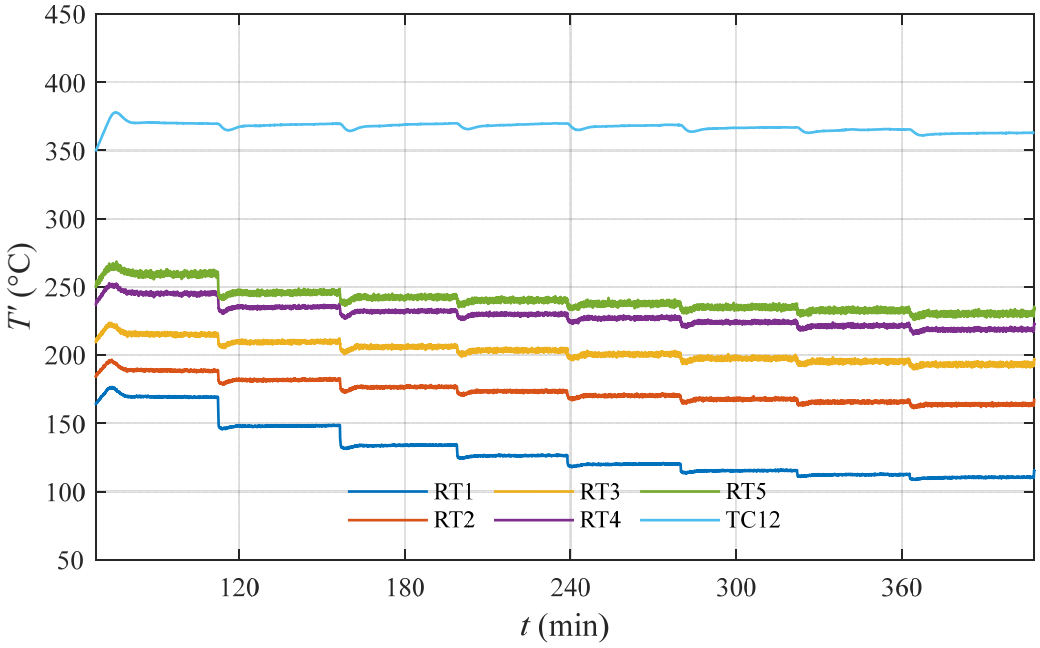

(b)

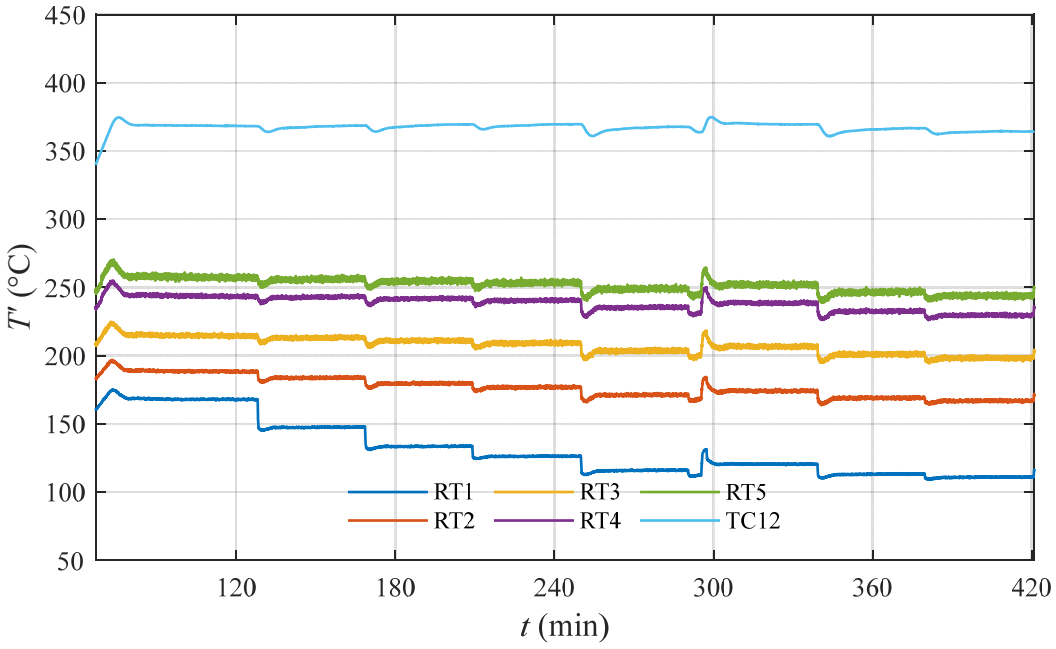

(c)

Figure B. 22 Time series of rake one measurements for (a) run 1, (b) run 2 and (c) run 3 of type C experiment (MC2 pipe).

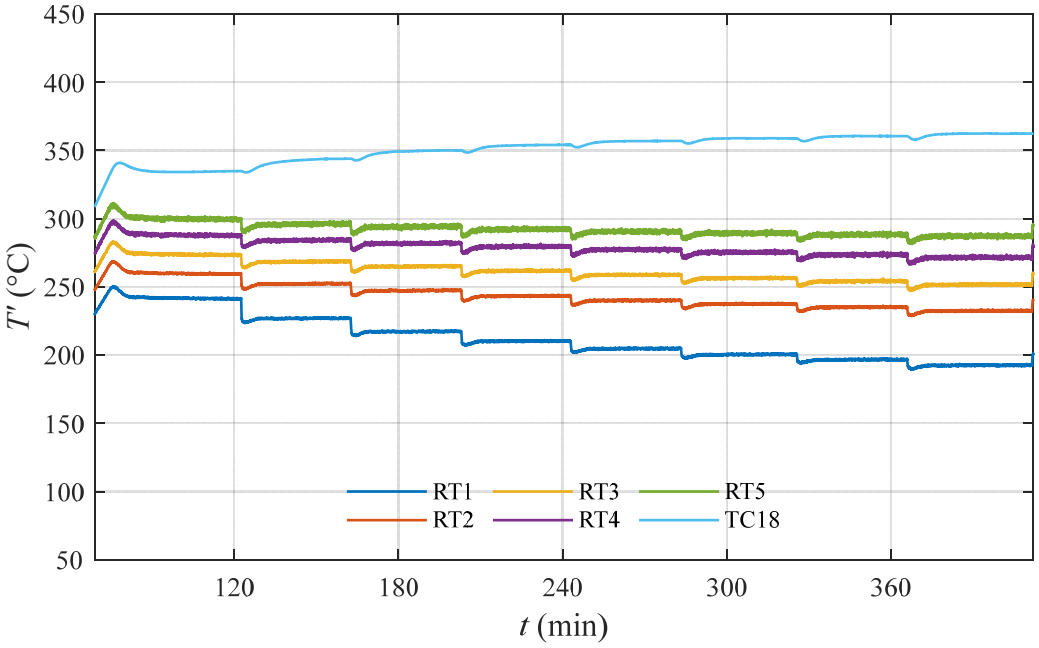
450
400
350
300
250
200
150
100
50
T′ (°C)
120
180
240
300
360
t (min)
RT1
RT2
RT3
RT4
RT5
TC18

(a)

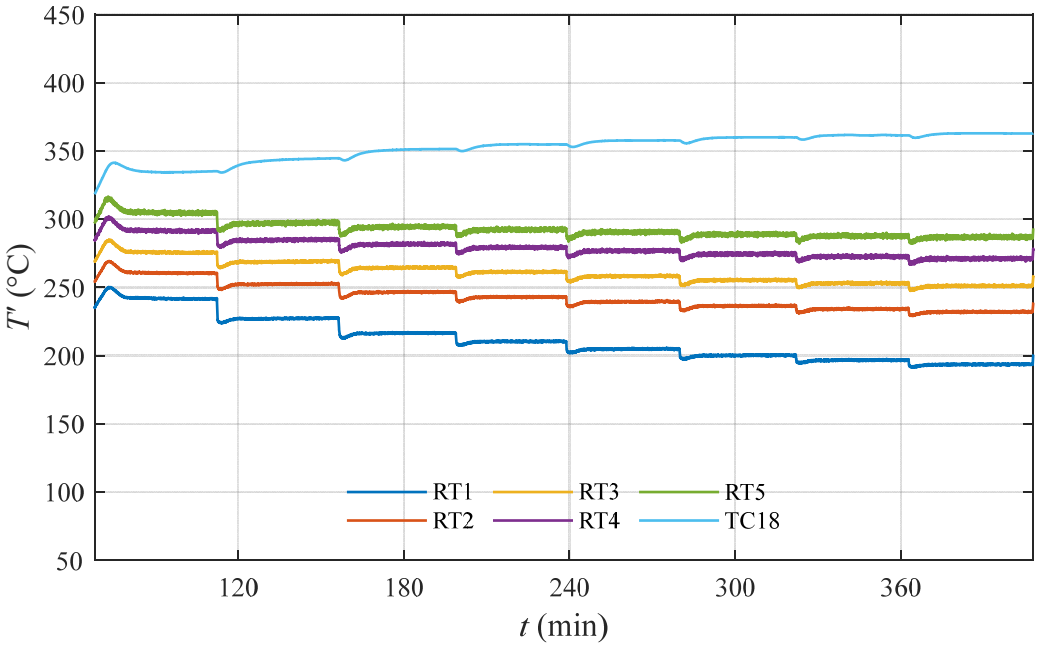
450
400
350
300
250
200
150
100
50
T′ (°C)
120
180
240
300
360
t (min)
RT1
RT2
RT3
RT4
RT5
TC18

(b)

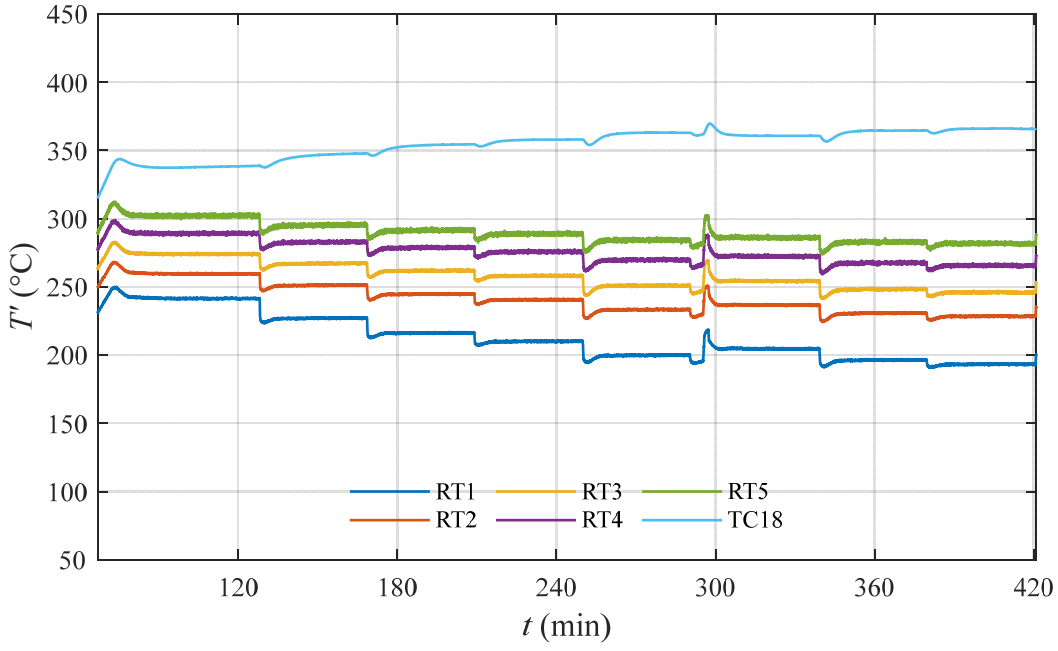

(c)

Figure B. 23 Time series of rake two measurements for (a) run 1, (b) run 2 and (c) run 3 of type C experiment (MC2 pipe).

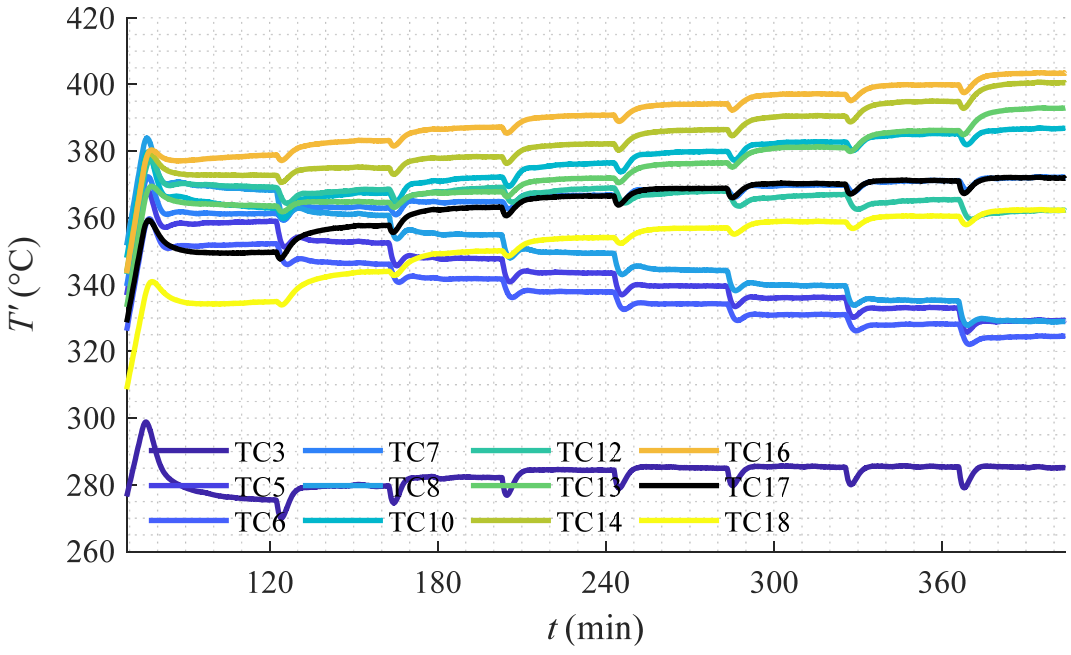

(a)

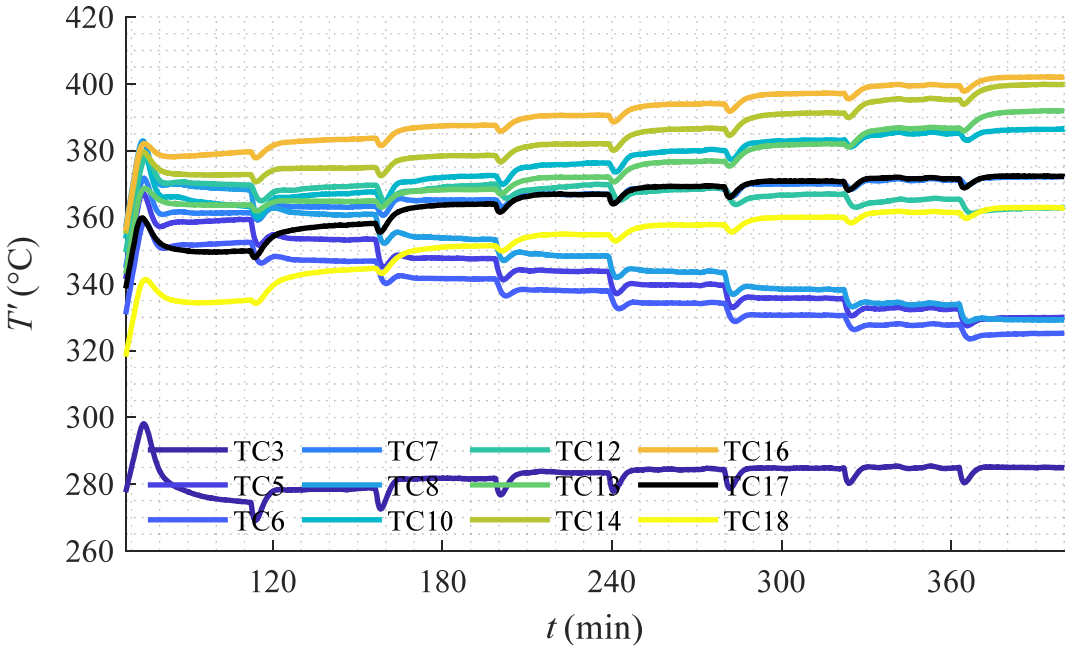

(b)

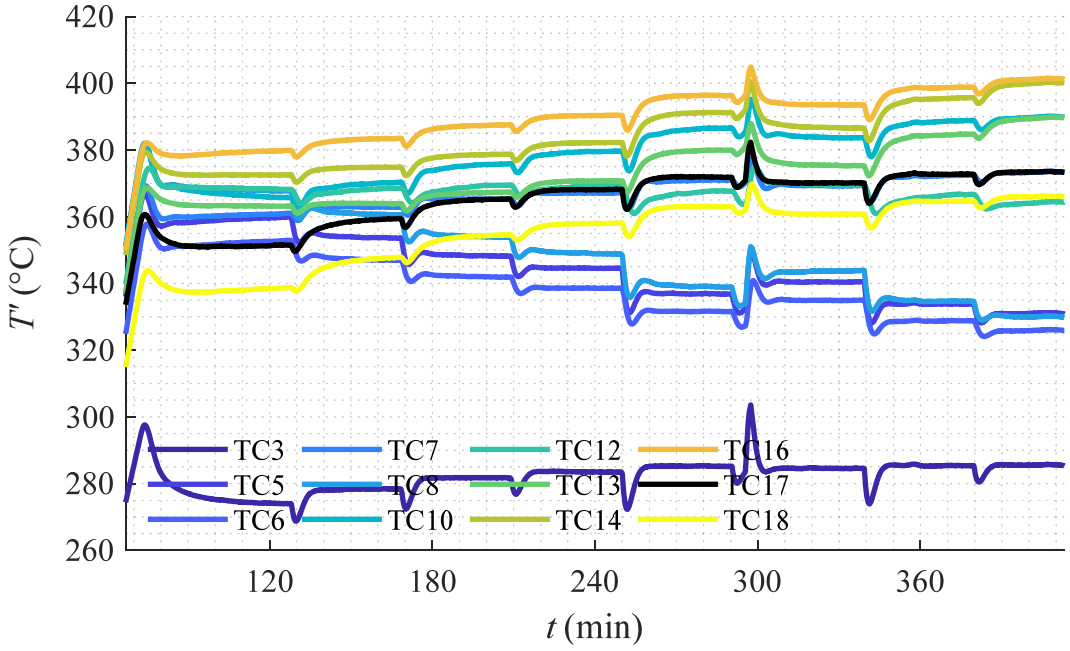

(c)

Figure B. 24 Time series of surface TC measurements for (a) run 1, (b) run 2 and (c) run 3 of type C experiment (MC2 pipe).

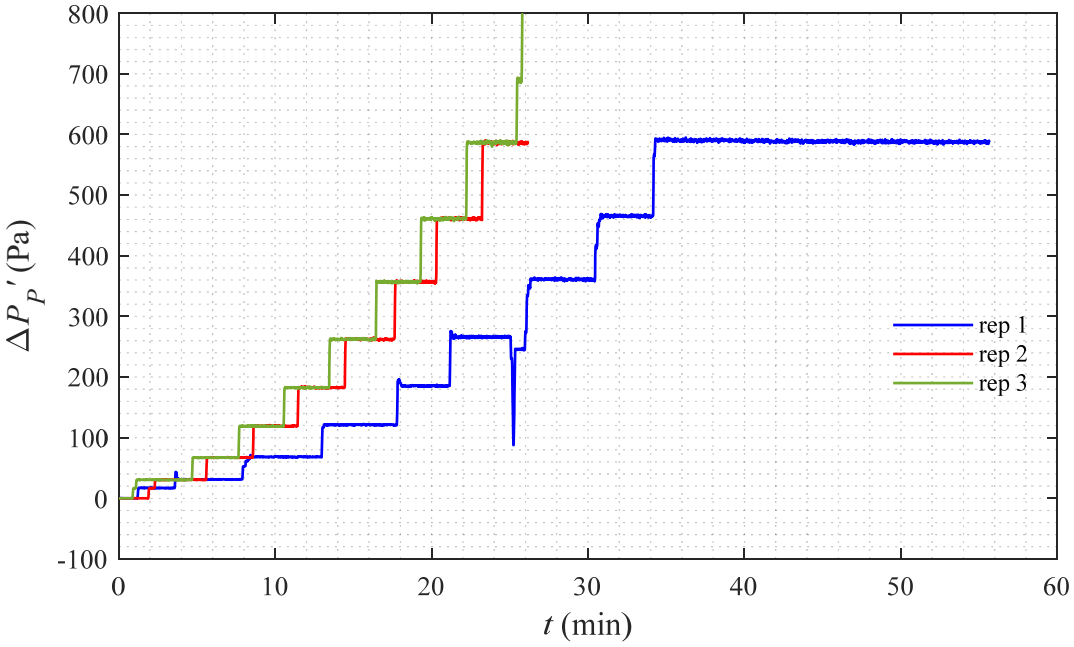

Figure B. 25 Changes of Pitot tube differential pressure over time for type A experiment (MB50 pipe).

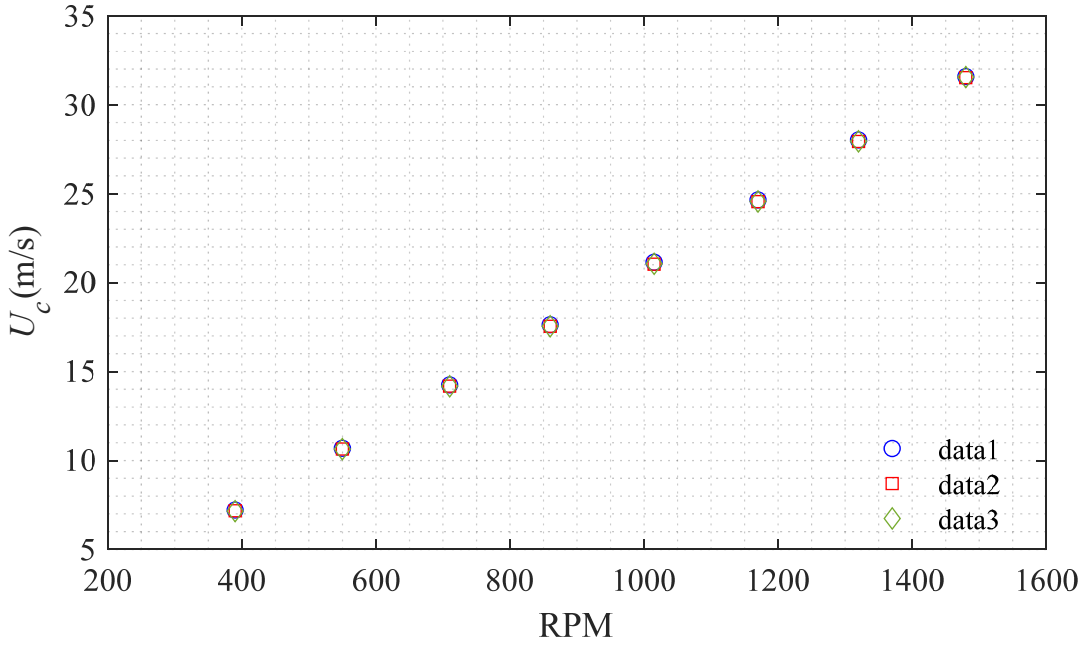

Figure B. 26 Variations of centerline velocity for different RPMs for type A experiment (MB50 pipe).

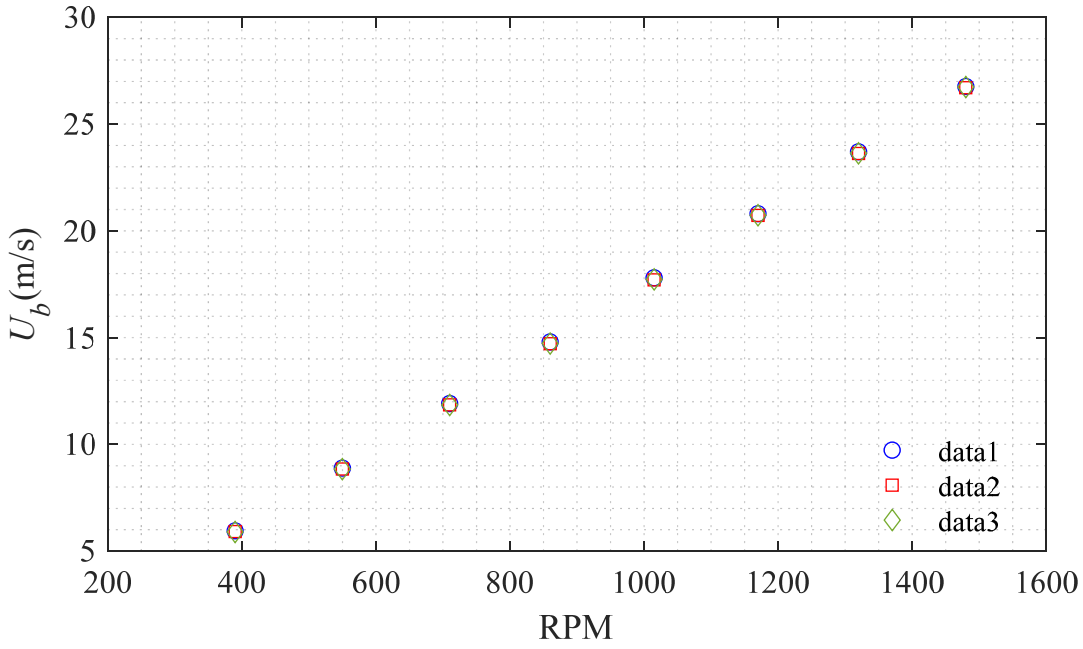

Figure B. 27 Bulk velocity changes with RPM for type A experiment (MB50 pipe).

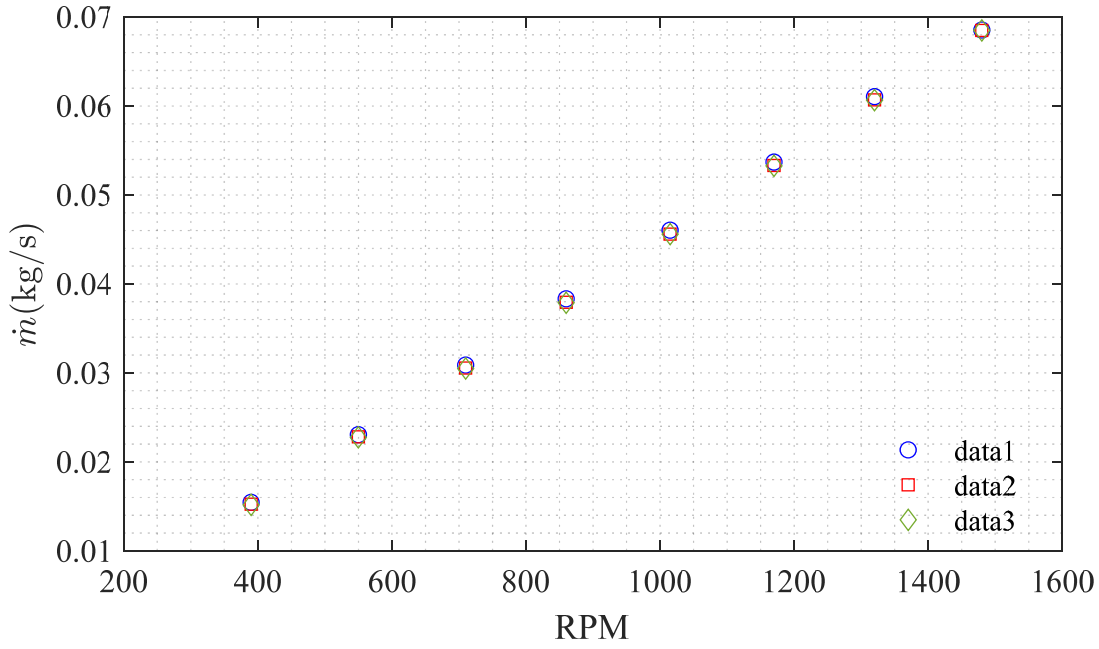

Figure B. 28 Changes of mass flow rate with RPM for type A experiment (MB50 pipe).

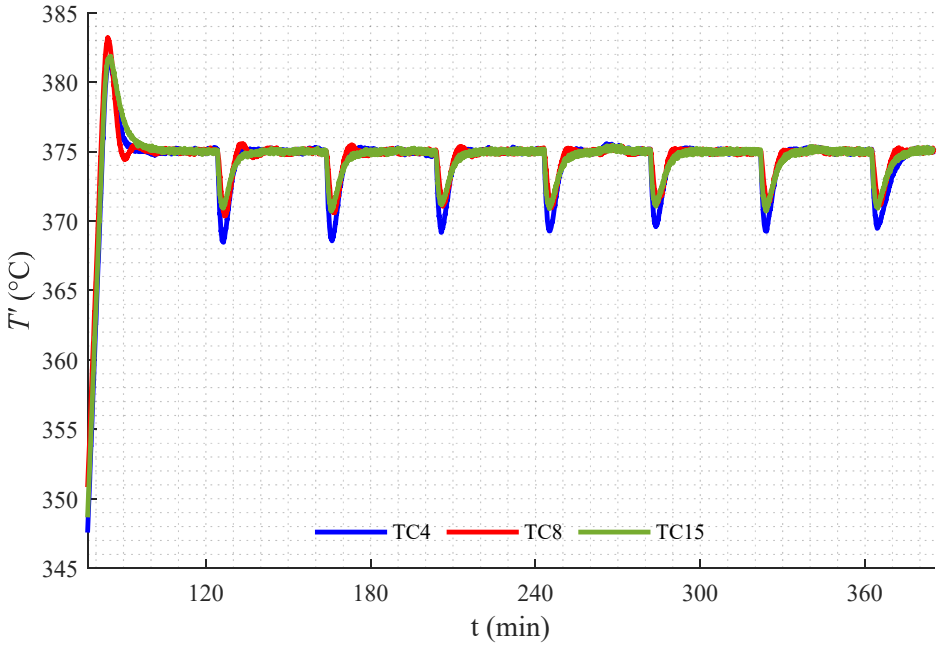
385
380
375
370
365
360
355
350
345
T′ (°C)
120
180
240
300
360
t (min)
TC4
TC8
TC15

(a)

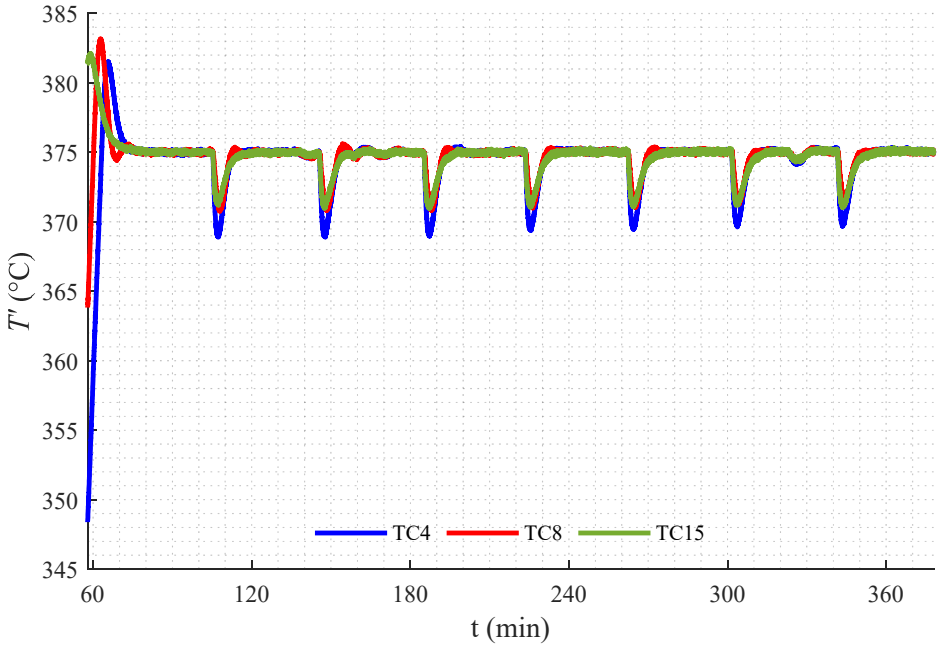
385
380
375
370
365
360
355
350
345
T′ (°C)
60
120
180
240
300
360
t (min)
TC4
TC8
TC15

(b)

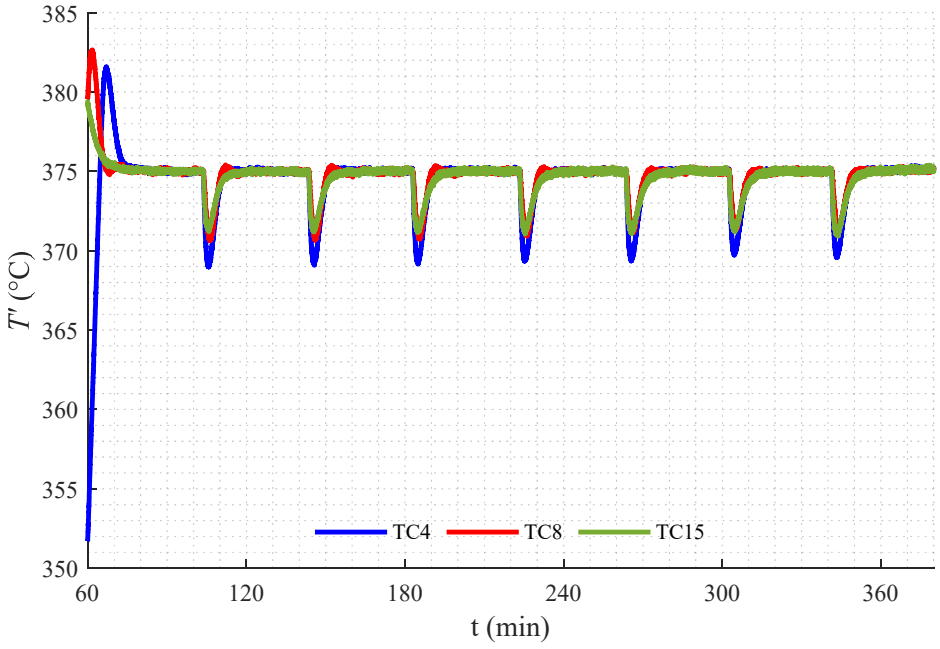

(c)

Figure B. 29 Time series of control thermocouple measurements for (a) run 1, (b) run 2 and (c) run 3 of type C experiment (MB50 pipe).

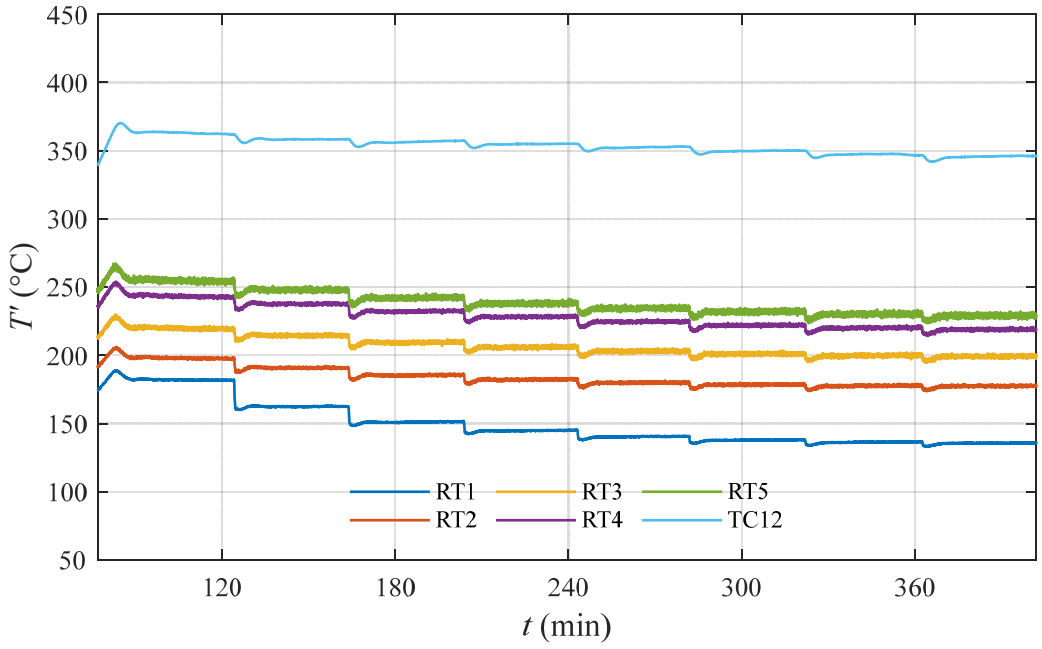

(a)

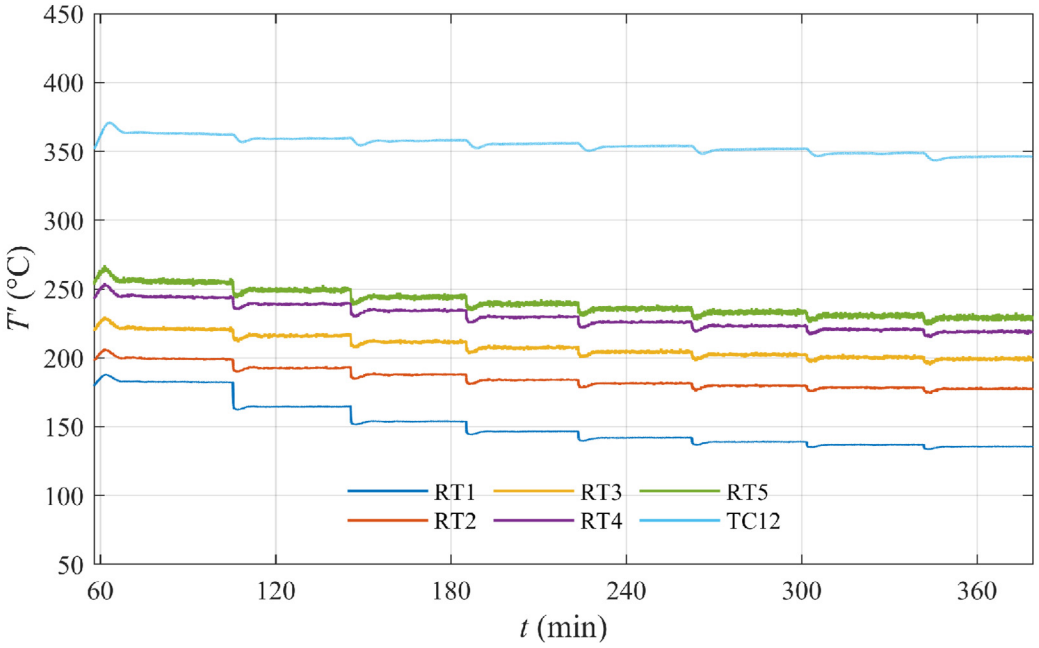

(b)

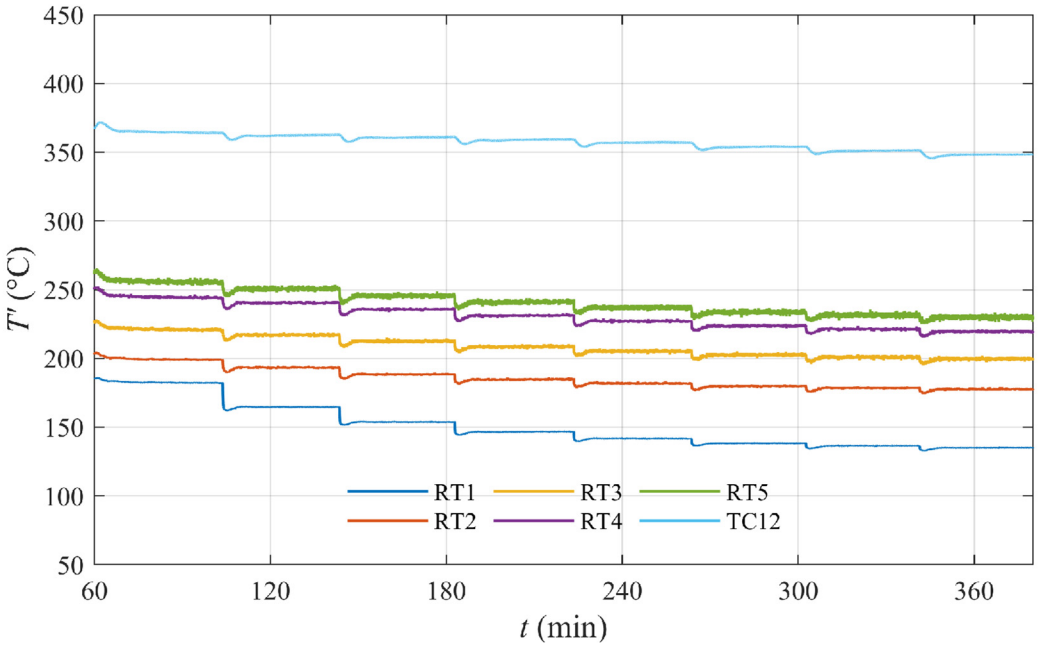

(c)

Figure B. 30 Time series of rake one measurements for (a) run 1, (b) run 2 and (c) run 3 of type C experiment (MB50 pipe).

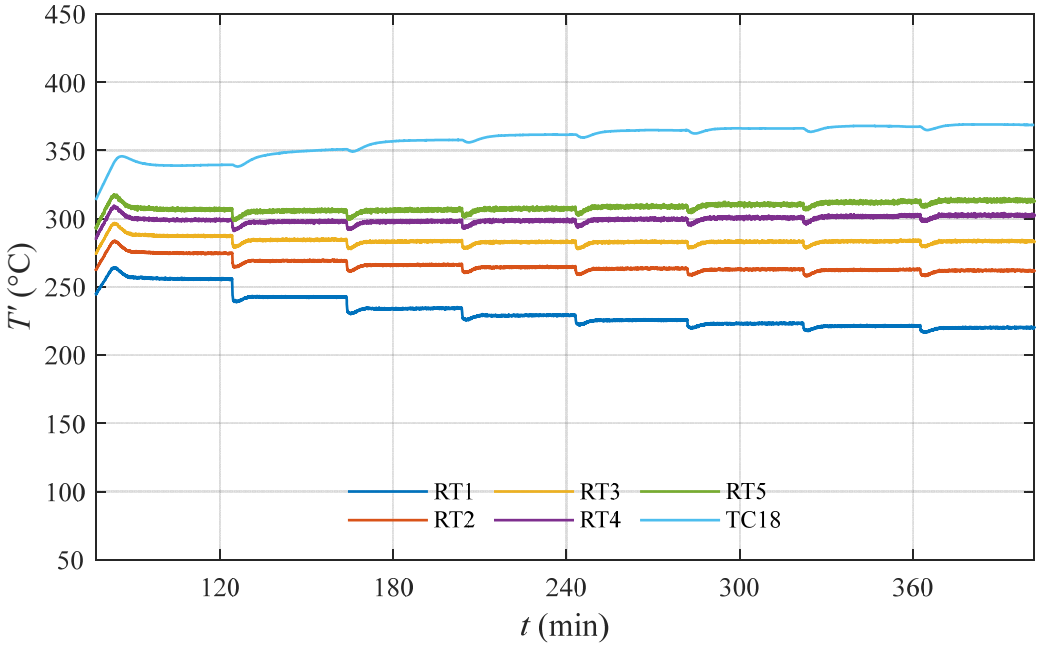
450
400
350
300
250
200
150
100
50
T′ (°C)
120
180
240
300
360
t (min)
RT1
RT2
RT3
RT4
RT5
TC18

(a)

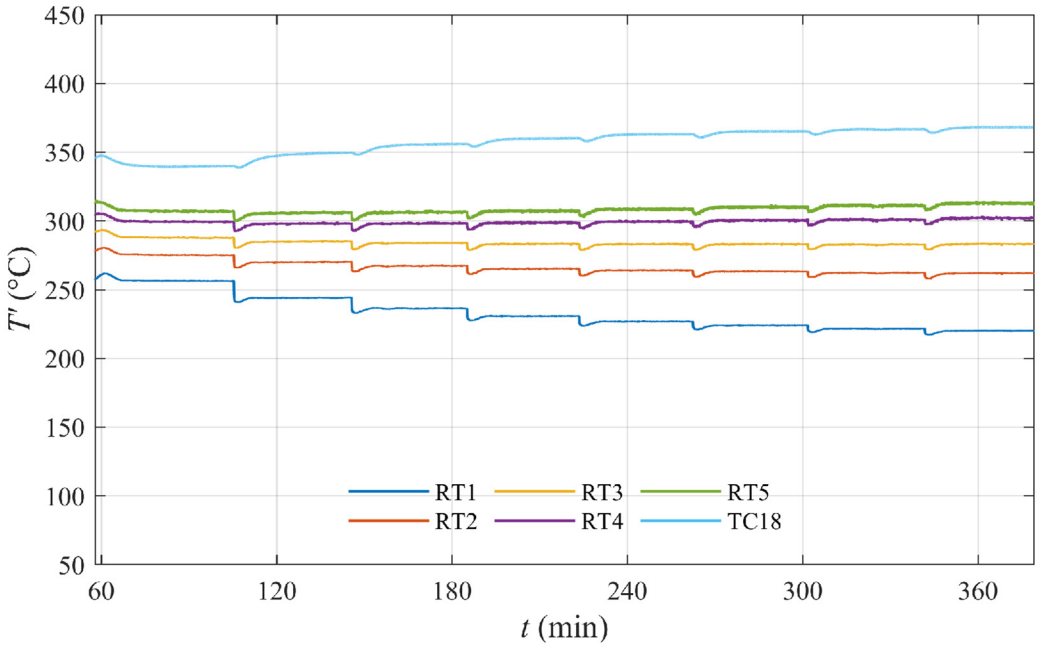
450
400
350
300
250
200
150
100
50
T′ (°C)
60
120
180
240
300
360
t (min)
RT1
RT2
RT3
RT4
RT5
TC18

(b)

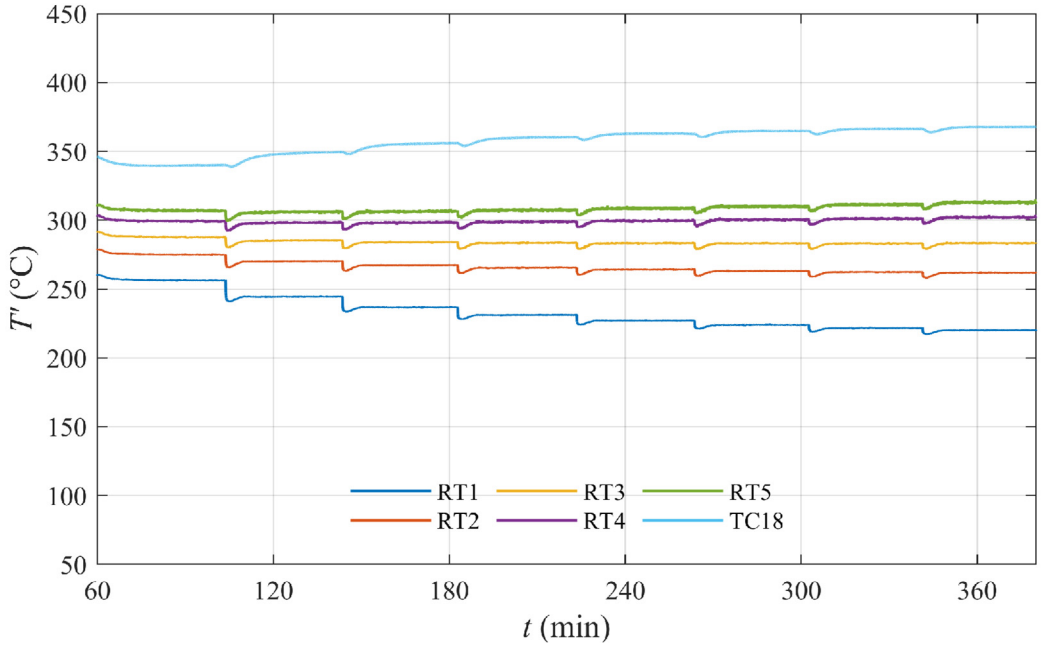

(c)

Figure B. 31 Time series of rake two measurements for (a) run 1, (b) run 2 and (c) run 3 of type C experiment (MB50 pipe).

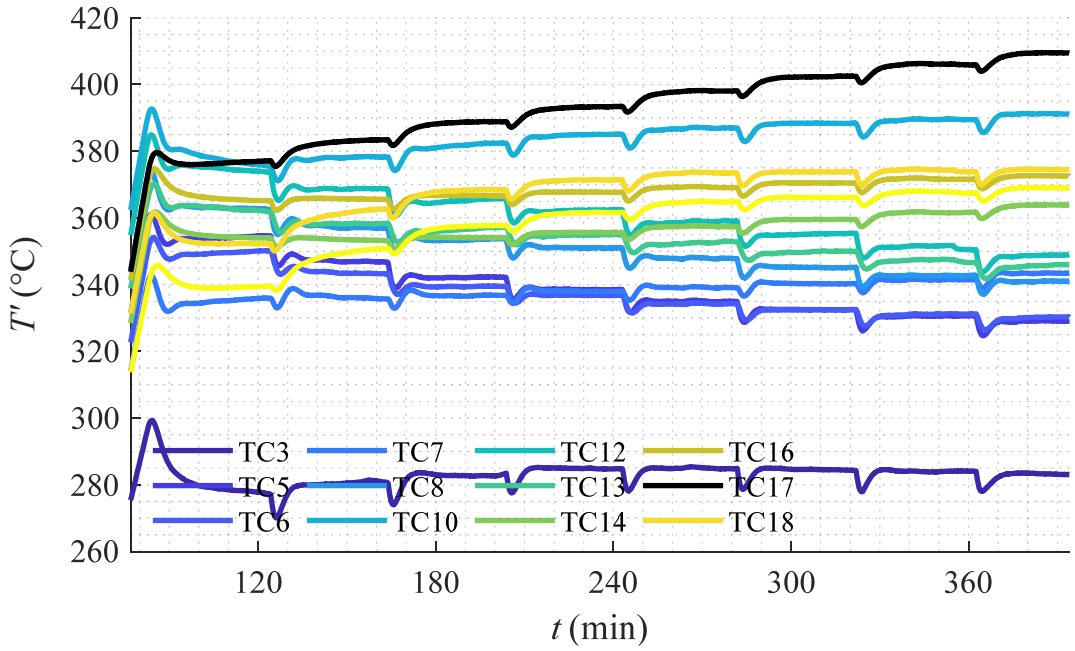

(a)

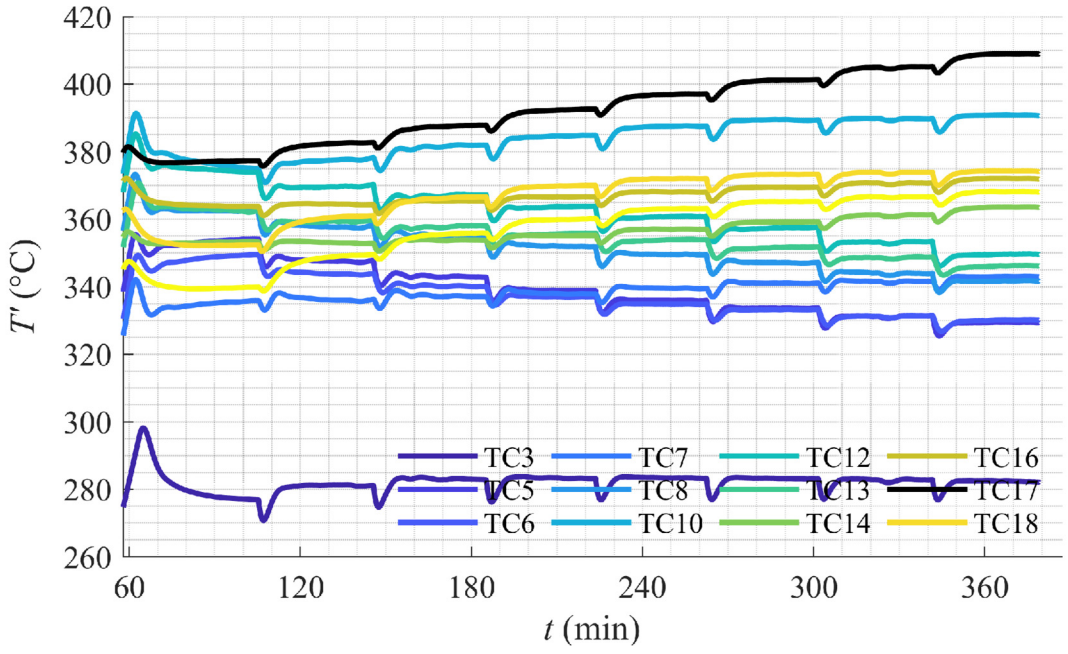

(b)

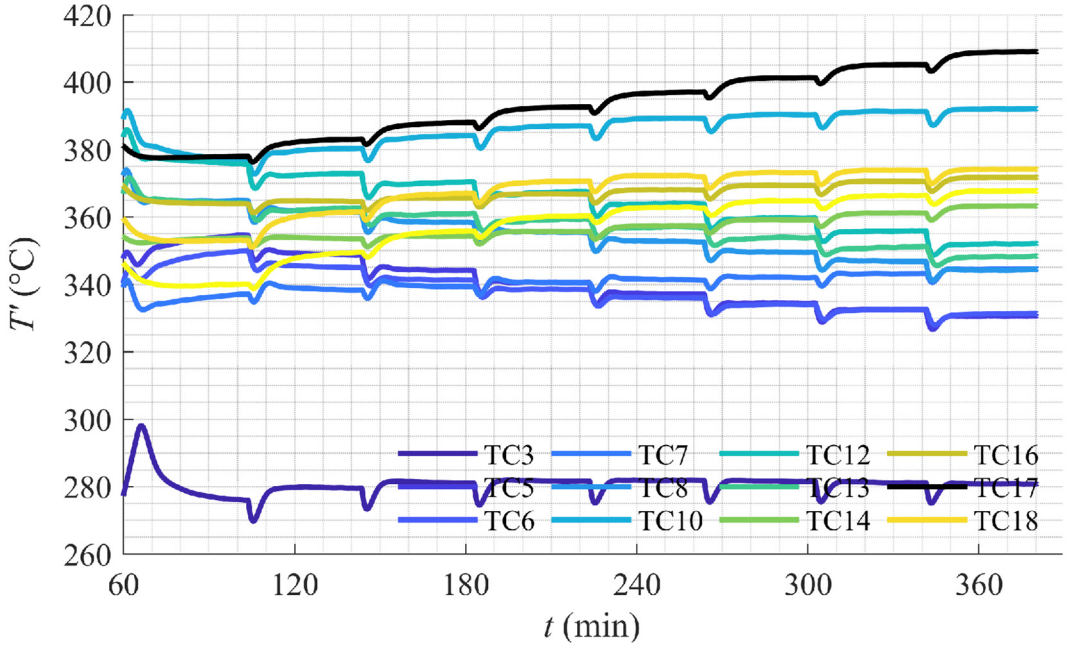

(c)

Figure B. 32 Time series of surface TC measurements for (a) run 1, (b) run 2 and (c) run 3 of type C experiment (MB50 pipe).

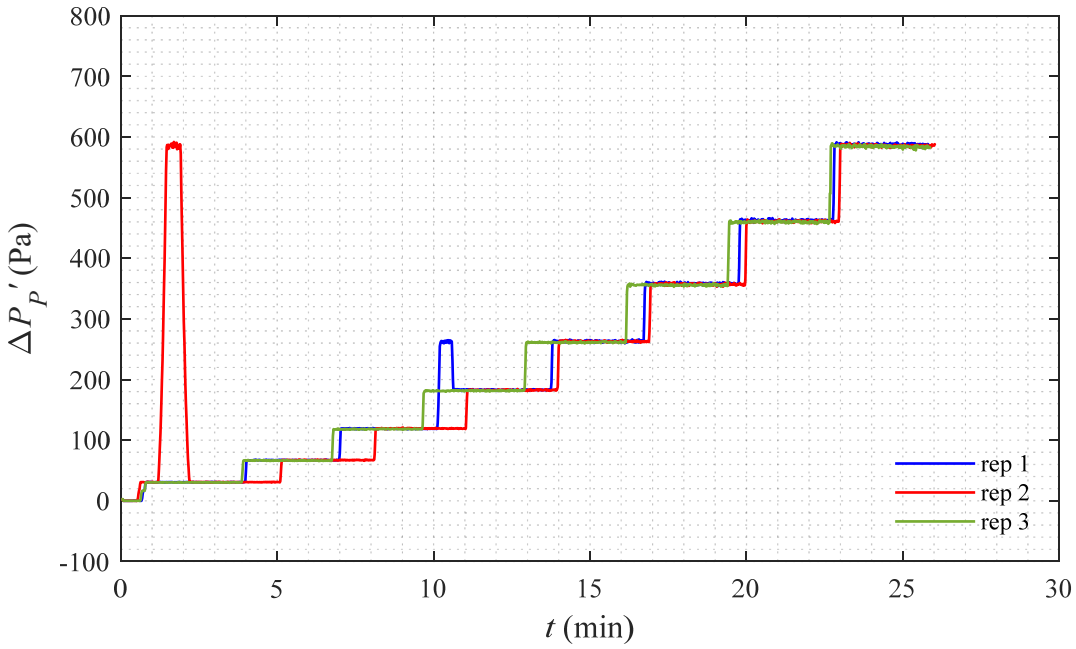

Figure B. 33 Changes of Pitot tube differential pressure over time for type A experiment (MB37 pipe).

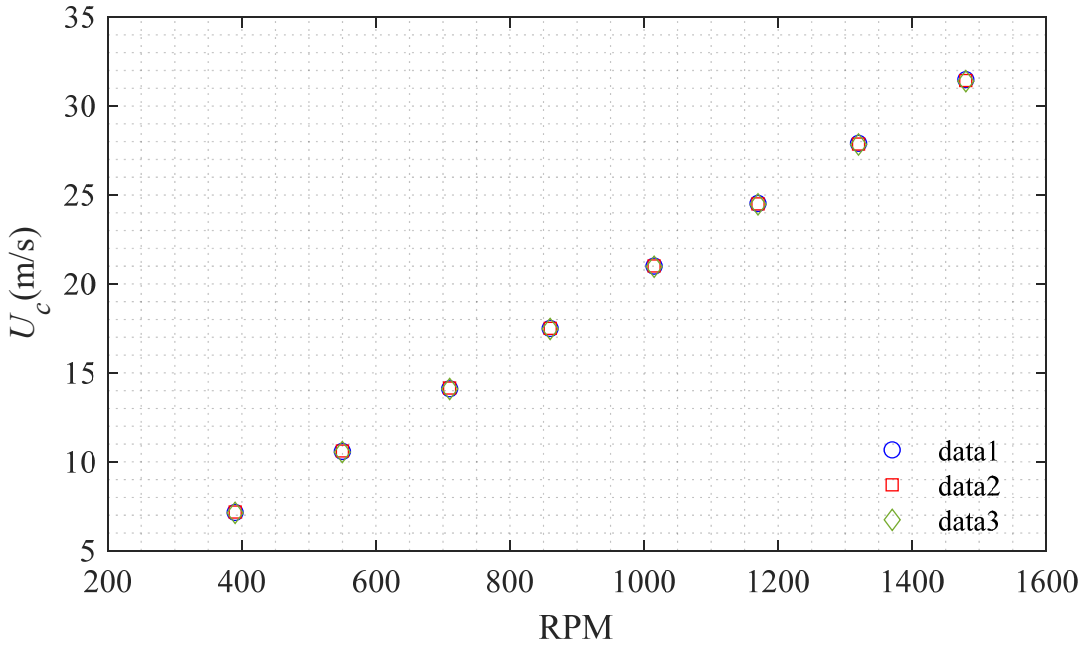

Figure B. 34 Variations of centerline velocity for different RPMs for type A experiment (MB37 pipe).

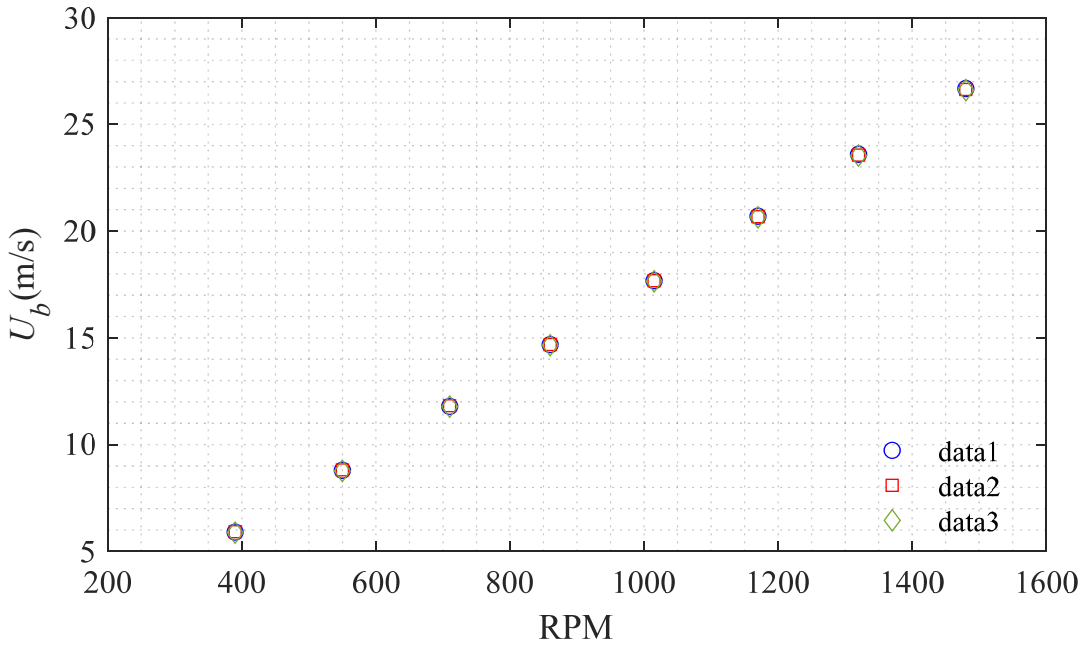

Figure B. 35 Bulk velocity changes with RPM for type A experiment (MB37 pipe).

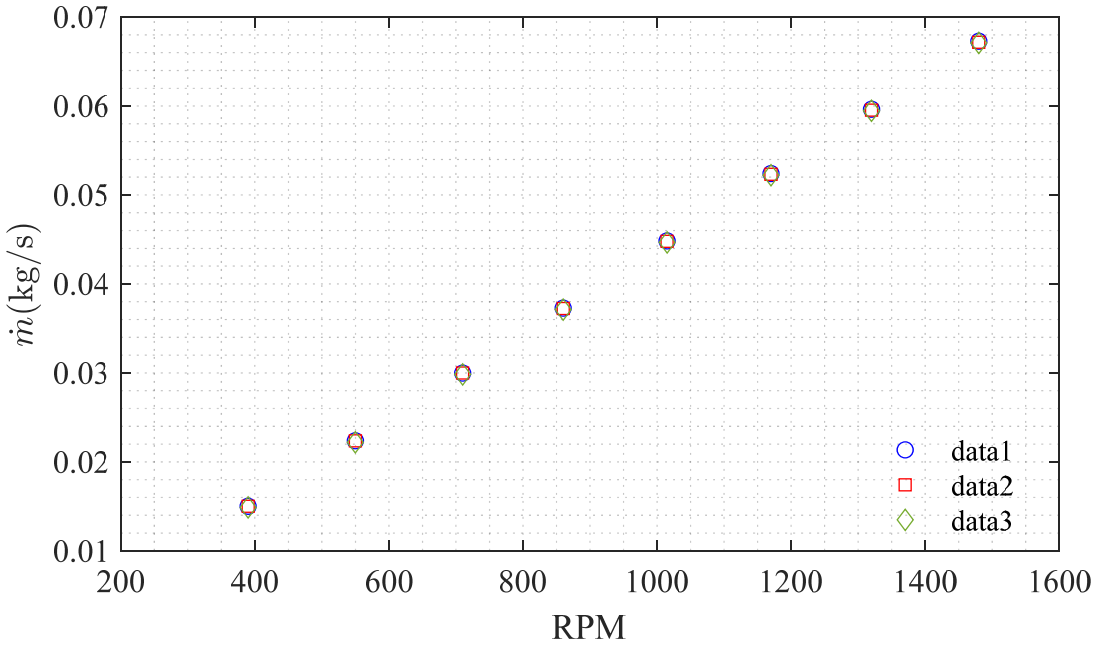

Figure B. 36 Changes of mass flow rate with RPM for type A experiment (MB37 pipe).

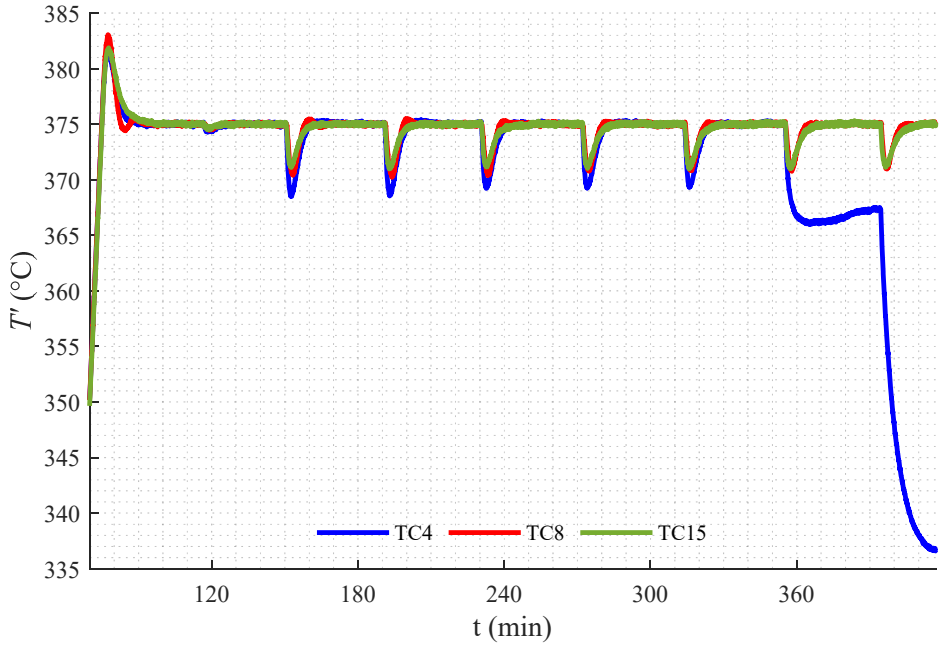

(a)

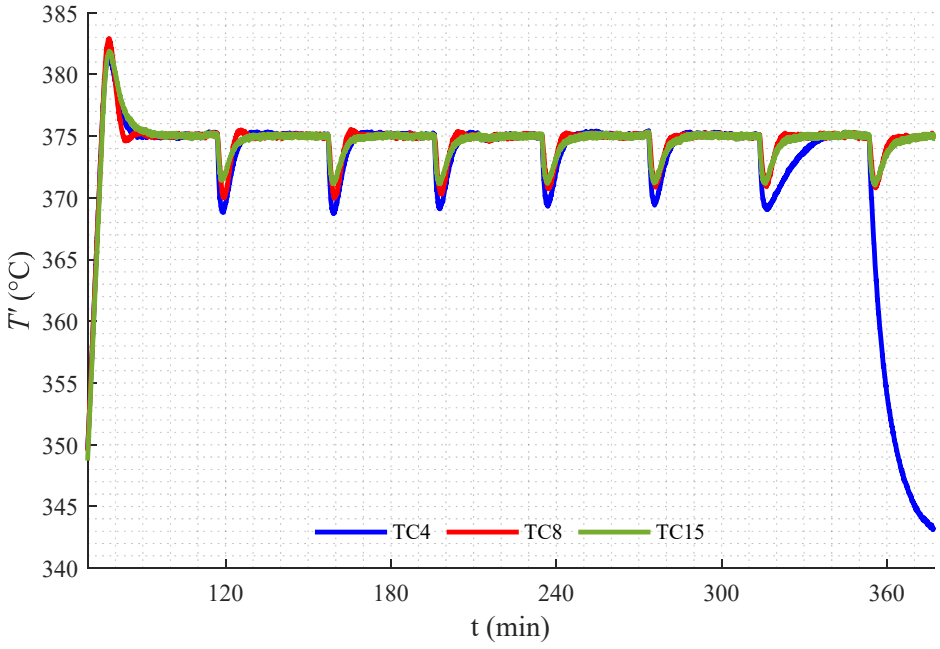

(b)

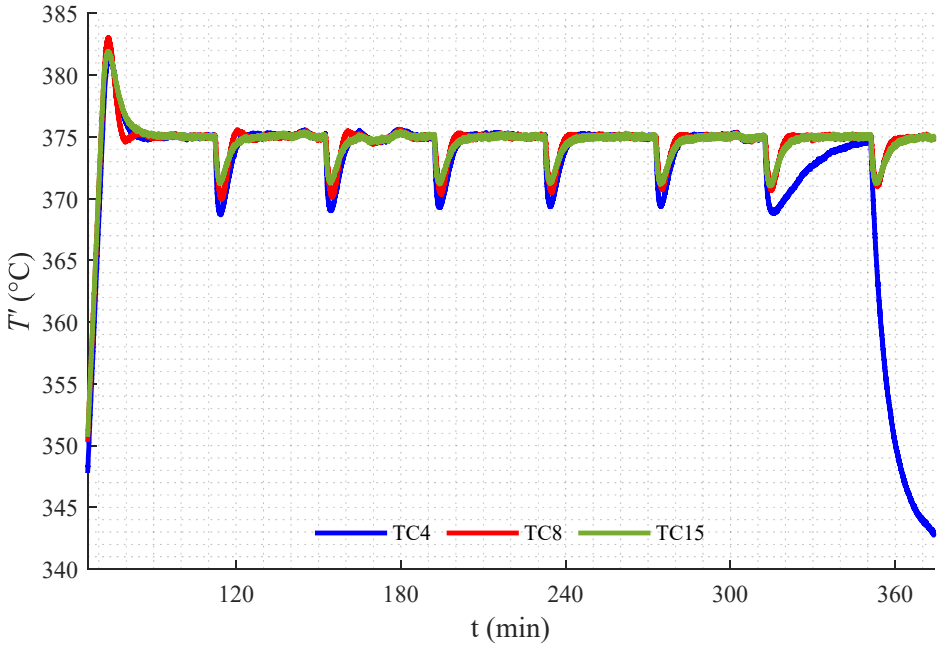

(c)

Figure B. 37 Time series of control thermocouple measurements for (a) run 1, (b) run 2 and (c) run 3 of type C experiment (MB37 pipe).

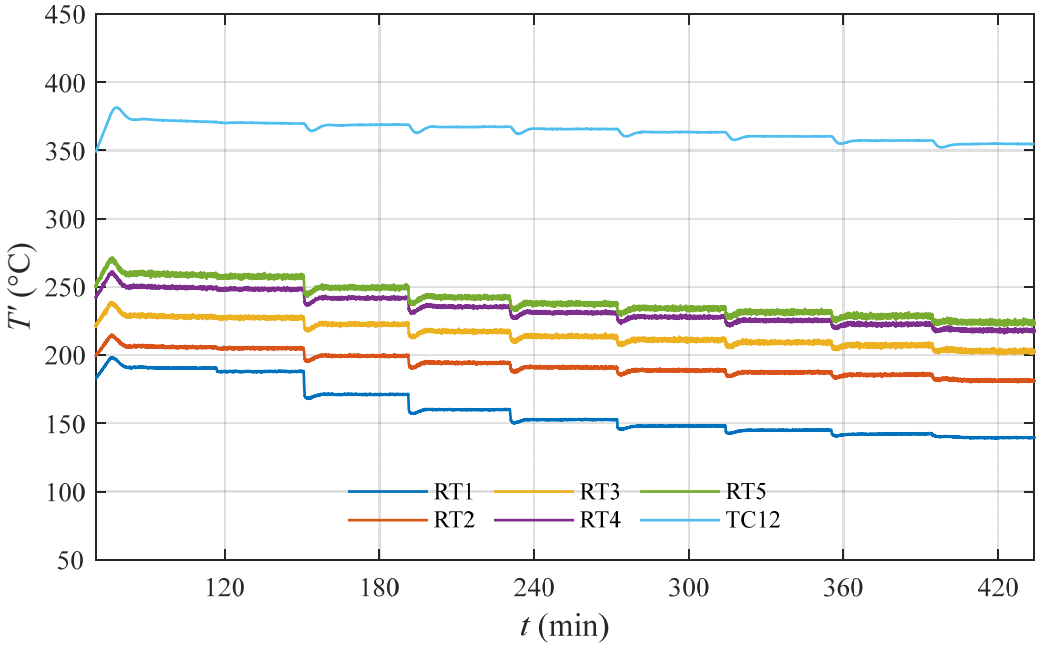
450
400
350
300
250
200
150
100
50
T′ (°C)
120
180
240
300
360
420
t (min)
RT1
RT2
RT3
RT4
RT5
TC12

(a)

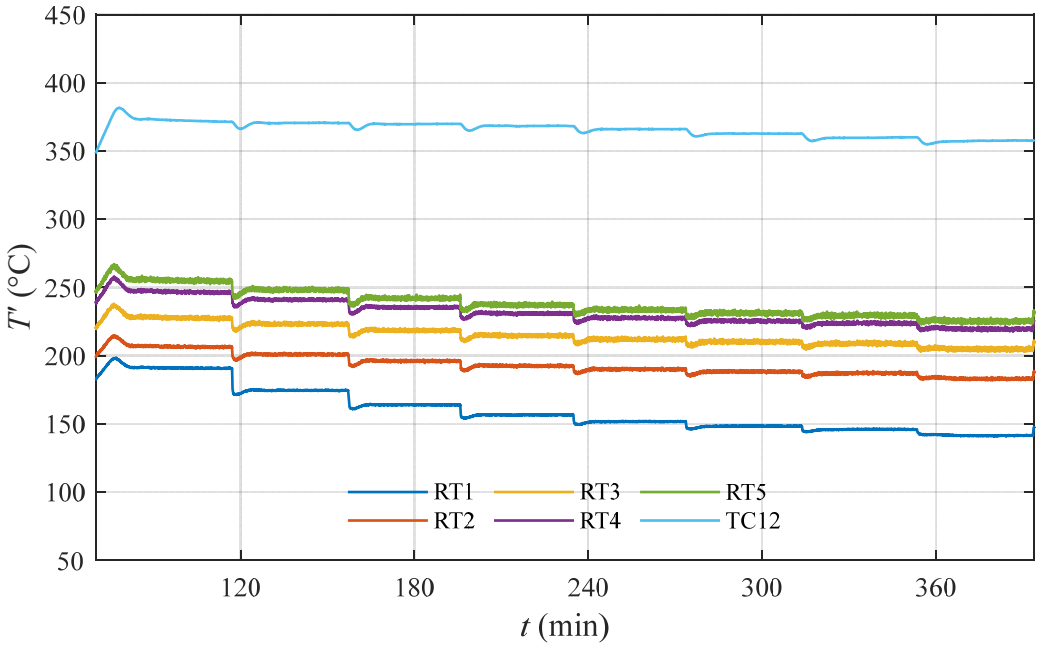
450
400
350
300
250
200
150
100
50
T′ (°C)
120
180
240
300
360
t (min)
RT1
RT2
RT3
RT4
RT5
TC12

(b)

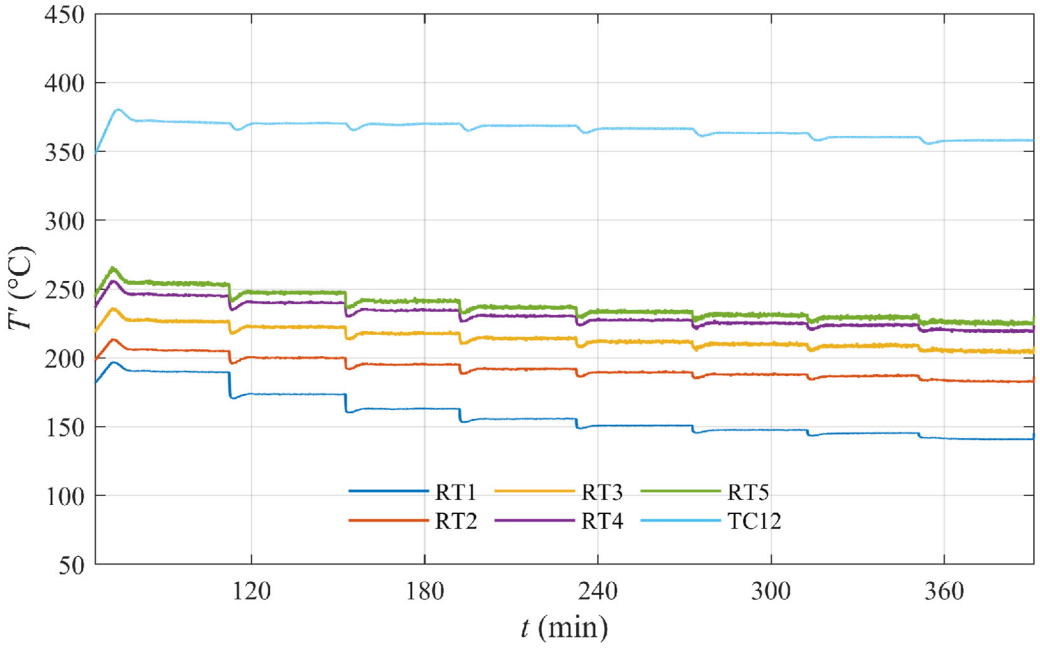

(c)

Figure B. 38 Time series of rake one measurements for (a) run 1, (b) run 2 and (c) run 3 of type C experiment (MB37 pipe).

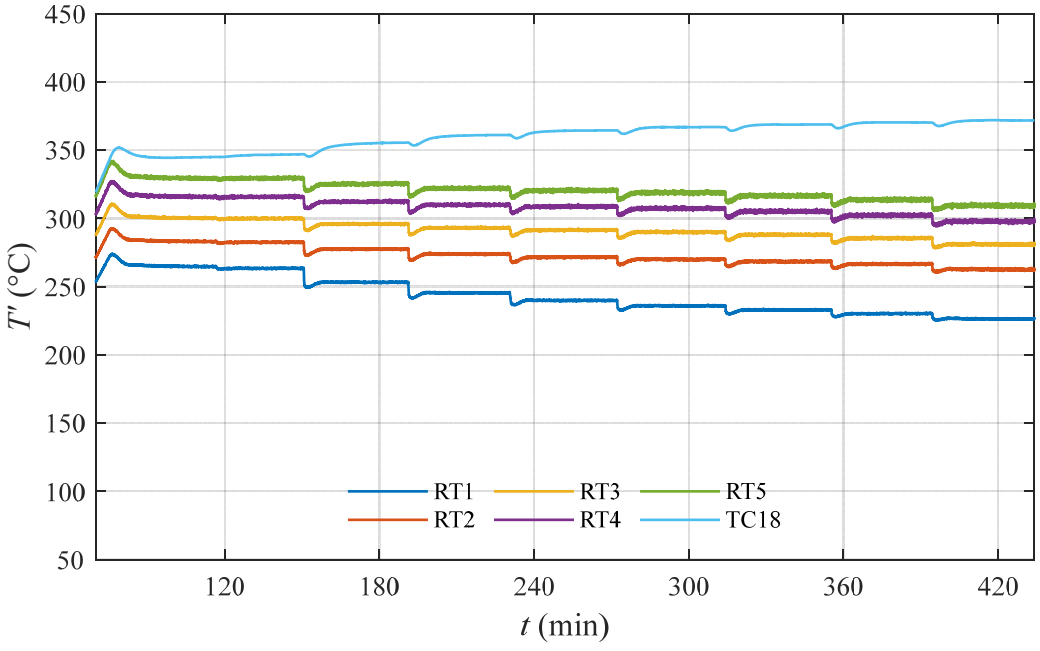

(a)

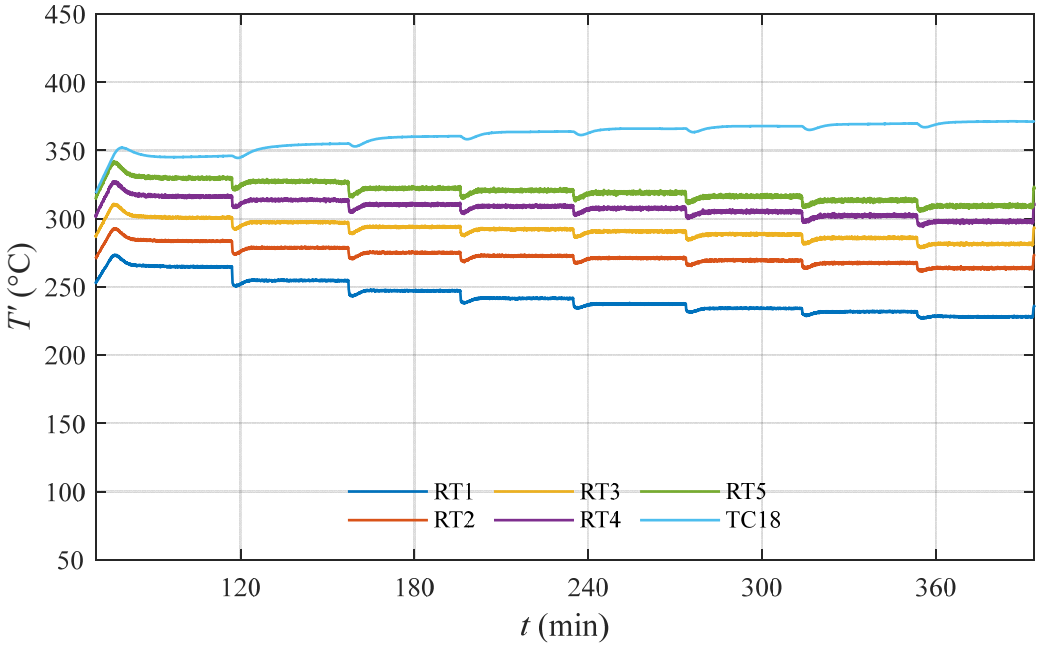

(b)

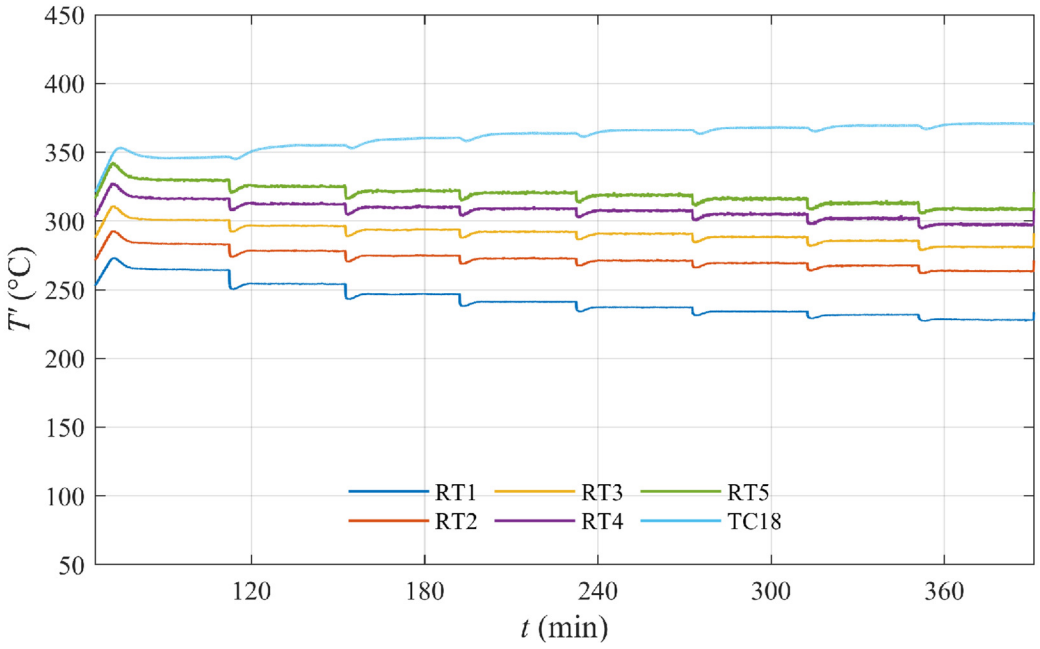

(c)

Figure B. 39 Time series of rake two measurements for (a) run 1, (b) run 2 and (c) run 3 of type C experiment (MB37 pipe).

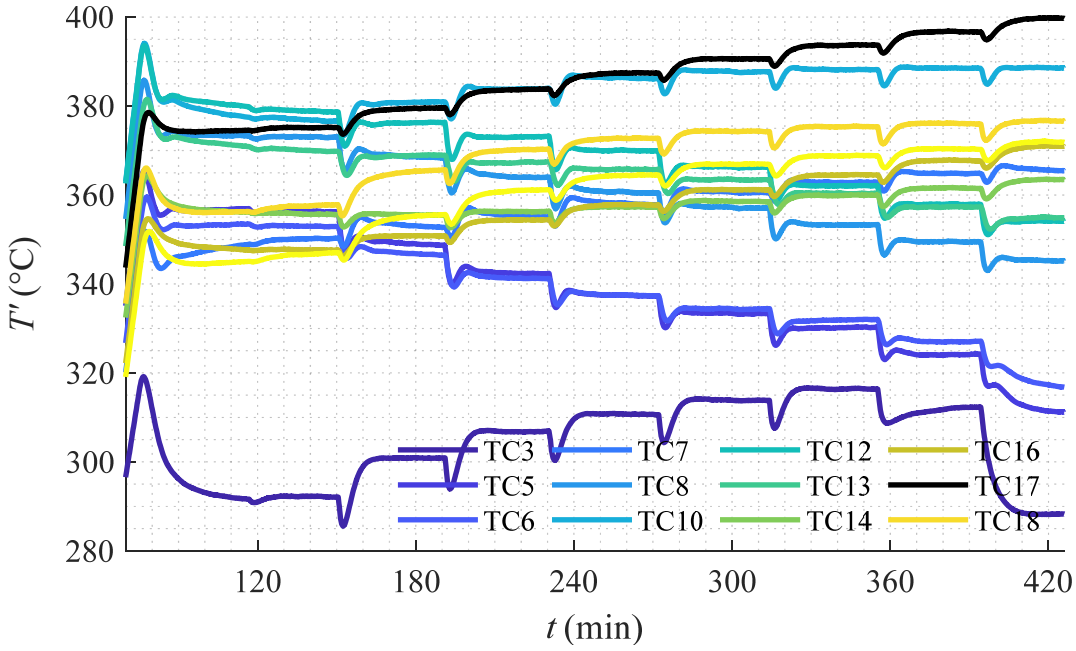
400
380
360
340
320
300
280
T′ (°C)
120
180
240
300
360
420
t (min)
TC3
TC5
TC6
TC7
TC8
TC10
TC12
TC13
TC14
TC16
TC17
TC18

(a)

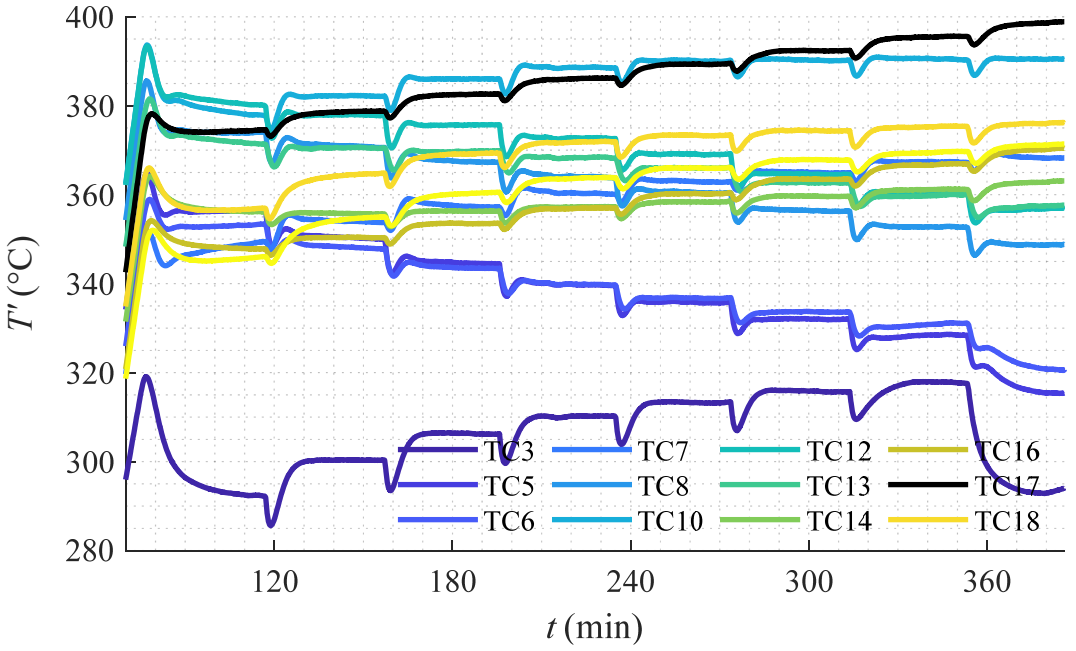
400
380
360
340
320
300
280
T′ (°C)
120
180
240
300
360
t (min)
TC3
TC5
TC6
TC7
TC8
TC10
TC12
TC13
TC14
TC16
TC17
TC18

(b)

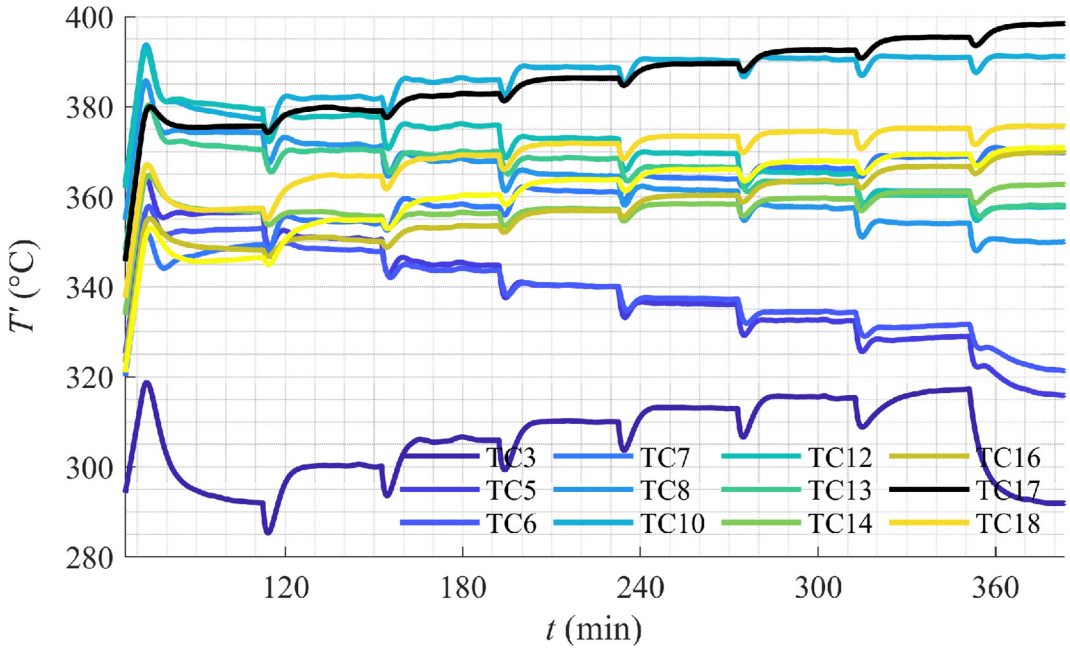

(c)

Figure B. 40 Time series of surface TC measurements for (a) run 1, (b) run 2 and (c) run 3 of type C experiment (MB37 pipe).

Table B.1. The resistances between the input terminals of the heaters.

Heater No. from the inlet to the outlet of test section	Resistance (Ω) between the inlets connected to the multimeter. O is connected X is disconnected		
	O X O	X O O	O O X
1	42.8	42.6	42.8
2	42.8	42.5	42.7
3	43.0	42.8	42.5
4	43.0	42.9	42.9
5	42.8	42.6	42.9
6	42.6	42.8	42.6
7	42.9	42.8	42.6
8	43.5	43.0	42.9
9	42.9	42.9	42.6
10	43.0	42.6	43.0
11	43.5	43.3	43.3
12	43.2	43.3	42.9
13	43.0	42.8	42.5

Appendix C.

Pressure transducer calibration

The calibration plots for the Pitot tube and test section transducers are in Figures C.1 to C.6. The vertical axis shows the applied pressure and the horizontal axis shows the measured voltages.

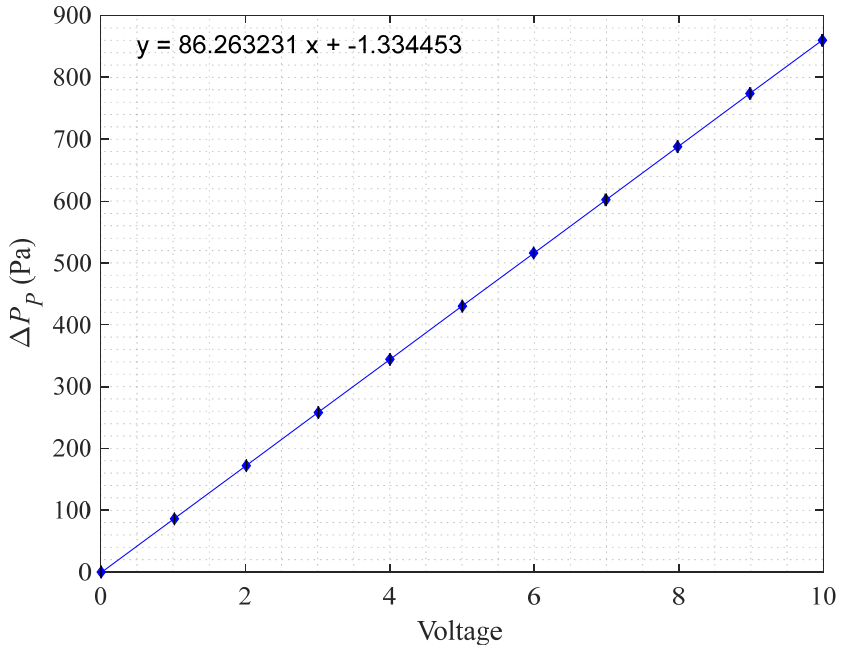

Figure C. 1 The calibration plot for the Pitot tube transducer for all experiments.

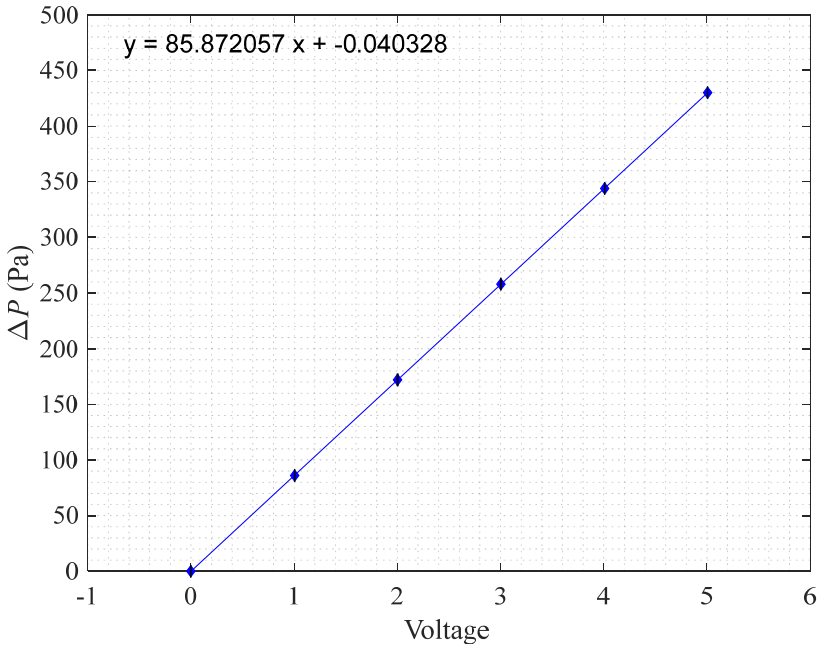

Figure C. 2 Calibration plot for test section transducer for all experiments.

Appendix D.

The wall distances of the thermocouples housed in the rakes

Table D.1 and D.2 shows the wall distances of the rake thermocouples for different experiments. Figure D.1 shows the photos taken from the rakes for the different experiments.

Table D. 1 The wall distance and wiring connections of upstream rake thermocouples.

Experiment	Thermocouple number	Wall distance (mm)
SM, type B and C experiments	RT1	25.4
	RT2	9.9
	RT3	4.9
	RT4	1.4
	RT5	0.4
MC1, type B and C experiments	RT1	25.2
	RT2	9.9
	RT3	4.8
	RT4	1.5
	RT5	0.6
MC2, MB37 and MB50, type B and C experiments	RT1	25.4
	RT2	10.0
	RT3	4.8
	RT4	1.4
	RT5	0.7

Table D. 2 The wall distance and wiring connections of downstream rake thermocouples.

Experiment	Thermocouple number	Wall distance (mm)
All experiments	RT1	25.4
	RT2	10.3
	RT3	4.93
	RT4	1.8
	RT5	0.7

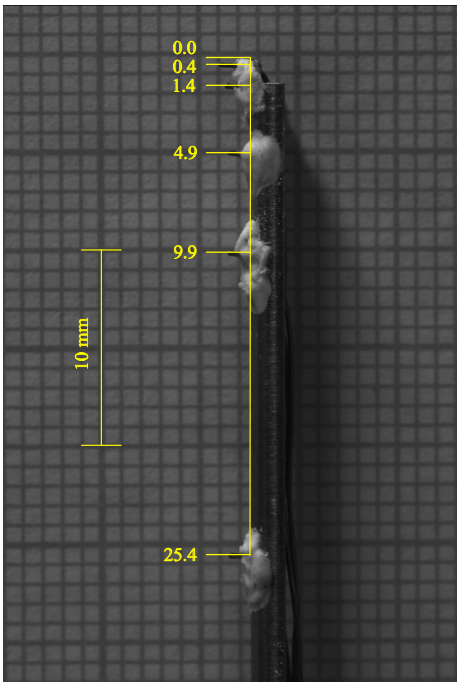

(a)

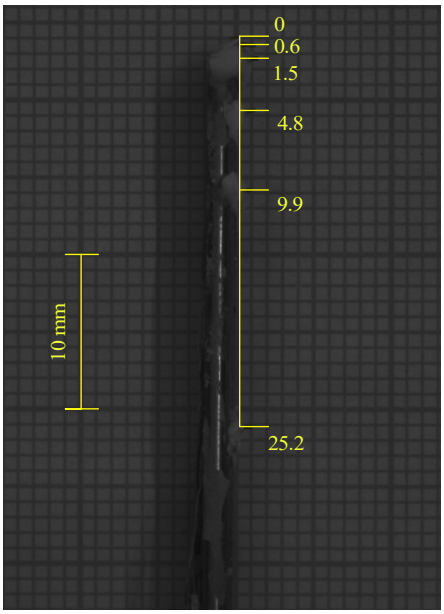

(b)

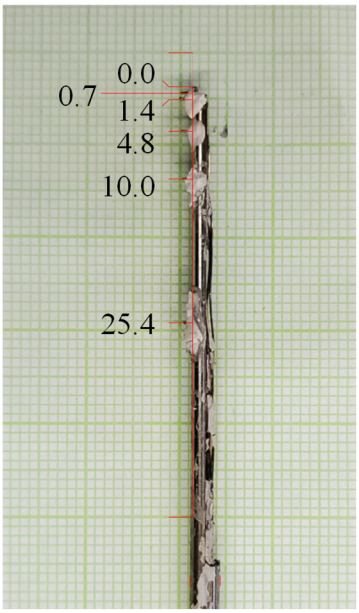

(c)

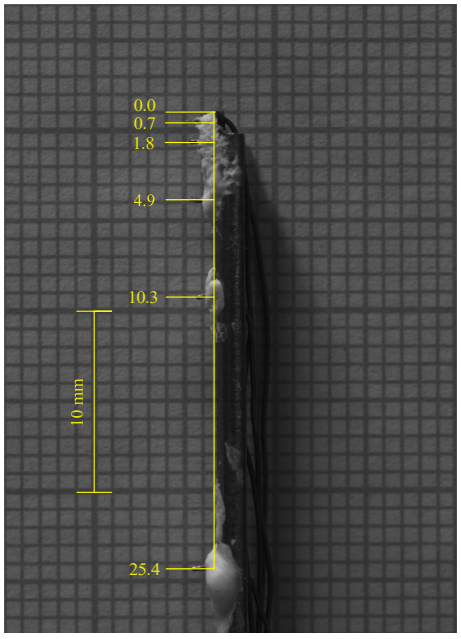

(d)

Figure D. 1 Photos taken from rake one to measure thermocouple wall distances for experiments in (a) SM and (b) MC1 and (c) 9, and (d) from rake two for all experiments.

Appendix E.

The propagation of uncertainty

The viscosity was evaluated from temperature using

$$\rho = aT^3 + bT^2 + cT + d \tag{E.1}$$

where a, b and c are constants. The uncertainty of density was obtained from

$$\delta_\rho = \sqrt{\left(\frac{\partial \rho}{\partial T}\delta_T\right)^2}, \text{ and} \tag{E.2}$$

$$\frac{\partial \rho}{\partial T} = 3aT^2 + 2bT + c \tag{E.3}$$

where temperature measurement uncertainties can be found from equation 4.30. C_p, k, and v can also be obtained from temperature using equations identical to F.1, but with different a, b, c and d values. Therefore, F.2 and F.3 was also used to find the uncertainty of these variables. The centerline velocity was obtained from Pitot measurements using equation 4.3. Uncertainty of U_c was obtained from

$$\delta_{U_c} = \sqrt{\left(\frac{\partial U_c}{\partial \rho}\delta_\rho\right)^2 + \left(\frac{\partial U_c}{\partial \Delta P_P}\delta_{\Delta P_P}\right)^2}, \tag{E.4}$$

where

$$\frac{\partial U_c}{\partial \rho} = -\sqrt{\frac{\Delta P_P}{2\rho^3}} \text{ and} \tag{E.5}$$

$$\frac{\partial U_c}{\partial \Delta P_P} = \sqrt{\frac{1}{2\rho \Delta P_P}}. \tag{E.6}$$

$\delta_{\Delta Pp}$ was found from Pitot transducer pressure measurements using equation 4.30. The uncertainty of Prandtl's friction obtained from equation 4.4 was found using

$$\delta_{f_p} = \sqrt{\left(\frac{\partial f_p}{\partial U_c}\delta_{U_c}\right)^2 + \left(\frac{\partial f_p}{\partial D}\delta_D\right)^2 + \left(\frac{\partial f_p}{\partial \nu}\delta_\nu\right)^2}, \tag{E.4}$$

where

$$\frac{\partial f_p}{\partial U_c} = \frac{2}{u_c \ln(10)\left(\frac{2}{2f_p^{3/2}} + \frac{2\nu\left(\sqrt{\frac{f_p}{8}}\left(B_1+\frac{3}{2\kappa}\right)+1\right)\left(\frac{DU_c}{2\nu\sqrt{f_p}\left(\sqrt{\frac{f_p}{8}}\left(B_1+\frac{3}{2\kappa}\right)+1\right)} - \frac{D\sqrt{f_p}U_c\left(B_1+\frac{3}{2\kappa}\right)}{16\nu\sqrt{\frac{f_p}{8}}\left(\sqrt{\frac{f_p}{8}}\left(B_1+\frac{3}{2\kappa}\right)+1\right)^2}\right)}{D\sqrt{f_p}U_c\ln(10)}\right)}, \tag{E.5}$$

$$\frac{\partial f_p}{\partial D} = \frac{2}{D \ln(10)\left(\frac{2}{2f_p^{3/2}} + \frac{2\nu\left(\sqrt{\frac{f_p}{8}}\left(B_1+\frac{3}{2\kappa}\right)+1\right)\left(\frac{DU_c}{2\nu\sqrt{f_p}\left(\sqrt{\frac{f_p}{8}}\left(B_1+\frac{3}{2\kappa}\right)+1\right)} - \frac{D\sqrt{f_p}U_c\left(B_1+\frac{3}{2\kappa}\right)}{16\nu\sqrt{\frac{f_p}{8}}\left(\sqrt{\frac{f_p}{8}}\left(B_1+\frac{3}{2\kappa}\right)+1\right)^2}\right)}{D\sqrt{f_p}U_c\ln(10)}\right)} \tag{E.6}$$

and

$$\frac{\partial f_p}{\partial \nu} = \frac{2}{\nu \ln(10)\left(\frac{2}{2f_p^{3/2}} + \frac{2\nu\left(\sqrt{\frac{f_p}{8}}\left(B_1+\frac{3}{2\kappa}\right)+1\right)\left(\frac{DU_c}{2\nu\sqrt{f_p}\left(\sqrt{\frac{f_p}{8}}\left(B_1+\frac{3}{2\kappa}\right)+1\right)} - \frac{D\sqrt{f_p}U_c\left(B_1+\frac{3}{2\kappa}\right)}{16\nu\sqrt{\frac{f_p}{8}}\left(\sqrt{\frac{f_p}{8}}\left(B_1+\frac{3}{2\kappa}\right)+1\right)^2}\right)}{D\sqrt{f_p}U_c\ln(10)}\right)}. \tag{E.7}$$

The uncertainty of pipe diameter at the Pitot, δ_D, was 0.1717 mm. The uncertainty of bulk velocity calculated from equation 4.5 was obtained from

$$\delta_{U_b} = \sqrt{\left(\frac{\partial U_b}{\partial U_c}\delta_{U_c}\right)^2 + \left(\frac{\partial U_b}{\partial f_p}\delta_{f_p}\right)^2}, \tag{E.8}$$

where

$$\frac{\partial U_b}{\partial U_c} = \frac{1}{\sqrt{\frac{f_p}{8}}\left(B_1+\frac{3}{2\kappa}\right)+1} \text{ and} \tag{E.9}$$

$$\frac{\partial U_b}{\partial f_p} = -\frac{U_c\left(B_1+\frac{3}{2\kappa}\right)}{16\sqrt{\frac{f_p}{8}}\left(\sqrt{\frac{f_p}{8}}\left(B_1+\frac{3}{2\kappa}\right)+1\right)^2}. \tag{E.10}$$

The uncertainty of *Re* was found using

$$\delta_{Re} = \sqrt{\left(\frac{\partial Re}{\partial U_b}\delta_{U_b}\right)^2 + \left(\frac{\partial Re}{\partial \nu}\delta_{\nu}\right)^2 + \left(\frac{\partial Re}{\partial D}\delta_{D}\right)^2}, \tag{E.11}$$

where

$$\frac{\partial Re}{\partial U_b} = \frac{D}{\nu}, \tag{E.12}$$

$$\frac{\partial Re}{\partial \nu} = \frac{U_b}{\nu} \text{ and} \tag{E.13}$$

$$\frac{\partial Re}{\partial D} = -\frac{DU_b}{\nu^2}. \tag{E.14}$$

The uncertainty of mass flow rate was obtained from

$$\delta_{\dot{m}} = \sqrt{\left(\frac{\partial \dot{m}}{\partial U_b}\delta_{U_b}\right)^2 + \left(\frac{\partial \dot{m}}{\partial \rho}\delta_{\rho}\right)^2 + \left(\frac{\partial \dot{m}}{\partial D}\delta_{D}\right)^2}, \tag{E.15}$$

where

$$\frac{\partial \dot{m}}{\partial \rho} = \frac{\pi D^2 U_b}{4}, \tag{E.16}$$

$$\frac{\partial \dot{m}}{\partial D} = \frac{\pi D U_b \rho}{2} \text{ and} \tag{E.17}$$

$$\frac{\partial \dot{m}}{\partial U_b} = \frac{\pi D^2 \rho}{4}. \tag{E.18}$$

The uncertainty of surface temperature was evaluated from

$$\delta_{T_s} = \sqrt{\sum_{i=13}^{17}\left(\frac{1}{4}\delta_{T_{TCi}}\right)^2}. \tag{E.19}$$

The uncertainty of bulk temperature was obtained from

$$\delta_{T_b} = \sqrt{\sum_{i=1}^{6}\left(\frac{\partial T_b}{\partial T_{RTi}}\delta_{T_{RTi}}\right)^2 + \sum_{i=1}^{5}\left(\frac{\partial T_b}{\partial r_i}\delta_{r_{u,i}}\right)^2}, \tag{E.20}$$

where

$$\frac{\partial T_b}{\partial T_{RTi}} = \frac{{r_{i+1}}^2 - {r_{i-1}}^2}{2{R_t}^2} \text{ and} \tag{E.21}$$

$$\frac{\partial T_b}{\partial r_i} = \frac{(T_{RTi-1} - T_{RTi+1})r_i}{{R_t}^2}. \tag{E.22}$$

The uncertainty of test section temperature was obtained from

$$\delta_{T_t} = \sqrt{\left(\frac{1}{2}\delta_{T_{b,u}}\right)^2 + \left(\frac{1}{2}\delta_{T_{b,d}}\right)^2}. \tag{E.23}$$

The uncertainty of Nu was obtained from

$$\delta_{Nu} = \sqrt{\left(\frac{\partial Nu}{\partial \dot{m}}\delta_{\dot{m}}\right)^2 + \left(\frac{\partial Nu}{\partial C_p}\delta_{C_p}\right)^2 + \left(\frac{\partial Nu}{\partial k}\delta_k\right)^2 + \left(\frac{\partial Nu}{\partial T_s}\delta_{T_s}\right)^2 + \left(\frac{\partial Nu}{\partial T_{u,b}}\delta_{T_{u,b}}\right)^2 + \left(\frac{\partial Nu}{\partial T_{u,d}}\delta_{T_{u,d}}\right)^2}. \tag{E.24}$$

where

$$\frac{\partial Nu}{\partial \dot{m}} = -\frac{C_p}{\pi L k}\ln\frac{T_s - T_{d,b}}{T_s - T_{u,b}}, \tag{E.25}$$

$$\frac{\partial Nu}{\partial C_p} = -\frac{\dot{m}}{\pi L k}\ln\frac{T_s - T_{d,b}}{T_s - T_{u,b}}, \tag{E.26}$$

$$\frac{\partial Nu}{\partial k} = \frac{\dot{m}C_p}{\pi L k^2}\ln\frac{T_s - T_{d,b}}{T_s - T_{u,b}}. \tag{E.27}$$

$$\frac{\partial Nu}{\partial T_s} = -\frac{\dot{m}C_p}{\pi L k}\frac{T_{d,b} - T_{u,b}}{(T_s - T_{u,b})(T_s - T_{d,b})}, \tag{E.28}$$

$$\frac{\partial Nu}{\partial T_{u,b}} = -\frac{\dot{m}C_p}{\pi L k}\frac{1}{T_s - T_{u,b}} \text{ and} \tag{E.29}$$

$$\frac{\partial Nu}{\partial T_{u,d}} = \frac{\dot{m}C_p}{\pi L k}\frac{1}{T_s - T_{d,b}}. \tag{E.30}$$

The uncertainty of bulk temperature of the test section was obtained from

$$\delta_{U_{t,b}} = \sqrt{\left(\frac{\partial U_{t,b}}{\partial \dot{m}}\delta_{U_b}\right)^2 + \left(\frac{\partial U_{t,b}}{\partial \rho}\delta_{\rho}\right)^2 + \left(\frac{\partial U_{t,b}}{\partial D}\delta_{D}\right)^2}, \tag{E.32}$$

where

$$\frac{\partial U_{t,b}}{\partial \dot{m}} = \frac{4}{\pi D_t^2 \rho_t}, \tag{E.33}$$

$$\frac{\partial U_{t,b}}{\partial \rho} = \frac{-4\dot{m}}{\pi D_t^2 \rho_t^2} \text{ and} \tag{E.34}$$

$$\frac{\partial U_{t,b}}{\partial D} = \frac{-8\dot{m}}{\pi D_t^3 \rho_t}. \tag{E.35}$$

The uncertainty of Re_t was found using equation F.11 to F.14 by substituting D, U_b and ν with D_t, $U_{t,b}$ and ν_t respectively. The uncertainty of f was obtained from

$$\delta_f = \sqrt{\left(\frac{\partial f}{\partial \Delta P}\delta_{\Delta P}\right)^2 + \left(\frac{\partial f}{\partial D_t}\delta_{D_t}\right)^2 + \left(\frac{\partial f}{\partial U_{t,b}}\delta_{U_{t,b}}\right)^2}, \tag{E.36}$$

where

$$\frac{\partial f}{\partial \Delta P} = 2\frac{1}{L}\frac{D}{\rho_t U_t^2}, \tag{E.37}$$

$$\frac{\partial f}{\partial D_t} = 2\frac{\Delta P}{L}\frac{1}{\rho_t U_t^2} \text{ and} \tag{E.38}$$

$$\frac{\partial f}{\partial U_{t,b}} = -4\frac{\Delta P}{L}\frac{D}{\rho_t U_t^3}. \tag{E.39}$$

Appendix F.

Evaluation of the Pitot tube accuracy

A three-step approach was taken to determine whether the Pitot tube measurements were accurate.

F.1. Step 1: Testing the transducer and data acquisition equipment

The pressure difference of the Pitot tube was measured once with a pressure transducer (test a) and again with a hand-held multimeter (test b). The multimeter was used to measure the differential pressure output of the Pitot tube with the blower set to different RPMs from 340 to 840. The results of the measurements are shown in Table A.1. The measurement resolution of the multimeter was 0.01 kPa, and it had only one input pressure terminal that measured absolute pressure. To estimate the differential pressure, the multimeter was connected first to the Pitot tube port that measures the total pressure. The total pressure measurements are shown in table 1 under the $P+$ column. After that, the multimeter was connected to the Pitot tube port that measures the static pressure. The static pressure measurements are shown in table 1 under the $P-$ column. The differential pressure of test b, shown in the ΔP_b column, was calculated by subtracting $P+$ from $P-$. The differential pressure of test a is shown under the ΔP_a column. The atmospheric room pressure at the time of measurement was 93.34 kPa. Figure A.1 shows the comparison between ΔP_a and ΔP_b. As can be seen, the results from the multimeter comply with the transducer results.

Table F. 1 The multimeter and transducer pressure measurements.

RPM	Total Pressure	Static Pressure	Dynamic Pressure	
	$P+$ (kPa)	$P-$ (kPa)	ΔP_b (kPa)	ΔP_a (kPa)
340	93.41	93.39	0.02	0.030
470	93.48	93.42	0.06	0.063
600	93.58	93.48	0.10	0.110
720	93.70	93.53	0.17	0.168
840	93.84	93.59	0.25	0.239

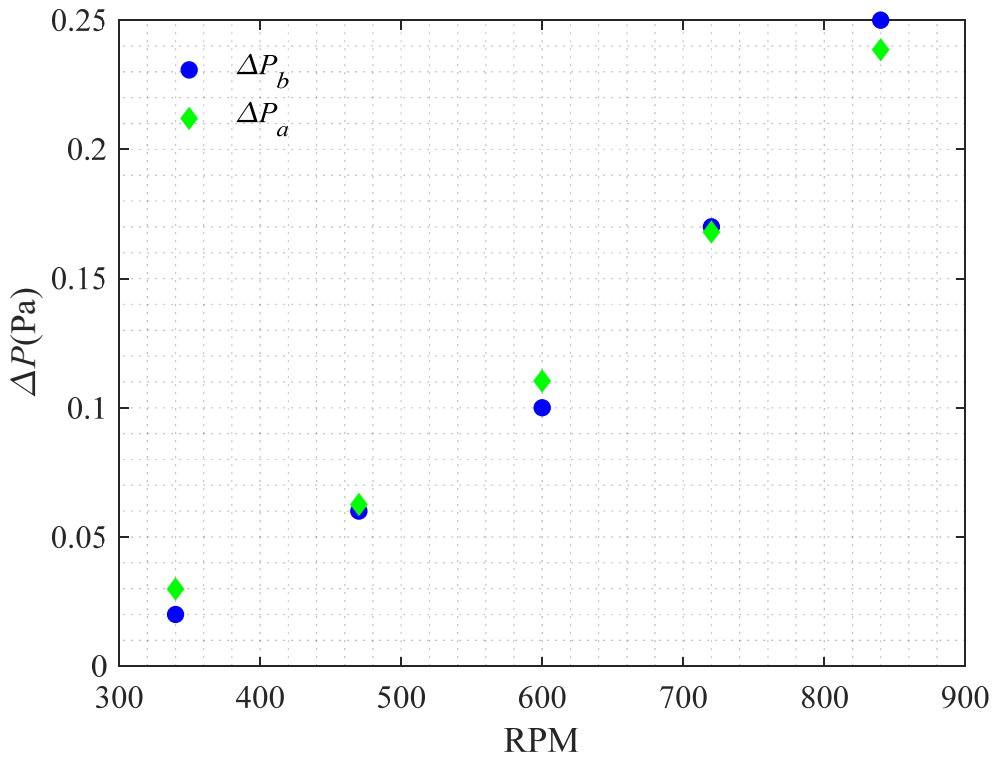

Figure F. 1 Comparison between ΔP_a and ΔP_b from Table A.1 for different RPMs.

F.2. Step 2: Testing the positioning of the Pitot

After the step 1 experiments were concluded, the position of the Pitot was readjusted, and then the Pitot tube differential pressure was measured at 840 RPM (test c). To adjust the Pitot tube, the two positions at which the Pitot meet the pipe wall was marked and then the Pitot was moved to the mid point of the marked locations. The differential pressure was logged for 5 minutes at 840 RPM after the adjustments. The average differential pressure of test c, ΔP_c, measured by the transducer was 233.68 Pa. In comparison, ΔP_a of test a at the same RPM was 238.35 Pa.

F.3. Step 3: Testing the integrity of the Pitot tube itself

The Pitot was replaced with another Pitot of the same size, and ΔP was logged at ambient (22°C) temperature and different RPMs (test d). Figures 1 and 2 show the results of test d measurements compared to test a. No significant changes can be seen between the two Pitot tube measurements.

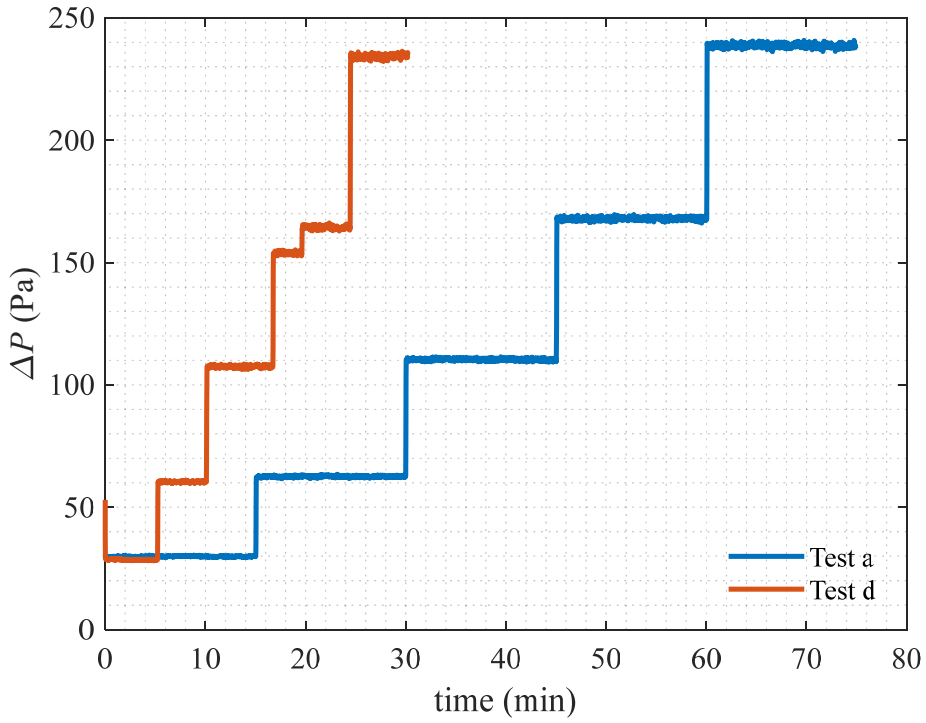

Figure F. 2 time trace of ΔP for test a and test d.